

**THE SILESIAN UNIVERSITY OF TECHNOLOGY**  
**FACULTY OF CHEMISTRY**  
**DEPARTMENT OF ORGANIC CHEMISTRY, BIOORGANIC**  
**CHEMISTRY AND BIOTECHNOLOGY**

**Ali Maruf, M.Eng.**

# **DOCTORAL DISSERTATION**

The collection of published and thematically related articles

*Trehalose releasing nanogels for autophagy stimulation*

**Supervisor: prof. dr hab. inż. Ilona Wandzik**

**Supporting supervisor: dr inż. Małgorzata Milewska**

**Gliwice 2024**

**STATEMENT 1**

I declare that my percentage contribution to the publication [P1] entitled “*Trehalose-Bearing Carriers to Target Impaired Autophagy and Protein Aggregation Diseases*” (published in **J. Med. Chem.** 2023, 66, 15613–15628. DOI: 10.1021/acs.jmedchem.3c01442) was 32%.

Justification: As part of this work, I served as a co-author for various tasks, including participation in searching for relevant literature, participation in writing of manuscript, creating figures (using BioRender or adapting from articles) and tables, preparing figure copyright permissions, managing citations, formatting the manuscript according to the journal’s style, assisting in revising the manuscript after peer review, and final proofreading.



Ali Maruf, M.Eng.  
(PhD candidate)

As the corresponding author of the above-mentioned publication, which is part of the doctoral thesis of Mr. Ali Maruf, I declare that the percentage contribution of the remaining co-authors can be estimated as follows:

Milewska M: 32%

Varga M: 4%

Wandzik I: 32%



prof. dr hab. inż. Ilona Wandzik  
(Supervisor / corresponding author)

## Trehalose-Bearing Carriers to Target Impaired Autophagy and Protein Aggregation Diseases

Ali Maruf,<sup>1</sup> Małgorzata Milewska,<sup>1</sup> Máté Varga, and Ilona Wandzik<sup>\*,1</sup>Cite This: *J. Med. Chem.* 2023, 66, 15613–15628

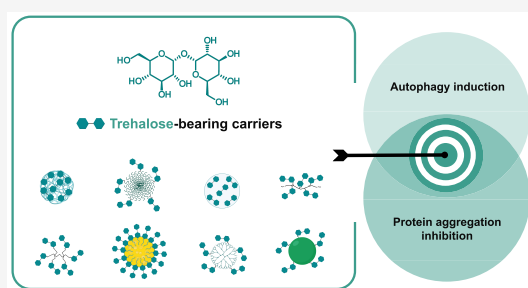
Read Online

ACCESS |

Metrics &amp; More

Article Recommendations

**ABSTRACT:** In recent years, trehalose, a natural disaccharide, has attracted growing attention because of the discovery of its potential to induce autophagy. Trehalose has also been demonstrated to preserve the protein's structural integrity and to limit the aggregation of pathologically misfolded proteins. Both of these properties have made trehalose a promising therapeutic candidate to target autophagy-related disorders and protein aggregation diseases. Unfortunately, trehalose has poor bioavailability due to its hydrophilic nature and susceptibility to enzymatic degradation. Recently, trehalose-bearing carriers, in which trehalose is incorporated either by chemical conjugation or physical entrapment, have emerged as an alternative option to free trehalose to improve its efficacy, particularly for the treatment of neurodegenerative diseases, atherosclerosis, nonalcoholic fatty liver disease (NAFLD), and cancers. In the current Perspective, we discuss all existing literature in this emerging field and try to identify key challenges for researchers intending to develop trehalose-bearing carriers to stimulate autophagy or inhibit protein aggregation.



## 1. SIGNIFICANCE

- Trehalose is considered a promising therapeutic candidate to combat autophagy-related disorders and diseases associated with protein aggregation.
- Given the increase in clinical trials of free trehalose and the problems associated with its poor bioavailability, it is expected that innovative strategies for the delivery of trehalose will be of great importance soon.
- Potential strategies for the development of trehalose-bearing carriers as alternatives to free trehalose have recently been the focus of extensive study.

## 2. INTRODUCTION

Trehalose is a naturally occurring homodisaccharide composed of two D-glucose units linked at their anomeric positions by an  $\alpha, \alpha'$ -1,1'-glycosidic bond. Trehalose is widely distributed in nature and is biosynthesized by many classes of organisms, such as bacteria, yeast, fungi, plants, and invertebrates. However, its biosynthetic pathways have not been found in vertebrates, including mammals.<sup>1,2</sup> In recent years, trehalose has attracted growing attention as a promising therapeutic thanks to numerous *in vitro* and *in vivo* studies indicating its ability to stimulate autophagy.<sup>3</sup> To date, the therapeutic potential of trehalose attributed to its autophagy stimulation effect has been studied for diseases such as diabetes and nonalcoholic fatty liver disease (NAFLD),<sup>4,5</sup> atherosclerosis,<sup>6,7</sup>

and ischemic-related diseases.<sup>8,9</sup> However, the main focus is to demonstrate the utility of trehalose in the treatment of neurodegenerative diseases, including Parkinson's disease (PD),<sup>10,11</sup> Lewy body dementia,<sup>12</sup> Alzheimer's disease (AD),<sup>13</sup> and amyotrophic lateral sclerosis (ALS).<sup>14</sup> Trehalose also exerts neuroprotection through antiaggregation effects.<sup>15,16</sup> Several studies have shown that trehalose can directly maintain the protein's structural integrity and limit the aggregation of pathologically misfolded proteins.<sup>17</sup>

Currently, there are several ongoing clinical trials with trehalose for the treatment of neurodegenerative diseases and other disorders where trehalose is believed to be an autophagy activator or inhibitor of protein aggregation. Recent clinical trials in various developmental stages are described in Table 1.

Unfortunately, the therapeutic application of trehalose has some limitations. Free trehalose has poor bioavailability because it can be readily hydrolyzed into glucose molecules by trehalase-specific enzyme, trehalase, which is found primarily in the small intestine.<sup>2</sup> Moreover, without external

Received: August 6, 2023

Revised: November 2, 2023

Accepted: November 15, 2023

Published: November 30, 2023



Table 1. Summary of Clinical Trials on Trehalose As an Active Ingredient<sup>a</sup>

disease	delivery	phase	stage	year (first posted)	clinical trial identifier	sponsor
spinocerebellar ataxia type 3	oral		recruiting	05/2020	NCT04399265	National University of Malaysia
spinocerebellar ataxia type 3	intravenous infusion	II/III	active, not recruiting	08/2022	NCT05490563	Seelos Therapeutics, Inc.
amyotrophic lateral sclerosis	intravenous infusion	II/III	recruiting	03/2020	NCT04297683	Merit E. Cudkowicz, MD
amyotrophic lateral sclerosis	intravenous infusion	II/III	enrolling by invitation	09/2021	NCT05136885	Merit E. Cudkowicz, MD
amyotrophic lateral sclerosis	intravenous infusion		available (expanded access)	10/2022	NCT05597436	Seelos Therapeutics, Inc.
acute coronary syndrome	intravenous infusion	II	unknown	09/2018	NCT03700424	Mashhad University of Medical Sciences
Alzheimer's disease	intravenous infusion	II	withdrawn (no results posted)	04/2022	NCT05332678	Seelos Therapeutics, Inc.
Parkinson's disease	oral	IV	not yet recruiting	05/2022	NCT05355064	Neuromed IRCCS
type 2 diabetes	oral	early I	recruiting	10/2022	NCT05593549	Medical College of Wisconsin

<sup>a</sup>Source: [www.clinicaltrials.gov](http://www.clinicaltrials.gov) (accessed on 1 September 2023).

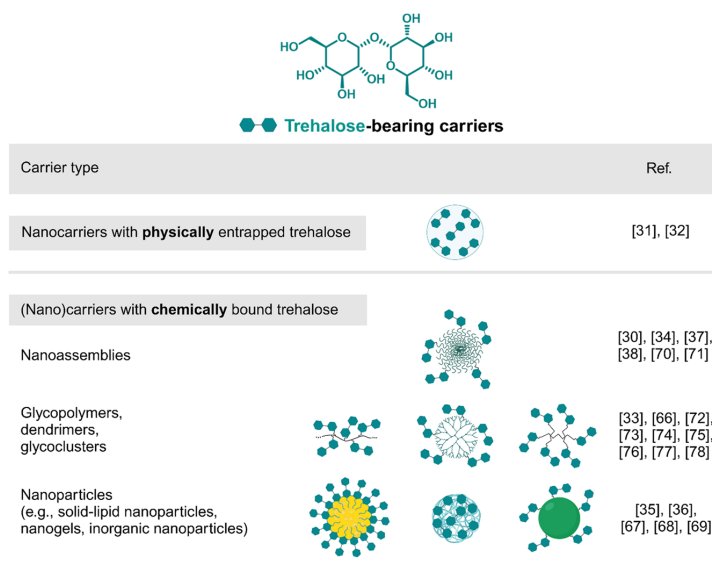
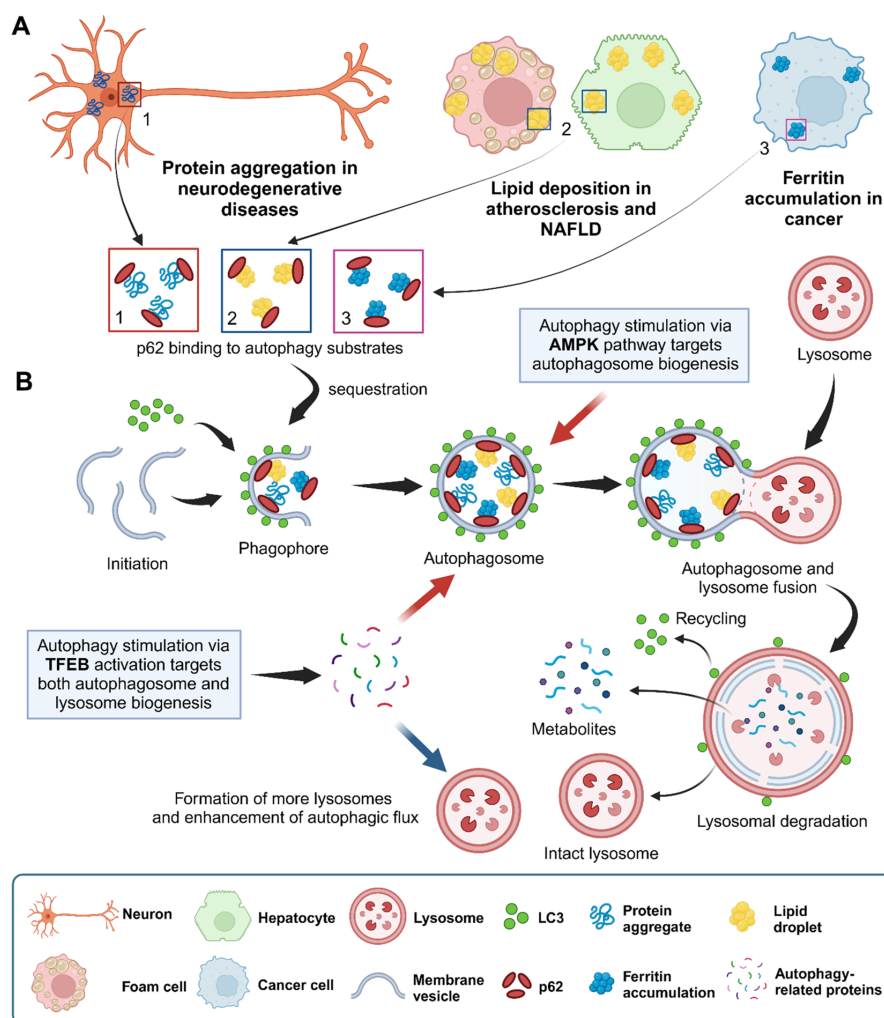


Figure 1. Chemical structure of trehalose and types of trehalose-bearing carriers for autophagy induction and inhibition of protein aggregation.

interventions (e.g., electroporation, ultrasound, and osmotic stress), free trehalose is poorly taken up by the cells because of its strong hydrophilicity that hampers its ability to cross phospholipid bilayers of the cell membrane.<sup>18</sup> Therefore, many studies suggest that trehalose should be used in relatively high doses of 100 mM (*in vitro*) and 2–3 g/kg/day and 2–4% (w/v) (*in vivo*; intraperitoneal and oral administration, respectively) to retain its potential.<sup>3</sup> Oral administration of high doses of trehalose is also undesirable given the recent report linking dietary trehalose to increased prevalence of epidemic *Clostridium difficile* strains.<sup>19</sup> Because of such limitations, it would be beneficial to improve the delivery of trehalose to specific target cells and tissues while also protecting trehalose from enzyme-induced hydrolysis. One of the strategies is the use of nanosized trehalose carriers in which trehalose can be incorporated either by chemical conjugation or by physical entrapment before administration. These nanocarriers have some advantages over simple trehalose conjugates, which are

another possible strategy to deliver trehalose. The use of trehalose-containing nanocarriers provides protection of trehalose against enzymatic degradation, improves the systemic circulation and bioavailability of trehalose, and could improve targeting of desired cells through the attachment of targeting moieties.

Trehalose-bearing carriers have been extensively developed for various biomedical applications, e.g., protein and peptide stabilization and delivery, gene delivery, bacteria-targeted applications, cell culture, and cryopreservation.<sup>20,21</sup> However, the field of their utilization to target autophagy induction or inhibition of protein aggregation is still in its infancy, and just over 20 trehalose-bearing carriers have currently been developed for these purposes. Trehalose-bearing carriers targeting these two effects can be categorized into several groups: nanocarriers with physically entrapped trehalose, nanoassemblies, glycopolymers, dendrimers, glycoclusters, and nanoparticles (e.g., solid lipid nanoparticles, inorganic



**Figure 2.** (A) Various autophagy substrates associated with impaired autophagy diseases. (B) Autophagy stimulation via the TFEB and AMPK pathways.

nanoparticles, and nanogels) (Figure 1). Moreover, the two approaches can be distinguished by the way in which trehalose is bound. In the first approach, trehalose is physically entrapped within a carrier or covalently bound through a labile bond. Thanks to this, it can be released. In the second strategy, trehalose is permanently bound to the carrier and nonreleasable, and the desired effect is studied for “poly-(trehalose)” species containing multiple copies of trehalose within one macromolecule or nanoparticle.

The current Review aims to discuss all of the trehalose-bearing carriers that have been developed to stimulate autophagy or inhibit protein aggregation, as well as to clarify perspectives for this field. The number of currently ongoing clinical trials on the use of free trehalose in therapies is constantly growing, and it is likely that future research in this area will include the study of trehalose carriers as an alternative to free trehalose.

### 3. TREHALOSE-BEARING CARRIERS FOR INDUCTION OF AUTOPHAGY

Autophagy is a highly conserved cellular recycling process that controls the degradation of damaged organelles and cytosolic proteins, including misfolded proteins. Many human disorders are strongly correlated with the malfunctioning of autophagy, including neurodegenerative diseases, atherosclerosis, NAFLD, and cancer.<sup>22–26</sup> Targeting autophagy stimulation can be a therapeutic approach for the degradation of aggregated proteins or Lewy bodies associated with neurodegeneration, removal of oxidized lipids associated with atherosclerosis, removal of triglycerides associated with NAFLD, and clearance of accumulated ferritin associated with cancer (Figure 2A).<sup>23,24</sup> Autophagy mechanisms can be categorized into three main types on the basis of how intracellular materials are transported to lysosomes, namely, microautophagy, macroautophagy, and chaperone-mediated autophagy. Macroautophagy is believed to

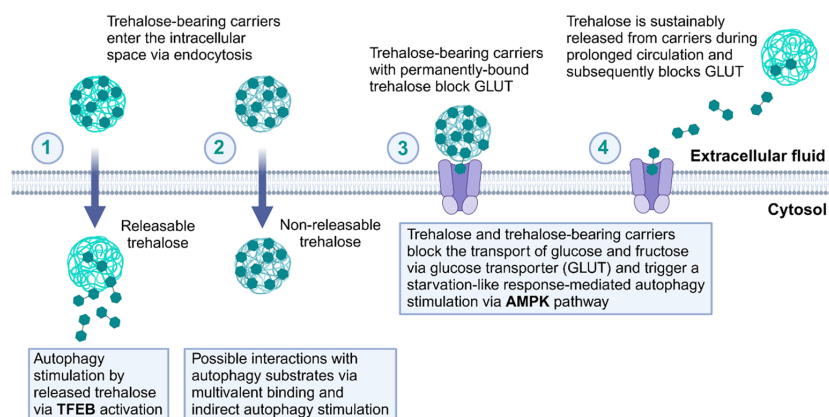


**Figure 3.** Four possible pathways through which trehalose-bearing carriers can stimulate autophagy.

be the main pathway with a significant catabolic potential for degrading cytoplasmic proteins and organelles. The term “autophagy” is usually used as a synonym for macroautophagy, and hereafter, when referring to the macroautophagy, we simply use the term “autophagy.”

The activation of autophagy leads to the binding of sequestosome 1 (SQSTM1/p62) to autophagy substrates, sequestration into double-membrane vesicles to form a phagophore involving microtubule-associated protein 1A/1B-light chain 3 (LC3), and the formation of the autophagosome (Figure 2B). The second step of autophagy is the fusion of the autophagosome with a lysosome to form the autolysosome, where the substrates can be degraded into metabolites by lysosomal proteases. Both p62 and LC3 are commonly used to quantify autophagic flux.

To date, two main pathways have been proposed by which trehalose kickstarts autophagy. The first pathway is that trehalose blocks the transport of glucose and fructose through glucose transporter family proteins (GLUTs), thereby generating a starvation like (low adenosine triphosphate) state, which in turn triggers autophagy via the activation of AMP-activated protein kinase (AMPK) and unc-51-like kinase 1 (ULK1).<sup>5,27,28</sup> The second pathway is that trehalose stimulates autophagy via transcription factor EB (TFEB) activation, which results in increased expression of lysosomal hydrolases and membrane proteins and various autophagy-related components.<sup>29</sup>

It follows from the above that the mechanisms of autophagy induction involving free trehalose have been extensively studied, but there are no reports on how carriers containing trehalose could function, especially those that contain covalently bound, nonreleasable trehalose. Several mechanisms of action of trehalose-bearing carriers can be hypothesized, including (1) the carrier penetrates the cell via endocytosis and releases trehalose inside the cell, which induces autophagy via TFEB; (2) the carrier decorated with pendant and permanently bound trehalose penetrates the cell via endocytosis and interacts directly with autophagy substrates, which causes indirect stimulation of autophagy; (3) the carrier causes a multivalent interaction with GLUT and consequently blocks the transporter and stimulates autophagy via the AMPK pathway; and (4) trehalose is released from the carrier in the extracellular space and interacts with GLUT, which results in a

similar effect (Figure 3). The current studies on trehalose-bearing carriers for autophagy stimulation are summarized in Table 2.

The first attempt to use trehalose-bearing carriers to stimulate autophagy came from the Seneci group. These carriers were fabricated through the conjugation of trehalose with squalene or betulinic acid and subsequent assembly into the corresponding nanoassemblies.<sup>37</sup> Such nanolipid conjugates were expected to facilitate cellular internalization and then induce autophagy upon trehalose release following the disassembly and hydrolysis of the ester bond through which trehalose is bound to squalene or betulinic acid residues. Unfortunately, none of the nanoassemblies induced autophagy *in vitro*, likely because of insufficient concentration of free trehalose resulting from the limited hydrolysis of ester linkage in the cell environment. In the next attempt, squalene–trehalose conjugates were bound via a biologically labile disulfide bond.<sup>38</sup> Two nanoassemblies from trehalose–monosqualene and trehalose–disqualene conjugates were fabricated. Nanoassemblies containing trehalose–disqualene conjugates demonstrated a higher efficacy in terms of autophagy induction than monosqualene analogues, free trehalose, and nonassembled precursors, as studied in LC3-overexpressed HeLa cells. According to the authors' hypothesis, this effect can be attributed to the greater permeability through the cellular membrane of the disqualenylated nanoassemblies containing more hydrophobic cores compared with the monosqualenylated nanoassemblies. The third approach attempting autophagy induction from the Seneci group involves trehalose-decorated gold nanoparticles prepared through the reduction of gold salt in the presence of thiol-terminated polyethylene glycol (PEG)–trehalose conjugate.<sup>36</sup> The trehalose–PEG gold nanoparticles cause measurable autophagy induction *in vitro* without any significant cytotoxicity in HeLa cells.<sup>36</sup>

Another strategy to target autophagy induction has been developed in our lab and concerns trehalose-rich nanogels with covalently attached but releasable trehalose.<sup>35</sup> The nanogels are designed on the basis of the previous studies on bulk hydrogels, which have shown that specific composition of polymeric network could ensure prolonged release of trehalose under physiologically relevant conditions.<sup>39</sup> As demonstrated, copolymerizing 6-O-acryloyl-trehalose with acrylamide-type

Table 2. Summary of Studies on Trehalose-Bearing Carriers for Autophagy Induction

carrier type	targeted disease	autophagy induction <i>in vitro</i> studies	autophagy induction <i>in vivo</i> studies	ref
trehalose, L-arginine, and phosphatidylserine-based nanomotors	atherosclerosis	expression of LC3-I, LC3-II, and p62 proteins in RAW 264.7 macrophages	antiatherosclerotic effects in ApoE <sup>-/-</sup> mice	30
hydroxypropyl- $\beta$ -CD-based oridonin and trehalose-loaded nanovesicles <sup>4</sup>	atherosclerosis	expression of mCherry-GFP-LC3B protein in RAW264.7 macrophages		31
trehalose-loaded manganese oxide-integrated mesoporous silica nanoparticles <sup>4</sup>	cancer	expression of LC3-I, LC3-II, and p62 proteins in PANC1 and 4T1 cancer cells	tumor growth inhibition in PANC1 tumor-bearing mice	32
trehalose glycopolymers with 20 or 40 pendant trehalose moieties	NAFLD	expression of AMPK(T172), LC3-I, and LC3-II proteins in mouse primary murine hepatocytes		33
trehalose-nucleolipid-based PLGA and solid lipid nanoparticles	neurodegeneration	expression of LC3-I and LC3-II proteins in BE(2)-M17 neuroblasts		34
trehalose-releasing nanogels	not specified		expression of GFP-LC3 and p62 proteins in transgenic zebrafish larvae; expression of mCherry-Atg8a and GFP-p62 proteins in transgenic <i>Drosophila</i> larvae	35
trehalose-coated gold nanoparticles	not specified	expression of LC3-I and LC3-II proteins in HeLa cervical cancer cells		36
trehalose-functionalized solid lipid nanoparticles	not specified	expression of LC3-I and LC3-II proteins in HeLa cervical cancer cells		37
trehalose-squalene-based nanoassemblies	not specified	expression of LC3-I, LC3-II, and mCherry-GFP-LC3B proteins in HeLa cervical cancer cells		38

<sup>4</sup>Trehalose is incorporated physically.

monomers allows the fabrication of materials that can sustainably release trehalose at pH 7.4 due to the interaction of the amide protons with the ester bond in adjacent acrylate units, which strongly accelerates ester hydrolysis (Figure 4A). Employing this acrylate/acrylamide approach, a series of nanosized trehalose-releasing hydrogels is synthesized by the reverse microemulsion method through photoinitiated free radical copolymerization of 6-*O*-acryloyl-trehalose and acrylamide and/or cationic (3-acrylamidopropyl)-trimethylammonium chloride.<sup>35</sup> The cationic monomer is selected to provide colloidal stability and to functionalize nanogels with positive charge, which would ensure electrostatic interactions with negatively charged membranes to enhance brain targeting via adsorptive-mediated transcytosis and make them potentially applicable to target neurodegenerative disorders. *In vivo* studies on transgenic zebrafish and *Drosophila* larvae show that cationic trehalose-releasing nanogels can significantly induce autophagy, as indicated by the increased levels of LC3 and autophagy-related protein Atg8 and downregulation of p62 levels, thereby proving their promising potential as trehalose delivery vehicles for autophagy stimulation.<sup>35</sup>

Recent nanosystems containing trehalose-conjugates have been fabricated by rapid mixing of amphiphilic trehalose-nucleolipid conjugates into solid lipid nanoparticles or by encapsulation of trehalose-nucleolipid conjugates into poly-(lactic-*co*-glycolic acid) nanoparticles through nanoprecipitation.<sup>34</sup> In both cases, thymidine-based lipids are coupled to trehalose through an ester moiety, which allows its enzymatic release in neuronal cells. *In vitro* assays in neuronal cells show efficient cellular uptake of these nanosystems and enhanced autophagy compared with those of molecular trehalose, as demonstrated by immunoblotting and transfection assays.

Autophagy plays also a crucial role in liver homeostasis, and can break down and remove hepatocellular lipid accumulation.<sup>40,41</sup> Hepatic autophagy is believed to play a protective role during NAFLD and nonalcoholic steatohepatitis (NASH), which is pathologically more advanced than NAFLD. DeBosch's group has recently investigated the effects of trehalose glycopolymers on hepatocyte CD53 blocking in basal and overnutrition contexts, which may be an effective way to reduce diseases that combine overnutrition and inflammation, such as NASH and type 2 diabetes.<sup>33</sup> It is believed that free trehalose blocks carbohydrate uptake into hepatocytes as a nonselective inhibitor of GLUT.<sup>27</sup> Therefore, the question arises whether polymers containing pendant trehalose can also block GLUT. One can hypothesize that trehalose glycopolymers can effectively block GLUT because of the possible multivalent interactions, that is, the so-called "carbohydrate cluster effect."<sup>42</sup> To elucidate this effect, two glycopolymers containing 20 or 40 repeating units of 6-*O*-acryloyl-trehalose were synthesized (pTreA20 and pTreA40, Figure 4B). They differed in the content and density of pendant trehalose, but their polymer backbones were identical. Both glycopolymers were tested as trehalase-resistant analogues in the *in vitro* model of NAFLD. While pTreA40 treatment in free fatty acid (FFA)-induced lipotoxicity of hepatocytes can significantly induce autophagy, as confirmed by the increased pAMPK (phosphorylated AMP-activated protein kinase) and LC3-II levels, pTreA20 can only slightly increase the autophagic activity, which is similar to free trehalose.

There are two reports in which trehalose-bearing carriers have been studied to target atherosclerosis. Atherosclerosis is a chronic disease characterized by inflammation in artery walls

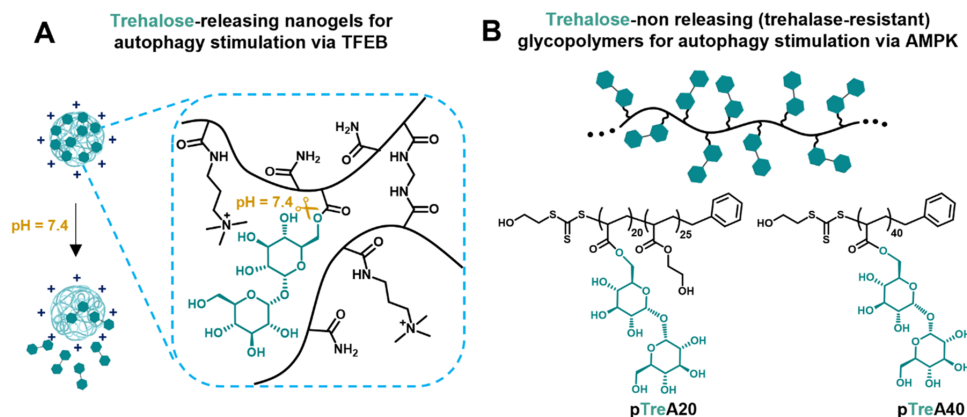


Figure 4. (A) Trehalose-releasing nanogels and (B) trehalose-nonreleasing glycopolymers to target two different pathways of autophagy stimulation.

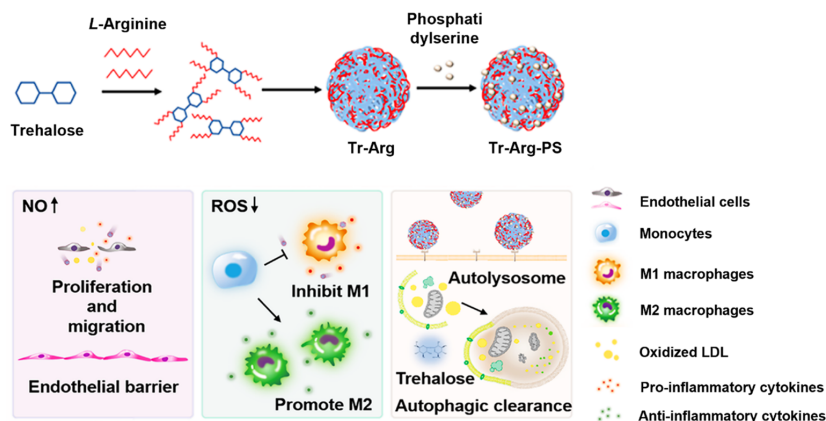


Figure 5. Synthesis and the antiatherosclerosis effects of Tr-Arg-PS nanomotors, including promoting endothelial repair, regulating phenotypic polarization of macrophages, and inducing macrophage autophagy. Adapted with permission from ref 30. Copyright 2022 American Chemical Society.

caused by lipid deposition that results in the formation of plaques and narrowing of blood arteries.<sup>43</sup> As a result of the increased production of reactive oxygen species (ROS)-mediated oxidative stress, the cellular recycling process (autophagy) is impaired as atherosclerosis progresses.<sup>43,44</sup> In the early to middle stages of atherosclerosis development, i.e., the formation of fatty streaks and intermediate lesions, autophagy is crucial for cholesterol efflux by macrophages and, thus, the reduction of foam cell formation.<sup>45–47</sup> Autophagy, however, demonstrates a protective effect (promotion of plaque stability) in advanced atherosclerotic lesions by enhancing macrophage survival and inhibiting necrotic core formation.<sup>48,49</sup>

The first approach to use trehalose carriers to enhance autophagy in atherosclerosis is trehalose-based nanomotors.<sup>30</sup> The nanomotors are constructed via double self-assembly of (i) trehalose conjugates containing four arginine molecules (Tr-Arg), and (ii) nanoparticles functionalized by phosphatidylserine, which allow the construction of Tr-Arg-PS nanomotors (Figure 5). According to the authors, the targeting mechanism of Tr-Arg-PS nanomotors is twofold. The first is to

accelerate the penetration of nanomotors into the target macrophages using nitric oxide (NO) as the driving force generated by the reaction between arginine and ROS in the interstitial fluid of atherosclerotic lesions. The second is to stimulate an “eat me” signal to macrophages to enhance cell uptake. Tr-Arg-PS nanomotors can stimulate autophagy in foam cells, as confirmed by a much lower p62 protein level compared with the negative control (foam cells without any treatments), and significantly reduce lipid deposition *in vitro*. Tr-Arg-PS nanomotors can enhance the *in vivo* targeting efficiency to atherosclerotic plaques by almost double compared with nanomotors, where the L-arginine component is substituted by L-lysine and, thus, NO cannot be generated. Tr-Arg-PS nanomotors can reduce aortic lesion area by ~20% in an atherosclerotic mice model after two months of treatments. The authors suggest that the induction of autophagy in foam cells may be due to the presence of trehalose in the nanomotors. Unfortunately, no suggestion is made as to how free trehalose can be released inside the cells from the nanomotors. Trehalose conjugates have been synthesized by substituting the sulfonated trehalose for the



Table 3. Summary of Studies on Trehalose-Bearing Carriers for Inhibition of Protein Aggregation

targeted disease	carrier type	model protein <sup>a</sup>	protein aggregation <i>in vitro</i> or <i>in vivo</i> studies	ref
neurodegenerative diseases	trehalose glycocluster with six pendant trehalose moieties	A $\beta$ (1–40)	cytotoxicity of A $\beta$ (1–40) aggregates toward mouse primary cortical neurons	66
	iron oxide nanoparticles coated with trehalose-containing polymeric network	lysozyme, A $\beta$ (1–40)	aggregation of mutant huntingtin inside HD150Q neuronal cells; aggregation of mutant huntingtin in HD transgenic mice	67
	trehalose-based nanoparticles from hydrothermal carbonization	lysozyme, A $\beta$ (1–40), insulin	aggregation of mutant huntingtin inside HD150Q neuronal cells; cytotoxicity of mutant huntingtin aggregates toward HD150Q neuronal cells; cytotoxicity of lysozyme amyloids toward CHO ovarian cells	68
	trehalose-coated gold nanoparticles		aggregation of mutant huntingtin inside HD150Q neuronal cells; cytotoxicity of mutant huntingtin aggregates toward HD150Q neuronal cells	69
	trehalose-functionalized biodegradable polylactide nanoparticles		aggregation of mutant huntingtin inside HD150Q neuronal cells; cytotoxicity of mutant huntingtin aggregates toward HD150Q neuronal cells; ROS generation inside lysozyme fibrils-treated HT22 mouse hippocampal neuronal cells	70
	trehalose-functionalized biodegradable polycarbonate-co-polylactide nanoparticles	A $\beta$ (1–42)	cytotoxicity of A $\beta$ (1–42) aggregates toward SH-SY5Y neuroblastoma cells	71
	trehalose-terminated polyglycerol dendrimers	lysozyme	aggregation of mutant huntingtin inside HD150Q neuronal cells	72
	trehalose glycopolymers of 6-acrylamido-6-deoxy-trehalose and acrylamide	A $\beta$ (1–40)	cytotoxicity of A $\beta$ (1–40) aggregates toward HeLa cervical cancer cells	73
	trehalose glycopolymers of 6-O-vinyladipoyl-trehalose or 6-O-vinylsebacoyl-trehalose	A $\beta$ (1–42)	cytotoxicity of A $\beta$ (1–42) aggregates toward HeLa cervical cancer cells	74
	localized insulin-derived amyloidosis	trehalose glycopolymers of 6-O-acryloyl-trehalose vinylbenzyl ether regioisomers	insulin	75
	trehalose glycopolymers of various trehalose vinylbenzyl ether regioisomers	insulin	76	
	trehalose glycopolymers of 6-O-methacryloyl-trehalose	insulin	77	
	trehalose glycopolymers with poly(lactide), poly(carbonate), or poly(caprolactone) backbone	insulin	78	

<sup>a</sup>Model protein used in aggregation studies under fibrillation-accelerating conditions in solution.

amino group of arginines. Therefore, it is questionable whether cleavage of the bound amino group to release free trehalose is possible inside cells.

Stimulation of autophagy to treat atherosclerosis is also targeted in the study on multiloading self-assembled nanovesicle systems composed of amphiphilic H9 peptide and hexadecyl phosphorylcholine loaded with physically entrapped trehalose and the (HP- $\beta$ -CD)/oridonin inclusion complex.<sup>31</sup> The synergistic effects of oridonin and trehalose can inhibit foam cell formation in RAW264.7 cells, and can reduce inflammatory cytokines IL-1 $\beta$ , IL-6, and TNF- $\alpha$  and promote the formation of autophagosomes, as confirmed by the increased level of LC3 in foam cells.<sup>31</sup>

The modulation of autophagy may also play a role in cancer treatment. The role of autophagy in cancer appears to be more complicated and is influenced by tumor type, disease stage, and host factors because of its dual role as a tumor suppressor and tumor promoter.<sup>50–52</sup> The concept that autophagy prevents the development of tumors is now well understood. However, once a tumor has become well-developed, autophagy processes are necessary to support uncontrolled cell proliferation and enhanced metabolic activity, thereby creating a dependence on autophagy for tumor survival.<sup>51–53</sup> In early tumor development, autophagy promotes ferroptosis-mediated tumor suppression by degrading accumulated ferritin in cancer cells.<sup>24,53</sup>

Chen's group has developed trehalose-loaded mSiO<sub>2</sub>@MnOx-mPEG nanoparticles for autophagy-enhanced cancer-cell ferroptosis.<sup>32</sup> The dual mechanism of action of nanoparticles starts by inhibiting GPX4 (glutathione peroxidase 4)-induced ferroptosis in cancer cells due to the high glutathione (GSH) consumption efficiency of nanoparticles. Second, the high consumption of GSH and sensitivity to pH-mediated nanoparticle degradation lead to the release of trehalose from nanocarrier systems, which induces autophagy and further facilitates ferroptosis through the nuclear receptor coactivator 4 (NCOA4)-mediated degradation of ferritin. Bare mSiO<sub>2</sub>@MnOx-mPEG nanoparticles exhibit a desirable mesoporous nanostructure, which can efficiently entrap trehalose molecules. Encapsulated trehalose can be quickly released upon exposure of nanoparticles to acidic pH and a high GSH level representing tumor microenvironments. Treatment with trehalose-loaded nanoparticles in pancreatic cancer cells enhances autophagosome and autolysosome formation, as well as shrunken mitochondria and normal nuclei without chromatin condensation, which indicate autophagy and enhanced cancer ferroptosis. In addition, GPX4 and p62 protein expression can be suppressed by treatments with trehalose nanoparticles compared with the control, while LC3-II and NCOA4 protein levels are enhanced with dose-dependent effects on cancer ferroptosis. An *in vivo* study in tumor-bearing mice indicates that treatments with nanoparticles can inhibit tumor growth by ~90% over 2 weeks of treatments compared with both free trehalose and negative control. These findings imply that nanoparticles boost the efficacy of trehalose for cancer treatment.

#### 4. TREHALOSE-BEARING CARRIERS FOR INHIBITION OF PROTEIN AGGREGATION

Polypeptides/proteins fold through different intermediates into their functional, native, three-dimensional conformation. At times, certain factors, such as environmental stress, mutations, or translational errors, can cause protein misfolding. Misfolded proteins can be refolded to their native states or

degraded by different cellular mechanisms. However, if these mechanisms fail, misfolded proteins can aggregate to form amorphous aggregates or assemble through prefibrillar species into highly ordered,  $\beta$ -sheet-rich aggregates with fibrous morphology called amyloids.<sup>54</sup> Such pathogenic amyloids can then form extracellular plaques or intracellular inclusions, which affects the healthy function of tissues and organs, and their increased accumulation is associated with the development of numerous incurable human disorders, both neurodegenerative and non-neuropathic.<sup>55–57</sup> Some examples of human polypeptides/proteins that possess an inherent tendency to form amyloid fibrils and corresponding disorders include  $\alpha$ -synuclein in PD, dementia with Lewy bodies (DLB), multiple system atrophy (MSA), amyloid- $\beta$  (A $\beta$ ) and tau in AD, mutant huntingtin in Huntington's disease (HD), ubiquitin in ALS, islet amyloid polypeptide (IAPP) in type 2 diabetes, or lysozyme in systemic lysozyme amyloidosis. Apart from endogenous proteins, several pharmaceutical polypeptides and proteins are also known to have a high propensity to form amyloid-like fibrils. An example is recombinant insulin, in which long-term subcutaneous administration can result in the development of localized insulin-derived amyloidosis at the injection sites. Stimulation of autophagy to disintegrate the formed amyloid deposits is one of the strategies that are developed to combat disorders associated with protein aggregation.<sup>26,58</sup> Another strategy targets amyloid formation and includes prevention of protein aggregation at an early stage.<sup>59</sup> Among many types of studied compounds, numerous low-molecular-weight natural saccharides, including trehalose, are identified as chemical chaperones, which can suppress protein aggregation.<sup>60–65</sup> Unfortunately, considering the high concentration required to observe the desired effect, the anti-amyloidogenic efficiency of saccharides is rather low. Some recent studies have found that this efficiency can be significantly amplified by creating synthetic structures bearing multiple copies of saccharides. For example, glycoclusters prepared by installing six trehalose, lactose, galactose, or glucose residues on a dipentaerythritol core significantly overperform compared with the corresponding mono- or disaccharides in retarding the formation of A $\beta$ 40 fibrils.<sup>66</sup> Particularly, the trehalose glycocluster causes an extremely significant retardation. Moreover, the trehalose glycocluster can protect neurons from A $\beta$ 40-induced cell death, although this neuroprotective activity is similar to free trehalose. The enhanced performance of trehalose-bearing carriers over the molecular trehalose in interfering with protein aggregation has also been demonstrated for several trehalose-bearing glycopolymers, dendrimers, nanoparticles, and nanoassemblies, and they are overviewed in Table 3.

The molecular mechanism explaining how trehalose-bearing carriers prevent proteins from aggregation into amyloid fibrils has not been studied, but on the basis of the various mechanisms postulated for trehalose, as well as for macromolecules/nanostructures,<sup>79–81</sup> at least four mechanisms can be hypothesized (Figure 6). The presence of multiple copies of trehalose within one species offers the possibility of binding via multiple binding points compared with the monovalent binding of a single trehalose molecule. Thus, the first mechanism comprises direct binding of "poly(trehalose)" to the protein enhanced by multivalent interactions (Figure 6A). In this way "poly(trehalose)" can stabilize a protein's structure but it can also prevent proteins from interacting with each other's. Alternatively, the "poly(trehalose)" can act indirectly

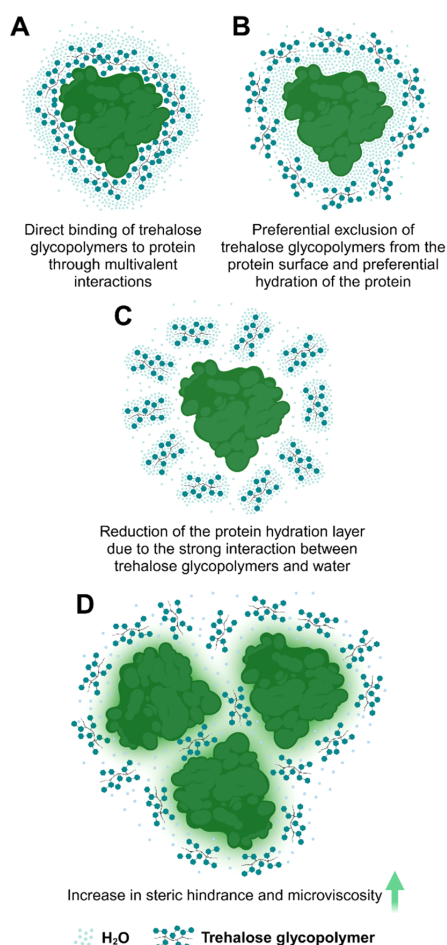


**Figure 6.** Possible mechanisms of the inhibition of protein aggregation by trehalose-bearing carriers (represented by trehalose glycopolymers).

by being preferentially excluded from the immediate vicinity of proteins, thus promoting the preferential hydration of the protein molecules, which increases their stability (Figure 6B). It is also possible that the antiaggregation effect is the result of the kosmotropic nature of trehalose, wherein stronger interactions between “poly(trehalose)” and water molecules than between the water molecules themselves reorganize the regular water structure, which causes a reduction in the hydration layer of proteins, thus enhancing intramolecular interactions (Figure 6C). Finally, antiamyloidogenic action of trehalose-bearing carriers can be attributed to their nano/macromolecular structure and results from an increase in steric hindrance in the solution and microviscosity, which restrict protein–protein interactions and limit protein movements (Figure 6D).

The results from the study of Miura and co-workers on  $A\beta(1-42)$  and  $A\beta(1-40)$  fibrillation have shown that trehalose glycopolymers prepared from 6-*O*-vinyladipoyl-trehalose<sup>74</sup> or 6-acrylamido-6-deoxy-trehalose<sup>73</sup> exhibit superior antiamyloidogenic properties over glycopolymers of

maltose or lactose and their corresponding disaccharide alcohols maltitol or lactitol. Furthermore,  $A\beta$  aggregates formed in the presence of trehalose glycopolymers have no cytotoxicity,<sup>73</sup> or their cytotoxicity is reduced compared with aggregates formed without any additives.<sup>74</sup> However, the effects are strongly affected by the structural features of the glycopolymers, e.g., the linker length between polymeric chains and sugar moieties. For example, the polymer with a shorter adipoyl linker [poly(6-*O*-vinyladipoyl-trehalose)] shows a strong aggregation inhibition effect compared with that of molecular trehalose, while poly(6-*O*-vinylsebacoyl-trehalose) with a longer alkyl side chain induces amyloid formation. As concluded, not only the structure of pendant saccharide but also the glycopolymer’s amphiphilicity play important roles in amyloid formation and inhibition. The counterparts for trehalose glycopolymers employed in these studies exhibit some structural differences, thus rendering them not perfectly comparable. They are also synthesized via noncontrolled polymerization techniques, and therefore, the uniformity in terms of molecular weight and dispersity among the compared glycomacromolecules cannot be guaranteed. Considering that the structural features of polymers can influence their effectiveness, the proper comparative study requires high structural similarity between counterparts regarding their molecular weight and dispersity, as well as the linking motif between the polymer chain and saccharide moiety. Following this direction, very recently, our group has presented a strategy for obtaining highly structurally comparable glycopolymers of trehalose and sucrose through reversible addition–fragmentation chain transfer (RAFT) polymerization of trehalose and sucrose acrylate analogues: 6-*O*-acryloyl-trehalose and 6-*O*-acryloyl-sucrose (Figure 7A).<sup>75</sup> The glycomonomers share several structural commonalities, including the same molecular weight, number of hydroxyl groups, functionalization with an acryloyl moiety on the primary hydroxyl group, and non-reducing character, as well as the enablement to afford polymers with terminal  $\alpha$ -D-glucopyranosyl moieties. As evaluated on recombinant human insulin, the studied glycopolymers demonstrate significantly amplified antiamyloidogenic performance over their corresponding molecular saccharides. The effects are concentration-dependent and are particularly prominent for higher concentrations at which glycopolymers not only retard fibrillation but also significantly decrease the amount of aggregated insulin and result in the formation of significantly shorter fibrils. Interestingly, both trehalose and sucrose glycopolymers give similar results indicating that antiamyloidogenic effectiveness is not particularly superior for trehalose decoration of the polymer, at least in the studied case.

Trehalose-bearing macromolecules have been extensively developed in the Maynard group,<sup>20</sup> and part of the research has been devoted to the study of various trehalose glycopolymers for stabilization of pharmaceutical proteins/polypeptides, including human recombinant insulin. Although the studies are not focused directly on the fibrillation and amyloid fibrils formation but rather on general stability against aggregation caused by heating and agitation, the results obtained provide several important conclusions regarding the influence of glycopolymer structure on their stabilization effect. With high probability, the results are also valid in view of fibrillation. They are also valuable to be included in the current discussion, because of the widespread use of pharmaceutical insulin and the recognized risk of the development of localized

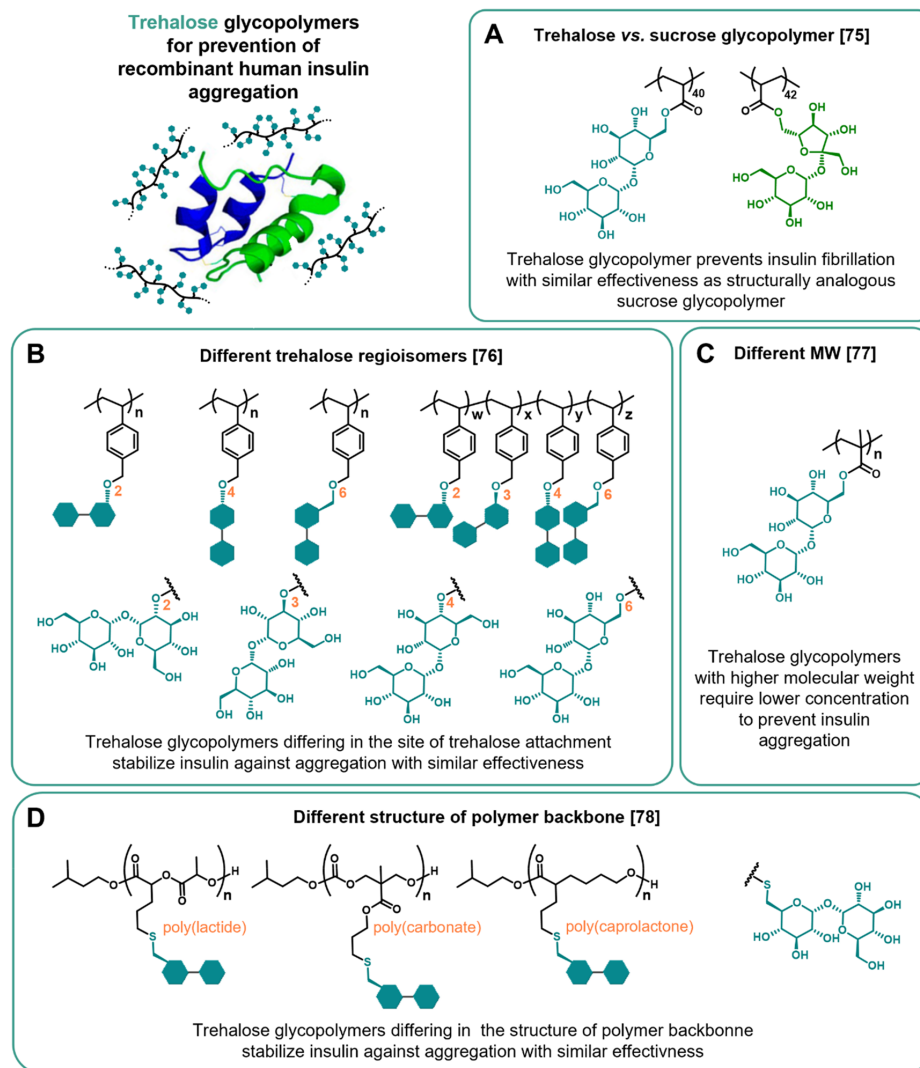


**Figure 7.** Overview of the studies on trehalose glycopolymers for the prevention of recombinant human insulin aggregation. Comparison between: (A) structurally analogous poly(6-*O*-trehalose acrylate) and poly(6-*O*-sucrose acrylate); (B) glycopolymers of different trehalose vinylbenzyl ether regioisomers; (C) poly(6-*O*-trehalose methacrylate)s with different molecular weight (MW); and (D) glycopolymers with poly(lactide), poly(carbonate), or poly(caprolactone) backbone.

amyloidosis associated with its administration. For example, the group has studied the effect of trehalose positional modification on glycopolymer's effectiveness by comparing polymers of various trehalose vinylbenzyl ether regioisomers (modified at 2-*O*, 3-*O*, 4-*O*, or 6-*O* position) (Figure 7B).<sup>76</sup> The differences in their effectiveness might potentially arise from their different conformational flexibilities, as determined by computational calculations. Unlike molecular trehalose at an equivalent concentration, all polymers inhibit insulin aggregation, but there are no significant differences between them. Despite the difference in conformational flexibility, all of the regioisomers retained the native clamshell conformation of trehalose. This is suggested to be more important for stabilization, which explains why no differences are observed

between regioisomers. Moreover, it turns out that stabilization effectiveness depends on the molecular weight, as recently found by studying poly(6-*O*-trehalose methacrylate)s.<sup>77</sup> Longer polymers require a lower concentration to completely prevent insulin aggregation (Figure 7C). Further development in the group has extended the library of trehalose glycopolymers by hydrolytically degradable macrostructures by changing the synthetic approach from radical polymerization of trehalose glycomonomers to postpolymerization modification. Specifically, thiolated trehalose is installed through radical-initiated thiol–ene reaction on allyl-substituted poly(lactide), poly(carbonate), or poly(caprolactone) (Figure 7D).<sup>78</sup> All of these glycopolymers stabilize insulin against aggregation with fairly similar effectiveness, thereby suggesting

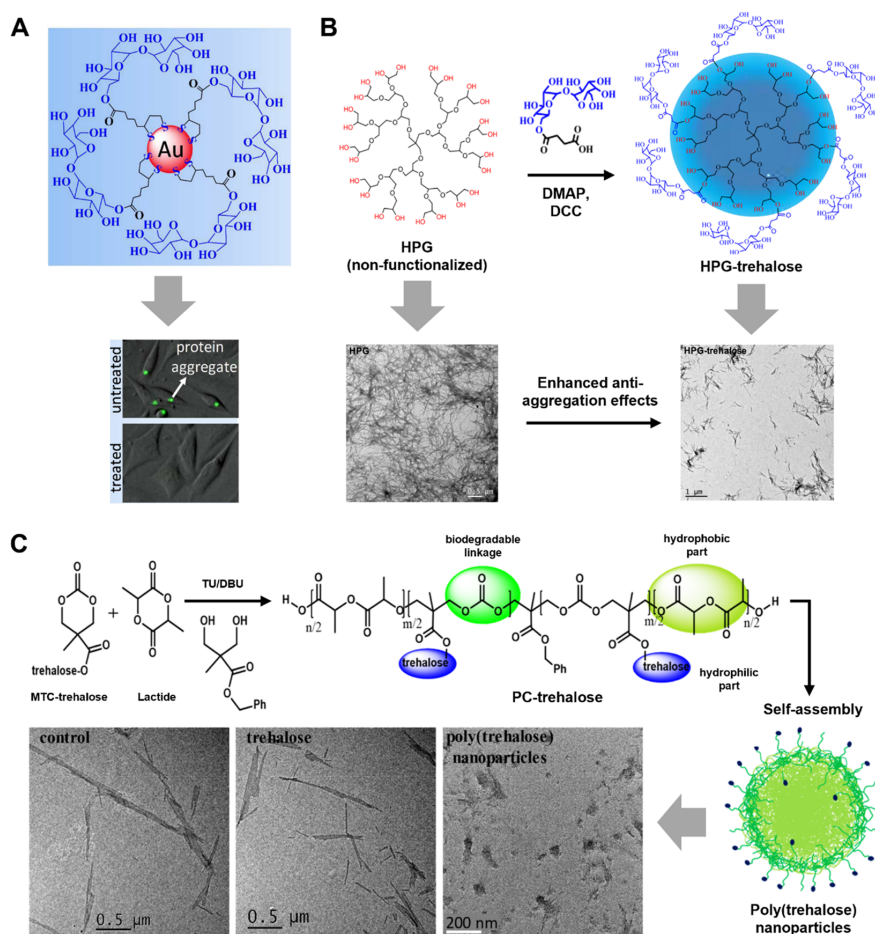


**Figure 8.** Overview of selected trehalose-bearing carriers developed in the Jana and Jana group for the inhibition of protein aggregation. (A) Trehalose-functionalized gold nanoparticle that can inhibit aggregation of polyglutamine-containing mutant proteins inside the neuronal cells. Adapted with permission from 69. Copyright 2017 American Chemical Society. (B) Synthetic pathway of trehalose-terminated hyperbranched polyglycerol dendrimers (HPG-trehalose) and its effect on preventing lysozyme fibrillation. Adapted with permission from 72. Copyright 2020 American Chemical Society. (C) Schematic pathway of trehalose-containing amphiphilic polycarbonate-co-poly lactide copolymer (PC-trehalose) and its self-assembly into poly(trehalose) nanoparticles for inhibition of A $\beta$  fibrillation. Adapted with permission from 71. Copyright 2023 American Chemical Society.

that the presence of trehalose is more significant than the structure of the backbone. It is hypothesized that the enhanced stabilizing properties of trehalose glycopolymers are strongly related to their nonionic surfactant character, i.e., hydrophilic side moieties with a hydrophobic backbone.

In recent years, anti-amyloidogenic activity has also been proven by the Jana and Jana group for several poly(trehalose)-type nanoparticles.<sup>82</sup> The first nanoparticles comprise plate-shaped nanoparticles decorated with trehalose, which are fabricated through the simple hydrothermal carbonization.<sup>68</sup> Other nanoparticles are based on a gold<sup>69</sup> or iron oxide<sup>67</sup> core and decorated with trehalose by using trehalose derivatives. Specifically, gold nanoparticles are engineered through the reduction of gold salt in the presence of a trehalose-lipoic acid derivative (Figure 8A).<sup>69</sup> In turn, iron oxide-cored nanoparticles are covered with polymeric coating containing trehalose fabricated through the polymerization of crotony-

lated trehalose, PEG-acrylate, and sulfoacrylate and/or aminoacrylate monomers. The presence of anionic, zwitterionic, or cationic units can be regulated by their ratio in order to improve cellular uptake and facilitate blood-brain barrier crossing.<sup>67</sup> The last type of poly(trehalose)-type nanoparticles developed in the group include polymer-based nanoparticles formed by self-assembly of trehalose-containing poly lactide<sup>70</sup> or polycarbonate-co-lactide.<sup>71</sup> These two self-assemblies differ in the composition of the polymer backbone, but more importantly, they also differ in the localization of trehalose within the polymer chain. Polycarbonate-co-poly lactide self-assemblies are based on polymers containing pendant trehalose moieties, which were obtained from trehalose-bearing cyclic carbonate monomer (Figure 8C).<sup>71</sup> In turn, in poly lactide self-assemblies, trehalose is localized at the end of polymeric chains because of being used as an initiation site in ring-opening polymerization. Additionally, poly lactide-based nanoparticles

are enriched with dopamine-terminated or arginine-terminated polylactide. In such a design, dopamine should provide the dopamine receptor-based neuron cell uptake, arginine should enhance cellular uptake because of its cationic charge, and trehalose should provide interactions with the aggregating protein. Unlike the previous nanoparticles, both self-assemblies are biodegradable, which is highly beneficial for *in vivo* applications because it will prevent potential long-lasting accumulation in the body. The performance of the colloidal nanoparticles developed by the Jana and Jana group in both *in vitro* and *in vivo* studies on inhibiting protein aggregation can be summarized as follows. The preliminary study on accelerated in-solution fibrillation of model amyloid-forming peptides/proteins, including lysozyme,<sup>67,68</sup> insulin,<sup>68</sup> A $\beta$ (1–40),<sup>67,68</sup> and A $\beta$ (1–42),<sup>71</sup> proved that these poly(trehalose) nanoparticles significantly outperform free trehalose in inhibiting amyloid fibrils formation. Some of them are also able to disintegrate preformed mature amyloid fibrils into smaller parts.<sup>67,71</sup> *In vitro* studies on the model neuronal cell line for HD (HD150Q) have proved that the poly(trehalose) nanoparticles have high cellular uptake,<sup>67–71</sup> as well as inhibit the intracellular aggregation of mutant huntingtin protein inside these cells,<sup>67–70</sup> and can strongly outperform free trehalose and trehalose-absent nanoparticles (if studied). In addition, nanoparticles can reduce the amyloidogenic cytotoxicity of amyloid fibrils of mutant huntingtin aggregates toward HD150Q neuronal cells,<sup>68–70</sup> lysozyme amyloids toward CHO ovarian cells<sup>68</sup> and A $\beta$ (1–42) aggregates toward SH-SY5Y neuroblastoma cells.<sup>71</sup> As revealed in an intracellular ROS generation study inside A $\beta$ (1–42) oligomers-treated SH-SY5Y neuroblastoma cells,<sup>71</sup> A $\beta$ (1–42) oligomer-treated cells produce intense intercellular ROS, while ROS generation is slightly reduced in the presence of trehalose and completely absent in cells pretreated with the poly(trehalose) nanoparticles. The authors hypothesize that the poly(trehalose) nanoparticles bind to A $\beta$ (1–42) oligomers through multivalent interactions and reduce interactions between A $\beta$ (1–42) oligomers and the cell membrane, thus preventing damage and cellular stress. Although the results from *in vitro* studies are encouraging, there is only one insight into the *in vivo* anti-amyloidogenic effectiveness of trehalose-bearing carriers, and it comes from the study on the HD-mouse model treated with zwitterionic poly(trehalose) nanoparticles containing iron oxide core.<sup>67</sup> The study has revealed that, upon intravenous administration of these nanoparticles, the number of mutant huntingtin aggregates in the brain is remarkably diminished, and their action seems to be more effective than that of trehalose-absent nanoparticles.

Besides the research on trehalose-containing nanoparticles, the Jana and Jana group has also carried out a study on the anti-amyloidogenic potential of trehalose-decorated hyperbranched polyglycerol dendrimers.<sup>72</sup> Dendrimers are synthesized through the simple coupling of carboxylated trehalose to terminal hydroxyls (Figure 8B). Through the study of lysozyme as a model amyloidogenic protein, the trehalose-terminated dendrimers have been found to have significantly better fibril-inhibiting ability than free trehalose and to also be more effective than nonfunctionalized hyperbranched polyglycerol dendrimers. Similarly to the poly(trehalose) nanoparticles, the trehalose-terminated dendrimers are able to enter neuronal cells, thereby reaching their cytoplasm and significantly hindering intracellular aggregation of mutant huntingtin.

## 5. CONCLUSIONS AND PERSPECTIVES

Trehalose-bearing carriers have emerged as superior alternatives to trehalose alone to induce autophagy or inhibit protein aggregation. The studies have successfully demonstrated the ability of these carriers to achieve improved efficacy with significantly lower amounts of trehalose. Trehalose-bearing carriers are shown to effectively interfere with the aggregation of several proteins/peptides in solution, including A $\beta$ (1–40 and 1–42), insulin, and lysozyme, and strongly suppress intracellular aggregation of mutant huntingtin inside neuronal cells. Surprisingly, while numerous studies have demonstrated the promising antiaggregation efficacy of trehalose-bearing carriers in relevant *in vitro* or *in vivo* neurodegenerative disease models, only one study is focused on recognizing their potential against neurodegenerative diseases through autophagy induction. Other autophagy-stimulating studies have addressed the treatment of atherosclerosis, cancer, or NAFLD or only look at the potential effects of autophagy in nondisease-specified *in vitro/in vivo* models. There is also a possibility that the carriers can have synergistic proautophagy and antiaggregation actions, especially to combat neurodegenerative diseases, that remain to be verified in future studies. Most of the discussed reports were published recently (2017 or later), and the field is still in its infancy. There are many unknowns to be elucidated and some limitations and challenges to address and overcome. There is also plenty of room for developing innovative trehalose-bearing carriers.

In the majority of the designed approaches, trehalose is chemically modified to become a part of the carrier. Proper functionalization of trehalose usually requires a troublesome, multistep synthesis and limits the preparation to large quantities. Thus, before trehalose-bearing carriers can be introduced into the clinic, the synthetic methodologies need to be improved. This is not an issue for carriers in which free trehalose is physically entrapped inside. Although the entrapment of free trehalose inside carriers may seem to be easier in preparation, surprisingly, only two such types of carriers have been developed so far. The reason may be the lack of any charge on trehalose, its small size, and good water solubility, which make it challenging to keep trehalose inside the carrier and prevent its premature release before reaching the targeted area. An undeveloped strategy for fabricating carriers with releasable trehalose includes trehalose entrapment via supramolecular forces, such as specific saccharide–lectin interactions or dynamic covalent complexation into cyclic boronate esters. Trehalose release from such carriers could be triggered by competitive displacement with free sugar molecules, e.g., glucose.

Trehalose moieties on glycopolymers are accessible for specific interactions with proteins through terminal  $\alpha$ -D-glucopyranosyl units (as has been shown on the example of interactions with concanavalin A),<sup>75</sup> and it renders trehalose-bearing carriers potentially “recognizable” by cells. While on the one hand, it might be favorable to improve their cellular uptake through enhanced interactions with cell surface proteins or even directly be responsible for their action, on the other hand, they probably could interact similarly not only with targeted cells but also with healthy cells and potentially affect their functions. Thus, the *in vivo* safety and metabolic fate of trehalose-bearing carriers require a thorough examination. Generally, to fully confirm the proautophagic and

antiaggregation effectiveness of trehalose-bearing carriers, more *in vivo* studies are required as most of the current results come from the research on *in vitro* models. Given that trehalose has the highest therapeutic potential for the treatment of neurodegenerative disorders, future research on trehalose-bearing carriers should also focus on effective brain targeting and blood–brain barrier crossing. The capability to integrate several functionalities within a single nanoparticle or macromolecular structure, as well as widely tailorable properties, makes targeted delivery utilizing carriers an especially promising approach.

The mechanism of action is still ambiguous for free trehalose and it is even more unknown for trehalose-bearing carriers. Usually, trehalose is permanently bound with the carrier, and the effect is studied for poly(trehalose)-type species. Given that the carriers are heavily decorated with trehalose, which makes them susceptible to multivalent interactions, it is highly likely that their mechanism of action may be completely different from that of free trehalose. The mechanism might also differ between various carriers depending on properties, such as the carrier size, its amphiphilicity, trehalose attachment position and linking motif, its incorporation density, or trehalose accessibility for interactions. Understanding the exact mechanisms and influence of the carriers' characteristics on their action would enable the rational design of trehalose-bearing carriers. Among all of the publications on trehalose-bearing carriers, only a few of them try to explain or hypothesize possible mechanisms of their action in inducing autophagy or inhibiting protein aggregation.

Finally, careful analysis of the publications discussed suggests some thoughts concerning experimental issues. In some studies, the lack of sufficient controls impedes our ability to definitively attribute the observed effect exclusively to the presence of trehalose as opposed to a potential influence from the carrier itself. Thus, it is recommended to use not only free trehalose but also carriers that do not contain or release trehalose or counterpart carriers containing other saccharides as another control. Next, protein fibrillation in solution is extremely dependent on concentration and external conditions, such as temperature, pH, speed of agitation, exposure to air–water interfaces, etc. Thus, uniform protocols for studying protein fibrillation are necessary to compare the results obtained for various trehalose-bearing carriers in different laboratories in order to enable identification of the most promising approach and the design of future research directions. Moreover, it should always be well evidenced that trehalose has, indeed, been conjugated as depicted, and at least  $^1\text{H}$  and  $^{13}\text{C}$  NMR spectra with an assignment of clue signals should be provided. Finally, when claiming that conjugated trehalose can be released from the carrier under physiological conditions, this possibility should be confirmed at least under stimulated conditions.

In summary, taking into account the still growing interest in therapeutic use of trehalose to target autophagy-related disorders and diseases associated with protein aggregation, it is expected that the coming years will also bring new studies on trehalose-bearing carriers. It would be highly desirable if future research could provide better understanding of how exactly trehalose-bearing carriers induce autophagy and affect protein fibrillation, as well as provide more insights on their *in vivo* efficacy and safety. The effort should also be put toward selective delivery, particularly effective brain targeting and

blood–brain barrier crossing, for the treatment of neurodegenerative disorders.

## ■ AUTHOR INFORMATION

### Corresponding Author

**Ilona Wandzik** – Department of Organic Chemistry, Bioorganic Chemistry and Biotechnology, Faculty of Chemistry, Silesian University of Technology, 44-100 Gliwice, Poland; Biotechnology Center, Silesian University of Technology, 44-100 Gliwice, Poland; [orcid.org/0000-0002-6592-4875](https://orcid.org/0000-0002-6592-4875); Email: [ilona.wandzik@polsl.pl](mailto:ilona.wandzik@polsl.pl)

### Authors

**Ali Maruf** – Department of Organic Chemistry, Bioorganic Chemistry and Biotechnology, Faculty of Chemistry, Silesian University of Technology, 44-100 Gliwice, Poland; Biotechnology Center, Silesian University of Technology, 44-100 Gliwice, Poland; Drug Research Program, Faculty of Pharmacy, University of Helsinki, 00014 Helsinki, Finland; [orcid.org/0000-0003-3807-4446](https://orcid.org/0000-0003-3807-4446)

**Malgorzata Milewska** – Department of Organic Chemistry, Bioorganic Chemistry and Biotechnology, Faculty of Chemistry, Silesian University of Technology, 44-100 Gliwice, Poland; Biotechnology Center, Silesian University of Technology, 44-100 Gliwice, Poland; [orcid.org/0000-0002-8395-7582](https://orcid.org/0000-0002-8395-7582)

**Máté Varga** – Department of Genetics, ELTE Eötvös Loránd University, Budapest H-1117, Hungary

Complete contact information is available at:

<https://pubs.acs.org/10.1021/acs.jmedchem.3c01442>

### Author Contributions

<sup>1</sup>These authors contributed equally.

### Notes

The authors declare no competing financial interest.

### Biographies

**Ali Maruf** is a Ph.D. student at Silesian University of Technology, Poland. He graduated with a Master's in biomedical engineering from Chongqing University, China. He has a great passion in drug delivery research. His current research focuses on developing nanogels for stimulating autophagy to treat impaired-autophagy-related disorders, such as neurodegenerative diseases, atherosclerosis, and fatty liver disease. He also explores nanogels for gene therapy, chemotherapy, and cryopreservation. Currently, Ali is conducting collaborative research on Parkinson's disease at University of Helsinki, Finland, under the supervision of Prof. Mikko Airavaara. His work aims to advance the understanding of Parkinson's disease and explore new therapeutic approaches.

**Malgorzata Milewska** received her Ph.D. in chemical sciences in 2020 from Silesian University of Technology in Gliwice, Poland, where she is currently an assistant professor. During her doctoral studies, she was awarded an international scholarship from the National Science Centre, Poland, to carry out 6 months of a research internship at the University of New South Wales in Sydney, Australia, in Prof. Martina Stenzel's group. Her main research interests focus on developing trehalose-containing polymers for biomedical applications.

**Máté Varga** is an associate professor at ELTE Eötvös Loránd University, Department of Genetics, where he also leads the ELTE Fish Genetics Group. He pursued his Ph.D. studies at the University of Pennsylvania where he first started to work with zebrafish. The main current research interest of Dr. Varga's group is the creation and characterization of zebrafish models for human monogenic diseases.

Previously, he performed pioneering research linking autophagy to zebrafish caudal fin regeneration and has been using zebrafish reporter lines to characterize the potential autophagy modulating effects of numerous small molecular compounds.

**Ilona Wandzik** received Ph.D. and D.Sc. degrees in chemical sciences from Silesian University of Technology, Poland. Her research interests include synthesis and characterization of bioactive compounds, especially compounds based on carbohydrates and nucleosides, as inhibitors of glycosidases and glycosyltransferases. The second stream of research focuses on hydrogels for biomedical applications. Current study in her group focuses on the use of nanogels as carriers for drug delivery to combat impaired autophagy and protein aggregation diseases.

### ACKNOWLEDGMENTS

The financial support from National Science Centre, Poland under the grant PRELUDIUM BIS 1 (2019/35/O/STS/02746) is gratefully acknowledged. The graphical abstract, Figures 1–4, and Figure 6 were created with [BioRender.com](https://www.biorender.com).

### ABBREVIATIONS

A $\beta$ , amyloid- $\beta$ ; AMPK, AMP-activated protein kinase; GLUT, glucose transporter; GSH, glutathione; HD, Huntington's disease; LC3, microtubule-associated protein 1A/1B-light chain 3; NAFLD, nonalcoholic fatty liver disease; ROS, reactive oxygen species; SQSTM1/p62, sequestosome 1; TFEB, transcription factor EB; Tr-Arg-PS, trehalose-based nanomotors bearing arginine and phosphatidylserine

### REFERENCES

- Ohtake, S.; Wang, Y. J. Trehalose: Current Use and Future Applications. *J. Pharm. Sci.* **2011**, *100* (6), 2020–2053.
- Richards, A. B.; Krakowka, S.; Dexter, L. B.; Schmid, H.; Wolterbeek, A. P. M.; Waalkens-Berendsen, D. H.; Shigoyuki, A.; Kurimoto, M. Trehalose: A Review of Properties, History of Use and Human Tolerance, and Results of Multiple Safety Studies. *Food Chem. Toxicol.* **2002**, *40* (7), 871–898.
- Hosseinpour-Moghaddam, K.; Caraglia, M.; Sahebkar, A. Autophagy Induction by Trehalose: Molecular Mechanisms and Therapeutic Impacts. *J. Cell Physiol* **2018**, *233* (9), 6524–6543.
- Xu, C.; Chen, X.; Sheng, W.-B.; Yang, P. Trehalose Restores Functional Autophagy Suppressed by High Glucose. *Reproductive Toxicology* **2019**, *85*, 51–58.
- DeBosch, B. J.; Heitmeier, M. R.; Mayer, A. L.; Higgins, C. B.; Crowley, J. R.; Kraft, T. E.; Chi, M.; Newberry, E. P.; Chen, Z.; Finck, B. N.; Davidson, N. O.; Yarasheski, K. E.; Hruz, P. W.; Moley, K. H. Trehalose Inhibits Solute Carrier 2A (SLC2A) Proteins to Induce Autophagy and Prevent Hepatic Steatosis. *Sci. Signal* **2016**, *9* (416), aac5472.
- Evans, T. D.; Jeong, S.-J.; Zhang, X.; Sergin, I.; Razani, B. TFEB and Trehalose Drive the Macrophage Autophagy-Lysosome System to Protect against Atherosclerosis. *Autophagy* **2018**, *14* (4), 724–726.
- Sergin, I.; Evans, T. D.; Zhang, X.; Bhattacharya, S.; Stokes, C. J.; Song, E.; Ali, S.; Dehestani, B.; Holloway, K. B.; Micevych, P. S.; Javaheri, A.; Crowley, J. R.; Ballabio, A.; Schilling, J. D.; Epelman, S.; Weihl, C. C.; Diwan, A.; Fan, D.; Zayed, M. A.; Razani, B. Exploiting Macrophage Autophagy-Lysosomal Biogenesis as a Therapy for Atherosclerosis. *Nat. Commun.* **2017**, *8* (1), 15750.
- Liu, S.; Yang, Y.; Gao, H.; Zhou, N.; Wang, P.; Zhang, Y.; Zhang, A.; Jia, Z.; Huang, S. Trehalose Attenuates Renal Ischemia-Reperfusion Injury by Enhancing Autophagy and Inhibiting Oxidative Stress and Inflammation. *American Journal of Physiology-Renal Physiology* **2020**, *318* (4), F994–F1005.
- Honma, Y.; Sato-Morita, M.; Katsuki, Y.; Mihara, H.; Baba, R.; Hino, K.; Kawashima, A.; Ariyasu, T.; Harada, M. Trehalose Alleviates Oxidative Stress-Mediated Liver Injury and Mallory-Denk Body Formation via Activating Autophagy in Mice. *Med. Mol. Morphol* **2021**, *54* (1), 41–51.
- Khalifeh, M.; Barreto, G. E.; Sahebkar, A. Trehalose as a Promising Therapeutic Candidate for the Treatment of Parkinson's Disease. *Br. J. Pharmacol.* **2019**, *176* (9), 1173–1189.
- Pupyshev, A. B.; Tikhonova, M. A.; Akopyan, A. A.; Tenditnik, M. V.; Dubrovina, N. I.; Korolenko, T. A. Therapeutic Activation of Autophagy by Combined Treatment with Rapamycin and Trehalose in a Mouse MPTP-Induced Model of Parkinson's Disease. *Pharmacol., Biochem. Behav.* **2019**, *177*, 1–11.
- Tanji, K.; Miki, Y.; Maruyama, A.; Mimura, J.; Matsumiya, T.; Mori, F.; Imaizumi, T.; Itoh, K.; Wakabayashi, K. Trehalose Intake Induces Chaperone Molecules along with Autophagy in a Mouse Model of Lewy Body Disease. *Biochem. Biophys. Res. Commun.* **2015**, *465* (4), 746–752.
- Du, J.; Liang, Y.; Xu, F.; Sun, B.; Wang, Z. Trehalose Rescues Alzheimer's Disease Phenotypes in APP/PS1 Transgenic Mice. *J. Pharm. Pharmacol.* **2013**, *65* (12), 1753–1756.
- Zhang, X.; Chen, S.; Song, L.; Tang, Y.; Shen, Y.; Jia, L.; Le, W. MTOR-Independent, Autophagic Enhancer Trehalose Prolongs Motor Neuron Survival and Ameliorates the Autophagic Flux Defect in a Mouse Model of Amyotrophic Lateral Sclerosis. *Autophagy* **2014**, *10* (4), 588–602.
- Khalifeh, M.; Barreto, G.; Sahebkar, A. Therapeutic Potential of Trehalose in Neurodegenerative Diseases: The Knowns and Unknowns. *Neural Regen Res.* **2021**, *16* (10), 2026.
- Khalifeh, M.; Read, M. I.; Barreto, G. E.; Sahebkar, A. Trehalose against Alzheimer's Disease: Insights into a Potential Therapy. *BioEssays* **2020**, *42* (8), 1900195.
- Emanuele, E. Can Trehalose Prevent Neurodegeneration? Insights from Experimental Studies. *Curr. Drug Targets* **2014**, *15* (5), 551–557.
- Abazari, A.; Meimetis, L. G.; Budin, G.; Bale, S. S.; Weissleder, R.; Toner, M. Engineered Trehalose Permeable to Mammalian Cells. *PLoS One* **2015**, *10* (6), No. e0130323.
- Collins, J.; Robinson, C.; Danhof, H.; Knetsch, C. W.; van Leeuwen, H. C.; Lawley, T. D.; Auchtung, J. M.; Britton, R. A. Dietary Trehalose Enhances Virulence of Epidemic *Clostridium Difficile*. *Nature* **2018**, *553* (7688), 291–294.
- Vinciguerra, D.; Gelb, M. B.; Maynard, H. D. Synthesis and Application of Trehalose Materials. *JACS Au* **2022**, *2* (7), 1561–1587.
- Stewart, S.; He, X. Intracellular Delivery of Trehalose for Cell Banking. *Langmuir* **2019**, *35* (23), 7414–7422.
- Lu, G.; Wang, Y.; Shi, Y.; Zhang, Z.; Huang, C.; He, W.; Wang, C.; Shen, H. Autophagy in Health and Disease: From Molecular Mechanisms to Therapeutic Target. *MedComm* **2022**, *3* (3), e150.
- Klionsky, D. J.; Petroni, G.; Amaravadi, R. K.; Baehrecke, E. H.; Ballabio, A.; Boya, P.; Bravo-San Pedro, J. M.; Cadwell, K.; Cecconi, F.; Choi, A. M. K.; Choi, M. E.; Chu, C. T.; Codogno, P.; Colombo, M. I.; Cuervo, A. M.; Deretic, V.; Dikic, I.; Elazar, Z.; Eskelinen, E.; Fimia, G. M.; Gewirtz, D. A.; Green, D. R.; Hansen, M.; Jäättelä, M.; Johansen, T.; Juhász, G.; Karantza, V.; Kraft, C.; Kroemer, G.; Ktistakis, N. T.; Kumar, S.; Lopez-Otin, C.; Macleod, K. F.; Madeo, F.; Martinez, J.; Meléndez, A.; Mizushima, N.; Münz, C.; Penninger, J. M.; Perera, R. M.; Piacentini, M.; Reggiori, F.; Rubinsztein, D. C.; Ryan, K. M.; Sadoshima, J.; Santambrogio, L.; Scorrano, L.; Simon, H.; Simon, A. K.; Simonsen, A.; Stolz, A.; Tavernarakis, N.; Tootze, S. A.; Yoshimori, T.; Yuan, J.; Yue, Z.; Zhong, Q.; Galluzzi, L.; Pietrocola, F. Autophagy in Major Human Diseases. *EMBO J.* **2021**, *40* (19), e108863.
- Hou, W.; Xie, Y.; Song, X.; Sun, X.; Lotze, M. T.; Zeh, H. J.; Kang, R.; Tang, D. Autophagy Promotes Ferroptosis by Degradation of Ferritin. *Autophagy* **2016**, *12* (8), 1425–1428.
- Fujikake, N.; Shin, M.; Shimizu, S. Association Between Autophagy and Neurodegenerative Diseases. *Front Neurosci* **2018**, *12*, 00255.



- (26) Djajadikerta, A.; Keshri, S.; Pavel, M.; Prestil, R.; Ryan, L.; Rubinsztein, D. C. Autophagy Induction as a Therapeutic Strategy for Neurodegenerative Diseases. *J. Mol. Biol.* **2020**, *432* (8), 2799–2821.
- (27) Mardones, P.; Rubinsztein, D. C.; Hetz, C. Mystery Solved: Trehalose Kickstarts Autophagy by Blocking Glucose Transport. *Sci. Signal* **2016**, *9* (416), fs2.
- (28) Mayer, A. L.; Higgins, C. B.; Heitmeier, M. R.; Kraft, T. E.; Qian, X.; Crowley, J. R.; Hyrc, K. L.; Beatty, W. L.; Yarasheski, K. E.; Hruz, P. W.; DeBosch, B. J. SLC2A8 (GLUT8) Is a Mammalian Trehalose Transporter Required for Trehalose-Induced Autophagy. *Sci. Rep.* **2016**, *6* (1), 38586.
- (29) Rusmini, P.; Cortese, K.; Crippa, V.; Cristofani, R.; Cicardi, M. E.; Ferrari, V.; Vezzoli, G.; Tedesco, B.; Meroni, M.; Messi, E.; Piccolella, M.; Galbati, M.; Garrè, M.; Morelli, E.; Vaccari, T.; Poletti, A. Trehalose Induces Autophagy via Lysosomal-Mediated TFEB Activation in Models of Motoneuron Degeneration. *Autophagy* **2019**, *15* (4), 631–651.
- (30) Wu, Z.; Zhou, M.; Tang, X.; Zeng, J.; Li, Y.; Sun, Y.; Huang, J.; Chen, L.; Wan, M.; Mao, C. Carrier-Free Trehalose-Based Nanomotors Targeting Macrophages in Inflammatory Plaque for Treatment of Atherosclerosis. *ACS Nano* **2022**, *16* (3), 3808–3820.
- (31) Li, Z.; Zhang, L.; Xue, C.; Zhang, Y.; Yu, Y.; Guo, X.; Zhang, Z. Hydroxypropyl- $\beta$ -Cyclodextrin/Oridonin and Trehalose Loaded Nanovesicles Attenuate Foam Cells Formation and Regulate the Inflammation. *Eur. Polym. J.* **2022**, *180*, 111596.
- (32) Yang, J.; Ding, L.; Yu, L.; Wang, Y.; Ge, M.; Jiang, Q.; Chen, Y. Nanomedicine Enables Autophagy-Enhanced Cancer-Cell Ferroptosis. *Sci. Bull. (Beijing)* **2021**, *66* (5), 464–477.
- (33) Higgins, C. B.; Adams, J. A.; Ward, M. H.; Greenberg, Z. J.; Milewska, M.; Sun, J.; Zhang, Y.; Chiquetto Paracatu, L.; Dong, Q.; Ballentine, S.; Li, W.; Wandzik, I.; Schuettel, L. G.; DeBosch, B. J. The Tetraspanin Transmembrane Protein CD53 Mediates Dyslipidemia and Integrates Inflammatory and Metabolic Signaling in Hepatocytes. *J. Biol. Chem.* **2023**, *299* (2), 102835.
- (34) Cunha, A.; Gaubert, A.; Verget, J.; Thiolat, M.-L.; Barthélémy, P.; Latxague, L.; Dehay, B. Trehalose-Based Nucleolipids as Nanocarriers for Autophagy Modulation: An In Vitro Study. *Pharmaceutics* **2022**, *14* (4), 857.
- (35) Maruf, A.; Milewska, M.; Kovács, T.; Varga, M.; Vellai, T.; Lalik, A.; Student, S.; Borges, O.; Wandzik, I. Trehalose-Releasing Nanogels: A Step toward a Trehalose Delivery Vehicle for Autophagy Stimulation. *Biomaterials Advances* **2022**, *138*, 212969.
- (36) Assoni, G.; Frapporti, G.; Colombo, E.; Gornati, D.; Perez-Carrion, M. D.; Palito, L.; Seneci, P.; Piccoli, G.; Arosio, D. Trehalose-Based Neuroprotective Autophagy Inducers. *Bioorg. Med. Chem. Lett.* **2021**, *40*, 127929.
- (37) Colombo, E.; Biocotino, M.; Frapporti, G.; Randazzo, P.; Christodoulou, M. S.; Piccoli, G.; Polito, L.; Seneci, P.; Passarella, D. Nanolipid-Trehalose Conjugates and Nano-Assemblies as Putative Autophagy Inducers. *Pharmaceutics* **2019**, *11* (8), 422.
- (38) Frapporti, G.; Colombo, E.; Ahmed, H.; Assoni, G.; Polito, L.; Randazzo, P.; Arosio, D.; Seneci, P.; Piccoli, G. Squalene-Based Nano-Assemblies Improve the Pro-Autophagic Activity of Trehalose. *Pharmaceutics* **2022**, *14* (4), 862.
- (39) Burek, M.; Wandzik, I. Trehalose-Rich, Degradable Hydrogels Designed for Trehalose Release under Physiologically Relevant Conditions. *Polymers (Basel)* **2019**, *11* (12), 2027.
- (40) Czaja, M. J. Function of Autophagy in Nonalcoholic Fatty Liver Disease. *Dig. Dis. Sci.* **2016**, *61* (5), 1304–1313.
- (41) Khambu, B.; Yan, S.; Huda, N.; Liu, G.; Yin, X.-M. Autophagy in Non-Alcoholic Fatty Liver Disease and Alcoholic Liver Disease. *Liver Res.* **2018**, *2* (3), 112–119.
- (42) Lundquist, J. J.; Toone, E. J. The Cluster Glycoside Effect. *Chem. Rev.* **2002**, *102* (2), 555–578.
- (43) Libby, P.; Buring, J. E.; Badimon, L.; Hansson, G. K.; Deanfield, J.; Bittencourt, M. S.; Tokgözoğlu, L.; Lewis, E. F. Atherosclerosis. *Nat. Rev. Dis. Primers* **2019**, *5* (1), 56.
- (44) Hassanpour, M.; Rahbarghazi, R.; Nouri, M.; Aghamohammadzadeh, N.; Safaei, N.; Ahmadi, M. Role of Autophagy in Atherosclerosis: Foe or Friend? *J. Inflamm.* **2019**, *16* (1), 8.
- (45) Sergin, I.; Razani, B. Self-Eating in the Plaque: What Macrophage Autophagy Reveals about Atherosclerosis. *Trends in Endocrinology & Metabolism* **2014**, *25* (5), 225–234.
- (46) Emanuel, R.; Sergin, I.; Bhattacharya, S.; Turner, J. N.; Epelman, S.; Settembre, C.; Diwan, A.; Ballabio, A.; Razani, B. Induction of Lysosomal Biogenesis in Atherosclerotic Macrophages Can Rescue Lipid-Induced Lysosomal Dysfunction and Downstream Sequelae. *Arterioscler. Thromb. Vasc. Biol.* **2014**, *34* (9), 1942–1952.
- (47) Ouimet, M.; Franklin, V.; Mak, E.; Liao, X.; Tabas, I.; Marcel, Y. L. Autophagy Regulates Cholesterol Efflux from Macrophage Foam Cells via Lysosomal Acid Lipase. *Cell Metab.* **2011**, *13* (6), 655–667.
- (48) Xiao, Q.; Che, X.; Cai, B.; Tao, Z.; Zhang, H.; Shao, Q.; Pu, J. Macrophage Autophagy Regulates Mitochondria-mediated Apoptosis and Inhibits Necrotic Core Formation in Vulnerable Plaques. *J. Cell Mol. Med.* **2020**, *24* (1), 260–275.
- (49) Liao, X.; Sluimer, J. C.; Wang, Y.; Subramanian, M.; Brown, K.; Pattison, J. S.; Robbins, J.; Martinez, J.; Tabas, I. Macrophage Autophagy Plays a Protective Role in Advanced Atherosclerosis. *Cell Metab.* **2012**, *15* (4), 545–553.
- (50) Debnath, J.; Gammoh, N.; Ryan, K. M. Autophagy and Autophagy-Related Pathways in Cancer. *Nat. Rev. Mol. Cell Biol.* **2023**, *24*, 560.
- (51) Chavez-Dominguez, R.; Perez-Medina, M.; Lopez-Gonzalez, J. S.; Galicia-Velasco, M.; Aguilar-Cazares, D. The Double-Edge Sword of Autophagy in Cancer: From Tumor Suppression to Pro-Tumor Activity. *Front. Oncol.* **2020**, *10*, 578418.
- (52) Lim, S. M.; Mohamad Hanif, E. A.; Chin, S.-F. Is Targeting Autophagy Mechanism in Cancer a Good Approach? The Possible Double-Edge Sword Effect. *Cell Biosci.* **2021**, *11* (1), 56.
- (53) Liu, L.; Li, L.; Li, M.; Luo, Z. Autophagy-Dependent Ferroptosis as a Therapeutic Target in Cancer. *ChemMedChem.* **2021**, *16* (19), 2942–2950.
- (54) Tyedmers, J.; Mogk, A.; Bukau, B. Cellular Strategies for Controlling Protein Aggregation. *Nat. Rev. Mol. Cell Biol.* **2010**, *11* (11), 777–788.
- (55) Chiti, F.; Dobson, C. M. Protein Misfolding, Amyloid Formation, and Human Disease: A Summary of Progress Over the Last Decade. *Annu. Rev. Biochem.* **2017**, *86* (1), 27–68.
- (56) Wilson, D. M.; Cookson, M. R.; Van Den Bosch, L.; Zetterberg, H.; Holtzman, D. M.; Dewachter, I. Hallmarks of Neurodegenerative Diseases. *Cell* **2023**, *186* (4), 693–714.
- (57) Calabrese, G.; Molzahn, C.; Mayor, T. Protein Interaction Networks in Neurodegenerative Diseases: From Physiological Function to Aggregation. *J. Biol. Chem.* **2022**, *298* (7), 102062.
- (58) Mpathia, Z.; Hone, E.; Tripathi, T.; Sargeant, T.; Martins, R.; Bharadwaj, P. Autophagy Modulation as a Treatment of Amyloid Diseases. *Molecules* **2019**, *24* (18), 3372.
- (59) Zaman, M.; Khan, A. N.; Wahiduzzaman; Zakariya, S. M.; Khan, R. H. Protein Misfolding, Aggregation and Mechanism of Amyloid Cytotoxicity: An Overview and Therapeutic Strategies to Inhibit Aggregation. *Int. J. Biol. Macromol.* **2019**, *134*, 1022–1037.
- (60) Abe, M.; Abe, Y.; Ohkuri, T.; Mishima, T.; Monji, A.; Kanba, S.; Ueda, T. Mechanism for Retardation of Amyloid Fibril Formation by Sugars in V $\lambda$ 6 Protein. *Protein Sci.* **2013**, *22* (4), 467–474.
- (61) Marasini, C.; Foderà, V.; Vestergaard, B. Sucrose Modulates Insulin Amyloid-like Fibril Formation: Effect on the Aggregation Mechanism and Fibril Morphology. *RSC Adv.* **2017**, *7* (17), 10487–10493.
- (62) Liu, R.; Barkhordarian, H.; Emadi, S.; Park, C.; Sierks, M. Trehalose Differentially Inhibits Aggregation and Neurotoxicity of Beta-Amyloid 40 and 42. *Neurobiol. Dis.* **2005**, *20* (1), 74–81.
- (63) Bashir, S.; Shamsi, A.; Ahmad, F.; Hassan, Md. I.; Kamal, M. A.; Islam, A. Biophysical Elucidation of Fibrillation Inhibition by Sugar Osmolytes in  $\alpha$ -Lactalbumin: Multispectroscopic and Molecular Docking Approaches. *ACS Omega* **2020**, *5* (41), 26871–26882.

- (64) Vilasi, S.; Iannuzzi, C.; Portaccio, M.; Irace, G.; Sirangelo, I. Effect of Trehalose on W7FW14F Apomyoglobin and Insulin Fibrillation: New Insight into Inhibition Activity. *Biochemistry* **2008**, *47* (6), 1789–1796.
- (65) Nayak, A.; Lee, C.-C.; McRae, G. J.; Belfort, G. Osmolyte Controlled Fibrillation Kinetics of Insulin: New Insight into Fibrillation Using the Preferential Exclusion Principle. *Biotechnol. Prog.* **2009**, *25* (5), 1508–1514.
- (66) Rajaram, H.; Palanivelu, M. K.; Arumugam, T. V.; Rao, V. M.; Shaw, P. N.; McGeary, R. P.; Ross, B. P. 'Click' Assembly of Glycoclusters and Discovery of a Trehalose Analogue That Retards A $\beta$ 40 Aggregation and Inhibits A $\beta$ 40-Induced Neurotoxicity. *Bioorg. Med. Chem. Lett.* **2014**, *24* (18), 4523–4528.
- (67) Debnath, K.; Pradhan, N.; Singh, B. K.; Jana, N. R.; Jana, N. R. Poly(Trehalose) Nanoparticles Prevent Amyloid Aggregation and Suppress Polyglutamine Aggregation in a Huntington's Disease Model Mouse. *ACS Appl. Mater. Interfaces* **2017**, *9* (28), 24126–24139.
- (68) Pradhan, N.; Shekhar, S.; Jana, N. R.; Jana, N. R. Sugar-Terminated Nanoparticle Chaperones Are  $10^2$ – $10^5$  Times Better Than Molecular Sugars in Inhibiting Protein Aggregation and Reducing Amyloidogenic Cytotoxicity. *ACS Appl. Mater. Interfaces* **2017**, *9* (12), 10554–10566.
- (69) Mandal, S.; Debnath, K.; Jana, N. R.; Jana, N. R. Trehalose-Functionalized Gold Nanoparticle for Inhibiting Intracellular Protein Aggregation. *Langmuir* **2017**, *33* (49), 13996–14003.
- (70) Mandal, S.; Debnath, K.; Jana, N. R.; Jana, N. R. Trehalose-Conjugated, Catechin-Loaded Polylactide Nanoparticles for Improved Neuroprotection against Intracellular Polyglutamine Aggregates. *Biomacromolecules* **2020**, *21* (4), 1578–1586.
- (71) Mandal, S.; Jana, D.; Dolai, J.; Sarkar, A. K.; Ghorai, B. K.; Jana, N. R. Biodegradable Poly(Trehalose) Nanoparticle for Preventing Amyloid Beta Aggregation and Related Neurotoxicity. *ACS Appl. Bio Mater.* **2023**, *6* (6), 2102–2110.
- (72) Mandal, S.; Panja, P.; Debnath, K.; Jana, N. R.; Jana, N. R. Small-Molecule-Functionalized Hyperbranched Polyglycerol Dendrimers for Inhibiting Protein Aggregation. *Biomacromolecules* **2020**, *21* (8), 3270–3278.
- (73) Wada, M.; Miyazawa, Y.; Miura, Y. A Specific Inhibitory Effect of Multivalent Trehalose toward A $\beta$ (1–40) Aggregation. *Polym. Chem.* **2011**, *2* (8), 1822.
- (74) Miura, Y.; You, C.; Ohnishi, R. Inhibition of Alzheimer Amyloid  $\beta$  Aggregation by Polyvalent Trehalose. *Sci. Technol. Adv. Mater.* **2008**, *9* (2), 024407.
- (75) Milewska, M.; Milewski, A.; Wandzik, I.; Stenzel, M. H. Structurally Analogous Trehalose and Sucrose Glycopolymers - Comparative Characterization and Evaluation of Their Effects on Insulin Fibrillation. *Polym. Chem.* **2022**, *13* (13), 1831–1843.
- (76) Messina, M. S.; Ko, J. H.; Yang, Z.; Strouse, M. J.; Houk, K. N.; Maynard, H. D. Effect of Trehalose Polymer Regioisomers on Protein Stabilization. *Polym. Chem.* **2017**, *8* (33), 4781–4788.
- (77) Gelb, M. B.; Maynard, H. D. Effect of Poly(Trehalose Methacrylate) Molecular Weight and Concentration on the Stability and Viscosity of Insulin. *Macromol. Mater. Eng.* **2021**, *306* (9), 2100197.
- (78) Pelegri-O'Day, E. M.; Bhattacharya, A.; Theopold, N.; Ko, J. H.; Maynard, H. D. Synthesis of Zwitterionic and Trehalose Polymers with Variable Degradation Rates and Stabilization of Insulin. *Biomacromolecules* **2020**, *21* (6), 2147–2154.
- (79) Jain, N. K.; Roy, I. Effect of Trehalose on Protein Structure. *Protein Sci.* **2009**, *18* (1), 24–36.
- (80) Balcão, V. M.; Vila, M. M. D. C. Structural and Functional Stabilization of Protein Entities: State-of-the-Art. *Adv. Drug Deliv. Rev.* **2015**, *93*, 25–41.
- (81) Ohtake, S.; Kita, Y.; Arakawa, T. Interactions of Formulation Excipients with Proteins in Solution and in the Dried State. *Adv. Drug Deliv. Rev.* **2011**, *63* (13), 1053–1073.
- (82) Debnath, K.; Sarkar, A. K.; Jana, N. R.; Jana, N. R. Inhibiting Protein Aggregation by Small Molecule-Based Colloidal Nanoparticles. *Acc. Mater. Res.* **2022**, *3* (1), 54–66.

**STATEMENT 2**

I declare that my percentage contribution to the publication [P2] entitled “*pH and Reduction Dual-Responsive Nanogels as Smart Nanocarriers to Resist Doxorubicin Aggregation*” (published in **Molecules** 2022, 27, 5983. DOI: 10.3390/molecules27185983) was 65%.

Justification: As part of this work, I served as a co-author for various tasks, including performing experiments: synthesizing anionic pH/reduction dual responsive nanogels, conducting drug release studies, measuring DLS and zeta potential, checking colloidal stability, preparing samples for cryoTEM, and assessing the cytotoxicity of nanogels in HCT 116 colon cancer cell line. Additionally, I was responsible for collecting and analyzing all experimental data, participating in writing of manuscript, creating figures and tables, managing citations, formatting the manuscript according to the journal’s style, assisting in revising the manuscript after peer review, and final proofreading.



Ali Maruf, M.Eng.

(PhD candidate)

As the corresponding author of the above-mentioned publication, which is part of the doctoral thesis of Mr. Ali Maruf, I declare that the percentage contribution of the remaining co-authors can be estimated as follows:

Milewska M: 10%

Lalik A: 5%

Wandzik I: 20%





prof. dr hab. inż. Ilona Wandzik

(Supervisor / corresponding author)

Article

# pH and Reduction Dual-Responsive Nanogels as Smart Nanocarriers to Resist Doxorubicin Aggregation

 Ali Maruf <sup>1,2</sup> , Małgorzata Milewska <sup>1,2</sup>, Anna Lalik <sup>2,3</sup> and Ilona Wandzik <sup>1,2,\*</sup> 
<sup>1</sup> Department of Organic Chemistry, Bioorganic Chemistry and Biotechnology, Faculty of Chemistry, Silesian University of Technology, Krzywoustego 4, 44-100 Gliwice, Poland

<sup>2</sup> Biotechnology Center, Silesian University of Technology, Krzywoustego 8, 44-100 Gliwice, Poland

<sup>3</sup> Department of Systems Biology and Engineering, Faculty of Automatic Control, Electronics and Computer Science, Silesian University of Technology, Akademicka 16, 44-100 Gliwice, Poland

\* Correspondence: ilona.wandzik@polsl.pl

**Abstract:** The use of smart nanocarriers that can modulate therapeutic release aided by biological cues can prevent undesirable cytotoxicity caused by the premature release of cytotoxic drugs during nanocarrier circulation. In this report, degradable nanocarriers based on pH/reduction dual-responsive nanogels were synthesized to encapsulate doxorubicin hydrochloride (DOX) and specifically boost the release of DOX in conditions characteristic of the cancer microenvironment. Nanogels containing anionic monomer 2-carboxyethyl acrylate (CEA) and *N,N'*-bis(acryloyl)cystamine (CBA) as a degradable crosslinker have been successfully synthesized via photoinitiated free radical polymerization. The loading process was conducted after polymerization by taking advantage of the electrostatic interaction between the negatively charged nanogels and the positively charged DOX. In this case, a high drug loading capacity (DLC) of up to 27.89% was achieved. The entrapment of DOX into a nanogel network could prevent DOX from aggregating in biological media at DOX concentrations up to ~160 µg/mL. Anionic nanogels had an average hydrodynamic diameter ( $d_H$ ) of around 90 nm with a negative zeta ( $\zeta$ ) potential of around -25 mV, making them suitable for targeting cancer tissue via the enhanced permeation effect. DOX-loaded nanogels formed a stable dispersion in different biological media, including serum-enriched cell media. In the presence of glutathione (GSH) and reduced pH, drug release was enhanced, which proves dual responsiveness. An in vitro study using the HCT 116 colon cancer cell line demonstrated the enhanced cytotoxic effect of the NG-CBA/DOX-1 nanogel compared to free DOX. Taken together, pH/reduction dual-responsive nanogels show promise as drug delivery systems for anticancer therapy.

**Keywords:** doxorubicin; drug delivery; glutathione; nanogel; stimuli-responsive



**Citation:** Maruf, A.; Milewska, M.; Lalik, A.; Wandzik, I. pH and Reduction Dual-Responsive Nanogels as Smart Nanocarriers to Resist Doxorubicin Aggregation. *Molecules* **2022**, *27*, 5983. <https://doi.org/10.3390/molecules27185983>

Academic Editor: Luigi Paduano

Received: 17 August 2022

Accepted: 9 September 2022

Published: 14 September 2022

**Publisher's Note:** MDPI stays neutral with regard to jurisdictional claims in published maps and institutional affiliations.



**Copyright:** © 2022 by the authors. Licensee MDPI, Basel, Switzerland. This article is an open access article distributed under the terms and conditions of the Creative Commons Attribution (CC BY) license (<https://creativecommons.org/licenses/by/4.0/>).

## 1. Introduction

Doxorubicin hydrochloride (DOX), an anthracycline family antibiotic, is one of the most effective chemotherapeutic drugs developed against a variety of cancers. Free DOX, however, tends to aggregate into fibril-like structures under physiological conditions, has poor bioavailability, and causes cardiotoxicity; therefore several nanocarriers containing DOX have been developed [1]. DOX-loaded PEGylated liposomes (Doxil) became the first therapeutic nanomedicine on the market with the FDA approval in 1995. More recently, two liposomal formulations have been approved (Lipodox and Myocet) and others are under clinical trials. Liposomal DOX formulations improved circulation time and reduced cardiotoxicity but low cellular uptake in the tumor microenvironment and a poor DOX release profile from the particles are still issues [2]. In the search for new carriers, polymer-based DOX nano delivery systems have drawn attention, and some of them have reached clinical trials. Among polymeric carriers, nano-scaled hydrogel platforms play a crucial role because they are biocompatible, have a high loading capacity, and possess a potential responsiveness to environmental stimuli [3–8]. These characteristics make polymer-based

nanodelivery systems widely studied as tumor drug carriers, with DOX being the most intensively studied [1]. Polysaccharide-based [9] and composite [10] nanogels have also been investigated for drug delivery applications. However, nanogels based on synthetic polymers offer better opportunities for surface modification and conjugation with ligands to target tumors. Several approaches have been utilized to fabricate bioresponsive nanogels of synthetic origin that are capable of facile loading and triggering release of DOX in response to the various biological signals specific to tumor microenvironments or the intracellular compartments of cancer cells. By combining several stimuli-responsive monomers and a suitable degradable crosslinker, dual-responsive or even multiresponsive DOX delivery systems can be produced, such as pH/temperature [11–15], pH/redox [16–23], or pH/temperature/redox [24].

Among the various stimuli, pH and reductive environments caused by the presence of glutathione (GSH) are the most prominent and characteristically distinctive stimuli in cancer cells. The pH of the tumor tissue (pH 6.4–7.0) is lower than that of healthy tissues (pH 7.2–7.5) [25]. Moreover, pH variations in the extracellular compartments of cells (pH 7.4) compared to the intracellular lysosomes (pH 4.5–5.0) [26] can provide a pH-responsive drug release. High concentrations of GSH reaching millimolar levels (2–10 mM) within cells and micromolar levels (2–20  $\mu$ M) in the blood plasma [27] facilitate the cleavage of disulfide bonds in intracellular compartments. Therefore, nanogels crosslinked by disulfide bonds are among the most extensively studied.

At acidic conditions, the controlled self-assembly of carboxyl-containing anionic nanogels with oppositely charged DOX can produce nanocarriers with a high drug loading and pH-sensitive drug release due to the decreased electrostatic interactions with the drug [16,21,22,24]. Another strategy for ensuring pH-sensitivity is the incorporation of protonable amino groups into the nanogel network since they are prone to swell at slightly acidic pH and thus can trigger drug release. In such a case, DOX is usually encapsulated by hydrophobic interactions, which results in a substantially lower DLC. The examples are nanogels containing tertiary amines [17,23].

In the previously mentioned examples of pH/reduction dual-responsive nanogels, DOX was incorporated by physical entrapment, mostly by controlled self-assembly or due to hydrophobic interactions. The drug was loaded during polymerization [19,20] or in the post-polymerization process [16,17,21–24]. In contrast, the Haag group developed pH/reduction dual-responsive nanogels where DOX was covalently conjugated to the biodegradable nanogel matrix via an acid-labile hydrazone linker and achieved a DLC of ~4 wt% [18].

The most effective way to obtain high DLCs relies on the controlled self-assembly of anionic polyelectrolyte-based nanogels with the positively charged DOX amine group. Free DOX itself is prone to aggregate under physiological conditions, which can influence the colloidal stability of nanocomplexes. By increasing the DOX content (DLC), it is more likely that nanogels will not be stable at high concentrations, which are demanded during the preparation of stock solutions for both *in vitro* and *in vivo* study purposes. The colloidal stability of DOX-loaded nanogels is usually not fully explained or not addressed. In light of the foregoing, this study was conducted with the main purpose of synthesizing nanogels that can encapsulate high content of DOX via an electrostatic interaction, maintain DOX-loaded nanogel stability in biological media, and enhance the DOX release profile in a cancer-like environment where the GSH level is high, and the environment is acidic. In this study, we compared the aggregation tendencies of free DOX (hydrochloride salt) with DOX complexed with nanogel carriers in physiological conditions to determine the encapsulation limit with regard to the colloidal stability of nanocarriers.

In this work, nanogels were synthesized via photoinitiated free radical polymerization (FRP) of *N,N*-dimethylacrylamide (DMAM) and 2-carboxyethyl acrylate (CEA) in the presence of a disulfide-type CBA crosslinker (Figure 1A). The anionic monomer, CEA, was chosen to provide the electrostatic interactions with the positively charged DOX. CBA was selected as the crosslinker to achieve accelerated drug release triggered by the high

concentration of GSH in the tumor cytoplasm. Polymerization was carried out by an inverse microemulsion technique to create the nanogels, which are able to form stable dispersions in various biological media, including serum-enriched media.

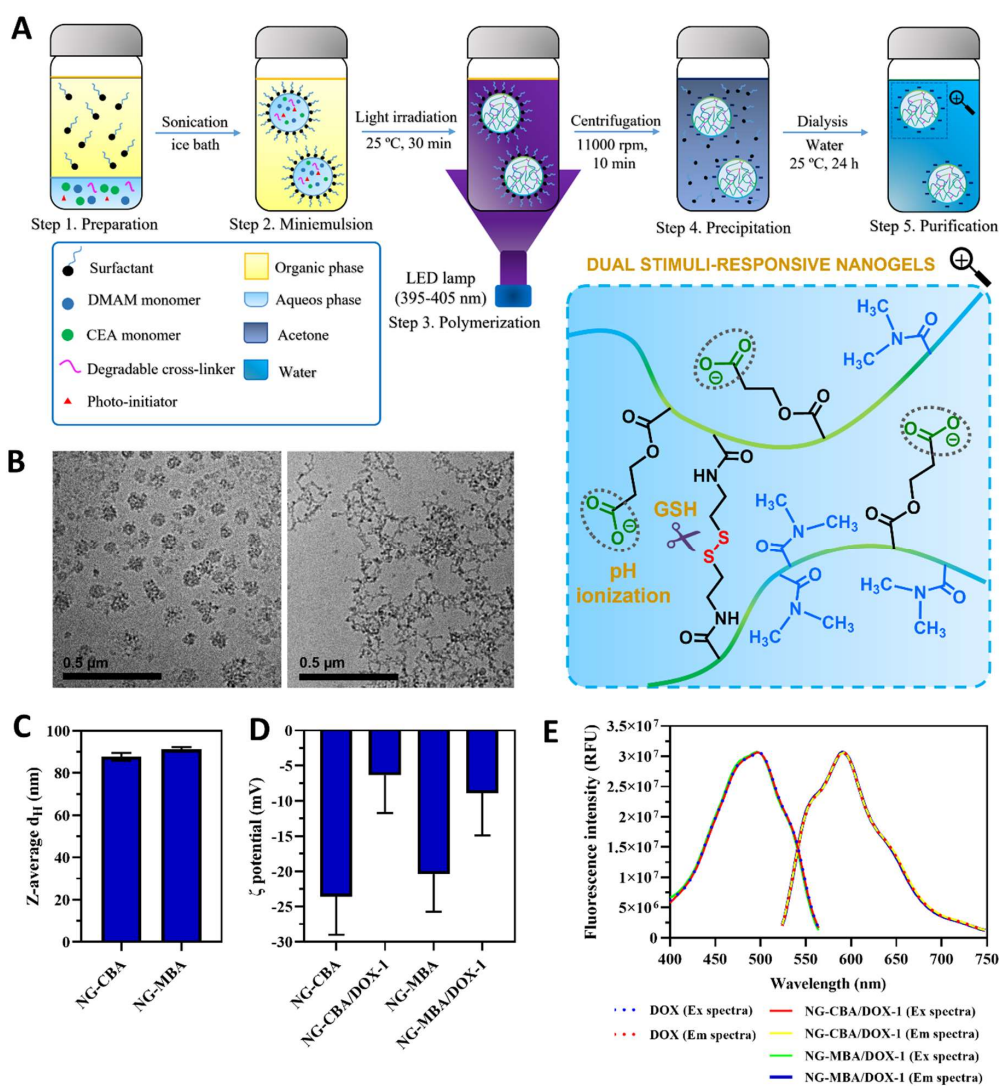


**Figure 1.** Nanogel synthesis and characterization. (A) A schematic diagram of the synthetic procedure of pH/reduction dual-responsive nanogels. (B) Cryo-TEM micrographs of NG-CBA with (right) and without (left) GSH treatment. Scale bar = 0.5 μm. (C) Z-average  $d_H$  of NG-CBA and NG-MBA nanogels in 1 mM KCl measured by DLS. Due to the interference of DOX fluorescence, DLS measurements of NG-CBA/DOX-1 and NG-MBA/DOX-1 nanogels were not possible. (D)  $\zeta$  potential of NG-CBA, NG-CBA/DOX-1, NG-MBA, and NG-MBA/DOX-1 nanogels in 1 mM KCl. (E) Fluorescence spectra of DOX and NG/DOX nanogels. The data were reported as mean  $\pm$  SD ( $n = 4$ ).

## 2. Results and Discussion

### 2.1. Synthesis and Characterization of DOX-Loaded pH/Reduction Dual-Responsive Nanogels

Dual stimuli-responsive nanogels were synthesized via FRP in inverse water-in-oil (w/o) miniemulsions using a photoinitiator (LAP) under optimized light irradiation at a wavelength of 395–405 nm (Figure 1A). The monomer composition and initiator concentration were based on our previously reported synthesis of trehalose-containing nanogels to ensure the relevant size and good stability of the nanogels [28]. DMAM was chosen as the main monomer, while CBA was used as the degradable disulfide crosslinker. To ensure the negative charge of nanogels, which is required for electrostatic interaction-mediated DOX loading, CEA monomer was incorporated. In all cases, a cyclohexane/Span 80 system was used as a continuous phase, whereas a PB solution containing monomers and LAP was used as the aqueous phase. Polymerizations were accomplished under LED irradiation at room temperature for 30 min with yields in the range of 60–65% depending on composition (Table 1). Moreover, in the same procedure, the reduction-insensitive nanogel crosslinked by MBA was prepared to compare the behavior of the nanogels in a reducing or non-reducing environment. For degradable nanogels, the notation NG-CBA was used, whereas the notation NG-MBA was adopted for non-degradable nanogels (Table 1). Both NG-CBA and NG-MBA nanogels had similar average sizes of around 90 nm, determined by DLS (Table 1, Figures 1C, S1 and S2). The cryo-TEM micrographs revealed a spherical shape with particle sizes similar to those of the DLS analysis (Figure 1B). Degradation induced by GSH led to the disintegration of the nanogel network, which was also observed using cryo-TEM.

**Table 1.** Monomer feed composition and physicochemical properties of nanogels.

Nanogel	Monomer Feed Composition <sup>a</sup>		Post-Polymerization Loading			DLC (%)	DLE (%)	d <sub>H</sub> (PdI) (nm)	ζ Potential (mV)
	CEA mg (mmol)	DMAM mg (mmol)	NG (mg)	DOX (mg)	CEA:DOX (mol:mol)				
NG-CBA	16.0 (0.111)	183.6 (1.852)	-	-	-	-	-	87.67 (0.30)	-23.6
NG-MBA	16.0 (0.111)	183.6 (1.852)	-	-	-	-	-	91.19 (0.38)	-20.4
NG-CBA/DOX-1	16.0 (0.111)	183.6 (1.852)	5.0	1.0	1:0.85	16.29	97.74	<sup>b</sup>	-6.33
NG-CBA/DOX-2	16.0 (0.111)	183.6 (1.852)	5.0	0.5	1:0.42	9.09	99.62	<sup>b</sup>	-18.6
NG-CBA/DOX-3	32.0 (0.222)	167.6 (1.691)	5.0	2.0	1:0.85	27.89	97.61	<sup>b</sup>	-11.3
NG-MBA/DOX-1	16.0 (0.111)	183.6 (1.852)	5.0	1.0	1:0.85	16.47	98.78	<sup>b</sup>	-8.92

<sup>a</sup> CBA or MBA were used in an equimolar quantity of 0.10 mmol, LAP was used at a concentration of 0.008 mmol, and the total mass of the monomers was 227.9 mg and 217.2 mg for NG-CBA and NG-MBA nanogels, respectively.

<sup>b</sup> DLS measurement of DOX-containing nanogels was not possible due to the interference of DOX fluorescence.

DOX was loaded into nanogel in the post-polymerization process. Three different compositions were prepared, differing in the molar ratios of anionic units of nanogel to DOX (NG-CBA/DOX-1,2) and the content of anionic units (NG-CBA/DOX-3). The unloaded NG-CBA and NG-MBA nanogels showed similar ζ potentials of -23.6 and -20.4 mV, respectively (Table 1, Figures 1D and S3–S8). After DOX loading, the ζ potential of the nanogels increased above -15 mV (Table 1, Figure 1D), depending on the DLC of DOX, due to the neutralizing effects of the positively charged DOX. DOX was loaded at DLCs ranging from 9.09 to 27.89% w/w, according to the molar ratio of anionic units of nanogel to DOX. Similar DLCs were observed in NG-CBA-DOX-1 and NG-MBA-DOX-1 nanogels due to the same molar amount of anionic CEA units in the structure.

In comparison to the similar design of nanogels with pH/reduction responsivity, the currently studied nanogels exhibited relatively satisfying DLCs (up to ~28% w/w). In post-polymerization loading, other pH/reduction dual-responsive nanogels were characterized by DLCs from 2.5 to 15.1% w/w [17,22–24]. They also displayed a comparable release profile, ranging from 50 to 70% within 12 h in a cancer-mimicking environment (acidic environment and high GSH levels), but only a limited release (less than 30%) under normal physiological conditions [17,22–24]. In contrast, covalent conjugation of DOX to pH/reduction dual-

responsive nanogels resulted in a significantly lower DLC (below 5% *w/w*), but it also enabled us to limit DOX release under physiological conditions (less than 10%), while accelerating it by almost six times in a cancer-like environment [18]. Additionally, as shown in Figure 1E, the nanogels (NG-CBA and NG-MBA) did not interfere with the fluorescence property of DOX, as indicated by identical (Ex/Em) fluorescence spectra.

## 2.2. Aggregation Behavior of DOX and DOX-Loaded pH/Reduction Dual-Responsive Nanogels

It is well known that DOX (hydrochloride salt) forms fibril-shaped aggregates under physiological conditions, and this can result in a decrease in the drug's intercellular transportation efficiency [29]. DOX solutions in PBS (pH 7.4) at concentrations above 40  $\mu\text{g}/\text{mL}$  start to aggregate. Considering DOX's  $\text{IC}_{50}$  is in the range of 0.06 to 0.50  $\mu\text{g}/\text{mL}$  depending on cancer cell line [30], one would not expect aggregation to be a problem. However, stock solutions are usually two orders of magnitude greater for biological assays. As a result, aggregation may cause a disturbance in reproducibility when a drug solution is dispensed. Therefore, aggregation of DOX in solutions should always be avoided. A substantial amount of DOX encapsulated in nanogel can also induce the aggregation of supramolecular structures formed after complexation. Our study revealed that DOX entrapment into the nanogel network could prevent aggregation at concentrations up to 160  $\mu\text{g}/\text{mL}$ .

Figure 2A,B shows how the NG-CBA/DOX-1 nanogel improved the solubility of DOX in 10 mM PB (pH 7.4). The transmittance value of free DOX at a concentration of 20  $\mu\text{g}/\text{mL}$  was nearly 100% over 3 days which indicates that the solution is free of insoluble aggregates. However, the transmittance value decreased over time at concentrations of 40–80  $\mu\text{g}/\text{mL}$ , indicating DOX aggregation (Figure 2A). DOX instantly aggregated and sedimented at a concentration of 100  $\mu\text{g}/\text{mL}$  (Figure 2B). Moreover, at this DOX concentration, the transmittance value was nearly zero. In contrast, the NG-CBA/DOX-1 nanogel containing 100  $\mu\text{g}/\text{mL}$  of DOX exhibited a transmittance value of 95%, which proves the lack of aggregation. The stability of NG-CBA and NG-CBA/DOX-1,2,3 nanogels was further studied in different biological media, including serum-enriched media, where nanoparticle dispersion might collapse and form aggregates. Figure 2C showed that both bare nanogel and DOX-containing nanogels were stable for at least 2 days in different biological media at a nanogel concentration of 100  $\mu\text{g}/\text{mL}$ . In the higher nanogel concentration of 1000  $\mu\text{g}/\text{mL}$ , the unloaded NG-CBA nanogel was stable in all tested media. However, the DOX-containing nanogels showed limited stability in serum-enriched media for both fresh solutions and solutions incubated at 37 °C; for 2 days (Figure 2D). The greater the DOX content, the greater the decrease in transparency. Therefore, in order to avoid any aggregation, NG-CBA-DOX-1 nanogel containing only 16.29 wt% of DOX was used for further drug release studies.



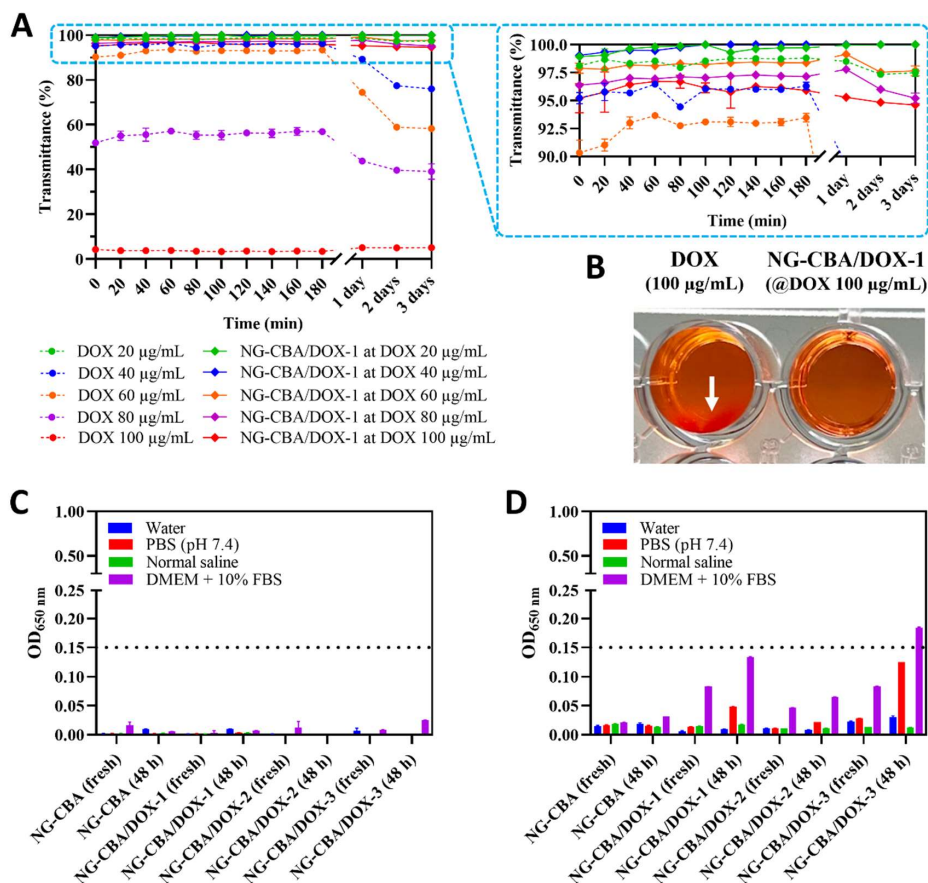


**Figure 2.** (A) DOX aggregation tendency in 10 mM PB (pH 7.4) at different concentrations (20, 40, 60, 80, and 100 µg/mL) compared to NG-CBA/DOX-1 nanogels (20, 40, 60, 80, and 100 µg/mL DOX) for 3 days at 37 °C. (B) Visual appearance of DOX 100 µg/mL and NG-CBA/DOX-1 nanogel containing 100 µg/mL DOX in 10 mM PB (pH 7.4) after 1 day at 37 °C. The white arrow indicates DOX aggregates. (C,D) Stability of NG-CBA, NG-CBA/DOX-1, NG-CBA/DOX-2, and NG-CBA-DOX-3 nanogels at concentrations of (C) 100 µg/mL and (D) 1000 µg/mL in different biological media for 48 h at 37 °C by OD 650 nm. Data were presented as mean ± SD (*n* = 4).

### 2.3. DOX Release Study

The drug release behaviors of nanogels containing DOX were investigated with and without GSH at pH values of 7.4 and 5.0 using the dialysis method. The cumulative release percentages of DOX-loaded in the nanogels versus time are plotted in Figure 3. In the absence of GSH, less than 33% of loaded DOX was released from the NG-CBA/DOX-1 nanogel in 12 h at pH 7.4. The DOX release was enhanced by GSH and in the presence of 5 mM GSH, nearly 50% of the loaded DOX was released within 12 h. Additional enhancement in DOX release was observed at pH 5.0 where the cumulative release percentage after 12 h reached 50 and 58% in the absence and presence of 5 mM GSH, respectively. Larger differences became apparent after 48 h, when almost complete release of DOX from NG-CBA-DOX-1 was observed at pH 5.0 in 5 mM GSH, while only 50% of DOX release occurred at pH 7.4 without reducing the environment.

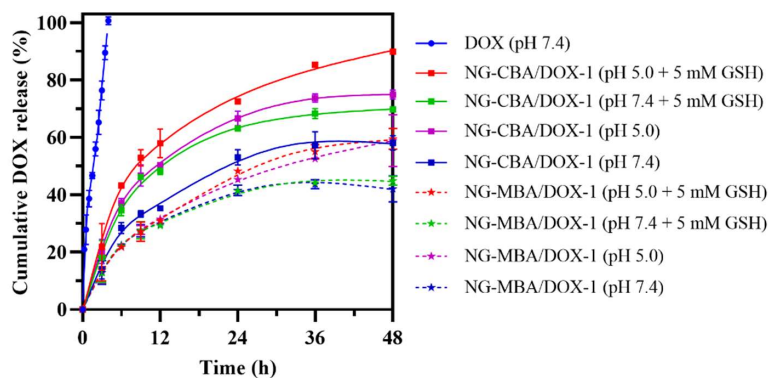


**Figure 3.** Drug release profile from NG-CBA/DOX-1 nanogels (squares and solid lines) and NG-MBA/DOX-1 nanogels (stars and dotted lines) in four solutions: GSH (0 and 5 mM) in PBS (pH 7.4 and 5.0). The nanogel concentrations were 250  $\mu\text{g}/\text{mL}$  and the solution temperature was 37  $^{\circ}\text{C}$ . The data were presented as mean  $\pm$  SD ( $n = 4$ ).

As expected, in the case of the NG-MBA/DOX-1 nanogel, which contains the reduction-insensitive crosslinker, no significant changes in DOX release were observed in the presence and absence of GSH. In turn, decreasing the pH of the environment from 7.4 to 5.0 increased the DOX release rate and the cumulative DOX release reached about 40 and 55%, respectively.

#### 2.4. Cytotoxicity Study in Cancer Cell Line

The cytotoxicity profile of DOX and the two nanogels, NG-CBA and NG-CBA/DOX-1, was assessed in the HCT 116 colon cancer cell line. Firstly, in vitro studies revealed that the unloaded nanogel NG-CBA was not cytotoxic to HCT 116 cells after incubation at different concentrations ranging from 17.5 to 600  $\mu\text{g}/\text{mL}$  (Figure 4A). Notably, DOX-loaded nanogels had a higher efficiency than free DOX in causing cytotoxic effects on cancer cells (Figure 4B). Moreover, one can speculate that the rate of drug release from GSH-mediated degradable nanogels will be even greater in cells with much higher GSH levels, such as breast or ovarian cancer cells [31].

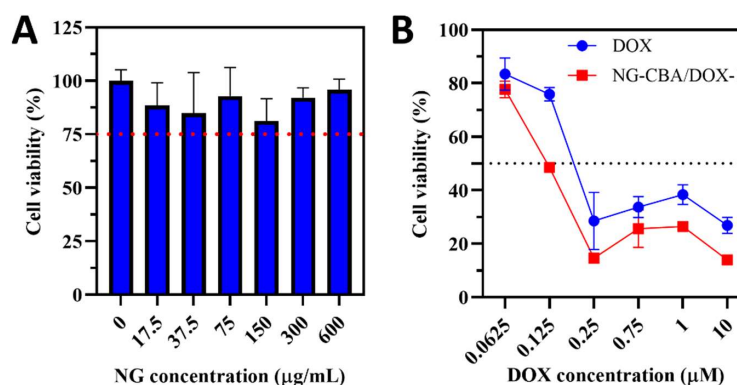


**Figure 4.** (A) Cytotoxicity profile of bare NG-CBA nanogels in the HCT 116 colon cancer cell line at different concentrations (17.5, 37.5, 75, 150, 300, and 600  $\mu\text{g}/\text{mL}$ ) after 48 h of incubation at 37  $^{\circ}\text{C}$ . (B) Cytotoxicity profile of DOX and NG-CBA/DOX-1 nanogel in the HCT 116 colon cancer cell line at different DOX concentrations (0.0625, 0.125, 0.25, 0.75, 1.0, and 10.0  $\mu\text{M}$ ) after 48 h of incubation at 37  $^{\circ}\text{C}$ . The data were presented as mean  $\pm$  SD ( $n = 4$ ).

### 3. Materials and Methods

#### 3.1. Materials and Reagents

##### 3.1.1. General Methods

Miniemulsion formation and nanogel redispersion were accomplished by ultrasonication using Sonics VCX 130 (Sonics & Materials, Inc., Newtown, CT, USA) using 60% and 40% amplitudes, respectively. Lyophilization of purified nanogels and DOX-loaded nanogels from frozen samples (in water, at  $-80\text{ }^{\circ}\text{C}$ ) was carried out under 0.035 mbar at  $-50\text{ }^{\circ}\text{C}$  (ALPHA 1-2 LDplus, CHRIST). A SpectraMax i3x Multi-Mode Microplate Reader (Molecular Devices, USA) was used for stability, cytotoxicity, and fluorescence assays. Phosphate buffered saline (PBS), phosphate buffer (PB), and normal saline solutions were freshly prepared. Deionized water (DI water) was produced using a reverse osmosis system (conductivity  $< 2\text{ }\mu\text{S/cm}$ ).

##### 3.1.2. Materials and Reagents for pH/Reduction Dual-Responsive Nanogels Synthesis

Doxorubicin hydrochloride (DOX, Cayman Chemical), (*N,N*-dimethylacrylamide (DMAM, Sigma Aldrich, Burlington, MA, USA), 2-carboxyethyl acrylate (CEA, Sigma Aldrich), *N,N'*-bis(acryloyl)cystamine (CBA, Alfa Aesar), *N,N'*-methylenebisacrylamide (MBA, Acros Organics, Geel, Belgium), lithium phenyl (2,4,6-trimethylbenzoyl)phosphinate (LAP, Carbosynth), Span 80 (Sigma Aldrich), cyclohexane (Chempur), acetone (Chempur), dimethyl sulfoxide (DMSO, Fisher Bioreagents, Pittsburgh, PA, USA), and dialysis membrane (Spectrum™ Spectra/Por™ 2 RC Dialysis Membrane, MWCO: 12–14 kDa).

##### 3.1.3. Materials and Reagents for Cell Culture and In Vitro Assays

HCT 116 colon cancer cell line (catalog no. CCL-247) was obtained from the American Type Culture Collection (ATCC, Manassas, VA, USA), Dulbecco's Modified Eagle Medium (DMEM, PAN Biotech), Fetal Bovine Serum (FBS, PAN Biotech, Aidenbach, Germany), PBS (PAN Biotech), and CCK-8 kit (Bimake).

#### 3.2. Synthesis of pH/Reduction Dual-Responsive Nanogels

pH/reduction dual-responsive nanogels were synthesized via free radical polymerization (FRP) in an inverse water-in-oil (w/o) miniemulsion. A 10:1 (*v:v*) water-in-oil (w/o) miniemulsion was composed of cyclohexane (10.0 mL) containing Span 80 (600 mg) as the organic continuous phase; the aqueous phase (1.0 mL) consisted of PB solution (pH 7.0) containing monomers and the photoinitiator LAP. The general procedure for the synthesis of nanogels was as follows (Figure 1A). Briefly, the aqueous phase was prepared in a 4 mL dark vial by adding CBA (26.0 mg, 0.10 mmol) and 0.2 M PB (pH 7.0) containing DMSO (10% *v/v*) with the main monomers: DMAM and CEA (amounts specified in Table 1). The mixture was vortexed for approximately 10–15 min to completely dissolve all the monomers. Finally, the solution of LAP initiator (2.3 mg, 0.008 mmol) was added. Then, the aqueous phase was transferred into a 20 mL glass vial containing a cold organic phase ( $4\text{ }^{\circ}\text{C}$ ) and sonicated at 60% amplitude for 5 min to create a miniemulsion. The vial was then wrapped with aluminum foil and photoirradiated from the bottom of the vial with High Power Light-Emitting Diodes (LEDs, 3 W, 395–405 nm) for 30 min. Nanogels were precipitated in cold acetone (40 mL), centrifuged at 11,000 rpm for 10 min, and washed twice with acetone. After air drying overnight, crude nanogels were redispersed in DI water and dialyzed against water for 24 h using a dialysis membrane (MWCO 12–14 kDa) with multiple media changes. Pure nanogel dispersions (after dialysis) were frozen at  $-80\text{ }^{\circ}\text{C}$  and lyophilized to obtain the nanogel powder. The MBA-crosslinked nanogels were synthesized using the same procedure as mentioned above, except CBA was replaced with MBA at the same molar ratio (Table 1).

##### 3.3. Loading of DOX into Anionic Nanogels

Post-polymerization loading of DOX into the nanogels was accomplished as follows. Initially, 5.0 mg of dry nanogel was placed in a 4 mL glass vial. Then, the DOX solution

(1.0 mg of DOX in 800  $\mu$ L of water) was added. After the nanogels swelled (approximately 5 min), the suspension was stirred in the dark overnight at 400 rpm. Afterward, the excess DOX was eliminated by dialysis using a dialysis membrane (MWCO 12–14 kDa) against DI water with multiple media changes. Finally, pure DOX-loaded nanogels were lyophilized and stored as nanogel powder.

#### 3.4. Nanogel Characterization

##### 3.4.1. Measurement of Drug Loading Efficiency (DLE) and Drug Loading Capacity (DLC)

The measurements of drug loading efficiency (DLE) and drug loading capacity (DLC) of nanogels were based on the fluorescence intensity using the standard curve of DOX in water (Ex/Em max of 498/593 nm,  $R^2 = 0.997$ ). According to the fluorescence spectra, both DOX and DOX-loaded nanogels share identical fluorescence spectra with the same Ex/Em max (Figure 1E). Following measurement of its fluorescence intensity, DOX-loaded nanogels were dispersed in DI water and diluted to a final concentration of 10.0  $\mu$ g/mL. DLE and DLC were then calculated using the following equations:

$$\text{DLE (\%)} = \frac{\text{actual loaded DOX}}{\text{Initial feed of DOX}} \times 100$$

$$\text{DLC (\%)} = \frac{\text{actual loaded DOX}}{\text{DOX} - \text{loaded nanogel}} \times 100$$

The Z-average hydrodynamic diameter ( $d_H$ ) and polydispersity index (PDI) of DOX-loaded nanogels (1.0 mg/mL) in 1 mM KCl solution or PBS (pH 7.4) were determined using a dynamic light scattering (DLS, Malvern, Zetasizer Nano 90S) system equipped with a 4 mV He–Ne ion laser ( $\lambda = 633$  nm) as the light source at a scattering angle of 90°. All samples were diluted from stock (10 mg/mL, prepared with sonication at 40% amplitude for 30 s) to the desired media concentration (1.0 mg/mL) without additional sonication. The  $\zeta$  potentials of bare nanogels and DOX-loaded nanogels were measured using electrophoretic light scattering (ELS) measurements (Malvern, Zetasizer Nano ZC) in 1 mM KCl solution.

##### 3.4.2. Cryogenic Transmission Electron Microscopy (cryo-TEM)

GSH-treated and untreated nanogels (500  $\mu$ g/mL) in DI water were observed under cryo-TEM using a Tecnai F20 X TWIN microscope (FEI Company, Hillsboro, Oregon, USA). Specimens were prepared via the vitrification of aqueous solutions on oxygen plasma-activated grids with holey carbon film (Quantifoil R 2/2; Quantifoil Micro Tools GmbH, Großlobichau, Germany).

##### 3.4.3. Measurement of DOX and DOX-Loaded Nanogel Aggregation in Biological Media

The aggregation of DOX was observed in 10 mM PB (pH 7.4) within 3 days. DOX was dispersed in 10 mM PB (pH 7.4) at various concentrations (20, 40, 60, 80, and 100  $\mu$ g/mL) and placed in a 48-well plate (volume: 1.0 mL for each concentration) and incubated at 37 °C. NG-CBA/DOX-1 at DOX concentrations of 20, 40, 60, 80, and 100  $\mu$ g/mL were also dispersed in 10 mM PB (pH 7.4, stock was prepared in water with sonication at 40% amplitude for 30 s). At predetermined time intervals (0, 20, 40, 60, 80, 100, 120, 140, 160, 180, 1440, 2880, and 4320 min), the samples were observed visually and their optical densities (OD) at 650 nm were measured. The absorbance value was converted to % transmittance using the following equation:

$$\text{Transmittance (\%)} = \text{antilog}(2 - \text{absorbance})$$

##### 3.4.4. Stability Study of Nanogel in Biological Media

For the stability study, stock solutions of nanogels were prepared in water with sonication at 40% amplitude for 30 s. The colloidal stability of bare NG-CBA and NG-

CBA/DOX-1,2,3 nanogels was measured at concentrations of 100 and 1000  $\mu\text{g}/\text{mL}$ , low and high concentrations, respectively, in different biological media, including water, PBS (pH 7.4), normal saline (0.90% *w/v* of NaCl), and DMEM + 10% FBS at 37 °C for 48 h. NG-CBA/DOX-1,2,3 (concentration: 100  $\mu\text{g}/\text{mL}$ ) contained DOX at concentrations of 16.29, 9.09, and 27.89  $\mu\text{g}/\text{mL}$ , respectively. Meanwhile, NG-CBA/DOX-1,2,3 (concentration: 1000  $\mu\text{g}/\text{mL}$ ) contained exactly 10 $\times$  more DOX: 162.9, 90.9, and 278.9  $\mu\text{g}/\text{mL}$ , respectively. The colloidal stability was observed by measuring OD at 650 nm in 96-well plates using a microplate reader. OD values ranging from 0.00–0.15 were considered a stable dispersion.

### 3.5. Drug Release Study

DOX release from the nanogel was analyzed using the dialysis method. Initially, a dispersion of nanogel at a concentration of 250  $\mu\text{g}/\text{mL}$  in relevant PBS (pH 7.4 or 5.0) containing 5 mM GSH or without GSH additive was prepared. Then 800  $\mu\text{L}$  of NG-CBA/DOX-1 or NG-MBA/DOX-1 at a DOX concentration of 40.7  $\mu\text{g}/\text{mL}$  or free DOX at 40.7  $\mu\text{g}/\text{mL}$  was placed into the dialysis capsule (QuixSep<sup>®</sup>, 1 mL) using a dialysis membrane (MWCO 12–14 kDa). The dialysis capsules were immersed in 40 mL of PBS (pH 7.4 with 0 or 5 mM GSH and pH 5.0 with 0 or 5 mM GSH) and incubated at 37 °C under continuous shaking (110 rpm). At each predetermined time interval of 3, 6, 12, 24, 36, and 48 h, 400  $\mu\text{L}$  of dissolution medium was withdrawn from each vial and replaced with the same amount of pre-warmed fresh medium. The amount of released DOX in the withdrawn samples was determined by measuring its fluorescence intensity using a  $\lambda_{\text{ex}}$  of 498 nm and  $\lambda_{\text{em}}$  of 593 nm and converting it to DOX concentration using a standard curve.

### 3.6. Cytotoxicity Study

For the cytotoxicity study, stock solutions of nanogels were prepared in water with sonication at 40% amplitude for 30 s. The cytotoxicity profile of NG-CBA/DOX-1 was assessed in the HCT 116 colon cancer cell line using a standard CCK-8 assay. For 24 h, HCT 116 colon cancer cells ( $5 \times 10^3$  cells/well) were seeded in 96-well plates in 100  $\mu\text{L}$  of DMEM + 10% FBS. Then, the cells were incubated with DOX and NG-CBA/DOX-1 at various concentrations of DOX (0.0625, 0.125, 0.25, 0.75, 1.0, and 10.0  $\mu\text{M}$ ) for 48 h. In addition, the cytotoxicity of bare NG-CBA was also evaluated at different concentrations of nanogels (17.5, 37.5, 75, 150, 300, and 600  $\mu\text{g}/\text{mL}$ ). The CCK-8 assay was carried out by adding 10  $\mu\text{L}$  of CCK-8 solution to each well after 2 h of incubation at 37 °C. The absorbance was then measured by a microplate reader at 450 nm. The relative cell viability (%) was expressed as a fraction of the percentage of cell growth occurring in the presence of nanogel vs. the absence of nanogel (control).

### 3.7. Statistical Analysis

GraphPad Prism Version 6.0 software (GraphPad, San Diego, CA, USA) was used for the statistical analysis. Data analysis was performed using one-way analysis of variance (ANOVA). The minimum level of significance was set at  $p < 0.05$ , with all data displayed as mean  $\pm$  SD ( $n = 4$ ).

## 4. Conclusions

Dual stimuli-responsive nanogels based on acrylic polymers have been produced in a facile and straightforward method. DOX-encapsulation was achieved by a facile diffusion process, forming a complex with ionized carboxylic groups of CEA units. Nanogels showed high DLCs (up to 27.89 wt%) and suitable nanoparticle size for enhanced permeation effects. More importantly, nanogels could prevent DOX from aggregating in biological media up to DOX concentrations of  $\sim 160$   $\mu\text{g}/\text{mL}$  (NG-CBA/DOX-1), whereas free DOX was only stable at concentrations lower than 40  $\mu\text{g}/\text{mL}$ .

DOX-encapsulated degradable nanogels showed enhanced release rates at lower pH (i.e., pH of 5.0) and in a reducing environment showing an obvious pH/reduction dual-responsive controlled drug release capability. In vitro studies revealed that the bare nanogel

was not cytotoxic to HCT 116 colon cancer cells, whereas DOX-containing nanogels were toxic against HCT 116 colon cancer cells with a better efficacy than free DOX. The presented nanogels were conveniently synthesized and exhibited excellent colloidal stability and cationic drug entrapment capability making them a promising alternative to existing DOX carrier systems. Additionally, nanogels can be further modified and conjugated with targeting ligands for active targeted delivery.

**Supplementary Materials:** The following supporting information can be downloaded at: <https://www.mdpi.com/article/10.3390/molecules27185983/s1>, Figure S1: Average size distribution ( $d_H$ ) of NG-CBA, ( $n = 4$ ); Figure S2: Average size distribution ( $d_H$ ) of NG-MBA, ( $n = 4$ ); Figure S3: Average zeta potential of NG-CBA, ( $n = 4$ ); Figure S4: Average zeta potential of NG-MBA, ( $n = 4$ ); Figure S5: Average zeta potential of NG-CBA/DOX-1, ( $n = 4$ ); Figure S6: Average zeta potential of NG-MBA/DOX-1, ( $n = 4$ ); Figure S7: Average zeta potential of NG-CBA/DOX-2, ( $n = 4$ ); Figure S8: Average zeta potential of NG-CBA/DOX-3, ( $n = 4$ ).

**Author Contributions:** Conceptualization, M.M. and I.W.; methodology, A.L. and I.W.; software, A.M.; validation, I.W.; formal analysis, A.M.; investigation, A.M. and A.L.; resources, I.W.; data curation, A.M. and A.L.; writing—original draft preparation, A.M. and I.W.; writing—review and editing, M.M. and I.W.; visualization, A.M.; supervision, M.M. and I.W.; project administration, I.W.; funding acquisition, I.W. All authors have read and agreed to the published version of the manuscript.

**Funding:** This study was financed by the PRELUDIUM BIS 1 (2019/35/O/ST5/02746) from the National Science Centre (NCN), Poland; the APC was financed by Rector's grant No 04/020/RGP20 from Silesian University of Technology.

**Institutional Review Board Statement:** Not applicable.

**Informed Consent Statement:** Not applicable.

**Data Availability Statement:** Not applicable.

**Conflicts of Interest:** The authors declare no conflict of interest.

**Sample Availability:** Not applicable.

## References

1. Kanwal, U.; Irfan Bukhari, N.; Ovais, M.; Abass, N.; Hussain, K.; Raza, A. Advances in nano-delivery systems for doxorubicin: An updated insight. *J. Drug Target.* **2018**, *26*, 296–310. [[CrossRef](#)]
2. Alyane, M.; Barratt, G.; Lahouel, M. Remote loading of doxorubicin into liposomes by transmembrane pH gradient to reduce toxicity toward H9c2 cells. *Saudi Pharm. J.* **2016**, *24*, 165–175. [[CrossRef](#)] [[PubMed](#)]
3. Kabanov, A.V.; Vinogradov, S.V. Nanogels as pharmaceutical carriers: Finite networks of infinite capabilities. *Angew. Chem. Int. Ed. Engl.* **2009**, *48*, 5418–5429. [[CrossRef](#)]
4. Li, C.; Obireddy, S.R.; Lai, W.F. Preparation and use of nanogels as carriers of drugs. *Drug Deliv.* **2021**, *28*, 1594–1602. [[CrossRef](#)] [[PubMed](#)]
5. Huang, D.; Qian, H.; Qiao, H.; Chen, W.; Feijen, J.; Zhong, Z. Bioresponsive functional nanogels as an emerging platform for cancer therapy. *Expert Opin. Drug Deliv.* **2018**, *15*, 703–716. [[CrossRef](#)] [[PubMed](#)]
6. Vashist, A.; Kaushik, A.; Vashist, A.; Bala, J.; Nikkhah-Moshaie, R.; Sagar, V.; Nair, M. Nanogels as potential drug nanocarriers for CNS drug delivery. *Drug Discov. Today* **2018**, *23*, 1436–1443. [[CrossRef](#)] [[PubMed](#)]
7. Neamtu, I.; Rusu, A.G.; Diaconu, A.; Nita, L.E.; Chiriac, A.P. Basic concepts and recent advances in nanogels as carriers for medical applications. *Drug Deliv.* **2017**, *24*, 539–557. [[CrossRef](#)]
8. Zhang, H.; Zhai, Y.; Wang, J.; Zhai, G. New progress and prospects: The application of nanogel in drug delivery. *Mater. Sci. Eng. C* **2016**, *60*, 560–568. [[CrossRef](#)]
9. Debele, T.A.; Mekuria, S.L.; Tsai, H.C. Polysaccharide based nanogels in the drug delivery system: Application as the carrier of pharmaceutical agents. *Mater. Sci. Eng. C* **2016**, *68*, 964–981. [[CrossRef](#)]
10. Mohammadi, M.; Arabi, L.; Alibolandi, M. Doxorubicin-loaded composite nanogels for cancer treatment. *J. Control. Release* **2020**, *328*, 171–191. [[CrossRef](#)]
11. Chiang, W.H.; Ho, V.T.; Huang, W.C.; Huang, Y.F.; Chern, C.S.; Chiu, H.C. Dual stimuli-responsive polymeric hollow nanogels designed as carriers for intracellular triggered drug release. *Langmuir* **2012**, *28*, 15056–15064. [[CrossRef](#)] [[PubMed](#)]
12. Dhanya, S.; Bahadur, D.; Kundu, G.C.; Srivastava, R. Maleic acid incorporated poly-(N-isopropylacrylamide) polymer nanogels for dual-responsive delivery of doxorubicin hydrochloride. *Eur. Polym. J.* **2013**, *49*, 22–32. [[CrossRef](#)]

13. Chiang, W.H.; Huang, W.C.; Chang, Y.J.; Shen, M.Y.; Chen, H.H.; Chern, C.S.; Chiu, H.C. Doxorubicin-Loaded Nanogel Assemblies with pH/Thermo-triggered Payload Release for Intracellular Drug Delivery. *Macromol. Chem. Phys.* **2014**, *215*, 1332–1341. [[CrossRef](#)]
14. Peng, H.; Huang, X.; Oppermann, A.; Melle, A.; Weger, L.; Karperien, M.; Wöll, D.; Pich, A. A facile approach for thermal and reduction dual-responsive prodrug nanogels for intracellular doxorubicin delivery. *J. Mater. Chem. B* **2016**, *4*, 7572–7583. [[CrossRef](#)] [[PubMed](#)]
15. Rao, K.M.; Suneetha, M.; Kumar, D.V.; Kim, H.J.; Seok, Y.J.; Han, S.S. Dual Responsive poly(vinyl caprolactam)-Based Nanogels for Tunable Intracellular Doxorubicin Delivery in Cancer Cells. *Pharmaceutics* **2022**, *14*, 852. [[CrossRef](#)]
16. Pan, Y.J.; Chen, Y.Y.; Wang, D.R.; Wei, C.; Guo, J.; Lu, D.R.; Chu, C.C.; Wang, C.C. Redox/pH dual stimuli-responsive biodegradable nanohydrogels with varying responses to dithiothreitol and glutathione for controlled drug release. *Biomaterials* **2012**, *33*, 6570–6579. [[CrossRef](#)]
17. Li, M.; Tang, Z.; Sun, H.; Ding, J.; Song, W.; Chen, X. pH and reduction dual-responsive nanogel cross-linked by quaternization reaction for enhanced cellular internalization and intracellular drug delivery. *Polym. Chem.* **2013**, *4*, 1199–1207. [[CrossRef](#)]
18. Zhang, X.; Achazi, K.; Steinhilber, D.; Kratz, F.; Dervede, J.; Haag, R. A facile approach for dual-responsive prodrug nanogels based on dendritic polyglycerols with minimal leaching. *J. Control. Release* **2014**, *174*, 209–216. [[CrossRef](#)]
19. Sousa-Herves, A.; Wedepohl, S.; Calderón, M. One-pot synthesis of doxorubicin-loaded multiresponsive nanogels based on hyperbranched polyglycerol. *Chem. Commun.* **2015**, *51*, 5264–5267. [[CrossRef](#)]
20. Chen, W.; Achazi, K.; Schade, B.; Haag, R. Charge-conversional and reduction-sensitive poly(vinyl alcohol) nanogels for enhanced cell uptake and efficient intracellular doxorubicin release. *J. Control. Release* **2015**, *205*, 15–24. [[CrossRef](#)]
21. Wu, H.; Jin, H.; Wang, C.; Zhang, Z.; Ruan, H.; Sun, L.; Yang, C.; Li, Y.; Qin, W.; Wang, C. Synergistic Cisplatin/Doxorubicin Combination Chemotherapy for Multidrug-Resistant Cancer via Polymeric Nanogels Targeting Delivery. *ACS Appl. Mater. Interfaces* **2017**, *9*, 9426–9436. [[CrossRef](#)] [[PubMed](#)]
22. Cuggino, J.C.; Gatti, G.; Picchio, M.L.; Maccioni, M.; Gugliotta, L.M.; Alvarez Igarzabal, C.I. Dually responsive nanogels as smart carriers for improving the therapeutic index of doxorubicin for breast cancer. *Eur. Polym. J.* **2019**, *116*, 445–452. [[CrossRef](#)]
23. Kumar, P.; Behl, G.; Kaur, S.; Yadav, N.; Liu, B.; Chhikara, A. Tumor microenvironment responsive nanogels as a smart triggered release platform for enhanced intracellular delivery of doxorubicin. *J. Biomater. Sci. Polym. Ed.* **2021**, *32*, 385–404. [[CrossRef](#)] [[PubMed](#)]
24. Zhan, Y.; Gonçalves, M.; Yi, P.; Capelo, D.; Zhang, Y.; Rodrigues, J.; Liu, C.; Tomás, H.; Li, Y.; He, P. Thermo/redox/pH-triple sensitive poly(N-isopropylacrylamide-co-acrylic acid) nanogels for anticancer drug delivery. *J. Mater. Chem. B* **2015**, *3*, 4221–4230. [[CrossRef](#)]
25. Hao, G.; Xu, Z.P.; Li, L. Manipulating extracellular tumour pH: An effective target for cancer therapy. *RSC Adv.* **2018**, *8*, 22182–22192. [[CrossRef](#)]
26. Zeng, J.; Shirihai, O.S.; Grinstaff, M.W. Modulating lysosomal pH: A molecular and nanoscale materials design perspective. *J. Life Sci.* **2020**, *2*, 25–37. [[CrossRef](#)]
27. Cheng, R.; Feng, F.; Meng, F.; Deng, C.; Feijen, J.; Zhong, Z. Glutathione-responsive nano-vehicles as a promising platform for targeted intracellular drug and gene delivery. *J. Control. Release* **2011**, *152*, 2–12. [[CrossRef](#)]
28. Maruf, A.; Milewska, M.; Kovács, T.; Varga, M.; Vellai, T.; Lalik, A.; Student, S.; Borges, O.; Wandzik, I. Trehalose-releasing nanogels: A step toward a trehalose delivery vehicle for autophagy stimulation. *Biomater. Adv.* **2022**, *138*, 212969. [[CrossRef](#)]
29. Zhu, L.; Yang, S.; Qu, X.; Zhu, F.; Liang, Y.; Liang, F.; Wang, Q.; Li, J.; Li, Z.; Yang, Z. Fibril-shaped aggregates of doxorubicin with poly-L-lysine and its derivative. *Polym. Chem.* **2014**, *5*, 5700–5706. [[CrossRef](#)]
30. Silva, V.R.; Corrêa, R.S.; Santos, L.S.; Soares, M.; Batista, A.A.; Bezerra, D.P. A ruthenium-based 5-fluorouracil complex with enhanced cytotoxicity and apoptosis induction action in HCT116 cells. *Sci. Rep.* **2018**, *8*, 288. [[CrossRef](#)]
31. Gamcsik, M.P.; Kasibhatla, M.S.; Teeter, S.D.; Colvin, O.M. Glutathione levels in human tumors. *Biomarkers* **2012**, *17*, 671–691. [[CrossRef](#)] [[PubMed](#)]

## Supplementary Information

### DLS measurements of nanogels

	Size (d.nm):	% Intensity:	St Dev (d.nm):
<b>Z-Average (d.nm):</b> 87.67	<b>Peak 1:</b> 117.8	91.6	63.37
<b>Pdl:</b> 0.307	<b>Peak 2:</b> 20.87	5.5	4.801
<b>Intercept:</b> 0.965	<b>Peak 3:</b> 4238	2.9	1293
<b>Result quality:</b> <b>Good</b>			

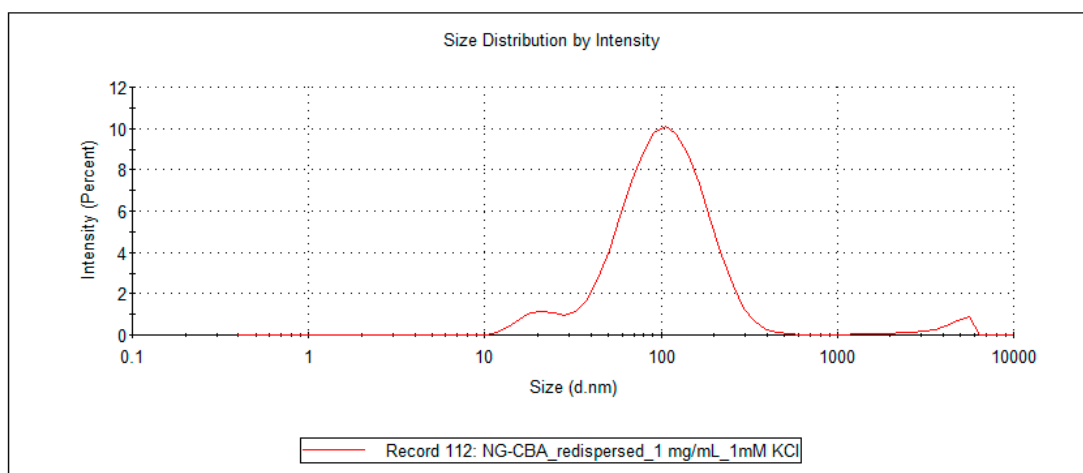


Figure S1. Average size distribution ( $d_H$ ) of NG-CBA, ( $n = 4$ ).

	Size (d.nm):	% Intensity:	St Dev (d.nm):
<b>Z-Average (d.nm):</b> 91.19	<b>Peak 1:</b> 142.3	83.8	73.17
<b>Pdl:</b> 0.380	<b>Peak 2:</b> 33.37	14.8	7.334
<b>Intercept:</b> 0.968	<b>Peak 3:</b> 5078	1.4	563.0
<b>Result quality:</b> <b>Good</b>			

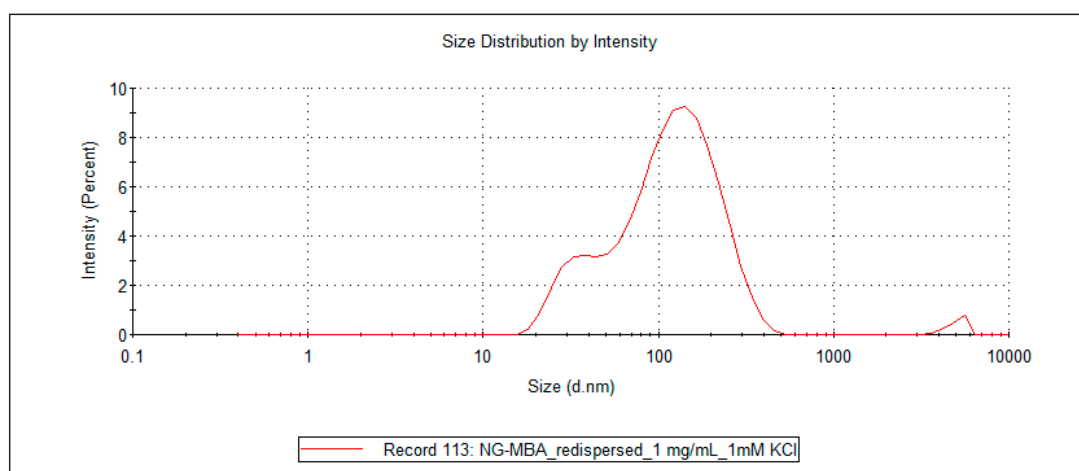
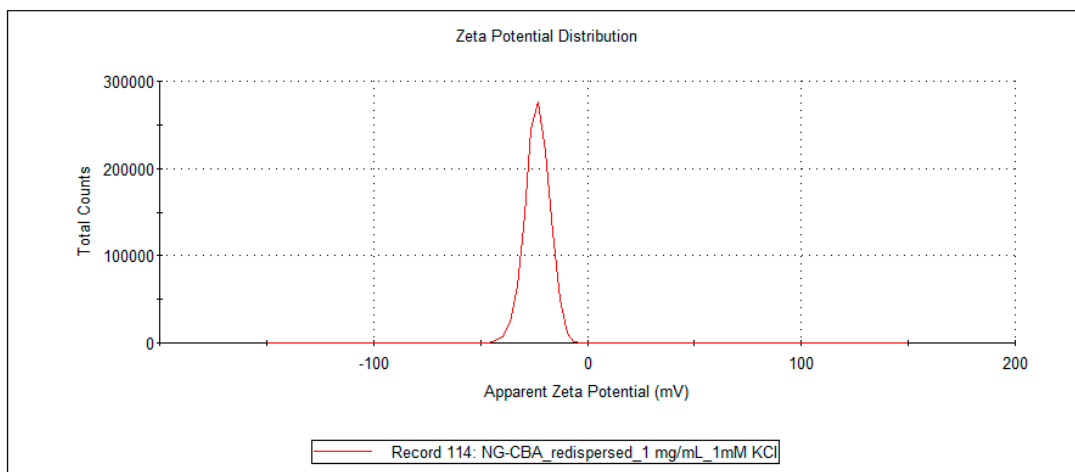


Figure S2. Average size distribution ( $d_H$ ) of NG-MBA, ( $n = 4$ ).



**Zeta potential measurements of nanogels**

	Mean (mV)	Area (%)	St Dev (mV)
<b>Zeta Potential (mV):</b> -23.6	<b>Peak 1:</b> -23.5	100.0	5.70
<b>Zeta Deviation (mV):</b> 5.40	<b>Peak 2:</b> 0.00	0.0	0.00
<b>Conductivity (mS/cm):</b> 0.203	<b>Peak 3:</b> 0.00	0.0	0.00
<b>Result quality :</b> Good			



**Figure S3.** Average zeta potential of NG-CBA, ( $n = 4$ ).

	Mean (mV)	Area (%)	St Dev (mV)
<b>Zeta Potential (mV):</b> -20.4	<b>Peak 1:</b> -20.3	100.0	5.40
<b>Zeta Deviation (mV):</b> 5.35	<b>Peak 2:</b> 0.00	0.0	0.00
<b>Conductivity (mS/cm):</b> 0.182	<b>Peak 3:</b> 0.00	0.0	0.00
<b>Result quality :</b> Good			

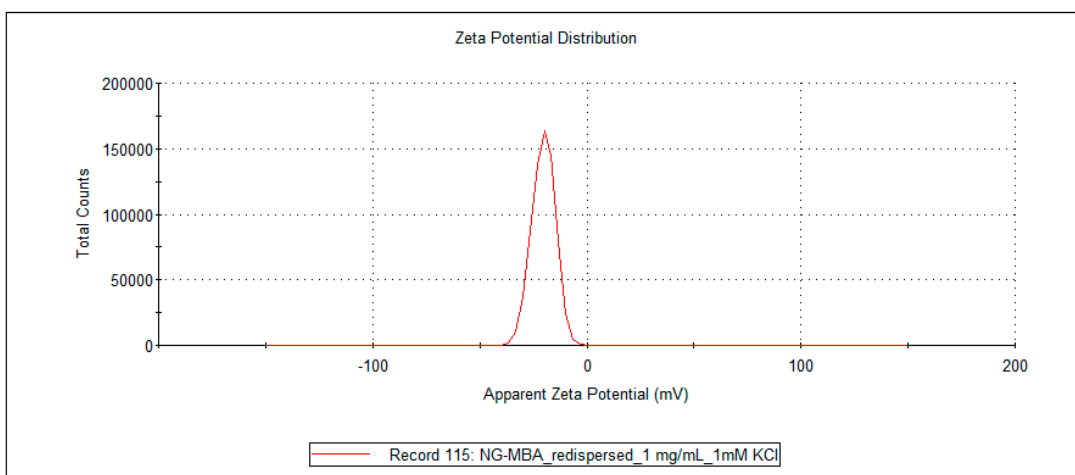


**Figure S4.** Average zeta potential of NG-MBA, ( $n = 4$ ).

## Publication [P2] Supplementary Information

	Mean (mV)	Area (%)	St Dev (mV)
<b>Zeta Potential (mV):</b> -6.33	<b>Peak 1:</b> -6.19	100.0	5.82
<b>Zeta Deviation (mV):</b> 5.42	<b>Peak 2:</b> 0.00	0.0	0.00
<b>Conductivity (mS/cm):</b> 0.163	<b>Peak 3:</b> 0.00	0.0	0.00
<b>Result quality : Good</b>			

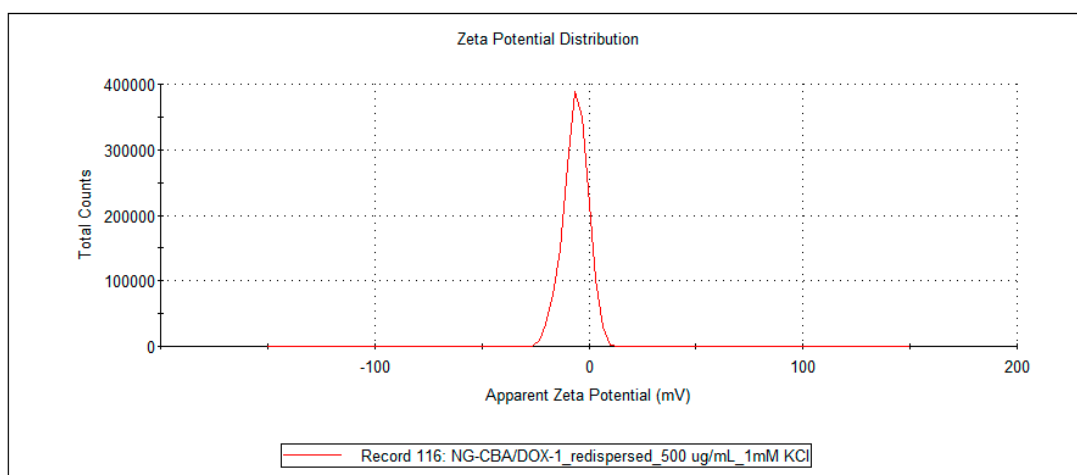


**Figure S5.** Average zeta potential of NG-CBA/DOX-1, ( $n = 4$ ).

	Mean (mV)	Area (%)	St Dev (mV)
<b>Zeta Potential (mV):</b> -8.92	<b>Peak 1:</b> -9.03	100.0	6.26
<b>Zeta Deviation (mV):</b> 5.98	<b>Peak 2:</b> 0.00	0.0	0.00
<b>Conductivity (mS/cm):</b> 0.171	<b>Peak 3:</b> 0.00	0.0	0.00
<b>Result quality : Good</b>			

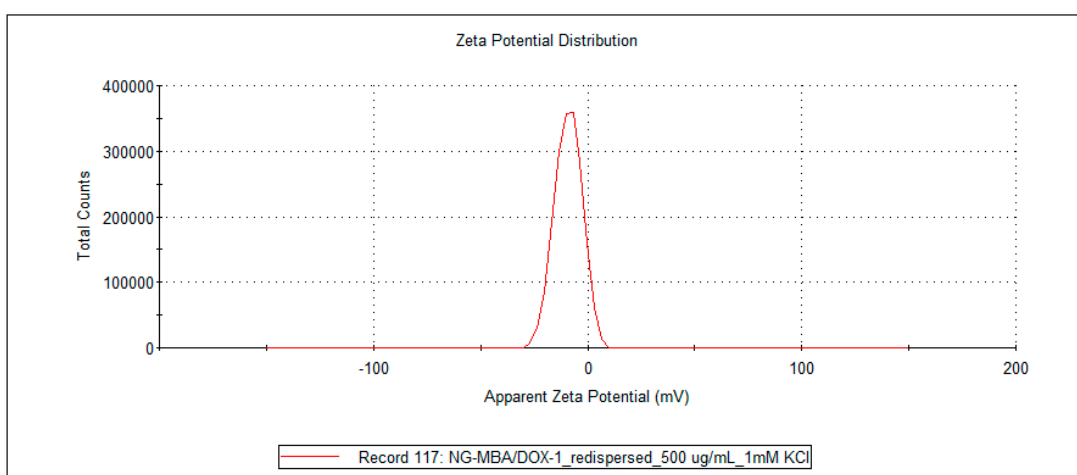


**Figure S6.** Average zeta potential of NG-MBA/DOX-1, ( $n = 4$ ).

## Publication [P2] Supplementary Information

	Mean (mV)	Area (%)	St Dev (mV)
<b>Zeta Potential (mV): -18.6</b>	<b>Peak 1:</b> -18.5	99.9	5.06
<b>Zeta Deviation (mV): 5.16</b>	<b>Peak 2:</b> 6.46	0.1	0.00
<b>Conductivity (mS/cm): 0.218</b>	<b>Peak 3:</b> 0.00	0.0	0.00
<b>Result quality : Good</b>			

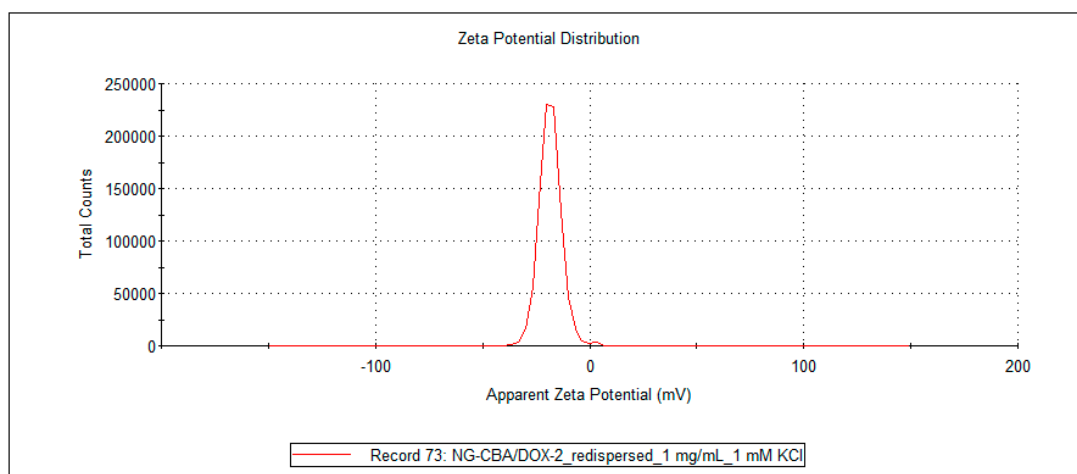


**Figure S7.** Average zeta potential of NG-CBA/DOX-2, ( $n = 4$ ).

	Mean (mV)	Area (%)	St Dev (mV)
<b>Zeta Potential (mV): -11.3</b>	<b>Peak 1:</b> -10.7	100.0	2.99
<b>Zeta Deviation (mV): 3.10</b>	<b>Peak 2:</b> 0.00	0.0	0.00
<b>Conductivity (mS/cm): 0.0729</b>	<b>Peak 3:</b> 0.00	0.0	0.00
<b>Result quality : Good</b>			

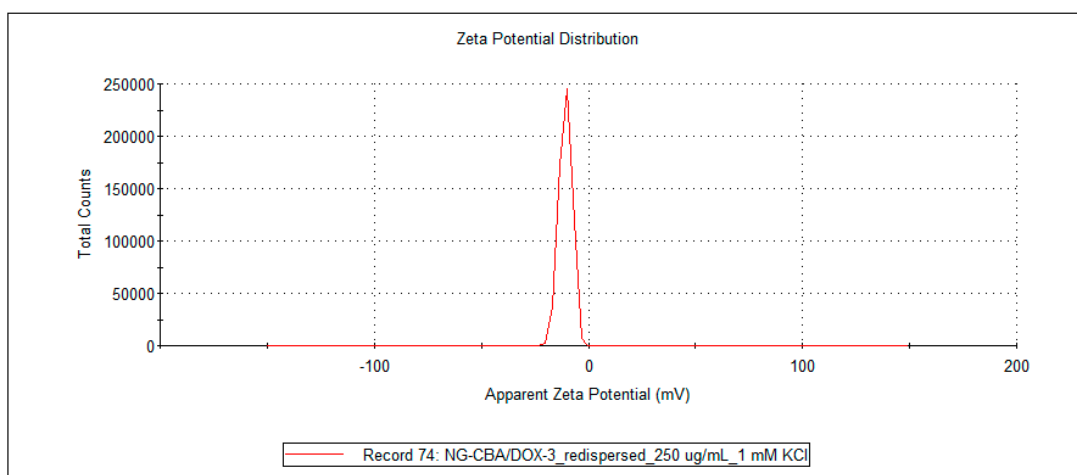


**Figure S8.** Average zeta potential of NG-CBA/DOX-3, ( $n = 4$ ).

**STATEMENT 3**

I declare that my percentage contribution to the publication [P3] entitled “*A Simple Synthesis of Reduction-Responsive Acrylamide-Type Nanogels for miRNA Delivery*” (published in **Molecules** 2023, 28, 761. DOI: 10.3390/molecules28020761) was 60%.

Justification: As part of this work, I served as a co-author for various tasks, including performing experiments: synthesizing cationic reduction-responsive nanogels, complexing miRNA with nanogels, evaluating the suitability of different dialysis membranes for miRNA release studies, conducting miRNA release studies, measuring DLS and zeta potential, checking colloidal stability, preparing samples for cryoTEM, synthesizing fluorescein-labelled nanogels, conducting cell uptake for confocal imaging, and assessing the cytotoxicity of nanogels in HCT 116 colon cancer cell line. Additionally, I was responsible for collecting and analyzing all experimental data, participating in writing of manuscript, creating figures and tables, managing citations, formatting the manuscript according to the journal’s style, assisting in revising the manuscript after peer review, and final proofreading.



Ali Maruf, M.Eng.

(PhD candidate)

As the corresponding author of the above-mentioned publication, which is part of the doctoral thesis of Mr. Ali Maruf, I declare that the percentage contribution of the remaining co-authors can be estimated as follows:

Milewska M: 10%

Group from the Department of Systems Biology and Engineering, Faculty of Automatic Control, Electronics and Computer Science, Silesian University of Technology, Poland (Lalik A, Student S): 10%

Wandzik I: 20%







prof. dr hab. inż. Ilona Wandzik

(Supervisor / corresponding author)

Article

# A Simple Synthesis of Reduction-Responsive Acrylamide-Type Nanogels for miRNA Delivery

 Ali Maruf <sup>1,2</sup> , Małgorzata Milewska <sup>1,2</sup>, Anna Lalik <sup>2,3</sup> , Sebastian Student <sup>2,3</sup>  and Ilona Wandzik <sup>1,2,\*</sup> 
<sup>1</sup> Department of Organic Chemistry, Bioorganic Chemistry and Biotechnology, Faculty of Chemistry, Silesian University of Technology, Krzywoustego 4, 44-100 Gliwice, Poland

<sup>2</sup> Biotechnology Center, Silesian University of Technology, Krzywoustego 8, 44-100 Gliwice, Poland

<sup>3</sup> Department of Systems Biology and Engineering, Faculty of Automatic Control, Electronics and Computer Science, Silesian University of Technology, Akademicka 16, 44-100 Gliwice, Poland

\* Correspondence: ilona.wandzik@polsl.pl

**Abstract:** MicroRNAs (miRNAs) have great therapeutic potential; however, their delivery still faces huge challenges, especially given the short half-life of naked miRNAs due to rapid hydrolysis or inactivation by abundant nucleases in the systemic circulation. Therefore, the search for reliable miRNA delivery systems is crucial. Nanogels are one of the more effective nanocarriers because they are biocompatible and have a high drug-loading capacity. In this study, acrylamide-based nanogels containing cationic groups and redox-sensitive crosslinkers were developed for cellular delivery of anti-miR21 (a-miR21). To achieve this, post-polymerization loading of a-miR21 oligonucleotides into nanogels was performed by utilizing the electrostatic interaction between positively charged nanogels and negatively charged oligonucleotides. Different molar ratios of the amine groups (N) on the cationic nanogel and phosphate groups (P) on the miRNA were investigated. An N/P ratio of 2 allowed high miRNA loading capacity (MLC, 6.7% *w/w*) and miRNA loading efficiency (MLE, 99.7% *w/w*). Successful miRNA loading was confirmed by dynamic light scattering (DLS) and electrophoretic light scattering (ELS) measurements. miRNA-loaded nanogels (NG/miRNA) formed stable dispersions in biological media and showed an enhanced miRNA release profile in the presence of glutathione (GSH). Moreover, the addition of heparin to dissociate the miRNA from the cationic nanogels resulted in the complete release of miRNA. Lastly, a cell uptake study indicated that NG/miRNA could be easily taken up by cancer cells.

**Keywords:** drug delivery; glutathione; miRNA; nanogel



**Citation:** Maruf, A.; Milewska, M.; Lalik, A.; Student, S.; Wandzik, I. A Simple Synthesis of Reduction-Responsive Acrylamide-Type Nanogels for miRNA Delivery. *Molecules* **2023**, *28*, 761. <https://doi.org/10.3390/molecules28020761>

Academic Editor: Luigi Paduano

Received: 21 November 2022

Revised: 31 December 2022

Accepted: 9 January 2023

Published: 12 January 2023



**Copyright:** © 2023 by the authors. Licensee MDPI, Basel, Switzerland. This article is an open access article distributed under the terms and conditions of the Creative Commons Attribution (CC BY) license (<https://creativecommons.org/licenses/by/4.0/>).

## 1. Introduction

MicroRNAs (miRNAs) are naturally occurring noncoding RNAs with short 18–25 nucleotide sequences that regulate gene expression at the post-transcriptional level [1]. Interest in developing miRNA-based therapies for cancer has risen sharply as growing evidence shows that miRNAs play important roles in regulating various cellular mechanisms (e.g., proliferation, programmed cell death, carcinogenesis, and tumor metastasis) [2–4]. However, naked extracellular miRNAs have a short half-life due to degradation by extracellular nucleases that are abundantly present in the blood plasma. Depending on the types of miRNAs, their half-lives range from 1.5 h to 13 h at 37 °C [5]. Moreover, miRNAs are not readily taken up by cells due to their hydrophilic nature, negative surface charge, and relatively high molecular weight (~7 kDa), which results in poor cellular uptake and internalization [6]. To address these problems various delivery systems have been developed during the last 20 years. Typically, there are two categories of miRNA delivery systems: viral and nonviral, with the most popular approach being viral vectors [7–9]. However, conventional viral vector systems are costly and difficult to produce on a large scale. Therefore, nonviral approaches are being extensively explored, since they offer advantages including easily tunable physicochemical properties, simplified production, high loading capacity, and

reduced biosafety concerns. Major approaches in this category involve the combination of nucleic acids with transfection reagents, such as inorganic, lipid, and polymeric-based nanoparticles [7–9]. Among polymeric nanocarriers, the most exciting innovations in nanomedicine for gene delivery are nanogels, because they are biocompatible, possess high loading capacity, and have potential responsiveness to environmental stimuli [10,11]. Recent studies have shown the promising use of synthetic nanogels as miRNA [12–17], siRNA [18], mRNA [19], and pDNA [20] delivery systems.

One of the first examples of an miRNA-based nanogel system was designed by Liu et al. [16]; a-miR21 was encapsulated within a polymer network by in situ polymerization of acrylamide and cationic N-(3-aminopropyl)methacrylamide, with ethylene glycol dimethacrylate as a crosslinker. According to the authors' hypothesis, nanocapsules containing miRNA were stable in physiological conditions (pH 7.4) and degraded at the lowered pH present in endosomes, releasing miRNA into the cytoplasm.

As commonly performed for other therapeutic genes, loading of miRNA is usually based on the controlled self-assembly of nanogel cationic groups and the anionic phosphate groups of nucleic acids by electrostatic complexation. The exception is the study presented by Dispenza et al. [17], who covalently conjugated a-miR31 into a poly(N-vinyl pyrrolidone)-based nanogel. The authors demonstrated that the covalent linkage of the miRNA to these nanogels does not affect its functionality in vitro.

Several examples of miRNA delivery systems are based on nanogels crosslinked by disulfide bonds, thus forming a redox-sensitive system [12–15]. Among the various stimuli, the reductive environment caused by the presence of glutathione (GSH) is the most prominent and characteristically distinctive stimulus in cancer cells. The cleavage of disulfide bonds in the intracellular compartments is favored because of high concentrations of GSH within cells (2–10 mM) in comparison to micromolar levels (2–20  $\mu$ M) in the blood plasma [21,22].

Shatsberg et al. developed reduction-responsive degradable nanogels, which were based on polyglycerol scaffold-containing amino groups [12]. Nanogels were prepared using an inverse nanoprecipitation technique, and miR34a was loaded by electrostatic interaction. The results showed that the nanogel with an optimal content of miR34a could inhibit glioblastoma progression by ~70% within 20 days post treatment. Javanmardi et al. developed PEGylated polyethylenimine redox-sensitive nanogels to encapsulate a-miR21 for the treatment of ovarian cancer in vitro [13,15]. Tumor cell apoptosis and suppression of tumor-associated angiogenesis were conducted on cis-Pt-sensitive ovarian cancer cells and were compared with the resistant cells, for which cisplatin cytotoxicity was remarkably enhanced after a-miR21-loaded nanogel treatment.

In another study, redox-sensitive nanogels were applied to deliver miR34a into transfection-resistant multiple myeloma cells [14]. Thiolated poly(glycidol)-based nanogels with covalently bound positively charged cell-penetrating peptides served as complexation agents for miRNA. Such complexation increased the amount of delivered miRNA, the degree of target gene regulation, and the inhibition of cell viability.

While the effectiveness of different miRNAs and their role as either oncogenes or tumor suppressors under certain conditions has been well established, many studies on synthetic smart nanogels have neglected to explicate the connection between miRNA loading capacity and release profile with different N/P ratios, either with or without the presence of biological stimuli [12–20], which is the main focus of this study. In the current study, we developed biodegradable reduction-sensitive nanogels for miRNA encapsulating and enhancing miRNA release in a cancer-mimicking environment where the GSH level is elevated (Figure 1). The study on miRNA release was also carried out in a GSH-free environment for comparison. Nanogels were synthesized via photoinitiated free-radical polymerization (FRP) of *N,N*-dimethylacrylamide (DMAM) and [2-(acryloyloxy)ethyl]trimethylammonium chloride (ATC) in the presence of a disulfide-type crosslinker. The cationic monomer, ATC, was chosen to provide the electrostatic interactions with the negatively charged miRNA. Anti-miR21 (a-miR21) oligonucleotide was used as a model of miRNA-based therapies due

to the fact that miR21 is known as an oncogenic miRNA, which is overexpressed in almost all cancers, and silencing miR21 can affect viability, apoptosis, and the cell cycle [23].

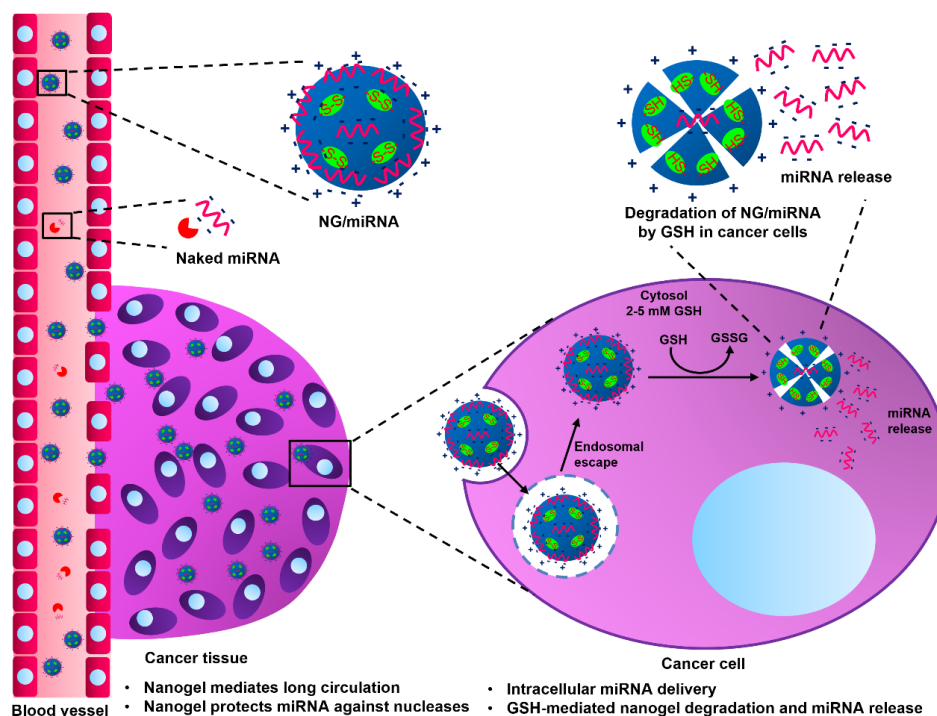


**Figure 1.** A schematic diagram of NG/miRNA in systemic circulation, miRNA protection against nucleases, enhanced permeability and retention (EPR)-mediated nanogel delivery to cancer tissue, cellular uptake, and intracellular miRNA release induced by GSH in cancer cells.

## 2. Results and Discussions

### 2.1. Synthesis and Characterization of NG/miRNA

Stimulus-responsive nanogels have been reported to be effective drug/gene delivery systems for the diagnosis and treatment of various human diseases [10,11]. In our previous study, we developed acrylamide-based trehalose-containing nanogels for autophagy modulation [24] and anionic biodegradable nanogels with high doxorubicin (DOX) loading capacity to prevent DOX from aggregating in biological media and enhance the release of DOX via pH/reduction stimuli [25]. In the design of miRNA-loaded nanogels, we used the same synthetic approach, the only differences being the monomer composition and initiator concentration. In this context, we synthesized reduction-responsive nanogels containing DMAM as the main monomer, [2-(acryloyloxy)ethyl]trimethylammonium chloride (ATC) as the cationic monomer, and *N,N'*-bis(acryloyl)cystamine (CBA) as a degradable crosslinker. Nanogels were synthesized via FRP in inverse water-in-oil (w/o) mini-emulsions under LED irradiation at room temperature for 30 min in yield of 56%. Details on monomer feed compositions are shown in Table S1.

The a-miR21 oligonucleotide was loaded into the nanogel in the post-polymerization process (Table S2). Three different compositions were prepared at different N/P molar ratios: 2, 5, and 10 (Table 1). The N/P ratio is defined as the molar ratio between the amine groups (N) on the cationic nanogel and the phosphate groups (P) on the miRNA.

**Table 1.** Physicochemical properties of bare nanogels and after loading with a-miR21 at different N/P ratios.

Nanogels	N/P Ratio	MLC (%)	MLE (%)	d <sub>H</sub> (PdI) (nm)	ζ Potential (mV)
NG	-	-	-	92.5 (0.43)	27.4
NG/a-miR21-1	10	1.4	100.0	109.2 (0.34)	24.2
NG/a-miR21-2	5	2.8	100.0	116.8 (0.36)	20.8
NG/a-miR21-3	2	6.7	99.7	122.1 (0.46)	11.9

The loading of a-miR21 at various N/P ratios was investigated by measurement of fluorescence intensity of nanogels loaded with Cy5-a-miR21 using a standard curve (Figures S1 and S2). In this regard, a relatively high miRNA loading capacity (MLC) of 6.7% *w/w* was achieved for NG/a-miR21-3. On the other hand, NG/a-miR21-1 and NG/a-miR21-2 indicated much lower MLCs of 1.4 and 2.8% *w/w*, respectively (Table 1, Figure 2A).

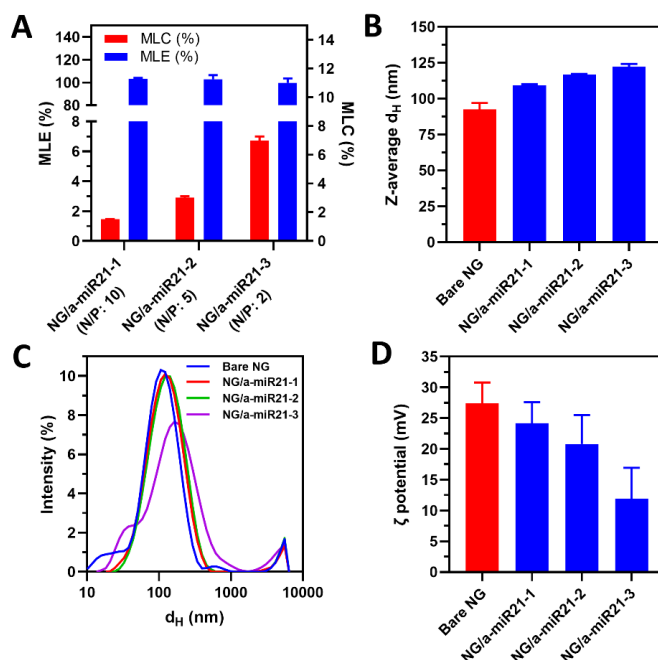


**Figure 2.** NG/miRNA characterization. (A) MLC and MLE of NG/a-miR21-1,2,3. (B,C) Z-average hydrodynamic diameter (d<sub>H</sub>) of bare NG and NG/a-miR21-1,2,3 in 1 mM KCl measured by DLS. (D) ζ potential of bare NG and NG/a-miR21-1,2,3 nanogels in 1 mM KCl measured by ELS. Data are reported as the mean ± SD (n = 4).

Interestingly, miRNA loading efficiency (MLE) was still guaranteed to be ~100% with the N/P ratio reduced from 10 to 2, which indicated that the negatively charged miRNAs possessed a strong electrostatic interaction with the positively charged nanogels for NG/a-miR21-1,2,3 (Table 1, Figure 2A).

Colloidal properties, such as the particle size and ζ potential of the nanogels, are among the factors that determine stability, transfection efficiency, and biocompatibility. Particle size and ζ potential values were determined before and after loading of a-miR21 at N/P = 2, 5, and 10. Bare NG had an average hydrodynamic diameter (d<sub>H</sub>) of ~90 nm. Increasing the N/P molar ratio from 2 to 10 resulted in a decrease in nanogel size from 122 to 109 nm (Table 1, Figure 2B,C). The ζ potential of bare NG (~27 mV) decreased to 24, 21, and 12 mV after successful miRNA loading into NG/a-miR21-1, NG/a-miR21-



2, and NG/a-miR21-3, respectively (Table 1, Figure 2D), due to the neutralizing effects from the negatively charged miRNA. As confirmed by cryogenic transmission electron microscopy (cryo-TEM), NG/a-miR21-3 had a spherical shape with a diameter of about 100 nm (Figure 3A). GSH treatment of NG/a-miR21-3 led to the disintegration of the nanogel network, indicating the cleavage of disulfide crosslinks (Figure 3B).

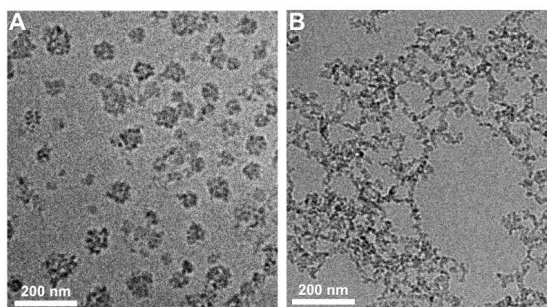


**Figure 3.** Cryo-TEM micrographs of NG/a-miR21-3 without (A) and with (B) GSH treatment. Scale bar = 200 nm.

The optimal size of nanoparticles to acquire the EPR effect in solid tumors is estimated in the range of 100 to 200 nm, bypassing the filtration barriers of the spleen and liver [26]. Additionally, slightly negative or neutral surface charges of nanoparticles are essential to achieve high plasma half-lives [26]. Therefore, NG/a-miR21-3 with an average  $d_H$  of 122 nm and  $\zeta$  potential of 11.9 mV is the best candidate to achieve both EPR-mediated tumor penetration and an increase in half-lives.

In order to deliver miRNA effectively, nanocarrier systems must be colloidal stable in biological media for both in vitro and in vivo study purposes. According to our previous study, unstable colloidal systems can be easily observed via their transmittance (T) value change in time, in which a T value above ~70% is regarded as stable dispersion. T values below 70% typically show visible aggregates of colloidal systems that are prone to sedimentation. According to the stability study, both bare NG and NG/a-miR21-3 at a concentration of 100  $\mu\text{g}/\text{mL}$  had excellent colloidal stability in five different media at 37  $^\circ\text{C}$  for 5 days as indicated by their T values (>98%) (Figure 4). Of the media selected, two contained fetal bovine serum (FBS).

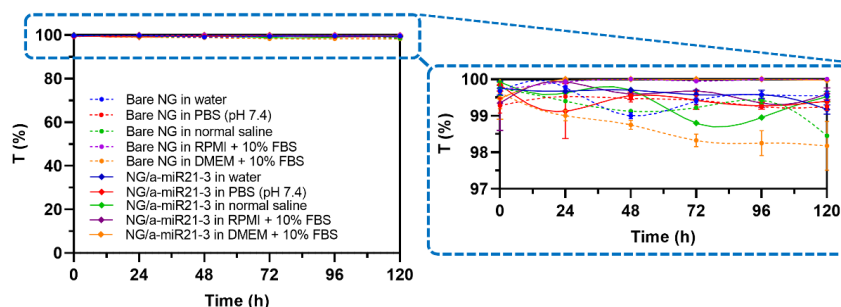


**Figure 4.** Transmittance values of bare NG and NG/a-miR21-3 dispersions for assessing their colloidal stability in different biological media at a working concentration of 100  $\mu\text{g}/\text{mL}$  for 5 days at 37  $^\circ\text{C}$ . Data are reported as the mean  $\pm$  SD (n = 4).

## 2.2. miRNA Release Study

The miRNA release profile from nanogel systems is usually not fully explained or not addressed. In this study, we investigated the release rate of miRNA from degradable nanogels in normal and GSH-containing cancer-mimicking environments.

As seen from Figure 5A, NG/a-miR21-1,2 had a delayed miRNA release in the normal condition (pH 7.4) until 9 h (~1.9% miRNA release). In contrast, NG/a-miR21-3 with a lower N/P ratio of 2 already showed a significant release at 3 h (~9.0% miRNA release), which was probably due to the weaker electrostatic interaction. On the other hand, in cancer-mimicking environments containing GSH, NG/a-miR21-1 showed enhanced release detected after 9 h (~6.8% miRNA release), and a significant release was observed from NG/a-miR21-2 in 3 h (~7.4% miRNA release) compared to that in pH 7.4 not containing GSH. At the same time, no significant change in the rate of miRNA release from NG/a-miR21-3 was observed in the medium with or without GSH.

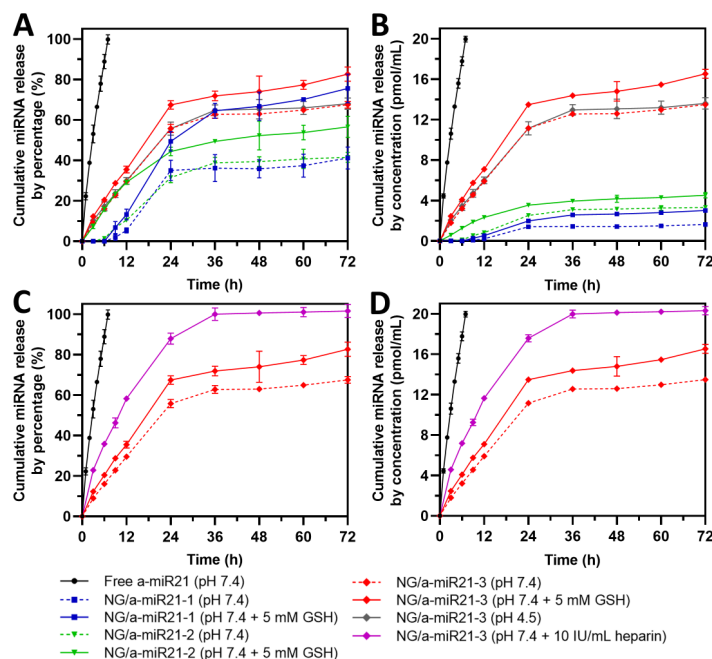


**Figure 5.** miRNA release profile by (A,C) percentage and (B,D) concentration from NG/a-miR21-1,2,3 at a nanogel concentration of 100 µg/mL with or without GSH treatment (5 mM GSH) in PBS (pH 7.4) at 37 °C for 72 h. NG/a-miR21-3 was also incubated in PBS (pH 4.5) and heparin-containing PBS (pH 7.4) at a concentration of 10 IU/mL. Free a-miR21 was equal to a-miR21 content in NG/a-miR21-3 to check the suitability of miRNA dialysis using a membrane with a molecular weight cutoff (MWCO) of ~100 kDa. Data are reported as the mean ± SD (n = 4).

After 24 h, miRNA release from NG/a-miR21-1,2,3 reached 35.0%, 31.6%, and 55.8%, respectively, in normal physiological conditions, whereas in GSH environments, the release was enhanced to 49.4%, 44.4%, and 67.4%, respectively. The results show that the hydrolysis of disulfide bonds and disintegration of the nanogel network in the presence of GSH had only a minor effect on the weakening of the electrostatic interaction between the nanogel cation units and the miRNA phosphate groups. However, it can be seen that this effect was greatest for the sample with the highest N/P ratio (NG/a-miR21-1). In this case, the miRNA was released much faster when GSH was present (Figure 5A). For samples with a lower N/P ratio (NG/a-miR21-2 and NG/a-miR21-3), only a small difference in miRNA release was observed after 72 h, whether GSH was present or not.

To be able to comprehensively compare the miRNA release behavior from NG/a-miR21-1,2,3, we also presented the release profile by concentration (pmol/mL) which can be seen in Figure 5B. It is visible that NG/a-miR21-3 had far more preferable miRNA release after 72 h (~16.5 pmol/mL) than NG/a-miR21-1 and NG/a-miR21-2 (~3.0 and

~4.5 pmol/mL, respectively). The release of miRNA was proportional to the miRNA content of the nanogels (MLC).

No significant difference was observed in miRNA release between acidic (pH 4.5) and neutral conditions (pH 7.4), which was attributed to the lack of a pH-responsive component in the nanogel (Figure 5A,B, dotted red curve vs. solid gray curve).

Biologic stability of nanoplexes is a prerequisite for successful transfection. To show the reversibility of the electrostatic interactions, strongly negatively charged heparin was added to NG/miRNA dispersions, which resulted in a significantly accelerated release of miRNA. The addition of heparin in a concentration of 10 IU/mL to the release medium resulted in the dissociation of miRNA/nanogel complexes, also demonstrating the reversibility of the complexation. The complete release of miRNA from NG/a-miR21-3 was observed after 36 h in the presence of heparin. It is worth mentioning that, in an environment without the presence of heparin, the complete release of miRNA was not observed during the experiment.

In addition, miRNA release kinetics from NG/a-miR21-3 in pH 7.4 + 5 mM GSH were fitted to five different models. The results indicated that the release kinetics were prone to follow Higuchi and first-order models ( $R^2 = 0.9460$  and  $0.9240$ , respectively) (Figure S11).

### 2.3. Cell Uptake

To observe the uptake of NG/miRNA by the cells, NG labeled with fluorescein (FL, green fluorescence) and miRNA labeled with Cy5 (red fluorescence) were used. Figure 6 shows the confocal laser scanning microscope images of the HCT 116 colon cancer cells after 3 h incubation with FL-NG/Cy5-a-miR21-3. FL-NG/Cy5-a-miR21-3 was effectively taken up by the cancer cells, which proved its ability to deliver miRNA into cells.

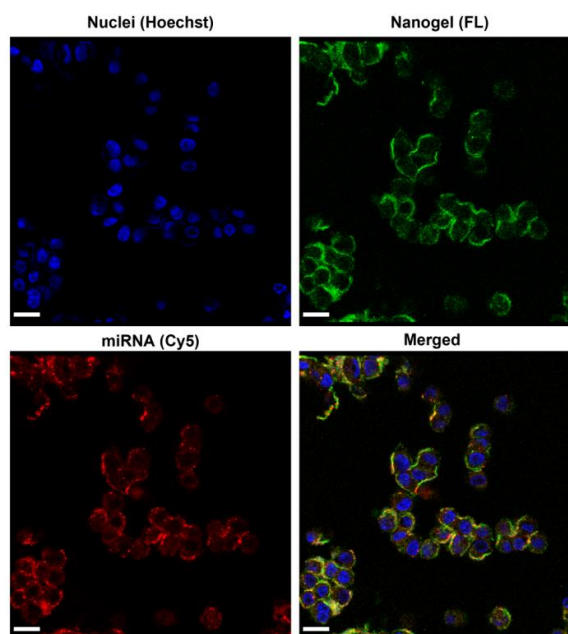


**Figure 6.** Cell uptake of FL-NG/Cy5-a-miR21-3 in HCT 116 colon cancer cell line (concentration: 500  $\mu\text{g/mL}$ ). Blue color indicates cell nuclei, green color indicates NG, and red color indicates miRNA. Scale bars = 20  $\mu\text{m}$ .

### 2.4. Cytotoxicity Profile

The cytotoxicity profile of bare NG was assessed in the HCT 116 colon cancer cell line, measured by cell viability (Figure 7). Bare NG had tolerable cytotoxicity (>75% cell

viability) up to 500  $\mu\text{g}/\text{mL}$ , indicating its suitability to be used as a safe miRNA delivery carrier.

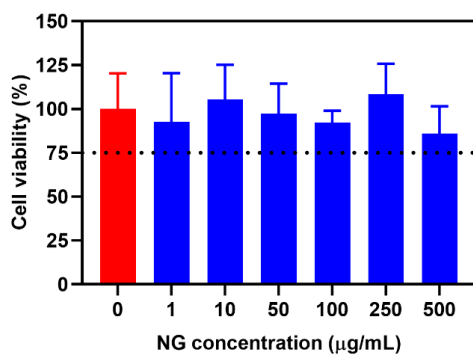


**Figure 7.** Cytotoxicity profile of bare NG in HCT 116 colon cancer cell line at different NG concentrations (0, 1, 10, 50, 100, 250, and 500  $\mu\text{g}/\text{mL}$ ) after 24 h of incubation at 37 °C. Data are presented as the mean  $\pm$  SD (n = 4).

### 3. Materials and Methods

#### 3.1. Materials and Reagents

##### 3.1.1. Materials and Reagents for GSH-Responsive Nanogel Synthesis

The materials and reagents used were as follows: anti-miR21 oligonucleotides (a-miR21) and cyanine5 (Cy5)-tagged a-miR21 (sequences T\*CAACCATCAGTCTGATAAGC\*T\*A and Cy5-T\*CAACCATCAGTCTGATAAGC\*T\*A, Future Synthesis), heparin sodium salt (IU  $\geq$  100/mg, MW: 8–25 kDa, Alfa Aesar, Haverhill, MA, USA), (*N,N*-dimethylacrylamide (DMAM, Sigma Aldrich, St. Louis, MO, USA), [2-(acryloyloxy)ethyl]trimethylammonium chloride (ATC, Sigma Aldrich), *N,N'*-bis(acryloyl)cystamine (CBA, Alfa Aesar), lithium phenyl (2,4,6-trimethylbenzoyl)phosphinate (LAP, Carbosynth, Compton, UK), fluorescein *O*-acrylate (Sigma Aldrich), Span 80 (Sigma Aldrich), cyclohexane (Chempur, Karlsruhe, Germany), acetone (Chempur), dimethyl sulfoxide (DMSO, Fisher Bioreagents, Pittsburgh, PA, USA), and dialysis membrane (Spectrum™ Spectra/Por™ 2 RC Dialysis Membrane, MWCO: 100 kDa).

##### 3.1.2. Materials and Reagents for Cell Culture and In Vitro Assays

The HCT 116 colon cancer cell line (catalog no. CCL-247) was obtained from the American Type Culture Collection (ATCC, Manassas, VA, USA), Dulbecco's modified Eagle medium (DMEM, PAN Biotech, Aidenbach, Germany), Roswell Park Memorial Institute 1640 (RPMI, PAN Biotech), fetal bovine serum (FBS, PAN Biotech), PBS (PAN Biotech), CCK-8 kit (Bimake, Houston, TX, USA), and Hoechst 33342 cell nuclei staining (Thermo Fisher Scientific, Waltham, MA, USA).

##### 3.1.3. General Methods

Ultrasonication at two different amplitudes: 40% and 60% using Sonics VCX 130 (Sonics & Materials, Inc., Newton, CT, USA) was conducted for redispersing nanogel powder and creating a water-in-oil (w/o) mini-emulsion, respectively. Purification of bare nanogels and NG/miRNA was achieved by a dialysis method following lyophilization in a freeze-dryer (ALPHA 1-2 LDplus, CHRIST) under 0.035 mbar at  $-50$  °C. Deionized water (DI water) was produced using a reverse osmosis system (conductivity < 2  $\mu\text{S}/\text{cm}$ ).

#### 3.2. Synthesis of GSH-Responsive Nanogels and Fluorescently Labeled Nanogels

Degradable nanogels were synthesized via free-radical polymerization (FRP) in an inverse w/o mini-emulsion according to our previous method [24,25]. A w/o mini-emulsion (10:1, v/v) was composed of 10.0 mL of cyclohexane containing Span-80 (600 mg) and

1.0 mL of PB solution (pH 7.0) containing monomers. The following steps were taken to synthesize nanogels: an aqueous phase was prepared in a 4 mL dark vial by adding CBA (26.0 mg, 0.10 mmol), with the main monomers DMAM and ATC (amounts specified in Table S1), and 0.2 M PB (pH 7.0) containing DMSO (10% *v/v*). The monomers were dissolved completely with a vortex. Then, the solution of the LAP initiator (2.3 mg, 0.008 mmol) was added. To create a mini-emulsion, the organic phase and aqueous phase were mixed and ultrasonicated at 60% amplitude for 5 min at 4 °C. The vial was protected from light with aluminum foil and placed over high-power light-emitting diodes (LEDs, 3 W, 395–405 nm) following photoirradiation for 30 min. To obtain nanogel powder, the suspension of nanogels was precipitated in 40 mL of cold acetone, centrifuged at 11,000 rpm for 10 min, and washed twice before air-drying overnight. On the next day, crude nanogels were dialyzed in a 100 kDa dialysis membrane against DI water. Dialysis was performed for 24 h with multiple media changes. Lastly, pure nanogel was frozen at −80 °C and lyophilized to obtain the nanogel powder. Fluorescently labeled nanogels (FL-NG) were synthesized with the same procedure but adding 0.5% *w/w* fluorescein *O*-acrylate in the aqueous phase.

### 3.3. miRNA Loading into Cationic Nanogels

The miRNA was loaded into cationic nanogels in a straightforward method. Briefly, bare nanogel powder (amounts specified in Table S2) was redispersed with 700 µL of water and sonicated at 40% amplitude for 30 s. Then, 100 µL of a-miR21 or Cy5-a-miR21 solution (concentration: 100 pmol/µL or equal to 0.725 µg/µL) was added to the nanogel dispersion. Three samples differing by N/P ratios of 10, 5, and 2 (mol/mol) were prepared to produce NG/a-miR21-1, NG/a-miR21-2, and NG/a-miR21-3, respectively. The mixtures containing relevant amounts of NG and a-miR21 were stirred overnight at 400 rpm under dark conditions. Then, dialysis was performed in a dialysis capsule (QuixSep®, 1 mL) using a dialysis membrane (MWCO 100 kDa) against 80 mL of DI water for 4 h. Finally, pure NG/a-miR21-1,2,3 was lyophilized and stored as a powder.

### 3.4. Nanogel Characterization

#### 3.4.1. Measurement of miRNA Loading Capacity (MLC) and miRNA Loading Efficiency (MLE)

The measurements of MLC and MLE were based on the fluorescence intensity, using a standard curve of Cy5-a-miR21 in PBS ( $R^2 = 1.000$ , Ex: 650 nm, Em: 675 nm). Briefly, lyophilized pure nanogel powders of NG/a-miR21-1,2,3 were redispersed in water at a concentration of 1.0 mg/mL, following dilution with PBS (pH 7.4) to a concentration of 25 µg/mL. Then, the fluorescence intensity of dispersions was measured and converted to the mass of a-miR21. MLC and MLE were then calculated using the following equations:

$$\text{MLC (\%)} = \frac{\text{Actual loaded miRNA (mg)}}{\text{NG/miRNA (mg)}} \times 100,$$

$$\text{MLE (\%)} = \frac{\text{Actual loaded miRNA (mg)}}{\text{Initial feed of miRNA (mg)}} \times 100.$$

#### 3.4.2. Dynamic Light Scattering (DLS)

The Z-average hydrodynamic diameter ( $d_H$ ) and polydispersity index (PDI) of freshly prepared bare NG and NG/a-miR21-1,2,3 (1.0 mg/mL) in 1 mM KCl solution were determined using dynamic light scattering (DLS) (Malvern, Zetasizer Nano 90S), the system was equipped with a 4 mV He–Ne ion laser ( $\lambda = 633$  nm) as the light source at a scattering angle of 90°. Similarly, the  $\zeta$  potentials of bare NG and NG/a-miR21-1,2,3 were measured using electrophoretic light scattering (ELS) measurements (Malvern, Zetasizer Nano ZC) in 1 mM KCl solution.

### 3.4.3. Cryogenic Transmission Electron Microscopy (Cryo-TEM)

NG/a-miR21-3 and GSH-treated NG (concentration: 500 µg/mL) were observed under cryo-TEM using a Tecnai F20 X TWIN microscope (FEI Company, Hillsboro, OR, USA).

### 3.4.4. Stability Study of Nanogel in Biological Media

The stability of bare NG and NG/a-miR21-3 was measured at working concentrations (100 µg/mL) in different biological media, namely, water, PBS (pH 7.4), normal saline (0.90% *w/v* of NaCl), RPMI + 10% FBS, and DMEM + 10% FBS, at 37 °C for 5 days. The colloidal stability was observed visually, and the optical density (OD) was measured at 650 nm. The OD value was converted to percentage transmittance using the following equation:

$$\text{Transmittance (\%)} = \text{antilog}(2 - \text{absorbance}).$$

### 3.4.5. miRNA Release Study

The miRNA release from NG/a-miR21-1,2,3 was analyzed using the dialysis method. Initially, a dispersion of nanogel (concentration: 100 µg/mL) was prepared in water. Then, 800 µL of NG/a-miR21-1,2,3 was placed into the dialysis capsule (QuixSep®, 1 mL) using a dialysis membrane (MWCO 100 kDa). Free a-miR21 at the same miRNA concentration as NG/a-miR21-3 was also prepared to evaluate the release of free miRNA (~7 kDa) through the 100 kDa membrane. The dialysis capsules were immersed in 40 mL of PBS (pH 7.4 with 0 or 5 mM GSH) and incubated at 37 °C under continuous shaking (110 rpm). In addition, NG/a-miR21-3 was also incubated in PBS (pH 4.5) to analyze the release profile in acidic conditions. Samples of miRNA release (400 µL, dissolution medium) were taken at predetermined time intervals (3, 6, 9, 12, 24, 36, 48, 60, and 72 h) and replaced with the same amount of prewarmed fresh medium. The amount of released miRNA in the withdrawn samples was determined by fluorescence analysis (Ex/Em max of 650/675 nm) converted to miRNA concentration using a standard curve ( $R^2 = 1.000$ ).

The miRNA release from NG/a-miR21-3 was also evaluated in the presence of a competing polyanion, heparin, at a concentration of 10 IU/mL.

## 3.5. Cell Culture and In Vitro Study

### 3.5.1. Cell Uptake Study by Confocal Microscopy

HCT 116 cancer cell lines ( $5 \times 10^3$  cells/well) were seeded in µ-Slide eight-well glass-bottom plates (ibidi, USA) in 200 µL of DMEM supplemented with 10% FBS and incubated at 37 °C for 24 h. Then, the medium was replaced with fresh DMEM + 10% FBS containing FL-NG/Cy5-a-miR21-3 (500 µg/mL) and cocultured for 3 h. FL (green) represents NG and Cy5 (red) represents miRNA. Cell nuclei were then stained with Hoechst 33342, 30 min before observation by confocal laser scanning microscopy (CLSM, Olympus FluoView FV1000, ZEISS, Dublin, CA, USA).

### 3.5.2. Cytotoxicity Study

The cytotoxicity profile of bare NG was assessed in HCT 116 cancer cell line using a standard CCK-8 assay. HCT 116 cells ( $5 \times 10^3$  cells/well) were seeded in 96-well plates in 100 µL of DMEM supplemented with 10% FBS and 1% antibiotics for 24 h, following incubation with bare nanogels at different concentrations (0, 1, 10, 50, 100, 250, and 500 µg/mL). CCK assay was performed by adding 10 µL of CCK-8 solution in each well following incubation at 37 °C for 2 h. The absorbance was then measured by a microplate reader at 450 nm. The relative cell viability (%) was expressed as a fraction of the percentage of cell growth occurring in the presence of nanogel vs. the absence of nanogel (control).

## 3.6. Statistical Analysis

GraphPad Prism Version 6.0 software (GraphPad, San Diego, CA, USA) was used for the statistical analysis. Data analysis was performed using one-way analysis of variance

(ANOVA). The significance level was set at  $p < 0.05$ , with all data displayed as mean  $\pm$  SD ( $n = 4$ ).

#### 4. Conclusions

Synthesis of acrylamide-based nanogels, containing a disulfide crosslinker via photoinitiated FRP in an inverse microemulsion technique, was developed. The successful encapsulation of miRNA into nanogels was carried out by self-assembly of nanogel cationic groups and miRNA anionic phosphate groups by electrostatic complexation. The miRNA-loaded nanogels characterized by a spherical shape ( $d_H$  about 100 nm) and a moderate positive charge ( $\zeta$  potential in the range of 12–24 mV) were able to form stable dispersions in various biological media, including serum-enriched media. The miRNA release studies demonstrated that the presence of GSH in the release environment had only a minor effect on miRNA release. Instead, a markedly accelerated release of miRNA was observed in the presence of a strong heparin polyanion, indicating the reversibility of the complexation. The miRNA-loaded nanogels were efficiently absorbed by HCT 116 cancer cells within a short incubation time and showed tolerable cytotoxicity, making them a promising miRNA delivery system.

**Supplementary Materials:** The following supporting information can be downloaded at <https://www.mdpi.com/article/10.3390/molecules28020761/s1>: Table S1. Monomer feed composition based on moles and mass; Table S2. Post-polymerization loading; Figure S1. Standard curve of Cy5-a-miR21 in PBS (pH 7.4); Figure S2. Fluorescence spectra of Cy5-a-miR21 and NG/Cy5-a-miR21 in PBS (pH 7.4); Figures S3–S6. Average size distributions ( $d_H$ ) of bare NG, NG/a-miR21-1, NG/a-miR21-2, and NG/a-miR21-3, respectively; Figures S7–S10. Average  $\zeta$  potentials of bare NG, NG/a-miR21-1, NG/a-miR21-2, and NG/a-miR21-3, respectively; Figure S11. NG/a-miR21-3 release data in pH 7.4 + 5 mM GSH fitted to zero-order, first-order, Korsmeyer–Peppas, Higuchi, and Hixon–Crowell models, respectively.

**Author Contributions:** Conceptualization, M.M. and I.W.; methodology, A.L. and I.W.; software, A.M.; validation, I.W.; formal analysis, A.M.; investigation, A.M., A.L. and S.S.; resources, I.W.; data curation, A.M., A.L. and S.S.; writing—original draft preparation, A.M. and I.W.; writing—review and editing, M.M. and I.W.; visualization, A.M. and S.S.; supervision, M.M. and I.W.; project administration, I.W.; funding acquisition, I.W. All authors have read and agreed to the published version of the manuscript.

**Funding:** This study was financed by the PRELUDIUM BIS 1 (2019/35/O/ST5/02746) from the National Science Center (NCN), Poland.

**Institutional Review Board Statement:** Not applicable.

**Informed Consent Statement:** Not applicable.

**Data Availability Statement:** Not applicable.

**Conflicts of Interest:** The authors declare no conflict of interest.

**Sample Availability:** Not applicable.

#### References

1. He, L.; Hannon, G.J. MicroRNAs: Small RNAs with a big role in gene regulation. *Nat. Rev. Genet.* **2004**, *5*, 522–531. [[CrossRef](#)] [[PubMed](#)]
2. Peng, Y.; Croce, C.M. The role of MicroRNAs in human cancer. *Signal Transduct. Target. Ther.* **2016**, *1*, 15004. [[CrossRef](#)] [[PubMed](#)]
3. Hwang, H.W.; Mendell, J.T. MicroRNAs in cell proliferation, cell death, and tumorigenesis. *Br. J. Cancer* **2006**, *94*, 776–780. [[CrossRef](#)] [[PubMed](#)]
4. Kim, J.; Yao, F.; Xiao, Z.; Sun, Y.; Ma, L. MicroRNAs and metastasis: Small RNAs play big roles. *Cancer Metastasis Rev.* **2018**, *37*, 5–15. [[CrossRef](#)] [[PubMed](#)]
5. Coenen-Stass, A.M.L.; Pauwels, M.J.; Hanson, B.; Martin Perez, C.; Conceição, M.; Wood, M.J.A.; Mäger, I.; Roberts, T.C. Extracellular microRNAs exhibit sequence-dependent stability and cellular release kinetics. *RNA Biol.* **2019**, *16*, 696–706. [[CrossRef](#)]

6. Lam, J.K.; Chow, M.Y.; Zhang, Y.; Leung, S.W. siRNA Versus miRNA as Therapeutics for Gene Silencing. *Mol. Ther. Nucleic Acids* **2015**, *4*, e252. [[CrossRef](#)]
7. Fu, Y.; Chen, J.; Huang, Z. Recent progress in microRNA-based delivery systems for the treatment of human disease. *ExRNA* **2019**, *1*, 24. [[CrossRef](#)]
8. Dasgupta, I.; Chatterjee, A. Recent Advances in miRNA Delivery Systems. *Methods Protoc.* **2021**, *4*, 10. [[CrossRef](#)]
9. Nayerossadat, N.; Maedeh, T.; Ali, P.A. Viral and nonviral delivery systems for gene delivery. *Adv. Biomed. Res.* **2012**, *1*, 27. [[CrossRef](#)]
10. Li, Y.; Maciel, D.; Rodrigues, J.; Shi, X.; Tomás, H. Biodegradable Polymer Nanogels for Drug/Nucleic Acid Delivery. *Chem. Rev.* **2015**, *115*, 8564–8608. [[CrossRef](#)]
11. Pinelli, F.; Sacchetti, A.; Perale, G.; Rossi, F. Is nanoparticle functionalization a versatile approach to meet the challenges of drug and gene delivery? *Ther. Deliv.* **2020**, *11*, 401–404. [[CrossRef](#)]
12. Shatsberg, Z.; Zhang, X.; Ofek, P.; Malhotra, S.; Krivitsky, A.; Scomparin, A.; Tiram, G.; Calderón, M.; Haag, R.; Satchi-Fainaro, R. Functionalized nanogels carrying an anticancer microRNA for glioblastoma therapy. *J. Control. Release* **2016**, *239*, 159–168. [[CrossRef](#)]
13. Javanmardi, S.; Tamaddon, A.M.; Aghamaali, M.R.; Ghahramani, L.; Abolmaali, S.S. Redox-sensitive, PEG-shielded carboxymethyl PEI nanogels silencing MicroRNA-21, sensitizes resistant ovarian cancer cells to cisplatin. *Asian J. Pharm. Sci.* **2020**, *15*, 69–82. [[CrossRef](#)]
14. Zilkowski, I.; Ziouti, F.; Schulze, A.; Hauck, S.; Schmidt, S.; Mainz, L.; Sauer, M.; Albrecht, K.; Jundt, F.; Groll, J. Nanogels Enable Efficient miRNA Delivery and Target Gene Downregulation in Transfection-Resistant Multiple Myeloma Cells. *Biomacromolecules* **2019**, *20*, 916–926. [[CrossRef](#)]
15. Javanmardi, S.; Abolmaali, S.S.; Mehrabanpour, M.J.; Aghamaali, M.R.; Tamaddon, A.M. PEGylated nanohydrogels delivering anti-MicroRNA-21 suppress ovarian tumor-associated angiogenesis in matrigel and chicken chorioallantoic membrane models. *Bioimpacts* **2022**, *12*, 449–461. [[CrossRef](#)]
16. Liu, C.; Wen, J.; Meng, Y.; Zhang, K.; Zhu, J.; Ren, Y.; Qian, X.; Yuan, X.; Lu, Y.; Kang, C. Efficient delivery of therapeutic miRNA nanocapsules for tumor suppression. *Adv. Mater.* **2015**, *27*, 292–297. [[CrossRef](#)]
17. Dispenza, C.; Sabatino, M.A.; Ajovalasit, A.; Ditta, L.A.; Ragusa, M.; Purrello, M.; Costa, V.; Conigliaro, A.; Alessandro, R. Nanogel-antimiR-31 conjugates affect colon cancer cells behaviour. *RSC Adv.* **2017**, *7*, 52039–52047. [[CrossRef](#)]
18. Tamura, A.; Oishi, M.; Nagasaki, Y. Efficient siRNA delivery based on PEGylated and partially quaternized polyamine nanogels: Enhanced gene silencing activity by the cooperative effect of tertiary and quaternary amino groups in the core. *J. Control. Release* **2010**, *146*, 378–387. [[CrossRef](#)]
19. Pottanam Chali, S.; Hüwel, S.; Rentmeister, A.; Ravoo, B.J. Self-Assembled Cationic Polypeptide Supramolecular Nanogels for Intracellular DNA Delivery. *Chemistry* **2021**, *27*, 12198–12206. [[CrossRef](#)]
20. Ahmed, M.; Narain, R. Intracellular delivery of DNA and enzyme in active form using degradable carbohydrate-based nanogels. *Mol. Pharm.* **2012**, *9*, 3160–3170. [[CrossRef](#)]
21. Gamcsik, M.P.; Kasibhatla, M.S.; Teeter, S.D.; Colvin, O.M. Glutathione levels in human tumors. *Biomarkers* **2012**, *17*, 671–691. [[CrossRef](#)]
22. Cheng, R.; Feng, F.; Meng, F.; Deng, C.; Feijen, J.; Zhong, Z. Glutathione-responsive nano-vehicles as a promising platform for targeted intracellular drug and gene delivery. *J. Control. Release* **2011**, *152*, 2–12. [[CrossRef](#)] [[PubMed](#)]
23. Bautista-Sánchez, D.; Arriaga-Canon, C.; Pedroza-Torres, A.; De La Rosa-Velázquez, I.A.; González-Barríos, R.; Contreras-Espinosa, L.; Montiel-Manríquez, R.; Castro-Hernández, C.; Fragoso-Ontiveros, V.; Álvarez-Gómez, R.M.; et al. The Promising Role of miR-21 as a Cancer Biomarker and Its Importance in RNA-Based Therapeutics. *Mol. Ther. Nucleic Acids* **2020**, *20*, 409–420. [[CrossRef](#)] [[PubMed](#)]
24. Maruf, A.; Milewska, M.; Kovács, T.; Varga, M.; Vellai, T.; Lalik, A.; Student, S.; Borges, O.; Wandzik, I. Trehalose-releasing nanogels: A step toward a trehalose delivery vehicle for autophagy stimulation. *Biomater. Adv.* **2022**, *138*, 212969. [[CrossRef](#)] [[PubMed](#)]
25. Maruf, A.; Milewska, M.; Lalik, A.; Wandzik, I. pH and Reduction Dual-Responsive Nanogels as Smart Nanocarriers to Resist Doxorubicin Aggregation. *Molecules* **2022**, *27*, 5983. [[CrossRef](#)]
26. Wu, J. The Enhanced Permeability and Retention (EPR) Effect: The Significance of the Concept and Methods to Enhance Its Application. *J. Pers. Med.* **2021**, *11*, 771. [[CrossRef](#)]

**Disclaimer/Publisher's Note:** The statements, opinions and data contained in all publications are solely those of the individual author(s) and contributor(s) and not of MDPI and/or the editor(s). MDPI and/or the editor(s) disclaim responsibility for any injury to people or property resulting from any ideas, methods, instructions or products referred to in the content.



## *Supplementary Information*

*for*

### **A Simple Synthesis of Reduction-Responsive Acrylamide-Type Nanogels for miRNA Delivery**

**Ali Maruf <sup>1,2</sup>, Małgorzata Milewska <sup>1,2</sup>, Anna Lalik <sup>2,3</sup>, Sebastian Student <sup>2,3</sup> and Ilona Wandzik <sup>1,2,\*</sup>**

<sup>1</sup> Department of Organic Chemistry, Bioorganic Chemistry and Biotechnology, Faculty of Chemistry, Silesian University of Technology, Krzywoustego 4, 44-100 Gliwice, Poland

<sup>2</sup> Biotechnology Center, Silesian University of Technology, Krzywoustego 8, 44-100 Gliwice, Poland

<sup>3</sup> Department of Systems Biology and Engineering, Faculty of Automatic Control, Electronics and Computer Science, Silesian University of Technology, Akademicka 16, 44-100 Gliwice, Poland

\* Correspondence: [ilona.wandzik@polsl.pl](mailto:ilona.wandzik@polsl.pl)

**Table S1.** Monomer feed composition based on moles and mass

Formulation <sup>a</sup>	DMAM		ATC		CBA		LAP	
	mg	mmol	mg	mmol	mg	mmol	mg	mmol
NG	183.6	1.852	21.5	0.111	26.0	0.099	2.3	0.008

<sup>a</sup>Total volume of aqueous phase and organic phase were 1 mL and 10 mL, respectively.

**Table S2.** Post-polymerization loading

Nanogels	NG (mg) <sup>a</sup>	ATC ( $\mu$ mol)	N/P ratio
NG	-	-	-
NG/a-miR21-1	5.0	2.38	10
NG/a-miR21-2	2.5	1.19	5
NG/a-miR21-3	1.0	0.48	2

<sup>a</sup> miRNA was loaded at concentration of 100 pmol/ $\mu$ L (100  $\mu$ L).

Standard curve of Cy5-a-miR21 in PBS (pH 7.4)

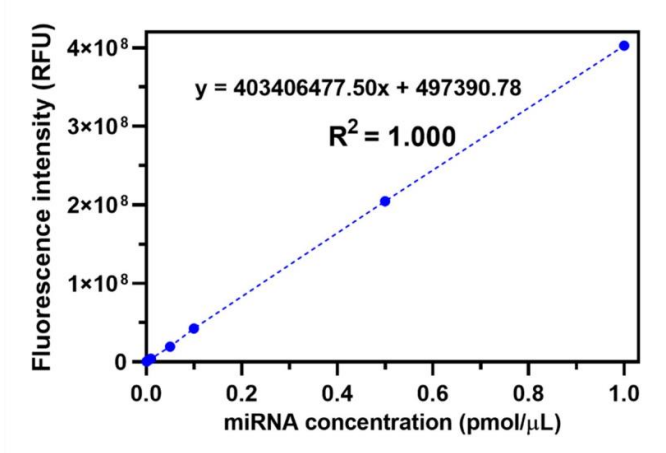


**Figure S1.** Standard curve of Cy5-a-miR21 in PBS (pH 7.4). The standard curve was created from different concentrations of a-miR21: 0.0005, 0.001, 0.005, 0.01, 0.05, 0.1, 0.5, and 1.0 pmol/μL. Data were reported as mean ± SD ( $n = 4$ ).

Fluorescence spectra of Cy5-a-miR21 and NG/Cy5-a-miR21

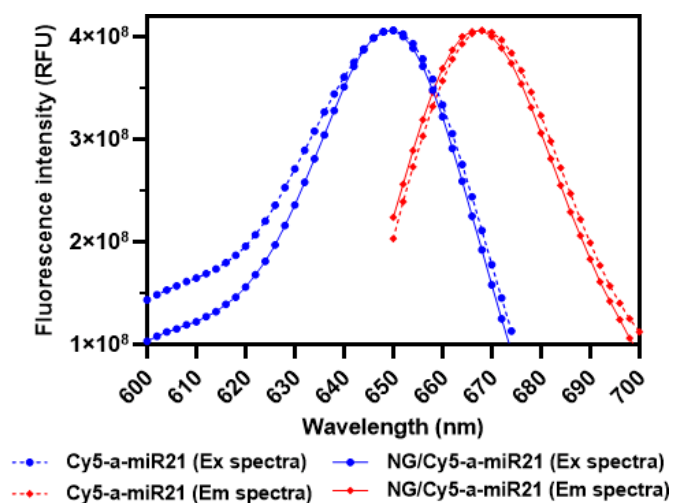


**Figure S2.** Fluorescence spectra of Cy5-a-miR21 and NG/Cy5-a-miR21 in PBS (pH 7.4). Both Cy5-a-miR21 and NG/Cy5-a-miR21 indicated the same Ex/Em max (regardless of a relatively different spectra particularly at 600–635 nm excitation area). For analysis purposes (standard curve generation, miRNA loading analysis, and miRNA release study) we used the maximum wavelengths: 650 and 675 nm for the Ex and Em, respectively.

DLS measurements of nanogels

	<b>Size (d.nm):</b>	<b>% Intensity:</b>	<b>St Dev (d.nm):</b>
<b>Z-Average (d.nm):</b> 92.47	<b>Peak 1:</b> 116.2	95.4	63.16
<b>Pdl:</b> 0.429	<b>Peak 2:</b> 4985	3.4	667.3
<b>Intercept:</b> 0.974	<b>Peak 3:</b> 591.0	1.3	142.6
<b>Result quality:</b> Good			

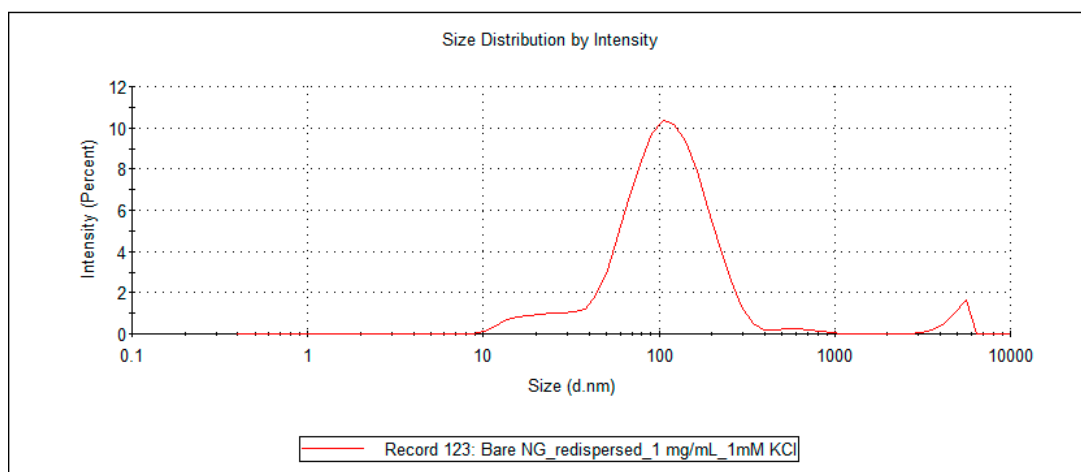


Figure S3. Average size distribution ( $d_H$ ) of bare NG in 1 mM KCl from four replications.

	<b>Size (d.nm):</b>	<b>% Intensity:</b>	<b>St Dev (d.nm):</b>
<b>Z-Average (d.nm):</b> 109.2	<b>Peak 1:</b> 136.6	96.9	73.50
<b>Pdl:</b> 0.341	<b>Peak 2:</b> 4792	3.1	840.9
<b>Intercept:</b> 0.965	<b>Peak 3:</b> 0.000	0.0	0.000
<b>Result quality:</b> Good			

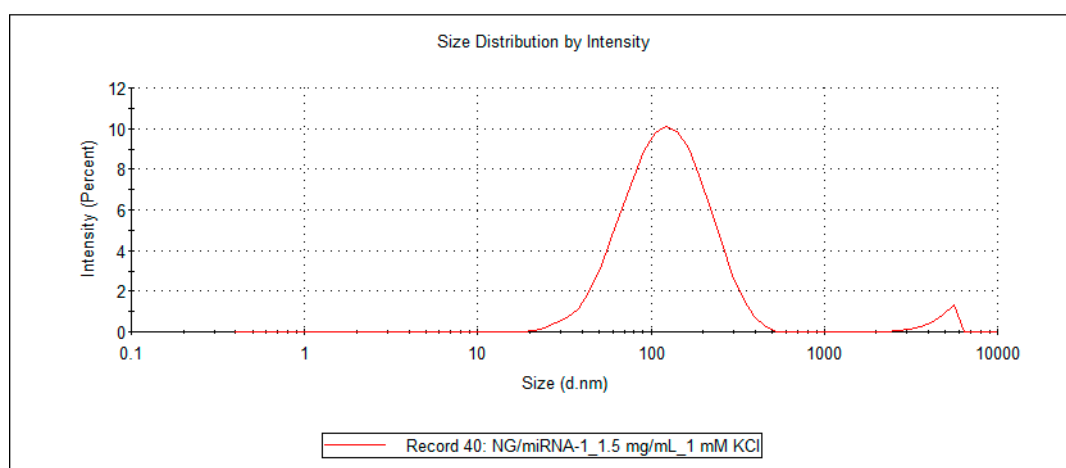
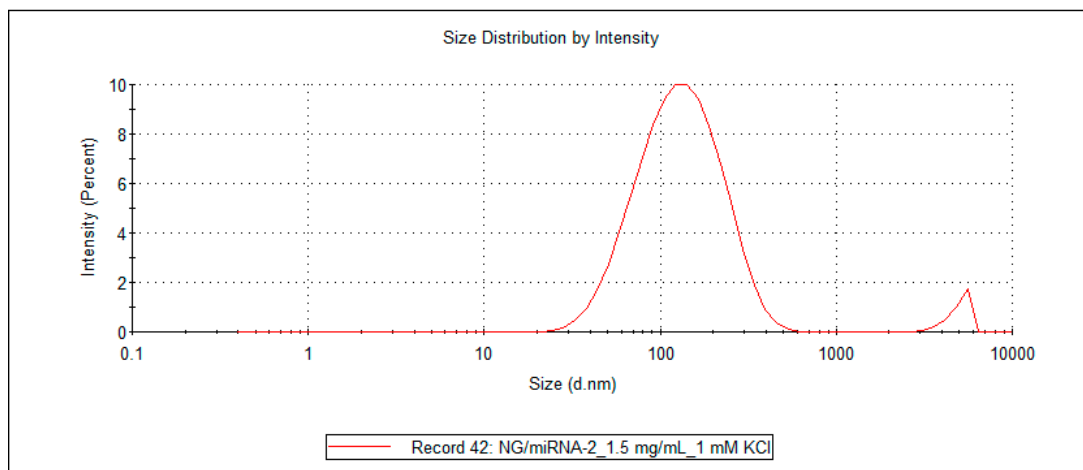


Figure S4. Average size distribution ( $d_H$ ) of NG/a-miR21-1 in 1 mM KCl from four replications.

	Size (d.nm):	% Intensity:	St Dev (d.nm):
<b>Z-Average (d.nm):</b> 116.8	<b>Peak 1:</b> 144.5	96.5	77.32
<b>Pdl:</b> 0.361	<b>Peak 2:</b> 4961	3.5	693.3
<b>Intercept:</b> 0.964	<b>Peak 3:</b> 0.000	0.0	0.000
<b>Result quality :</b> Good			



**Figure S5.** Average size distribution ( $d_H$ ) of NG/a-miR21-2 in 1 mM KCl from four replications.

	Size (d.nm):	% Intensity:	St Dev (d.nm):
<b>Z-Average (d.nm):</b> 122.1	<b>Peak 1:</b> 191.3	95.1	160.9
<b>Pdl:</b> 0.457	<b>Peak 2:</b> 4390	4.9	997.9
<b>Intercept:</b> 0.952	<b>Peak 3:</b> 0.000	0.0	0.000
<b>Result quality :</b> Good			

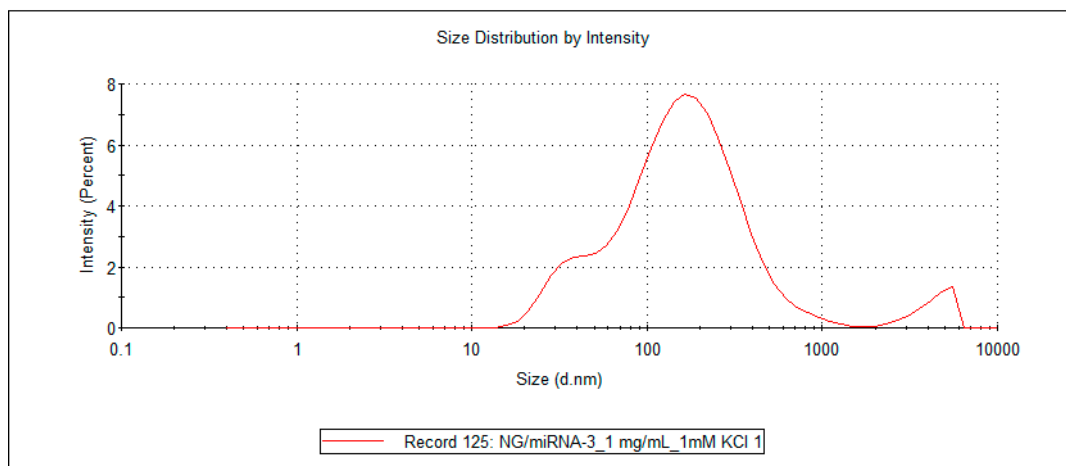


**Figure S6.** Average size distribution ( $d_H$ ) of NG/a-miR21-3 in 1 mM KCl from four replications.

**Zeta potential ( $\zeta$ ) measurements of nanogels**

	Mean (mV)	Area (%)	St Dev (mV)
<b>Zeta Potential (mV): 27.4</b>	<b>Peak 1: 27.4</b>	<b>100.0</b>	<b>3.69</b>
<b>Zeta Deviation (mV): 3.40</b>	<b>Peak 2: 0.00</b>	<b>0.0</b>	<b>0.00</b>
<b>Conductivity (mS/cm): 0.183</b>	<b>Peak 3: 0.00</b>	<b>0.0</b>	<b>0.00</b>

**Result quality : Good**

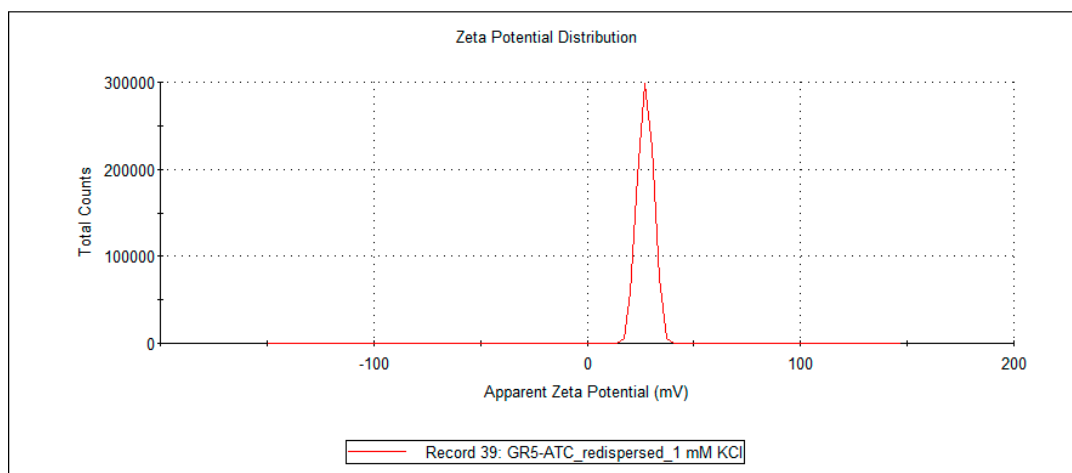


**Figure S7.** Average  $\zeta$  potential of bare NG in 1 mM KCl from four replications.

	Mean (mV)	Area (%)	St Dev (mV)
<b>Zeta Potential (mV): 24.2</b>	<b>Peak 1: 24.2</b>	<b>100.0</b>	<b>3.54</b>
<b>Zeta Deviation (mV): 3.43</b>	<b>Peak 2: 0.00</b>	<b>0.0</b>	<b>0.00</b>
<b>Conductivity (mS/cm): 0.187</b>	<b>Peak 3: 0.00</b>	<b>0.0</b>	<b>0.00</b>

**Result quality : Good**

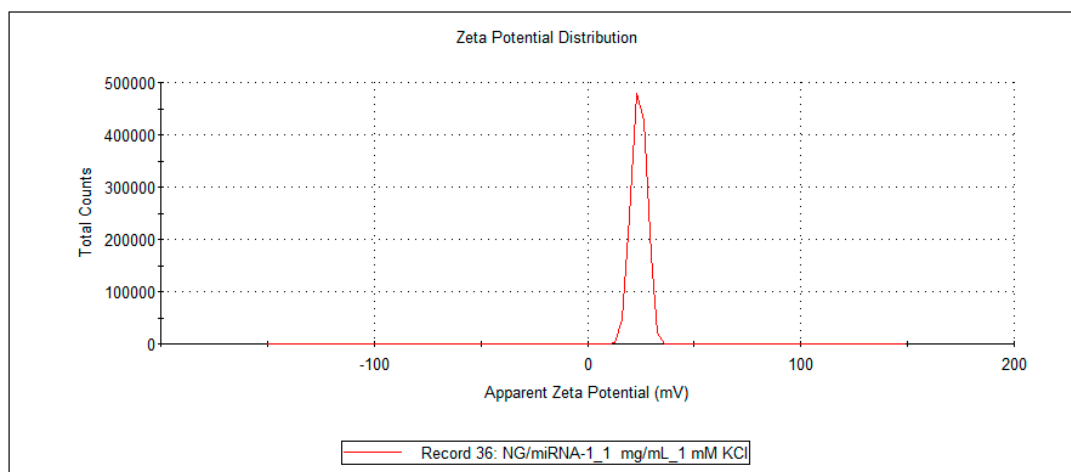


**Figure S8.** Average  $\zeta$  potential of NG/a-miR21-1 in 1 mM KCl from four replications.

## Publication [P3] Supplementary Information

	Mean (mV)	Area (%)	St Dev (mV)
<b>Zeta Potential (mV):</b> 20.8	<b>Peak 1:</b> 20.8	100.0	4.93
<b>Zeta Deviation (mV):</b> 4.71	<b>Peak 2:</b> 0.00	0.0	0.00
<b>Conductivity (mS/cm):</b> 0.221	<b>Peak 3:</b> 0.00	0.0	0.00
<b>Result quality :</b> Good			

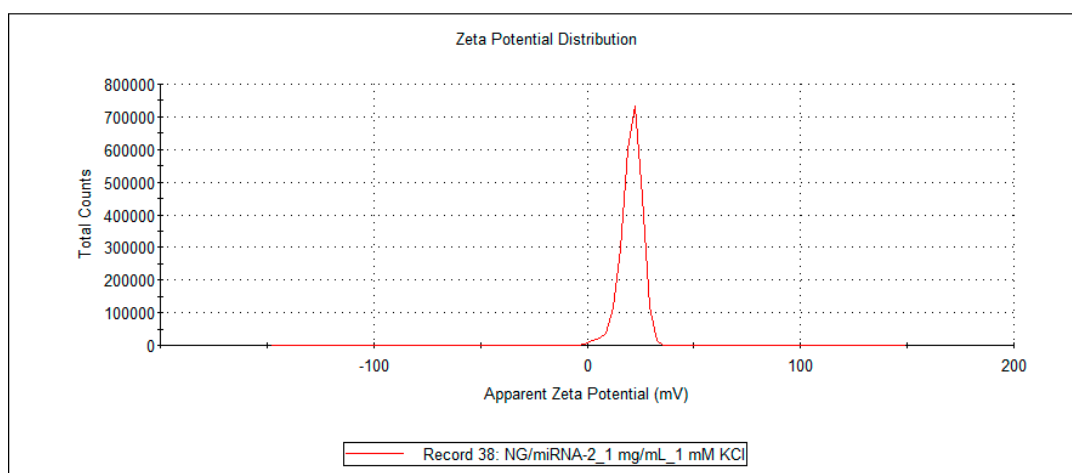


**Figure S9.** Average  $\zeta$  potential of NG/a-miR21-2 in 1 mM KCl from four replications.

	Mean (mV)	Area (%)	St Dev (mV)
<b>Zeta Potential (mV):</b> 11.9	<b>Peak 1:</b> 12.0	100.0	6.07
<b>Zeta Deviation (mV):</b> 6.04	<b>Peak 2:</b> 0.00	0.0	0.00
<b>Conductivity (mS/cm):</b> 0.170	<b>Peak 3:</b> 0.00	0.0	0.00
<b>Result quality :</b> Good			

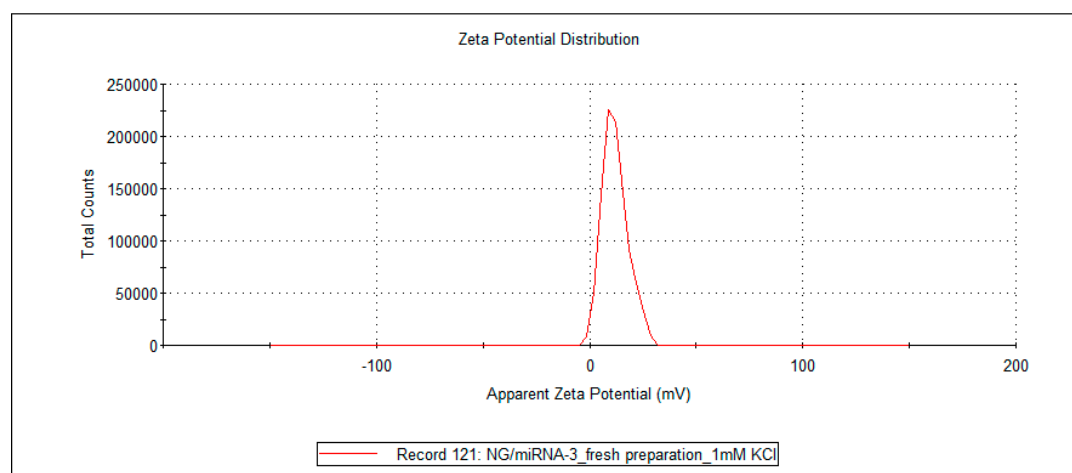


**Figure S10.** Average  $\zeta$  potential of NG/a-miR21-3 in 1 mM KCl from four replications.

MiRNA release kinetics from nanogels

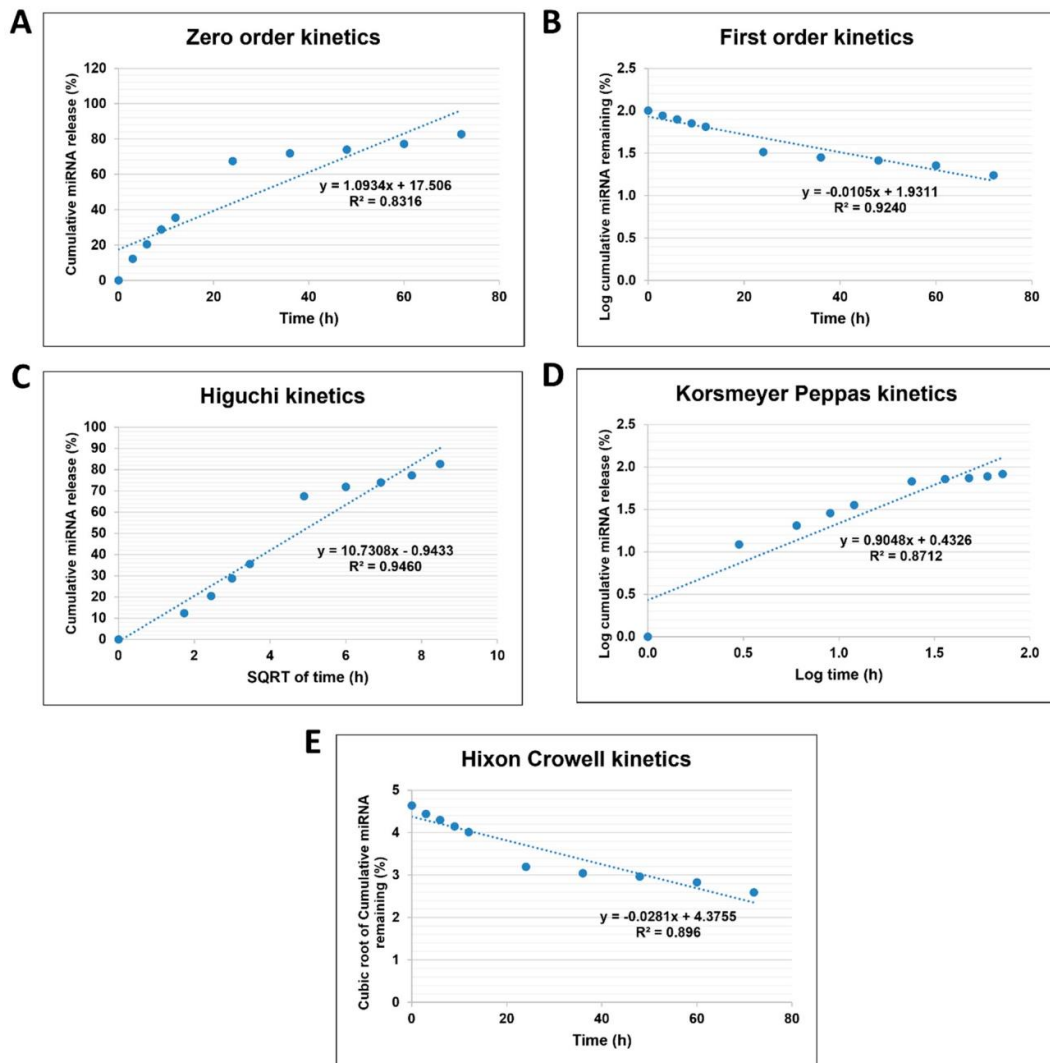


**Figure S11.** NG/a-miR21-3 release data in pH 7.4 + 5 mM GSH fitted to (A) zero order, (B) first order, (C) Higuchi, (D) Korsmeyer Peppas, and (E) Hixon Crowell models.



**STATEMENT 4**

I declare that my percentage contribution to the publication [P4] entitled “*Trehalose-releasing nanogels: A step toward a trehalose delivery vehicle for autophagy stimulation*” (published in **Biomater. Adv.** 2022, 138, 212969. DOI: 10.1016/j.bioadv.2022.212969) was 30%.

Justification: As part of this work, I served as a co-author for various tasks, including performing experiments: synthesizing trehalose-releasing nanogels, conducting trehalose release study and the enzymatic assay, measuring DLS and zeta potential, checking colloidal stability, preparing samples for cryoTEM, synthesizing fluorescein-labelled nanogels, conducting cell uptake for confocal imaging, and conducting the hemocompatibility assay in University of Coimbra, Portugal. Additionally, I was responsible for collecting and analyzing some part of the experimental data, participating in writing of manuscript, creating figures and tables, managing citations, formatting the manuscript according to the journal’s style, assisting in revising the manuscript after peer review, and final proofreading.



Ali Maruf, M.Eng.

(PhD candidate)

As the corresponding author of the above-mentioned publication, which is part of the doctoral thesis of Mr. Ali Maruf, I declare that the percentage contribution of the remaining co-authors can be estimated as follows:

Milewska M: 35%

Group from the Department of Genetics, ELTE Eotvos Lorand University, Hungary (Kovács T, Varga M, Vellai T): 10%

Group from the Department of Systems Biology and Engineering, Faculty of Automatic Control, Electronics and Computer Science, Silesian University of Technology, Poland (Lalik A, Student S): 7%

Borges O: 3%

Wandzik I: 15%



prof. dr hab. inż. Ilona Wandzik

(Supervisor / corresponding author)

Contents lists available at [ScienceDirect](https://www.sciencedirect.com)

Biomaterials Advances

journal homepage: [www.journals.elsevier.com/materials-science-and-engineering-c](http://www.journals.elsevier.com/materials-science-and-engineering-c)

## Trehalose-releasing nanogels: A step toward a trehalose delivery vehicle for autophagy stimulation

Ali Maruf<sup>a,b</sup>, Małgorzata Milewska<sup>a,b,\*</sup>, Tibor Kovács<sup>c</sup>, Máté Varga<sup>c,d</sup>, Tibor Vellai<sup>c,d</sup>, Anna Lalik<sup>b,e</sup>, Sebastian Student<sup>b,e</sup>, Olga Borges<sup>f,g</sup>, Ilona Wandzik<sup>a,b,\*</sup>

<sup>a</sup> Department of Organic Chemistry, Bioorganic Chemistry and Biotechnology, Faculty of Chemistry, Silesian University of Technology, Krzywoustego 4, 44-100 Gliwice, Poland

<sup>b</sup> Biotechnology Center, Silesian University of Technology, Krzywoustego 8, 44-100 Gliwice, Poland

<sup>c</sup> Department of Genetics, ELTE Eötvös Loránd University, Pázmány P. stry. 1/C, Budapest H-1117, Hungary

<sup>d</sup> ELKH-ELTE Genetics Research Group, Pázmány P. stry. 1/C, Budapest H-1117, Hungary

<sup>e</sup> Department of Systems Biology and Engineering, Faculty of Automatic Control, Electronics and Computer Science, Silesian University of Technology, Akademicka 16, 44-100 Gliwice, Poland

<sup>f</sup> Center for Neuroscience and Cell Biology, University of Coimbra, 3000-515 Coimbra, Portugal

<sup>g</sup> Faculty of Pharmacy, University of Coimbra, 3000-548 Coimbra, Portugal

### ARTICLE INFO

#### Keywords:

Autophagy  
Colloidal stability  
Drug delivery  
Nanogel  
Trehalose

### ABSTRACT

Trehalose has been widely studied as a treatment for a variety of human disorders due to its ability to stimulate autophagy. Trehalose, however, is poorly adsorbed and is hydrolyzed in the intestinal mucosa, and oral delivery requires relatively high doses to induce autophagy. The parenteral injection of trehalose-releasing nanogels proposed in this study offers an alternative mode of delivery. This study aimed to develop stable colloidal dispersions of trehalose-rich nanogels that could sustainably release trehalose under physiologically relevant conditions. The nanogel design was based on the covalent incorporation of 6-*O*-acryloyl-trehalose within a polymer network. A series of nine trehalose-rich nanogels with highly conjugated trehalose (up to 59 % w/w) were synthesized and shown to sustainably release trehalose at a rate that is not dose dependent. The nanogels were optimized to keep colloidal stability in serum-enriched cell culture media. The stable nanogels were not cytotoxic to primary HUVECs. Two selected nanogels with opposite surface charges were subjected to extended in vitro characterization that included a cellular uptake study and a hemocompatibility assay. Both nanogels were efficiently taken up by HUVECs during a short incubation. They also proved not to be hemolytic to human RBCs in concentrations up to 2.0 mg/mL. Finally, an in vivo autophagy stimulation study employing transgenic zebrafish and *Drosophila* larvae demonstrated that prolonged exposure to a cationic trehalose-releasing nanogel can induce autophagic activity in in vivo systems without any detectable toxicity.

### 1. Introduction

$\alpha,\alpha$ -Trehalose is a naturally occurring, non-reducing disaccharide composed of two D-glucopyranosyl units. The molecule is very well known for its ability to stabilize biomacromolecules in stress conditions [1]. Recently, numerous in vitro and in vivo studies have confirmed an additional biologically important feature of trehalose, namely the ability to induce autophagy [2,3]. Autophagy is highly regulated process that results in the removal of cellular debris. The process is important in homeostasis and other cellular functions. Failure of autophagy can result

in a wide range of abnormalities in humans, leading to neurodegenerative disorders, diabetes, and other disease states [4].

In preclinical studies, many research groups have explored the impact of trehalose-induced autophagy on a variety of disorders, including Parkinson's disease (PD) [5,6], Lewy body disease [7], Alzheimer's disease (AD) [8], diabetes and non-alcoholic fatty liver disease (NAFLD) [9,10], atherosclerosis [11,12], amyotrophic lateral sclerosis (ALS) [13], and ischemic-related diseases [14–16]. The [ClinicalTrials.gov](https://www.clinicaltrials.gov) database also records several trials exploring the potential impacts of trehalose on AD, NAFLD, acute coronary syndrome, and other

\* Corresponding authors at: Department of Organic Chemistry, Bioorganic Chemistry and Biotechnology, Faculty of Chemistry, Silesian University of Technology, Krzywoustego 4, 44-100 Gliwice, Poland.

E-mail addresses: [malgorzata.milewska@polsl.pl](mailto:malgorzata.milewska@polsl.pl) (M. Milewska), [ilona.wandzik@polsl.pl](mailto:ilona.wandzik@polsl.pl) (I. Wandzik).

<https://doi.org/10.1016/j.bioadv.2022.212969>

Received 11 January 2022; Received in revised form 26 May 2022; Accepted 1 June 2022

Available online 4 June 2022

2772-9508/© 2022 Published by Elsevier B.V.

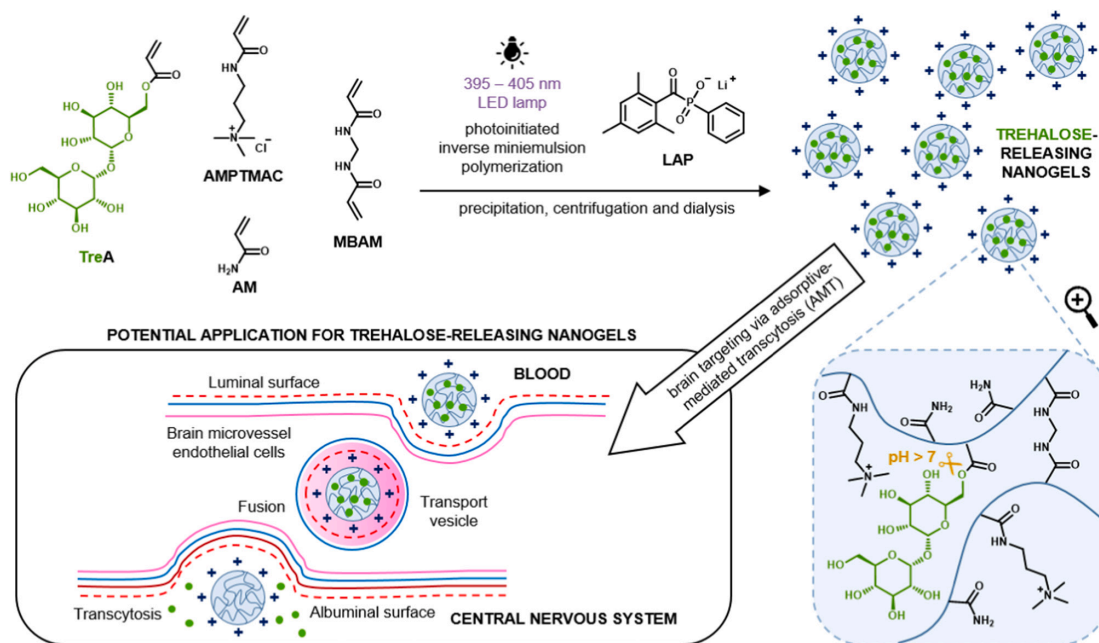


Fig. 1. Scheme illustrating the synthesis and potential application of trehalose-releasing nanogels for brain targeting via AMT.

diseases. Most studies in animal models indicate that the induction of autophagy by trehalose requires the use of high, 100 mM concentrations of trehalose to ensure effectiveness [2,3]. The dose commonly used for intraperitoneal administration is 2–3 g/kg/day, while for oral administration is 2–4 % w/v in drinking water. The necessity for such high doses of trehalose is twofold. While the high hydrophilicity of trehalose results in poor penetration through cell membranes, it is also the case that the presence of intestinal trehalase, an enzyme that hydrolyzes trehalose into two glucose molecules, impedes its oral absorption. To improve the bioavailability of trehalose, nano formulations that are capable of releasing trehalose under physiologically relevant conditions would be an alternative to the classical alternatives. Such trehalose delivery vehicles could reduce its required dosage, prolong circulation time, and protect trehalose against trehalase-mediated rapid hydrolysis.

Several polymeric materials containing covalently bound trehalose have been synthesized and studied for wide range of applications, e.g., as protein stabilizers [17–20], nonviral nucleic acid carriers [21,22], thermogelling hydrogel matrices for 3D cell culture [23,24], anti-adhesives to inhibit bacterial infections [25], and magnetic nanoparticles for mycobacteria detection [26]. In addition, some trehalose-bearing nanoparticles have been developed as neuroprotective agents [27–29]. While nanocarriers facilitating the release of substantial amounts of trehalose have yet to be developed, two reports on this topic have been published, recently. Colombo et al., have developed trehalose nanolipid-assemblies and investigated their effect on autophagy stimulation *in vitro* [30]. Their results showed that the nanolipids did not induce autophagy, which may be due to the limited hydrolytic cleavage of the trehalose conjugate and insufficient trehalose release. In their subsequent study, trehalose-bearing PEG-Au nanoparticles were synthesized and demonstrated moderate autophagy stimulation in LC3-overexpressed HeLa cells after 48 h [31]. Trehalose was bound to 4.6 nm-size nanoparticles via a triazole moiety utilizing a click chemistry protocol. The moderate effectiveness of this approach may result from the poor hydrolysis of this moiety.

When considering the development of an effective polymeric nanocarrier for the treatment of neurodegenerative disorders, successful

delivery to the central nervous system (CNS) needs to be considered [32–35]. Therapeutic strategies involve either bypassing or crossing the blood-brain barrier (BBB) to access the CNS. The former can be achieved via intranasal administration of the nanocarrier, which is preferably smaller than 100 nm. This route is, in some cases, more effective than drug delivery by conventional oral and intravenous routes. The second approach, which enables nanoparticles to cross the BBB, could be realized via receptor-mediated transcytosis, which requires decoration of nanoparticles with specific ligands, or adsorptive-mediated transcytosis (AMT), which utilizes electrostatic interactions. Particle surface charge provided by specific ionic moieties can promote the pathway by which nanoparticles are internalized in cells. Cationic residues can provide beneficial electrostatic interactions with the negatively charged luminal side of the BBB, resulting in endocytotic internalization via AMT [32–34].

Given the promising therapeutic potential for trehalose-releasing nanocarriers, the present study is focused on the development of nanogels containing covalently bound trehalose that can be sustainably released via hydrolysis. Nanogels are nanosized hydrogels, i.e., three-dimensional networks formed by crosslinked polymer chains. They are characterized by a wide range of beneficial properties such as biocompatibility, high surface-to-volume ratio, high loading capacity, and potential responsivity to environmental stimuli. These characteristics make them widely studied as potential drug delivery carriers [35–37].

Recently we have developed bulk hydrogels containing up to 52 % w/w covalently bound trehalose which could be released in physiologically relevant conditions [38]. Trehalose has been incorporated into the polymer network by copolymerization of the appropriate acrylamide-type monomers with trehalose monoacrylate. The presence of primary and secondary acrylamide units significantly accelerates hydrolysis of the ester moiety in acrylate units at pH >7.0 [39] and sustained release of trehalose can be realized at circumneutral conditions. Working from this foundation, we have developed nanosized hydrogels as trehalose delivery vehicles for potential parenteral administration. A series of trehalose-releasing nanogels have been synthesized via photoinitiated free radical polymerization (FRP) of trehalose monoacrylate and

**Table 1**  
Formulation and physicochemical characteristics of trehalose-releasing nanogels.

Samples	TreA (Trehalose) feed (% w/w) <sup>a</sup>	AMPTMAC feed (% w/w) <sup>a</sup>	AM feed (% w/w) <sup>a</sup>	Pure yield (%) <sup>b</sup>	CTre (% w/w) <sup>c</sup>	d <sub>H</sub> (PdI) in DMEM (nm)	ζ-potential (mV)
TNG1-AM	17.9 (15.4)	55.4	17.9	91	13.9 ± 1.6	Aggregated	35.8
TNG2	35.7 (30.7)	55.4	–	85	27.6 ± 0.8	163 (0.21)	38.0
TNG3	44.6 (38.3)	46.5	–	86	33.3 ± 0.5	126 (0.18)	40.9
TNG4	59.9 (51.5)	31.3	–	74	46.9 ± 0.8	127 (0.18)	41.5
TNG5-AM	59.9 (51.5)	15.6	15.6	77	46.6 ± 1.4	213 (0.26)	32.9
TNG6-AM	59.9 (51.5)	7.8	23.4	70	45.4 ± 0.6	187 (0.23)	37.6
TNG7-AM	67.7 (58.2)	7.8	15.6	73	53.3 ± 2.3	115 (0.21)	22.8
TNG8	72.3 (62.2)	18.8	–	61	57.2 ± 0.8	81 (0.19)	25.5
TNG9-AM	75.5 (64.9)	–	15.6	54	58.6 ± 0.3	116 (0.22)	–5.7

Note: MBAM was used in all formulations at 8.9 % w/w.

<sup>a</sup> Calculated based on nanogel formulations.

<sup>b</sup> Calculated based on weight after purification.

<sup>c</sup> Calculated based on enzymatic assay. Data are presented as mean ± SD (n = 3).

carefully selected acrylamide-type monomers: acrylamide (AM) and (3-acrylamidopropyl)-trimethylammonium chloride (AMPTMAC) by an inverse microemulsion technique (Fig. 1). The cationic monomer, AMPTMAC was chosen in order to provide the electrostatic interactions with negatively charged membranes desired in brain targeting. In turn, the presence of AM units beneficially boosts trehalose release.

## 2. Materials and methods

### 2.1. Materials and reagents

#### 2.1.1. General methods

Ultrasonication was carried out using Sonics VCX 130 (Sonics & Materials, Inc., USA), in which 60 % of amplitude was used for obtaining a miniemulsion and 40 % of amplitude was used for redispersion of nanogel powder. Freeze drying was carried out under 0.035 mbar at –50 °C (ALPHA 1–2 LDplus, CHRIST). NMR spectra were recorded in deuterated solvents (Deutero GmbH) with internal standards using an NMR spectrometer operating at 600 MHz (Varian). A SpectraMax i3x Multi-Mode Microplate Reader (Molecular Devices, USA) was used in stability, cytotoxicity, fluorescence, and enzymatic trehalose assays. The amount of conjugated trehalose and the cumulative trehalose release were determined enzymatically using a Trehalose Assay Kit (Megazyme International, Ireland) following a microplate assay procedure. Phosphate buffered saline (PBS) and 5 % dextrose in normal saline (D5NS) solutions were freshly prepared. Deionized water (DI water) was produced using a reverse osmosis system (conductivity <2 μS/cm).

#### 2.1.2. Materials and reagents for trehalose-releasing nanogels synthesis

6-O-acryloyl-α,α'-trehalose (TreA) [38], acrylamide (AM, Acros Organics), N,N'-methylenebisacrylamide (MBAM, Acros Organics), 3-acrylamidopropyltrimethylammonium chloride (AMPTMAC, 75 % w/

w in H<sub>2</sub>O, Sigma Aldrich), lithium phenyl (2,4,6-trimethylbenzoyl) phosphinate (LAP, Carbosynth), fluorescein O-acrylate (Sigma Aldrich), Span 80 (Sigma Aldrich), cyclohexane (Chempur), acetone (Chempur), PBS tablets (Sigma Aldrich), dialysis membrane (Spectrum™ Spectra/Por™ 2 RC Dialysis Membrane, MWCO: 12–14 kDa). TreA was synthesized following our previously described method [38].

#### 2.1.3. Materials and reagents for cell culture and in vitro assays

Human umbilical vein endothelial cells (HUVECs, Merck Millipore), EndoGRO-LS Complete Culture Media Kit, primary cell medium with low serum (including EndoGRO Basal Medium (SCME-BM) and Supplement Kit, Merck Millipore), Dulbecco's Modified Eagle Medium (DMEM, PAN Biotech), Roswell Park Memorial Institute 1640 (RPMI, PAN Biotech), Fetal Bovine Serum (FBS, PAN Biotech), PBS (PAN Biotech), antibiotic antimycotic solution (100×) containing penicillin, streptomycin, and amphotericin B (Sigma Aldrich), CCK-8 kit (Bimake), and Hoechst 33342 cell nuclei staining (Thermo Fisher Scientific). Cyanmethemoglobin (CMH), Drabkin's reagent, and Brij 35 solution (Sigma Aldrich), Triton-X-100, and DI water.

### 2.2. Synthesis of trehalose-releasing nanogels and fluorescently labelled nanogels

A series of trehalose-releasing nanogels with different compositions (Table 1, Table S1, Fig. 2A, B) were synthesized via an inverse miniemulsion FRP. A 10:1 (v:v) water-in-oil (w/o) miniemulsion was composed of cyclohexane (10.0 mL) containing Span 80 (600 mg) as the organic continuous phase and the aqueous phase (1.0 mL) consisted of PBS solution (pH 6.0) containing monomers and photoinitiator LAP. The general procedure for the synthesis of nanogels was as follows (Fig. S1). Briefly, the aqueous phase was prepared in 4-mL dark vial by placing MBAM (20.0 mg), TreA (amount specified in Fig. 2B and Table S1) and

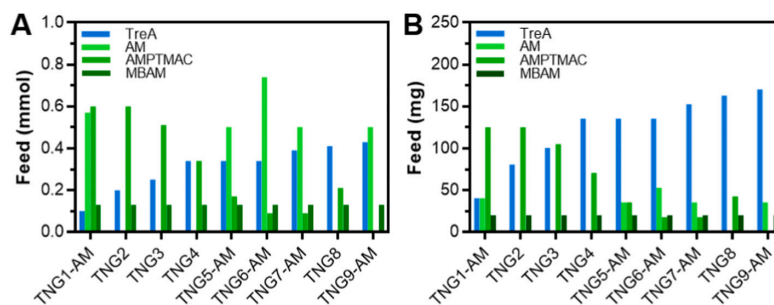


Fig. 2. Initial feed of trehalose-releasing nanogels expressed as (A) moles and (B) mass.

PBS solutions of AM, and/or AMPTMAC (amounts specified in Fig. 2B and Table S1). The mixture was vortexed for approximately 10–15 min to completely dissolve all the monomers. Finally, the solution of LAP initiator (2.3 mg) was added, and the aqueous phase was then transferred into a 20-mL transparent vial containing the cold organic phase (4 °C). The emulsion was prepared by sonicating the mixture using an ultrasonicator with an amplitude of 60 % for 5 min on ice. The reaction vial was then wrapped in aluminum foil and photoirradiated from the bottom of the vial with High Power Light-Emitting Diodes (LEDs, 3 W, 395–405 nm) for 30 min. Afterwards, the product was precipitated in 40 mL of acetone and centrifuged at 14610 ×g for 10 min. The precipitate was then washed twice with 40 mL of acetone, centrifuged, and air-dried overnight. Crude product was dispersed in DI water and purified by dialysis (MWCO 12–14 kDa) against H<sub>3</sub>PO<sub>4</sub> solution (pH 5.0) for 24 h with multiple media changes and DI water as the last change. Finally, the nanogel dispersion was freeze-dried, yielding white fluffy powder which was stored at 4 °C prior to use.

Fluorescently labelled nanogels were prepared following the procedure described above using 0.5 % w/w fluorescein *O*-acrylate in the monomer feed. Fluorescein *O*-acrylate was dissolved in PBS (pH 7.0) containing 10 % DMSO and incubated for one day before use.

### 2.3. Nanogel characterization

#### 2.3.1. Dynamic light scattering (DLS)

The Z-average mean hydrodynamic diameter ( $d_H$ ) and polydispersity index (PDI) of trehalose-releasing nanogels in DMEM and in DMEM +10 % FBS (1.0 mg/mL) were determined by Dynamic Light Scattering (DLS) (Malvern, Zetasizer Nano 90S) equipped with a 4 mV He-Ne ion laser ( $\lambda = 633$  nm) as the light source at a scattering angle of 90°. All samples were diluted from stock (10 mg/mL, prepared with sonication at 40 % amplitude for 30 s) to the desired media (1.0 mg/mL) without further co-sonication. The dispersant setting for DMEM and DMEM +10 % FBS was set manually according to the literature [40]. The viscosity of DMEM and DMEM +10 % FBS was set at 1.03 and 1.05 cP, respectively. The zeta potential ( $\zeta$ -potential) of trehalose-releasing nanogels was measured by Electrophoretic Light Scattering (ELS) measurement (Malvern, Zetasizer Nano ZC) in 1 mM KCl solution.

#### 2.3.2. Cryogenic transmission electron microscopy (cryo-TEM)

Nanogels at a concentration of 500  $\mu$ g/mL in DI water were observed under cryo-TEM using a Tecnai F20 X TWIN microscope (FEI Company, Hillsboro, Oregon, USA) equipped with field emission gun, operating at an acceleration voltage of 200 kV. Images were recorded with a Gatan Rio 16 CMOS 4 k camera (Gatan Inc., Pleasanton, California, USA) and processed with Gatan Microscopy Suite (GMS) software (Gatan Inc., Pleasanton, California, USA). Specimens were prepared via the vitrification of aqueous solutions on grids with holey carbon film (Quantifoil R 2/2; Quantifoil Micro Tools GmbH, Großlobbichau, Germany). Prior to use, the grids were activated for 15 s in oxygen plasma using a Femto plasma cleaner (Diener Electronic, Ebhausen, Germany). Cryo-TEM samples were prepared by applying a droplet (3  $\mu$ L) of the dispersion to the grid, blotting with filter paper and immediately freezing in liquid ethane using a fully automated blotting device (Vitrobot Mark IV, Thermo Fisher Scientific, Waltham, Massachusetts, USA). Once prepared, the vitrified specimens were kept under liquid nitrogen until they were inserted into a cryo-TEM holder (Gatan 626, Gatan Inc., Pleasanton, USA) and analyzed in the TEM at –178 °C.

#### 2.3.3. Viscosity and density measurements of trehalose-releasing nanogels

Nanogels at concentration of 1.0 mg/mL were dispersed in normal saline solution (0.90 % w/v of NaCl) and their dynamic viscosity, kinematic viscosity, and density were measured using automatic viscometer SVM3001 (Anton Paar GmbH, Austria). Samples were loaded using XSample™ 600 (5 mL per loading) and the temperature was conditioned using XSample™ heating controller to reach 37 °C prior to

measurement.

#### 2.3.4. Trehalose release study by <sup>1</sup>H NMR spectroscopy

PBS (pH 7.4) in D<sub>2</sub>O containing 1 % v/v antibiotic antimycotic solution (1 mL) was added to pre-weighed nanogel lyophilizate (10 mg), left for 15 min to swell, cooled in an ice bath and sonicated for 30 s to disperse the nanogel (10 mg/mL). Then, 700  $\mu$ L of the nanogel dispersion was transferred to an NMR tube and the <sup>1</sup>H NMR spectrum was recorded (0 h). Afterwards, the NMR tube was placed in an incubator at 37 °C under continuous shaking (250 rpm), and at prescribed time intervals (24, 72 and 168 h) the tube was withdrawn to acquire an <sup>1</sup>H NMR spectrum. Finally, trehalose was fully cleaved from nanogels by treating the dispersion directly in the NMR tube with 70  $\mu$ L of 1 M NaOD at 70 °C for 1 h. The dispersion was then cooled to room temperature and, following complete release of trehalose, the <sup>1</sup>H NMR spectrum was recorded.

#### 2.3.5. Determination of conjugated trehalose (CTre)

Trehalose content in nanogels was determined after complete alkaline hydrolysis of the ester bond in trehalose acrylate units. Briefly, 300  $\mu$ L of nanogel dispersion at a concentration of 100  $\mu$ g/mL in PBS (pH 7.4) was treated with 30  $\mu$ L of 1 M NaOH and incubated at 70 °C for 1 h. Then, 30  $\mu$ L of 1 M HCl was added for neutralization and the resulting mixture was subjected to enzymatic determination of trehalose based on a standard curve. Trehalose was determined enzymatically using Trehalose Assay Kit in microplate assay procedure. According to procedure, trehalose was hydrolysed to D-glucose by trehalase, then released D-glucose was phosphorylated by hexokinase and adenosine-5'-triphosphate (ATP) to glucose-6-phosphate, which was oxidized by nicotinamide-adenine dinucleotide phosphate (NADP<sup>+</sup>) to gluconate-6-phosphate with the formation of reduced nicotinamideadenine dinucleotide phosphate (NADPH). The amount of NADPH formed in this reaction was measured by the increase in absorbance at 340 nm. The absorbance was recorded using microplate absorbance reader. Each determination was made in triplicate. CTre (% w/w) was expressed as a fraction of the percentage of weight of trehalose in nanogel vs weight of nanogel.

#### 2.3.6. Trehalose release study by enzymatic determination

Lyophilized nanogel powders (10.0 mg) were immersed in 1.0 mL of DI water for 15 min before sonication at 40 % of amplitude for 30 s, providing a stock of dispersed nanogels at a concentration of 10 mg/mL. Then, the stock dispersion was diluted to a final concentration of 100  $\mu$ g/mL (16 mL) in PBS (pH 7.4) containing 1 % v/v antibiotic antimycotic solution in a 20-mL glass vial. The dispersion was then placed in an incubator at 37 °C under continuous shaking (250 rpm). Aliquots (800  $\mu$ L) were withdrawn at pre-determined time intervals (0, 12, 24, 36, 48, 60, 72, 84, 96, 108, 120, and 168 h) and frozen at –20 °C. Following collection of the samples, all samples were thawed and released trehalose was determined enzymatically based on a standard curve using Trehalose Assay Kit according to procedure described above in Section 2.3.5. Note: enzymatic assay was used to quantify the amount of trehalose liberated into the media. Trehalose, which is still covalently bound to the nanogel network is not hydrolysed by the trehalase enzyme and thus is not determined in the test.

#### 2.3.7. Stability of trehalose-releasing nanogels in various media

Colloidal stability of nanogels at concentration of 1.0 mg/mL containing 1 % v/v antibiotic antimycotic solution was tested in different media, including DI water, PBS (pH 7.4), D5NS, DMEM +10 % FBS, RPMI +10 % FBS, and primary cell medium (low serum) for 0, 2, 6, 24, 48, and 72 h (37 °C) by measuring optical density (OD) at 650 nm in 96-well plates using a microplate reader.

## 2.4. Cell culture and in vitro study

### 2.4.1. Cytotoxicity study

The cytotoxicity of trehalose-releasing nanogels was assessed using a standard CCK-8 assay. HUVECs ( $5 \times 10^3$  cells/well) were seeded in 96-well plates in 100  $\mu$ L of primary cell medium and then cultured with stable trehalose-releasing nanogels at various concentrations (0, 100, 250, 500, and 1000  $\mu$ g/mL) for 24 h. Thereafter, 10  $\mu$ L of CCK-8 was added and incubated for 2 h. The absorbance was measured by a microplate reader at 450 nm. The relative cell viability (%) was expressed as a fraction of percentage of cell growth occurring in the presence of nanogel vs the absence of nanogel (control).

### 2.4.2. In vitro cell uptake

The nanogel uptake was evaluated in HUVECs by confocal laser scanning microscopy (CLSM, Olympus FluoView FV1000, ZEISS, USA). Cells were seeded in 6-well plates at the density of  $1 \times 10^5$  cells/well in 2 mL of primary cell medium and incubated at 37 °C for 24 h. Next, the culture media was replaced with fresh media containing TNG7-AM or TNG9-AM (500  $\mu$ g/mL) in each well and observed under CLSM at 3 h of co-culture.

### 2.4.3. Hemolysis study

Two selected nanogels (TNG7-AM and TNG9-AM) were tested for their hemolytic properties. Anonymous blood samples were used in the hemolysis assay. Blood was collected from healthy volunteers at the Clinical Laboratory Analysis of Faculty of Pharmacy (University of Coimbra, Portugal). A written informed consent was obtained from all participants. The hemolysis assay was performed according to the literature (NCL Method ITA-1) [41].

Whole blood was collected in heparinized tubes and diluted with  $1 \times$  PBS to obtain final concentration of total blood hemoglobin (TBHd) of 10 mg/mL  $\pm$  2 mg/mL. Then, a volume of 100  $\mu$ L of different concentrations (100, 250, 500, 1000, and 2000  $\mu$ g/mL) of TNG7-AM and TNG9-AM,  $1 \times$  PBS (negative control), Triton-X-100 (positive control), and PFH (plasma free hemoglobin) were added to PBS (700  $\mu$ L) in different tubes. Then, 100  $\mu$ L of TBHd was added and incubated at 37 °C for 3 h  $\pm$  15 min. To evaluate sample interference in hemolysis assay, trehalose-releasing nanogels at different concentrations (without TBHd addition) were prepared and incubated at the same time and condition to normalize the absorbance value and avoid false positive results. Then, the mixture was centrifuged at 800  $\times$ g for 15 min. In the final step, 100  $\mu$ L of supernatant from each repetition tube and 100  $\mu$ L of cyanmethemoglobin (CMH) reagent were added to a 96-well plate and shaken gently before reading. The CMH reagent was prepared by mixing 1000 mL Drabkin's reagent and 0.5 mL of 30 % Brij 35 solution. The absorbance was read at 540 nm. The percentage of hemolysis was calculated by the following equation:

$$\text{Hemolysis (\%)} = \frac{\text{Test sample OD540} - \text{Negative control OD540}}{\text{Positive control OD540} - \text{Negative control OD540}} \times 100$$

## 2.5. In vivo autophagy stimulation study

### 2.5.1. Zebrafish husbandry

Wild type (AB) and Tg(CMV:GFP-Lc3) [42] transgenic zebrafish used in this study were maintained and bred in the fish facility of ELTE Eötvös Loránd University according to standard protocols [43,44].

### 2.5.2. Trehalose-releasing nanogels treatment and sample preparation for microscopy

TNG7-AM or TNG9-AM were dispersed in distilled water to create 5 mg/mL stock solutions. At 1 day post fertilization (dpf), zebrafish embryos born from an AB  $\times$  Tg(CMV:GFP-Lc3) cross were dechorionated and transferred into E3 medium with a final concentration of 500  $\mu$ g/mL of TNG7-AM or TNG9-AM, respectively. (For controls, a similar volume

of distilled water was added to the medium). Until larvae reached 5 dpf, they were raised under standard conditions in an incubator. At that time, the transgenic larvae were immobilized using 0.16 mg/mL tricaine methanesulfonate (Sigma Aldrich).

The 3xmCherry-Atg8a [45] and GFP-Ref (2)P/GFP-p62 [46,47] *Drosophila* lines were provided by Gábor Juhász. During treatment, flies were kept at 25 °C on a dried food medium (Ready Mix Food for *Drosophila* - Philip Harris, B8A03876). At 0–4 h old, synchronized embryos were collected and transferred to medium, which either contained TNG7-AM (final concentration: 500  $\mu$ g/mL – dispersed in distilled water) or was only supplemented with the same volume of water, for controls. At 90–94 h old (continuously treated) L3 feeding larvae were dissected for fluorescent microscopy. Nuclei of fat bodies were stained with Hoechst (0.1 mg/mL, Molecular Probes, 33,342) and 13.5  $\mu$ L cover solution (4:1 – glycerol:PBS) was applied.

### 2.5.3. Fluorescence microscopy

Zebrafish larvae were immobilized using 4 % methyl cellulose (Sigma Aldrich, M7140) and imaged under a Zeiss SteREO Lumar.V12 microscope equipped with a NeoLumar S 0.8 $\times$  objective and a COOLLED pE-300lite light source.

Fluorescent images of *Drosophila* samples were captured with a Zeiss Axioimager Z2 upright microscope (with objective Plan-Neofluar 40 $\times$  0.75 NA) equipped with ApoTome. AxioVision 4.82 and Image J 1.52c software [48] were used to examine and evaluate data.

### 2.5.4. Western blotting

Western blot samples were prepared from 40 zebrafish larvae (5 dpf) per sample. Larvae were washed in 200  $\mu$ L distilled water and homogenized using 200  $\mu$ L 2 $\times$  Laemmli Sample Buffer (Bio-Rad, 161–0737). 15  $\mu$ L samples were run on 4–20 % Mini-PROTEAN® TGX™ Gel. After blocking with 3 % Milk Powder (Blotting-Grade Blocker, Bio-Rad 170–6404), samples were dissolved in TBST, membranes were probed with anti-SQSTM1/p62 (1:1000, rabbit, Cell Signaling Technology, 5114), anti-GAPDH (rabbit, 1:5000; Sigma Aldrich, G9545), anti-rabbit IgG alkaline phosphatase (1:1000, Sigma Aldrich, A3687) antibodies, and developed by NBT-BCIP solution (Sigma Aldrich, 72,091).

## 2.6. Statistical analysis

General characterization and in vitro study: data obtained were reported as the mean  $\pm$  SD ( $n = 3$ ). GraphPad Prism Version 6.0 software (GraphPad, USA) was used for the statistical analysis. One-way analysis of variance (ANOVA) by Tukey's test was used to reveal differences among the groups. Unpaired *t*-test (two tails) was employed to see if there is a significant difference between two groups. The difference significance levels were set at \* $p < 0.05$ , \*\* $p < 0.01$ , \*\*\* $p < 0.001$ , \*\*\*\* $p < 0.0001$ , and <sup>ns</sup> $p > 0.05$ .

In vivo study in zebrafish and *Drosophila*: For statistical analysis of fluorescence microscopy, results were determined using R Studio (Version 3.4.3) [49]. The distribution of samples (to decide normal or not) was tested with Lilliefors-test. If the distribution was normal, an *F*-test was performed to compare variances. In cases where variances were equal, a one-sample *t*-test was conducted (every sample had normal distribution and equal variances). The levels of significance were indicated as follows: \* $p < 0.05$ , \*\* $p < 0.01$ , \*\*\* $p < 0.001$  and <sup>ns</sup> $p > 0.05$ . Plots were created using the *ggplot2* package [50].

## 3. Results and discussions

### 3.1. Synthesis and characterization of trehalose-releasing nanogels

There are many ways in which nanogels can be synthesized, including physical self-assembly, homo- or heterogeneous polymerization of monomers in the presence of a crosslinker, cross-linking of pre-fabricated polymers, and template-assisted nanofabrication of nanogel

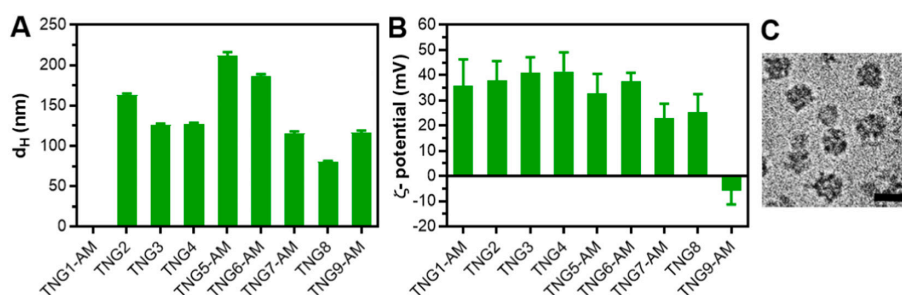


**Fig. 3.** (A) Z-average hydrodynamic diameter ( $d_H$ ) of trehalose-releasing nanogels in DMEM. Data are presented as mean  $\pm$  SD ( $n = 3$ ). (B)  $\zeta$ -potential of trehalose-releasing nanogels in 1 mM KCl. Data are presented as mean  $\pm$  SD ( $n = 3$ ). SD for  $\zeta$ -potential was directly obtained from the instrument. (C) Cryo-TEM image of TNG7-AM. Scale bar = 50 nm.

particles [51]. Variation in the synthesis method as well as variation in the choice of specific monomers allows customization of nanogel structure and contributes to a wide range of nanogel properties. Herein, carefully selected monomers were chosen to fabricate a variety of trehalose-releasing nanogels in which TreA units are distributed within a crosslinked acrylamide-type polymer network. Incorporation of trehalose in this way yields nanogels that can potentially be used as trehalose delivery systems from which trehalose is released at pH > 7.0 due to the sustained cleavage of ester bonds.

A series of nine trehalose-releasing nanogels with different compositions (Table 1) were synthesized via FRP in w/o miniemulsions. Fig. 1 shows the monomer structures and synthetic procedures used to construct the respective nanogels. The monomer composition was carefully selected in the subsequent preliminary experiments by focusing on yield, stability, trehalose release profile, hydrodynamic size and distribution, and cytotoxicity. In all cases a cyclohexane/Span 80 system was used as a continuous phase, while PBS solution (pH 6.0) containing monomers (TreA, AM, AMPTMAC), crosslinker (MBAM), and photoinitiator (LAP) was used as an aqueous phase. Polymerizations were accomplished under LED irradiation at room temperature for 30 min with yields in the range of 54–91 %, depending on composition. For a series of five nanogels containing AM, the notation TNGx-AM was utilized, while for the four nanogels that did not include AM, the notation TNGx was adopted (Table 1). The amount of trehalose incorporated into the nanogels was determined enzymatically after pretreating nanogels with strong alkali and is presented in Table 1 as CTre (% w/w). Under these conditions all trehalose is cleaved into solution, as confirmed by <sup>1</sup>H NMR spectroscopy (Fig. 6C); specifically, in the range of trehalose signals (3.25–5.10 ppm), only sharp signals characteristic of free trehalose are present rather than the broad signals characteristic of trehalose bound to the nanogel matrix (Fig. 6B). It was possible to obtain

nanogels containing up to 59 % w/w of trehalose with reasonable yield. Increasing the trehalose feed in the formulations (from ~15 % w/w to ~65 % w/w) correlated well with the amount of incorporated trehalose, (CTre from ~14 % w/w to ~59 % w/w, Table 1, Fig. S2).

The size of trehalose nanogels in DMEM, which was chosen as a commonly utilized biological medium, was determined via DLS and expressed as the Z-average hydrodynamic diameter ( $d_H$ ). These results are presented in Fig. 3A and Table 1. In the absence of serum, eight nanogels were well-dispersed and showed a range of  $d_H$  between 81 and 213 nm with a relatively narrow PDI (~0.2). Measurement of  $d_H$  for TNG1-AM was not possible due to its rapid aggregation in DMEM. TNG8 showed the smallest  $d_H$  compared to other formulations, which was around 81 nm. Meanwhile, TNG7-AM and TNG9-AM showed a relatively similar  $d_H$  values, which were about 115 nm. Cryo-TEM observation revealed that TNG7-AM had a uniformly spherical shape with a small diameter  $d_{TEM} < 50$  nm (Fig. 3C). In general, the trehalose-releasing nanogels fabricated under these conditions were in the desired range for long-circulating nanocarriers (70–200 nm) [35].

The nanogels demonstrated  $\zeta$ -potentials in the range of -5.7 to +41.5 mV as determined by ELS (Table 1, Fig. 3B), with the highest positive value for TNG4 (+41.5 mV) and the lowest positive value for TNG7-AM (+22.8 mV). The lack of correlation between AMPTMAC content in the initial feed and the  $\zeta$ -potential of positively charged nanogels may indicate that the final monomeric composition of nanogels differed from that in the original formulations. The overall positive surface charge of TNG1–8 nanogels was ensured by the permanent quaternary ammonium cations in the AMPTMAC units. These nanogels, however, also contained some negative charge due to the presence of carboxylate anions from the residual photoinitiator moieties. These residual moieties are responsible for the negative  $\zeta$ -potential of TNG9-AM, in which AMPTMAC units are absent. The TNG9-AM nanogel was

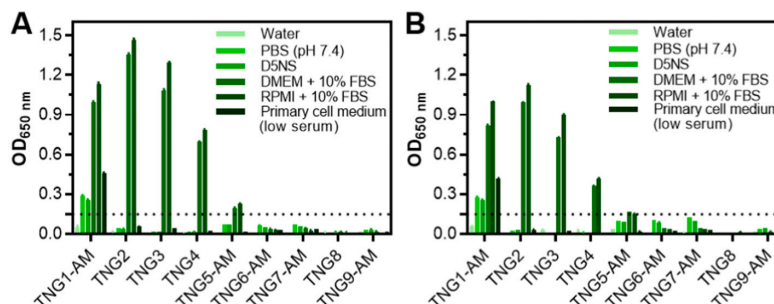


**Fig. 4.** Stability of trehalose-releasing nanogels in different media at physiological temperature (37 °C). Nanogels were incubated in DI water, PBS (pH 7.4), D5NS, DMEM+10 % FBS, RPMI+10 % FBS, and primary cell medium (low serum) at concentration of 1000  $\mu$ g/mL for (A) 0 h and (B) 72 h. Data are presented as mean  $\pm$  SD ( $n = 3$ ).

synthesized to explore the influence of a negative surface charge on the stability of nanogel dispersions in physiological conditions, cell uptake, and cytotoxicity relative to positively charged analogues.

$\zeta$ -potential is frequently used as an initial indication of the colloidal stability. The colloidal stability of nanotherapeutics in biological media is crucial for nanocarriers intended for injection. Stability in saline media is a prerequisite for in vitro study and in preparation for intravenous injection (in normal saline or D5NS solution). Dispersion in biological solution often causes the aggregation of nanoparticles, impacting cellular uptake and the toxicity profile of nanoparticles. In most cases, the in-situ formation of aggregates following the intravenous administration of nanotherapeutics will lead to rapid clearance in the liver and RES, thereby limiting the probability that the nanoparticles reach their therapeutic targets [52]. According to the common guidelines in drug delivery literature, colloidal stability increases with increasing  $\zeta$ -potential due to the stabilizing effect of the electrostatic repulsive forces in nanoparticles containing like-charged ions. Generally, nanoparticles with absolute value of  $\zeta$ -potential >30 mV, 30–20 mV, 20–10 mV and 10–0 mV are considered as highly stable, moderately stable, relatively stable and highly unstable, respectively. However,  $\zeta$ -potential is only one factor that contributes to colloidal stability - steric interactions and van der Waals forces also consider strongly in colloidal stability [53].

Figs. 4 and S3 present data on the colloidal stability of the trehalose nanogels at 37 °C over time in six different media, i.e., DI water, PBS (pH 7.4), D5NS, DMEM+10 % FBS, RPMI+10 % FBS, and primary cell medium with low serum content. The colloidal stability was evaluated by visual observation and quantified based on the measurement of OD at 650 nm, with the assumption that values above 0.15 OD indicate aggregation. All of the nanogels formed stable colloids in DI water, but significant differences became apparent when comparing their stability in other media (Fig. 4, Fig. S3A-D). In solutions of high ionic strength, the repulsive forces that typically stabilize nanogel dispersion can be reduced due to the screening of electrostatic interactions. These conditions may result in the collapse of the colloidal system. This circumstance is reflected in the results for nanogel TNG1-AM, the only nanogel that was not stable and aggregated at high ionic strength (in PBS pH 7.4 and D5NS). TNG1-AM was also the only nanogel that aggregated in low serum content primary cell medium. The formulation for nanogel TNG2 contained the same amount of AMPTMAC as that for TNG1-AM, but it differed in the content of AM and TreA units. TNG1-AM and TNG2 also had similar  $\zeta$ -potential. The fact that TNG2 is stable in these three media indicates that either increased TreA or decreased AM content strongly improves colloidal stability. The most prominent differences in stability were observed in high serum content (10 % FBS) DMEM and RPMI. In these conditions nanogel TNG1–4 readily aggregates, nanogel TNG5 is characterized by moderate stability, and nanogel TNG6–9 formed highly stable and long-lasting (at least 3 days, Fig. 4B) dispersions. The stability in these media seems to strongly depend on the AMPTMAC content. It is particularly noticeable when comparing nanogels TNG4–6, which are characterized by similar trehalose content; the successive decrease in stability with increasing AMPTMAC content in serum-containing medium reflects a destabilization effect related to a high content of the cationic moiety. It is also very likely that a positive effect on colloidal stability was mediated by trehalose. Nanogels TNG5-AM and TNG-8 were synthesized with similar AMPTMAC content, but only TNG-8, which contained approximately 10 % more trehalose, was stable in all the tested media. Similar beneficial effects of trehalose-containing glycopolymers on the colloidal stability of polyplexes in culture media have been hypothesized by Reineke, et al. [21,54]. It is likely that the hydrophilic nature of trehalose-decorated nanoparticles may be a factor influencing colloidal stability, reflecting a stabilization mechanism based on short-range repulsive hydration forces [52].

The colloidal stability of nanoparticles in serum-containing media is also influenced by interaction with serum proteins that could induce a protein corona formation [55,56]. The formation of a protein corona

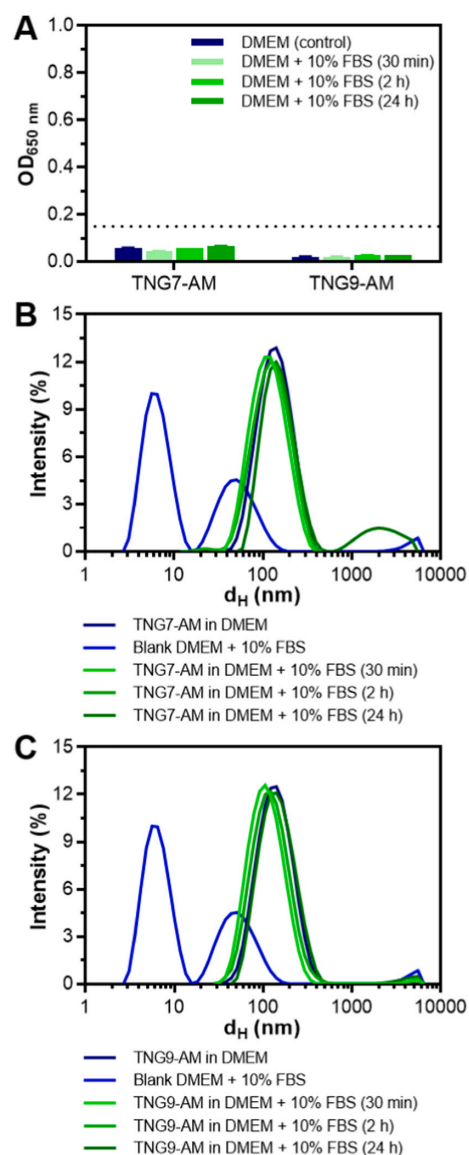
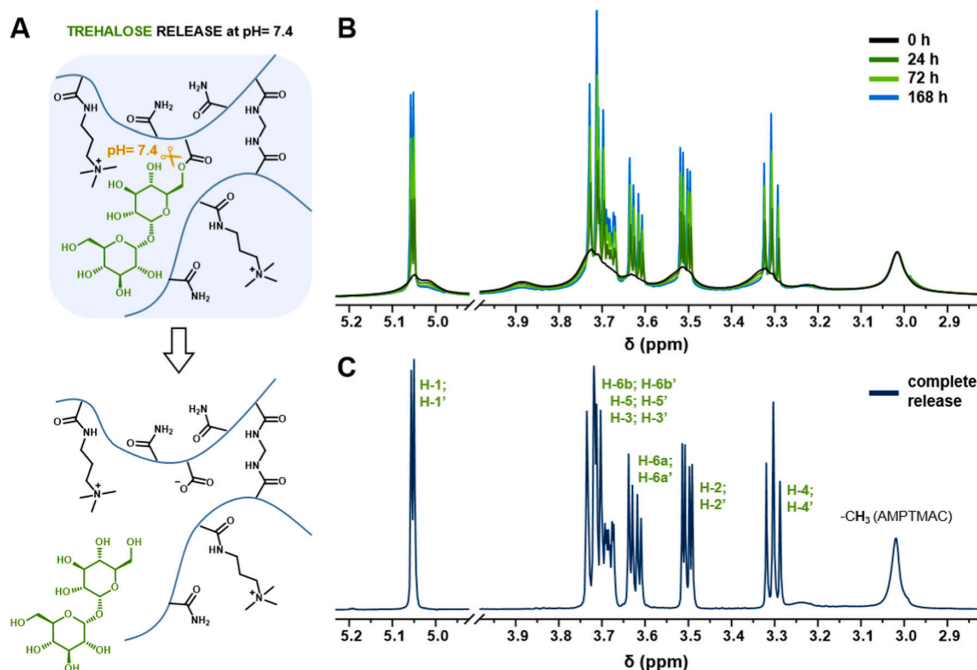


Fig. 5. Stability of TNG7-AM and TNG9-AM nanogels in DMEM containing 10 % FBS at concentration of 1000 µg/mL within 30 min, 2 h, and 24 h (37 °C) based on (A) OD readout at 650 nm and (B, C) DLS.

typically reduces the stability of nanoparticles and enhances clearance by the reticuloendothelial system (RES). Our experiments on nanogel dispersions TNG7-AM and TNG9-AM in DMEM containing 10 % FBS demonstrated that interactions with serum proteins was highly probable (Fig. 5). First, no colloid aggregation was detected (Fig. 5A). Moreover, in DLS data, we observed the disappearance of a small peak corresponding to serum proteins and there was no significant shift in the nanogel peak in DMEM containing 10 % FBS (as compared to DLS data of DMEM containing 10 % FBS and DLS data of nanogels in DMEM without FBS, respectively) suggesting that serum proteins are interacting with the particle surface (Fig. 5B,C). Furthermore, the results of DLS analysis after 2 h and 24 h of incubation demonstrated that the size of particles remained essentially unchanged, indicating that no





**Fig. 6.** Trehalose release from TNG7-AM (10 mg/mL) evidenced by  $^1\text{H}$  NMR spectroscopy. (A) Schematic presentation of trehalose release from the nanogel network via the hydrolytic cleavage of the ester bond at pH 7.4. (B) Section of  $^1\text{H}$  NMR spectra of TNG7-AM before and during the release of trehalose at pH 7.4, 37 °C. All spectra are normalized to the signal at 3.0 ppm corresponding to  $-\text{CH}_3$  protons from AMPTMAC units. (C) Section of  $^1\text{H}$  NMR spectrum of TNG7-AM after complete release of trehalose achieved by the treatment of TNG7-AM with 1 M NaOH at 70 °C for 1 h.

aggregation occurred over time. Surprisingly, it did not matter whether the nanogels are positively or negatively charged, as both TNG7-AM and TNG9-AM exhibited similar behavior. These two nanogels were selected as the most promising for *in vivo* assays. Additional measurement of viscosity and density of nanogel dispersions: TNG7-AM and TNG9-AM in normal saline solution (37 °C, nanogel concentration 1.0 mg/mL) showed similar dynamic viscosity, kinematic viscosity, and density in comparison to normal saline solution (0.71 cP, 0.71 cSt, and 1.00 g/mL for nanogels, and 0.69 cP, 0.69 cSt, and 1.00 g/mL for normal saline) (Table S2). This indicates that the nanogels could be suitable for intravenous injection.

### 3.2. Trehalose release

The nanogels were designed to include covalently attached trehalose that can be liberated via the hydrolysis of an ester bond (Fig. 6A). The ester bond in acrylate units is rather resistant to hydrolysis at physiologically relevant temperatures. This hydrolysis, however, can be substantially accelerated by the incorporation of primary or secondary acrylamide-type comonomers within the hydrogel network, as we have shown recently [38,39].

The successful and sustained release of trehalose from the nanogels at pH 7.4, 37 °C is well reflected in  $^1\text{H}$  NMR spectra (Fig. 6B). The intensity of sharp peaks corresponding to protons of free trehalose increased with increasing incubation time, while the broad peaks originating from protons of trehalose still bound to the nanogel network decreased.

The accurate release of trehalose at pH 7.4, 37 °C was followed by enzymatic determination of trehalose concentrations, and the release profiles are shown in Fig. 7A-C. Data are presented in terms of both percentage and concentration ( $\mu\text{g}/\text{mL}$ ). These two types of analysis allow observation of different aspects of trehalose release. Specifically,

release presented as a percentage allows comparison of the release rates, while release presented as a concentration provides information about the nanogel's performance in the context of the amount of released trehalose. Although, the smallest amount of trehalose was released from nanogel TNG1-AM, which has the lowest content of trehalose, the relative level of trehalose in the nanogel was not generally predictive of the relative level of trehalose release (Fig. 2, Fig. 7B). For example, TNG6-AM demonstrated the highest level of trehalose release but is characterized by a moderate trehalose content. This behavior is the consequence of the strong influence of an acrylamide-type comonomer on the hydrolysis. Further analysis revealed that both the content and the structure of the acrylamide-type comonomer significantly influence its impact on hydrolysis. Examining nanogels TNG4-6 containing similar amounts of conjugated trehalose, it is clear that the release rate, and thus the amount of released trehalose, is increasing in a manner that correlates with the ratio of AM to AMPTMAC that is incorporated into the matrix. This results from the fact that primary amides accelerate the hydrolysis more effectively than secondary amides [39]. Therefore when ratio of AM (primary amide) to AMPTMAC (secondary amide) increases, the hydrolysis of ester bond and thus trehalose release increases, which can be seen in the series TNG4, TNG5-AM, and TNG6-AM (Fig. 2, Fig. 7A). Another clear correlation is observed in the series of nanogels that contain only AMPTMAC and trehalose, and do not contain AM. In the series TNG2, TNG3 and TNG4 content of AMPTMAC decreases, while content of trehalose increases. Trehalose release is the lowest in TNG4 containing the highest trehalose content, and trehalose release is the highest in TNG2 containing the highest amount of AMPTMAC in the series, although trehalose content is the lowest. The general conclusion is that the lower the percentage of acrylamide-type units in the polymeric network, the more slowly trehalose is released.

An important observation was made by comparing trehalose release at different nanogel concentrations for two selected nanogels: TNG4 and

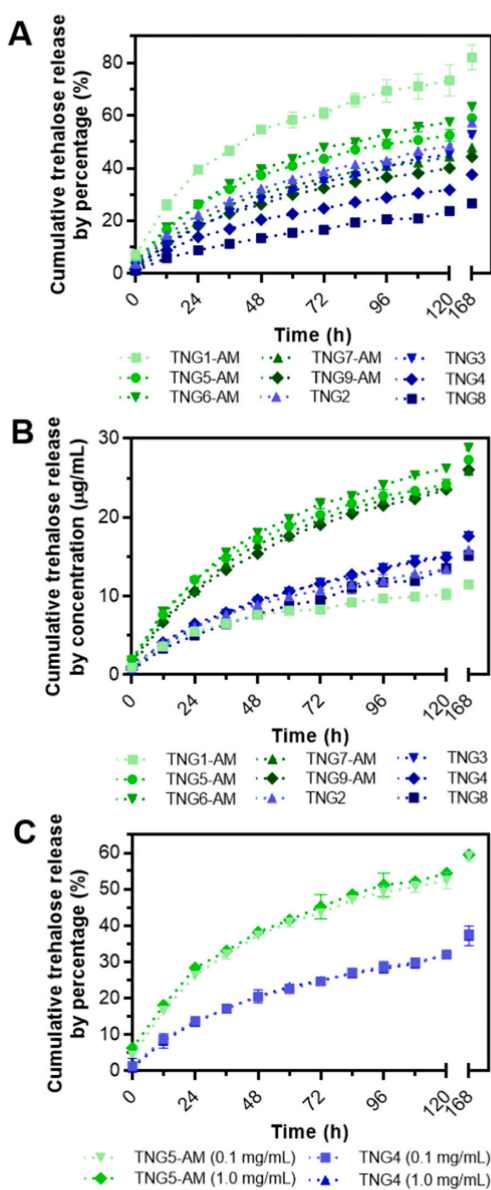


Fig. 7. Profiles of trehalose release from trehalose-containing nanogels. Cumulative trehalose release by (A) percentage and (B) concentration in PBS (pH 7.4, 37 °C, nanogels concentration = 100 µg/mL). (C) Comparison of cumulative trehalose release by percentage of TNG4 and TNG5-AM at low concentration (100 µg/mL) and high concentration (1000 µg/mL) in PBS (pH 7.4, 37 °C). Data are presented as mean ± SD (n = 3).

TNG5-AM. The release profile by percentage and by concentration for these nanogels is presented in Fig. 7C and Fig. S4A, B, respectively. The amount of released trehalose is proportional to the nanogel concentration (e.g., 11.53 µg/mL and 119.35 µg/mL after 72 h for TNG4 = 100 and 1000 µg/mL, respectively) (Fig. S4A, B), but the release rate is not concentration-dependent (Fig. 7C). This property is highly desirable for identifying the best dosage for further treatment.

### 3.3. Cytotoxicity, hemocompatibility, and cell uptake

The main purpose of this study was to prepare non-cytotoxic nanogels which maintain colloidal stability under cell culture conditions, exhibit high and sustainable trehalose release, and contain the positive surface charge required to utilize AMT for traversing the BBB. It has been shown that nanoparticles with high ζ-potential (high positive charge) cause immediate toxicity to the BBB [32]. Taking this into account, only a nanogel exhibiting a moderate positive charge could potentially be utilized for in vivo studies. In addition, most of the studies performed to date that utilize stroke, AD, or PD animal models have used nanoparticles with diameters between 50 nm to 100 nm [33]. Ultimately, it is challenging to fabricate a single nanogel that will meet all these requirements and a reasonable compromise should be considered. The diversity of specific properties of the nanogels was visualized by spider graphs with a scale from 0 to 5, with 5 being the most desirable (Fig. 8, Table S3). It can be clearly seen that nanogels TNG1–5 (Fig. 8A) perform poorly compared to nanogels TNG6–9 (Fig. 8B) mainly due to the lack of stability in serum-enriched media and a high ζ-potential. These properties scored highly for cationic TNG7-AM and anionic TNG9-AM, the latter serving as a non-AMPTMAC-containing nanogel. Moreover, these two nanogels contain the highest amount of CTre and reasonable trehalose release rate.

Non-cytotoxic trehalose-releasing nanogels that possess high hemocompatibility can be safely administered in vivo. Here, we used primary HUVECs as model endothelial cells for studying the in vitro cytotoxicity of nanoparticles, particularly those intended for parenteral delivery [57].

Four nanogels (TNG6–9), which have a reduced AMPTMAC content, were used in cell viability studies. Three independent assays demonstrated that HUVECs show excellent viability with nanogel concentrations of up to 1.0 mg/mL (Fig. 9, Fig. S5). Interestingly, some of the nanogels induce cell proliferation in the range of 100–500 µg/mL. This effect might be related to trehalose release from nanogels, since free trehalose shows some positive impact on cell viability (Fig. 9). TNG5-AM, which represents the transition of unstable nanogels to stable nanogels (Fig. 4A, B), demonstrated dose-dependent cytotoxicity to HUVECs - its high doses (500 and 1000 µg/mL) reduced cell viability by >25 % (Fig. 9, Fig. S5A, B). Unexpectedly, while TNG5-AM nanogel contains 3.2 % w/w less AMPTMAC monomer relative to TNG8 nanogel, it contains relatively high amount of AM monomer (15.6 % w/w), it demonstrates lower CTre (by ~10.6 % w/w), and a 2.6-fold larger hydrodynamic size than TNG8 (Table 1, Fig. 2, 3A), which might also influence its cytotoxicity profile in high doses.

For hemolysis and cell uptake assays, only two oppositely charged nanogels were studied: TNG7-AM and TNG-9-AM.

To evaluate the hemocompatibility of trehalose-rich nanogels, we utilized a hemolysis assay as an indicator of hemoglobin release induced by disruption of RBC membranes. The evaluation of hemolytic activity is a prerequisite for any medication that will contact blood, and the potential for erythrocyte lysis is important to understand while considering in vivo applications of nanogel formulations. The American Society for Testing and Materials (ASTM) has prescribed that <5 % hemolysis is considered non-hemolytic [58]. As seen in Fig. 10 and Fig. S6, neither of the nanogels selected for the study induced hemolysis at concentrations of up to 2.0 mg/mL. The fluorescently labelled nanogels synthesized for cellular uptake analysis demonstrated similar behavior (Fig. S7).

Last but not least, the small size of the nanogels should ensure the cellular uptake and intracellular delivery of nanogels facilitated by receptor-mediated endocytosis [59]. To investigate cellular uptake, we incorporated fluorescein O-acrylate within the nanogel network, yielding fluorescence properties with an excitation maximum and emission maximum at 491 nm and 519 nm, respectively (Fig. S8). Upon incubation with HUVECs (3 h, 37 °C), FITC-TNG7-AM could be taken up by the cells as observed under CLSM (Fig. 11). Interestingly, anionic nanogel FITC-TNG9-AM was also efficiently taken up by the cells during

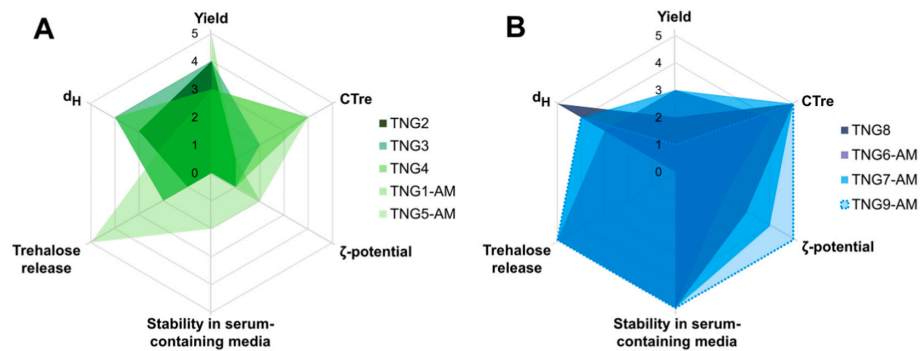


Fig. 8. Spider graphs of (A) unstable and (B) stable nanogels, showing their characteristics in terms of yield, CTre,  $\zeta$ -potential, stability in serum-containing DMEM, trehalose release, and  $d_H$ . Spider graphs were constructed according to the scoring classifications described in Table S3 on a scale from 0 to 5, with 5 being the most desirable.

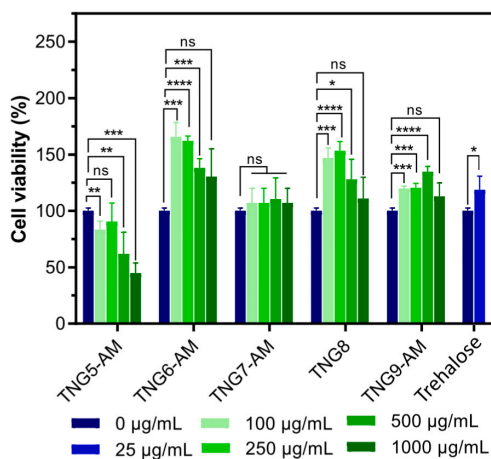


Fig. 9. Cytotoxicity of trehalose-releasing nanogels in HUVECs at different concentrations (0, 100, 250, 500, and 1000  $\mu\text{g/mL}$ ) after 24 h of incubation (37  $^{\circ}\text{C}$ , CCK-8). Data are presented as mean  $\pm$  SD ( $n = 4$ ).

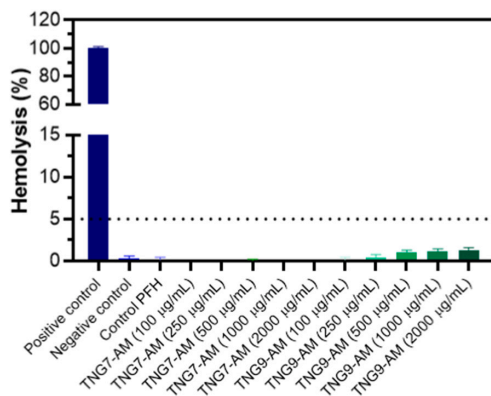


Fig. 10. Hemolytic properties of TNG7-AM and TNG9-AM evaluated at different concentrations (100, 250, 500, 1000, and 2000  $\mu\text{g/mL}$ ) compared to the positive control, negative control, and control PFH (plasma free hemoglobin). Data are presented as mean  $\pm$  SD ( $n = 3$ ).

short incubation (Fig. S9). However, further studies on intracellular delivery routes and endosomal escape need to be conducted to better understand the potential for cytoplasmic delivery of trehalose.

#### 3.4. In vivo autophagy stimulation by trehalose-releasing nanogels

To test whether trehalose-releasing nanogels can induce elevated levels of autophagy in a physiological setting, we tested their effects using two different paradigms. First, using a well-established zebrafish transgenic reporter line [42], we checked if prolonged exposure to trehalose-releasing nanogels has effects on the mortality of animals and/or induces elevated levels of autophagy. During a 4-day-long treatment period (between 1- and 5-days post fertilization – dpf) with 500  $\mu\text{g/mL}$  of TNG7-AM or TNG9-AM, no changes in mortality of transgenic zebrafish larvae could be observed. The treated larvae, however, showed a significant increase in reporter-activity upon exposure to TNG7-AM but not to TNG9-AM (Fig. 12A, B). Furthermore, in larvae treated with TNG7-AM, an increased rate of Sqstm1/p62 degradation could also be observed, marking an increase in autophagic activity [60,61].

To further test the in vivo autophagic-enhancing potential of TNG7-AM, we also raised *Drosophila* larvae on a medium supplemented with the nanogel. After 3 days of continuous exposure, we were able to detect significantly elevated levels of mCherry-Atg8a-positive structures in the fat bodies of transgenic *3xmCherry-Atg8a* larvae (Fig. 12D-F). A similar treatment regime also resulted in a decrease in the abundance of GFP-p62-positive structures in the fat bodies of *GFP-p62* animals (Fig. 12G-I). These results suggest that prolonged exposure to TNG7-AM can result in enhanced autophagic activity in in vivo systems without any detectable toxicity.

#### 4. Conclusion

Trehalose has significant therapeutic potential due to its ability to induce autophagy. In this context, we have synthesized and characterized a series of trehalose-rich nanogels capable of hydrolytic release of covalently bound trehalose in physiological conditions. The primary aim of this study was to fabricate nanogels with the ability to maintain colloidal stability in serum-enriched cell culture media while also exhibiting substantial and sustained release of trehalose. A series of nine nanogels were synthesized, and four of them that contained >50 % w/w of trehalose were also colloiddally stable in several biological media, e.g., D5NS, DMEM +10 % FBS, RPMI +10 % FBS, and primary cell medium. Trehalose appears to have beneficial effects on stability in biological media. The cationic TNG7-AM nanogel was selected as the most promising for brain targeting via an AMT mechanism due to its moderate positive surface charge ( $\zeta$ -potential +22.8 mV) and other favorable

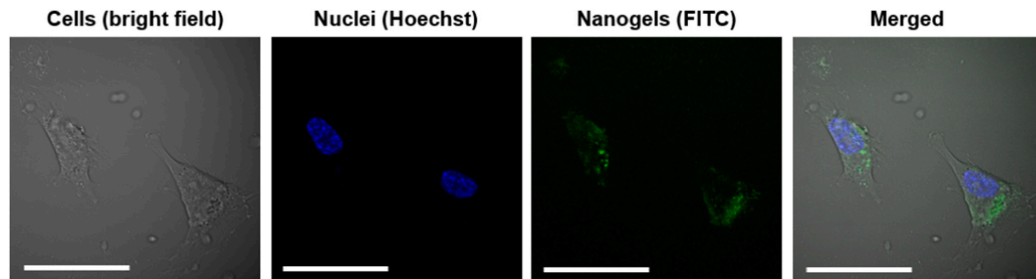


**Fig. 11.** In vitro cell uptake of TNG7-AM by HUVECs observed under CLSM (500 μg/mL, 3 h). Bright field indicates HUVECs, blue color indicates cell nuclei, and green color indicates TNG7-AM (scale bars = 50 μm).

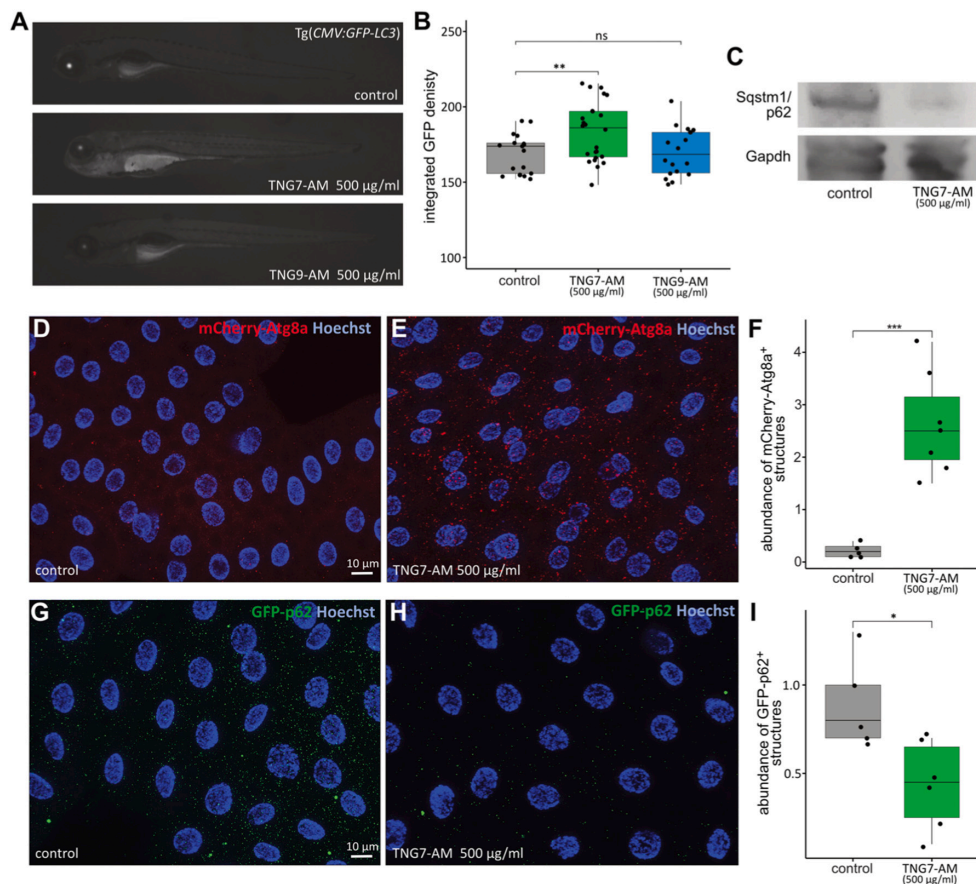


**Fig. 12.** In vivo autophagy-enhancing effects of trehalose-releasing nanogels. (A-B) Transgenic zebrafish larvae of the autophagy-reporter line Tg(CMV:GFP-Lc3) showed significantly enhanced fluorescence after 4 days of treatment with TNG7-AM, but not with TNG9-AM. (C) Zebrafish treated with TNG7-AM also showed a decrease in Sqstm1/p62 accumulation. (D-F) In the fat bodies of *3xmCherry-Atg8a* transgenic *Drosophila* larvae raised on TNG7-AM-containing medium, the number of mCherry-Atg8a-positive structures increases. (G-I) Fat bodies of *GFP-p62* transgenic animals show a marked decrease in the number of GFP-p62-positive structures, as compared with control.

properties, e.g., small size ( $d_H = 115$  nm,  $d_{TEM} < 50$  nm), high trehalose content (53 % w/w), a sustained and non-dose-dependent release of trehalose at pH 7.4 (31 % after 2 days), lack of cytotoxicity against HUVECs, and lack of hemolytic activity toward RBCs. Preliminary in vivo studies on zebrafish and *Drosophila* larvae demonstrated significant induction of autophagic activity in the presence of TNG7-AM nanogel,

making it a promising nanocarrier for gaining further insights into mechanisms for trehalose delivery to the CNS in in vivo models.

**CRedit authorship contribution statement**

Ali Maruf: Investigation, Formal analysis, Visualization, Data

Curation, Writing - original draft preparation.

Małgorzata Milewska: Conceptualization, Methodology, Investigation, Resources, Visualization, Writing - original draft preparation, Writing - Review & Editing,

Tibor Kovács: Methodology, Investigation, Visualization.

Máté Varga: Methodology, Investigation, Resources, Visualization, Writing - original draft preparation.

Tibor Vellai: Resources, Writing - original draft preparation.

Anna Lalik: Methodology, Investigation.

Sebastian Student: Investigation, Data Curation, Visualization.

Olga Borges: Resources, Supervision, Writing - Review & Editing.

Ilona Wandzik: Conceptualization, Methodology, Writing - Original Draft preparation, Writing - Review & Editing, Supervision, Project administration, Funding acquisition.

### Declaration of competing interest

The authors declare that they have no known competing financial interests or personal relationships that could have appeared to influence the work reported in this paper.

### Acknowledgements

This study was co-financed by the PRELUDIUM BIS 1 (2019/35/O/ST5/02746) from the National Science Centre (NCN), Poland. AM would like to acknowledge The Polish National Agency for Academic Exchange (NAWA) under the project no. POWR.03.03.00-IP.08-00-P13/18 for financial support of an internship at the University of Coimbra, Portugal. In vivo studies were part of the ELTE Thematic Excellence Programme 2020 supported by the Hungarian National Research, Development and Innovation Office (TKP2020-IKA-05). This work was supported by the OTKA grants (Hungarian Scientific Research Fund) K109349 and K132439, MEDinPROT Protein Science Research Synergy Program (provided by the Hungarian Academy of Sciences; HAS), the European Union and the State of Hungary, co-financed by the European Regional Development Fund (VEKOP-2.3.2-16-2017-00014). TV was supported by the ELKH/MTA-ELTE Genetics Research Group (01062). The authors would like to thank Anita Rázcz at the ELTE Animal Facility for diligent animal care and Tünde Lestyán MSc student for her help with the experiments.

### Appendix A. Supplementary data

Supplementary data to this article can be found online at <https://doi.org/10.1016/j.bioadv.2022.212969>.

### References

- N.K. Jain, I. Roy, Effect of trehalose on protein structure, *Protein Sci.* 18 (2009) 24–36, <https://doi.org/10.1002/pro.3>.
- K. Hosseinpour-Moghaddam, M. Caraglia, A. Sahebkar, Autophagy induction by trehalose: molecular mechanisms and therapeutic impacts, *J. Cell. Physiol.* 233 (2018) 6524–6543, <https://doi.org/10.1002/jcp.26583>.
- H.J. Lee, Y.S. Yoon, S.J. Lee, Mechanism of neuroprotection by trehalose: controversy surrounding autophagy induction, *Cell Death Dis.* 9 (2018) 712, <https://doi.org/10.1038/s41419-018-0749-9>.
- D.J. Klionsky, G. Petroni, R.K. Amaravadi, E.H. Baehrecke, A. Ballabio, P. Boya, J. Bravo-San Pedro, K. Cadwell, F. Cecconi, A.M.K. Choi, M.E. Choi, C.T. Chu, P. Codogno, M.I. Colombo, A.M. Cuervo, V. Deretic, I. Dikic, Z. Elazar, E. Eskelinen, F. Pietrocola, Autophagy in major human diseases, *EMBO J.* 40 (2021), e108863, <https://doi.org/10.15252/embj.2021108863>.
- M. Khalifeh, G.E. Barreto, A. Sahebkar, Trehalose as a promising therapeutic candidate for the treatment of Parkinson's disease, *Br. J. Pharmacol.* 176 (2019) 1173–1189, <https://doi.org/10.1111/bph.14623>.
- A.B. Pupyshv, M.A. Tikhonova, A.A. Akopyan, M.V. Tenditnik, N.I. Dubrovina, T. A. Korolenko, Therapeutic activation of autophagy by combined treatment with rapamycin and trehalose in a mouse MPTP-induced model of Parkinson's disease, *Pharmacol. Biochem. Behav.* 177 (2019) 1–11, <https://doi.org/10.1016/j.pbb.2018.12.005>.
- K. Tanji, Y. Miki, A. Maruyama, J. Mimura, T. Matsumiya, M. Mori, T. Imaizumi, K. Itoh, K. Wakabayashi, Trehalose intake induces chaperone molecules along with autophagy in a mouse model of Lewy body disease, *Biochem. Biophys. Res. Commun.* 465 (2015) 746–752, <https://doi.org/10.1016/j.bbrc.2015.08.076>.
- J. Du, Y. Liang, F. Xu, B. Sun, Z. Wang, Trehalose rescues Alzheimer's disease phenotypes in APP/PS1 transgenic mice, *J. Pharm. Pharmacol.* 65 (2013) 1753–1756, <https://doi.org/10.1111/jphp.12108>.
- C. Xu, X. Chen, W.B. Sheng, P. Yang, Trehalose restores functional autophagy suppressed by high glucose, *Reprod. Toxicol.* 85 (2019) 51–58, <https://doi.org/10.1016/j.reprotox.2019.02.005>.
- B.J. DeBosch, M.R. Heitmeier, A.L. Mayer, C.B. Higgins, J.R. Crowley, T.E. Kraft, M. Chi, E.P. Newberry, Z. Chen, B.N. Finck, N.O. Davidson, K.E. Yarasheski, P. W. Hruz, K.H. Moley, Trehalose inhibits solute carrier 2A (SLC2A) proteins to induce autophagy and prevent hepatic steatosis, *Sci. Signal.* 9 (2016), ra21, <https://doi.org/10.1126/scisignal.aac5472>.
- T.D. Evans, S.J. Jeong, X. Zhang, I. Sergin, B. Razani, TFEB and trehalose drive the macrophage autophagy-lysosome system to protect against atherosclerosis, *Autophagy* 14 (2018) 724–726, <https://doi.org/10.1080/15548627.2018.1434373>.
- I. Sergin, T.D. Evans, X. Zhang, S. Bhattacharya, C.J. Stokes, E. Song, S. Ali, B. Dehestani, K.B. Holloway, P.S. Micevych, A. Javaheri, Exploiting macrophage autophagy-lysosomal biogenesis as a therapy for atherosclerosis, *Nat. Commun.* 8 (2017) 1–20, <https://doi.org/10.1038/ncomms15750>.
- X. Zhang, S. Chen, L. Song, Y. Tang, Y. Shen, L. Jia, W. Le, MTOR-independent, autophagic enhancer trehalose prolongs motor neuron survival and ameliorates the autophagic flux defect in a mouse model of amyotrophic lateral sclerosis, *Autophagy* 10 (2014) 588–602, <https://doi.org/10.4161/auto.27710>.
- S. Liu, Y. Yang, H. Gao, N. Zhou, P. Wang, Y. Zhang, A. Zhang, Z. Jia, S. Huang, Trehalose attenuates renal ischemia-reperfusion injury by enhancing autophagy and inhibiting oxidative stress and inflammation, *Am. J. Physiol. Renal Physiol.* 318 (2020) F994–F1005, <https://doi.org/10.1152/ajprenal.00568.2019>.
- L. Zhu, Y. Yuan, L. Yuan, L. Li, F. Liu, J. Liu, Y. Chen, Y. Lu, J. Cheng, Activation of TFEB-mediated autophagy by trehalose attenuates mitochondrial dysfunction in cisplatin-induced acute kidney injury, *Theranostics* 10 (2020) 5829–5844, <https://doi.org/10.7150/thno.44051>.
- Y. Honma, M. Sato-Morita, Y. Katsuki, H. Mihara, R. Baba, K. Hino, A. Kawashima, T. Ariyasu, M. Harada, Trehalose alleviates oxidative stress-mediated liver injury and mallor-denk body formation via activating autophagy in mice, *Med. Mol. Morphol.* 54 (2021) 41–51, <https://doi.org/10.1007/s00795-020-00258-2>.
- T.M. O'Shea, M.J. Webber, A.A. Aimetti, R. Langer, Covalent incorporation of trehalose within hydrogels for enhanced long-term functional stability and controlled release of biomacromolecules, *Adv. Healthc. Mater.* 4 (2015) 1802–1812, <https://doi.org/10.1002/adhm.201500334>.
- N. Boehnke, J.K. Kammeyer, R. Damoiseau, H.D. Maynard, Stabilization of glucagon by trehalose glycopolymer nanogels, *Adv. Funct. Mater.* 28 (2018), 1705475, <https://doi.org/10.1002/adfm.201705475>.
- Y. Liu, J. Lee, K.M. Mansfield, J.H. Ko, S. Sallam, C. Wesdemiotis, H.D. Maynard, Trehalose glycopolymer enhances both solution stability and pharmacokinetics of a therapeutic protein, *Bioconj. Chem.* 28 (2017) 836–845, <https://doi.org/10.1021/acs.bioconjchem.6b00659>.
- M.S. Messina, J.H. Ko, Z. Yang, M.J. Strouse, K.N. Houk, H.D. Maynard, Effect of trehalose polymer regioisomers on protein stabilization, *Polym. Chem.* 8 (2017) 4781–4788, <https://doi.org/10.1039/C7PY00700K>.
- A. Sizovs, L. Xue, Z.P. Tolstyka, N.P. Ingle, Y. Wu, M. Cortez, T.M. Reineke, Poly (Trehalose): sugar-coated nanocomplexes promote stabilization and effective polyplex-mediated siRNA delivery, *J. Am. Chem. Soc.* 135 (2013) 15417–15424, <https://doi.org/10.1021/ja404941p>.
- Z.P. Tolstyka, H. Phillips, M. Cortez, Y. Wu, N. Ingle, J.B. Bell, P.B. Hackett, T. M. Reineke, Trehalose-based block copolymerizations promote polyplex stabilization for lyophilization and in vivo pdNA delivery, *ACS Biomater. Sci. Eng.* 2 (2016) 43–55, <https://doi.org/10.1021/acsbiomaterials.5b00312>.
- M. Burek, S. Wańkiewicz, A. Lalik, S. Student, T. Bieg, I. Wandzik, Thermoresponsive microgels containing trehalose as soft matrices for 3D cell culture, *Biomater. Sci.* 5 (2017) 234–246, <https://doi.org/10.1039/c6bm00624h>.
- S. Student, M. Milewska, Z. Ostrowski, K. Gut, I. Wandzik, Microchamber microfluidics combined with thermogellable glycomicrogels – platform for single cells study in an artificial cellular microenvironment, *Mater. Sci. Eng. C* 119 (2021), 111647, <https://doi.org/10.1016/j.msec.2020.111647>.
- Y. Li, N. Ariotti, B. Aghaei, E. Pandzic, S. Ganda, M. Willcox, M. Sanchez-Felix, M. Stenzel, Inhibition of S. Aureus infection of human umbilical vein endothelial cells (HUVECs) by trehalose- and glucose-functionalized gold nanoparticles, *Angew. Chem. Int. Ed. Engl.* 60 (2021) 22652–22658, <https://doi.org/10.1002/anie.202106544>.
- X. Chen, B. Wu, K.W. Jayawardana, N. Hao, H.S. Jayawardana, R. Langer, A. Jaklenec, M. Yan, Magnetic multivalent trehalose glycopolymer nanoparticles for the detection of mycobacteria, *Adv. Healthc. Mater.* 5 (2016) 2007–2012, <https://doi.org/10.1002/adhm.201600071>.
- N. Pradhan, S. Shekhar, N.R. Jana, N.R. Jana, Sugar-terminated nanoparticle chaperones are 102–105 times better than molecular sugars in inhibiting protein aggregation and reducing amyloidogenic cytotoxicity, *ACS Appl. Mater. Interfaces* 9 (2017) 10554–10566, <https://doi.org/10.1021/acsami.7b01886>.
- K. Debnath, N. Pradhan, B.K. Singh, N.R. Jana, N.R. Jana, Poly(trehalose) nanoparticles prevent amyloid aggregation and suppress polyglutamine aggregation in a Huntington's disease model mouse, *ACS Appl. Mater. Interfaces* 9 (2017) 24126–24139, <https://doi.org/10.1021/acsami.7b06510>.
- S. Mandal, K. Debnath, N.R. Jana, N.R. Jana, Trehalose-functionalized gold nanoparticle for inhibiting intracellular protein aggregation, *Langmuir* 33 (2017) 13996–14003, <https://doi.org/10.1021/acs.langmuir.7b02202>.

- [30] E. Colombo, M. Biotocino, G. Frapporti, P. Randazzo, M.S. Christodoulou, G. Piccoli, L. Polito, P. Seneci, D. Passarella, Nanolipid-trehalose conjugates and Nano-assemblies as putative autophagy inducers, *Pharmaceutics* 11 (2019) 422, <https://doi.org/10.3390/pharmaceutics11080422>.
- [31] G. Assoni, G. Frapporti, E. Colombo, D. Gornati, M.D. Perez-Carrion, L. Polito, P. Seneci, G. Piccoli, D. Arosio, Trehalose-based neuroprotective autophagy inducers, *Bioorg. Med. Chem. Lett.* 40 (2021), 127929, <https://doi.org/10.1016/j.bmcl.2021.127929>.
- [32] D. Furtado, M. Björnmalm, S. Ayton, A.I. Bush, K. Kempe, F. Caruso, Overcoming the blood-brain barrier: the role of nanomaterials in treating neurological diseases, *Adv. Mater.* 30 (2018), e1801362, <https://doi.org/10.1002/adma.201801362>.
- [33] C. Saraiva, C. Praça, R. Ferreira, T. Santos, L. Bernardino, Nanoparticle-mediated brain drug delivery: overcoming blood-brain barrier to treat neurodegenerative diseases, *J. Control. Release* 235 (2016) 34–47, <https://doi.org/10.1016/j.jconrel.2016.05.044>.
- [34] T. Patel, J. Zhou, J.M. Piepmeier, W.M. Saltzman, Polymeric nanoparticles for drug delivery to the central nervous system, *Adv. Drug Deliv. Rev.* 64 (2012) 701–705, <https://doi.org/10.1016/j.addr.2011.12.006>.
- [35] A. Vashist, A. Kaushik, A. Vashist, J. Bala, R. Nikkha-Moshaie, V. Sagar, M. Nair, Nanogels as potential drug nanocarriers for CNS drug delivery, *Drug Discov. Today* 23 (2018) 1436–1443, <https://doi.org/10.1016/j.drudis.2018.05.018>.
- [36] I. Neamtu, A.G. Rusu, A. Diaconu, L.E. Nita, A.P. Chiriac, Basic concepts and recent advances in nanogels as carriers for medical applications, *Drug Deliv.* 24 (2017) 539–557, <https://doi.org/10.1080/10717544.2016.1276232>.
- [37] H. Zhang, Y. Zhai, J. Wang, G. Zhai, New progress and prospects: the application of nanogel in drug delivery, *Mater. Sci. Eng. C Mater. Biol. Appl.* 60 (2016) 560–568, <https://doi.org/10.1016/j.msec.2015.11.041>.
- [38] M. Burek, I. Wandzik, Trehalose-rich, degradable hydrogels designed for trehalose release under physiologically relevant conditions, *Polymers (Basel)* 11 (2019) 2027, <https://doi.org/10.3390/polym11122027>.
- [39] M. Burek, S. Waskiewicz, A. Lalik, I. Wandzik, Hydrogels with novel hydrolytically labile trehalose-based crosslinks: small changes-big differences in degradation behavior, *Polym. Chem.* 9 (2018) 3721–3726, <https://doi.org/10.1039/C8PY00488A>.
- [40] M. Zou, S. Cai, Z. Zhao, L. Chen, Y. Zhao, X. Fan, S. Chen, A novel polydimethylsiloxane microfluidic viscometer fabricated using microwire-molding, *Rev. Sci. Instrum.* 86 (2015), 104302, <https://doi.org/10.1063/1.4933388>.
- [41] B.W. Neun, E. Cedrone, M.A. Dobrovolskaia, NCL method ITA-1: analysis of hemolytic properties of nanoparticles, <https://ncl.cancer.gov/resources/assay-cascade-protocols>, <https://doi.org/10.17917/V9AP-D094>.
- [42] C. He, C.R. Bartholomew, W. Zhou, D.J. Klionsky, Assaying autophagic activity in transgenic GFP-Lc3 and GFP-gabarap zebrafish embryos, *Autophagy* 5 (2009) 520–526, <https://doi.org/10.4161/auto.5.4.7768>.
- [43] P. Aleström, L. D'Angelo, P.J. Midtlyng, D.F. Schorderet, S. Schulte-Merker, S. F. Sohm, S. Warner, Zebrafish: housing and husbandry recommendations, *Lab. Anim.* 54 (2020) 213–224, <https://doi.org/10.1177/0023677219869037>.
- [44] M. Westerfield, *The Zebrafish Book*, fourth ed., University of Oregon Press, Oregon, Eugene, 2000.
- [45] N.S. Katheder, R. Khezri, F. O'Farrell, S.W. Schultz, A. Jain, M.M. Rahman, K. O. Schink, T.A. Theodosiou, T. Johansen, G. Juhász, D. Bilder, A. Brech, H. Stenmark, T.E. Rusten, Microenvironmental autophagy promotes tumour growth, *Nature* 541 (2017) 417–420, <https://doi.org/10.1038/nature20815>.
- [46] K. Piracs, P. Nagy, A. Varga, Z. Venkei, B. Erdi, K. Hegedus, G. Juhasz, Advantages and limitations of different p62-based assays for estimating autophagic activity in *drosophila*, *PLoS One* 7 (2012), e44214, <https://doi.org/10.1371/journal.pone.0044214>.
- [47] Y.Y. Chang, T.P. Neufeld, An Atg1/Atg13 complex with multiple roles in TOR-mediated autophagy regulation, *Mol. Biol. Cell* 20 (2019) 2004–2014, <https://doi.org/10.1091/mbc.e08-12-1250>.
- [48] C.A. Schneider, W.S. Rasband, K.W. Eliceiri, NIH image to ImageJ: 25 years of image analysis, *Nat. Methods* 9 (2012) 671–675, <https://doi.org/10.1038/nmeth.2089>.
- [49] RStudio Team, RStudio: integrated development for R, RStudio, PBC, Boston, MA, 2020. <http://www.rstudio.com/>.
- [50] H. Wickham, *ggplot2: elegant graphics for data analysis*, ISBN 978-3-319-24277-4, Springer-Verlag, New York, 2016, <https://ggplot2.tidyverse.org>.
- [51] A.V. Kabanov, S.V. Vinogradov, Nanogels as pharmaceutical carriers: finite networks of infinite capabilities, *Angew. Chem. Int. Ed. Engl.* 48 (2009) 5418–5429, <https://doi.org/10.1002/anie.200900441>.
- [52] T.L. Moore, L. Rodriguez-Lorenzo, V. Hirsch, S. Balog, D. Urban, C. Jud, B. Rothen-Rutishauser, M. Lattuada, A. Petri-Fink, Nanoparticle colloidal stability in cell culture media and impact on cellular interactions, *Chem. Soc. Rev.* 44 (2015) 6287–6305, <https://doi.org/10.1039/c4cs00487f>.
- [53] S. Bhattacharjee, DLS and zeta potential - what they are and what they are not? *J. Control. Release* 235 (2016) 337–351, <https://doi.org/10.1016/j.jconrel.2016.06.017>.
- [54] S. Srinivasachari, Y. Liu, L.E. Pevette, T.M. Reineke, Effects of trehalose click polymer length on pDNA complex stability and delivery efficacy, *Biomaterials* 28 (2007) 2885–2898, <https://doi.org/10.1016/j.biomaterials.2007.01.037>.
- [55] K. Obst, G. Yealland, B. Balzus, E. Miceli, M. Dimde, C. Weise, M. Eravci, R. Bodmeier, R. Haag, M. Calderon, N. Charbaji, S. Hedtrich, Protein Corona formation on colloidal polymeric nanoparticles and polymeric nanogels: impact on cellular uptake, toxicity, immunogenicity, and drug release properties, *Biomacromolecules* 18 (2017) 1762–1771, <https://doi.org/10.1021/acs.biomac.7b00158>.
- [56] N. Hayakawa, T. Yamada, Y. Kitayama, T. Takeuchi, Cellular interaction regulation by protein Corona control of molecularly imprinted polymer nanogels using intrinsic proteins, *ACS Appl. Polym. Mater.* 2 (2020) 1465–1473, <https://doi.org/10.1021/acsapm.9b01149>.
- [57] Y. Cao, Y. Gong, L. Liu, Y. Zhou, X. Fang, C. Zhang, Y. Li, J. Li, The use of human umbilical vein endothelial cells (HUVECs) as an in vitro model to assess the toxicity of nanoparticles to endothelium: a review, *J. Appl. Toxicol.* 37 (2017) 1359–1369, <https://doi.org/10.1002/jat.3470>.
- [58] ASTM, E2524-08 American Standard, Standard Test Method for Analysis of Hemolytic Properties of Nanoparticles, ASTM International, West Conshohocken, PA, USA, 2013.
- [59] D. Li, C.F. van Nostrum, E. Mastrobattista, T. Vermonden, W.E. Hennink, Nanogels for intracellular delivery of biotherapeutics, *J. Control. Release* 259 (2017) 16–28, <https://doi.org/10.1016/j.jconrel.2016.12.020>.
- [60] M. Varga, E. Fodor, T. Vellai, Autophagy in zebrafish, *Methods* 75 (2015) 172–180, <https://doi.org/10.1016/j.jymeth.2014.12.004>.
- [61] D.J. Klionsky, A.K. Abdel-Aziz, S. Abdelfatah, M. Abdellatif, A. Abdoli, S. Abel, H. Abeliovich, M.H. Abildgaard, Y.P. Abudu, A. Acevedo-Arozena, I. E. Adamopoulos, K. Adeli, T.E. Adolph, A. Adornetto, F. Aflaki, G. Agam, A. Agarwal, B.B. Aggarwal, M. Agnello, C.K. Tong, Guidelines for the use and interpretation of assays for monitoring autophagy (4th edition)1, *Autophagy* 17 (2021) 1–382, <https://doi.org/10.1080/15548627.2020.1797280>.

## *Supplementary Information*

*for*

### **Trehalose-releasing nanogels: a step towards a trehalose delivery vehicle for autophagy stimulation**

Ali Maruf<sup>1,2</sup>, Małgorzata Milewska<sup>1,2,\*</sup>, Tibor Kovács<sup>3</sup>, Máté Varga<sup>3</sup>, Tibor Vellai<sup>3,4</sup>, Anna Lalik<sup>2,5</sup>, Sebastian Student<sup>2,5</sup>, Olga Borges<sup>6,7</sup>, Ilona Wandzik<sup>1,2,\*</sup>

<sup>1</sup> Department of Organic Chemistry, Bioorganic Chemistry and Biotechnology, Faculty of Chemistry, Silesian University of Technology, Krzywoustego 4, 44-100 Gliwice, Poland

<sup>2</sup> Biotechnology Center, Silesian University of Technology, Krzywoustego 8, 44-100 Gliwice, Poland

<sup>3</sup> Department of Genetics, ELTE Eötvös Loránd University, Pázmány P. stny. 1/C, Budapest, Hungary

<sup>4</sup> ELKH-ELTE Genetics Research Group, Pázmány Péter sétány 1/C, Budapest, H-1117, Hungary

<sup>5</sup> Department of Systems Biology and Engineering, Faculty of Automatic Control, Electronics and Computer Science, Silesian University of Technology, Akademicka 16, 44-100 Gliwice, Poland

<sup>6</sup> Center for Neuroscience and Cell Biology, University of Coimbra, 3000-515 Coimbra, Portugal

<sup>7</sup> Faculty of Pharmacy, University of Coimbra, 3000-548 Coimbra, Portugal

\* Corresponding author.

E-mail addresses: ilona.wandzik@polsl.pl (IW), malgorzata.milewska@polsl.pl (MM)

**Formulation of trehalose-rich nanogels**

**Table S1.** Formulation of trehalose-releasing nanogels based on moles and mass feeding

Samples	Formulation based on moles and mass (mmol (mg))			
	TreA	AM	AMPTMAC	MBAM
<b>TNG1-AM</b>	0.102 (40.3)	0.567 (40.3)	0.605 (125.0)	0.130 (20.0)
<b>TNG2</b>	0.203 (80.6)	-	0.605 (125.0)	0.130 (20.0)
<b>TNG3</b>	0.254 (100.6)	-	0.508 (105.0)	0.130 (20.0)
<b>TNG4</b>	0.341 (135.1)	-	0.341 (70.5)	0.130 (20.0)
<b>TNG5-AM</b>	0.341 (135.1)	0.496 (35.3)	0.171 (35.3)	0.130 (20.0)
<b>TNG6-AM</b>	0.341 (135.1)	0.744 (52.9)	0.085 (17.6)	0.130 (20.0)
<b>TNG7-AM</b>	0.385 (152.7)	0.496 (35.3)	0.085 (17.6)	0.130 (20.0)
<b>TNG8</b>	0.412 (163.1)	-	0.206 (42.5)	0.130 (20.0)
<b>TNG9-AM</b>	0.430 (170.3)	0.500 (35.3)	-	0.130 (20.0)

**Viscosity and density of trehalose-releasing nanogels**

**Table S2.** Viscosity and density of trehalose-releasing nanogels at 37 °C

Sample	Dynamic viscosity (cP)				Kinematic viscosity (cSt)				Density (g/mL)			
	Read 1	Read 2	Read 3	Mean	Read 1	Read 2	Read 3	Mean	Read 1	Read 2	Read 3	Mean
Normal saline solution (0.90% w/v of NaCl)	0.6932	0.6910	0.6908	<b>0.6917</b>	0.6935	0.6923	0.6911	<b>0.6923</b>	0.9996	0.9981	0.9995	<b>0.9991</b>
PBS (pH 7.4)	0.6861	0.6858	0.6834	<b>0.6851</b>	0.6862	0.6866	0.6833	<b>0.6854</b>	0.9998	0.9988	1.000	<b>0.9996</b>
Nanogel <b>TNG7-AM*</b> in normal saline solution	0.7134	0.7157	0.7073	<b>0.7121</b>	0.7135	0.7159	0.7074	<b>0.7123</b>	0.9999	0.9997	0.9999	<b>0.9998</b>
Nanogel <b>TNG9-AM*</b> in normal saline solution	0.7113	0.7106	0.7095	<b>0.7105</b>	0.7116	0.7114	0.7097	<b>0.7109</b>	0.9996	0.9989	0.9987	<b>0.9994</b>

\*Nanogel concentration 1 mg/mL



**Scoring parameters for spider graphs**

**Table S3.** Scoring parameters for spider graphs

<b>Properties</b>	<b>Score 0</b>	<b>Score 1</b>	<b>Score 2</b>	<b>Score 3</b>	<b>Score 4</b>	<b>Score 5</b>
Yield (%)	<50	50-60	61-70	71-80	81-90	>90
d <sub>H</sub> (nm)	aggregated	251-300	201-250	151-200	100-150	<100
Stability in DMEM + 10% FBS within 3 days	>0.300	0.201-0.300	0.101-0.200	0.076-0.100	0.050-0.075	<0.050
CTre (%)	13-20	21-28	29-36	37-44	45-52	>52
Trehalose release after 7 days (µg/mL)	<15.1	15.1-17.5	17.6-20.0	20.1-22.5	22.6-25.0	>25.0
ζ-potential (mV)	>44	38-44	31-37	24-30	17-23	<17

Note: Scale from 0 to 5, with 5 being the best.

**Illustration of synthesis procedure**

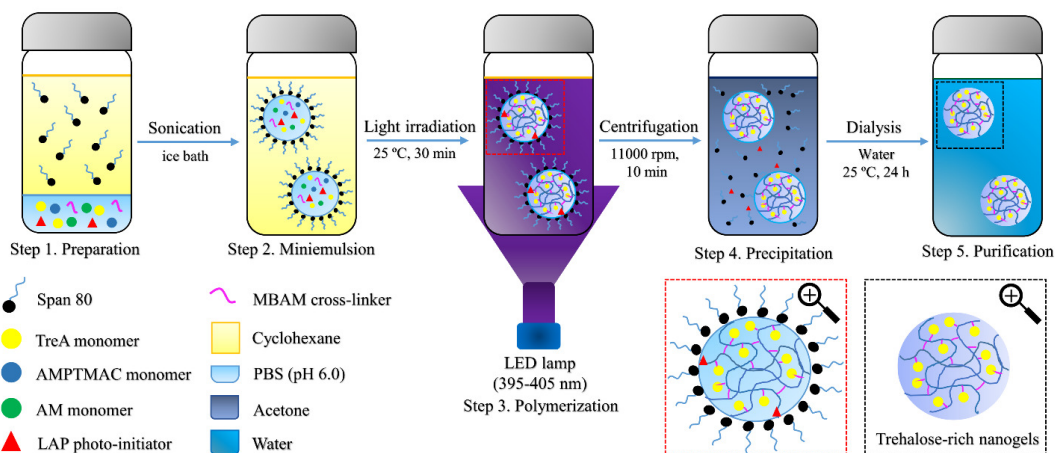


**Figure S1.** Scheme illustrating the synthesis procedure of trehalose-releasing nanogels

**Actual trehalose conjugated**

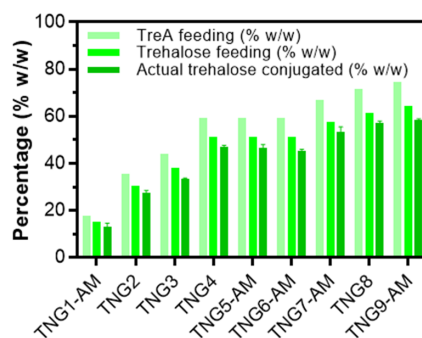


**Figure S2.** Actual trehalose conjugated compared to the recipe. Data are presented as mean  $\pm$  SD ( $n = 3$ ).

Stability of trehalose-releasing nanogels in 6 different media based on OD readout at 650 nm

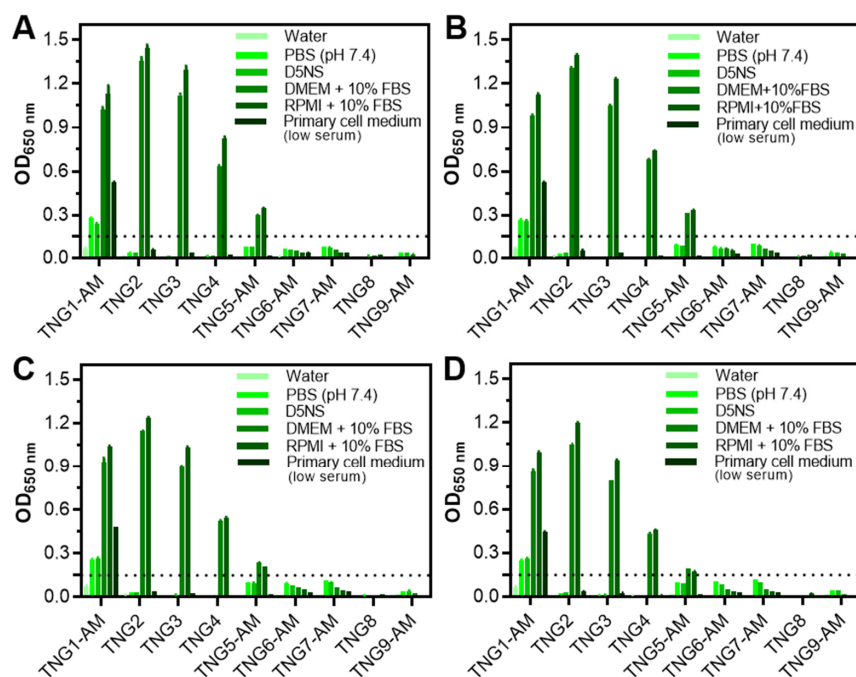


**Figure S3.** Stability of trehalose-releasing nanogels in six different media at physiological temperature (37 °C). Nanogels were incubated in water, PBS (pH 7.4), D5NS, DMEM + 10% FBS, RPMI + 10% FBS, and primary cell media (low serum) at concentration of 1000 µg/mL within (A) 2 h, (B) 6 h, (C) 24 h, and (D) 48 h. Data are presented as mean ± SD (*n* = 3).

Trehalose release at different concentrations

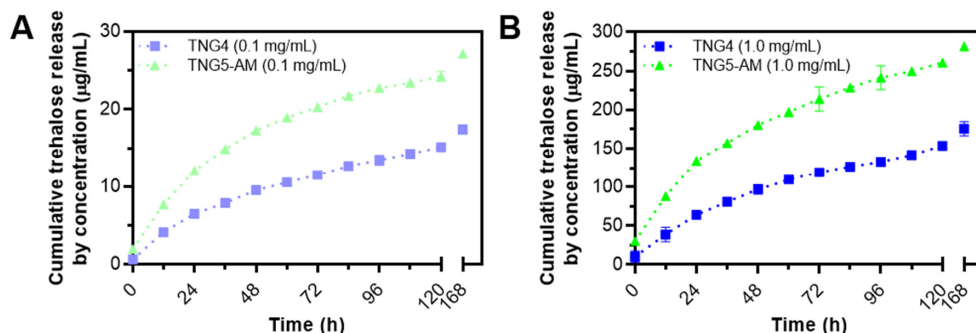


**Figure S4.** (A,B) Comparison of cumulative trehalose release of **TNG4** and **TNG5-AM** at low concentration (100 µg/mL) and high concentration (1000 µg/mL) in PBS (pH 7.4) at physiological temperature (37 °C). Data are presented as mean ± SD (*n* = 3).

Cytotoxicity of trehalose-releasing nanogels in HUVECs

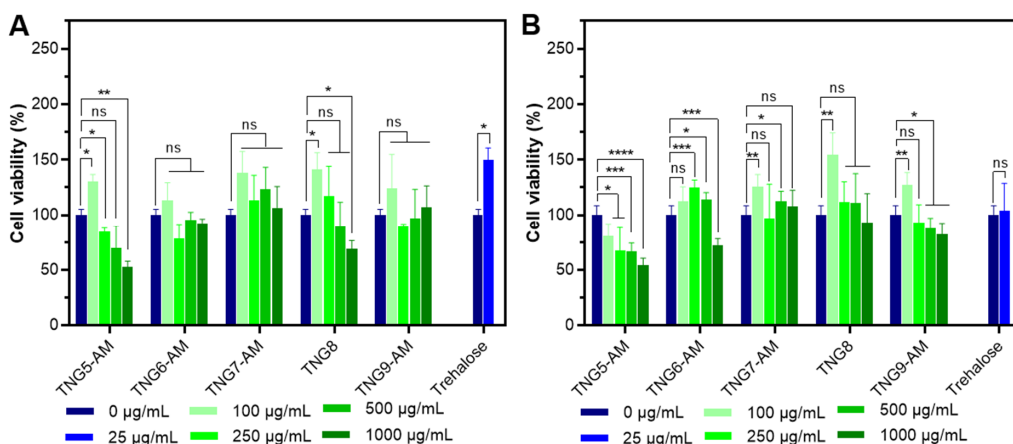


**Figure S5.** (A,B) Cytotoxicity of trehalose-releasing nanogels in HUVECs cells at different concentrations (0, 100, 250, 500, 750, and 1000 µg/mL) after 24 h of incubation (CCK-8, second and third independent assay). Data are presented as mean ± SD (*n* = 3).

**Hemolytic property of trehalose-releasing nanogels**

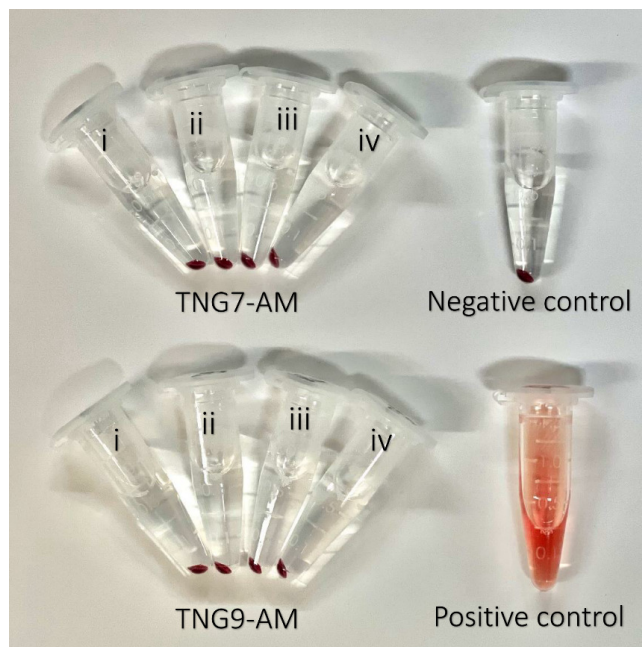


**Figure S6.** Representative images of *in vitro* hemolysis assay: The samples of **TNG7-AM** and **TNG9-AM** were tested at different concentrations, (i) 100 µg/mL, (ii) 250 µg/mL, (iii) 500 µg/mL, (iv) 1000 µg/mL, and 2000 µg/mL (picture not shown), compared to the positive control and negative control.

**Hemolytic property of fluorescently labelled nanogels**

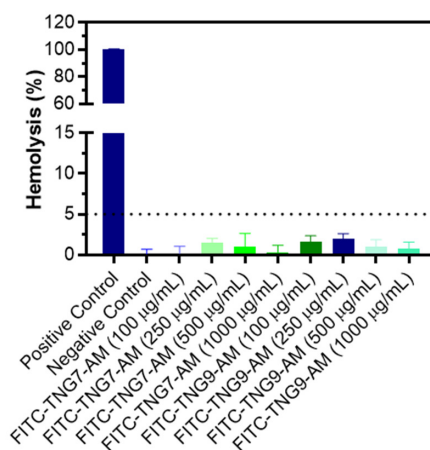


**Figure S7.** Hemolytic property of **FITC-TNG7-AM** and **FITC-TNG9-AM** at different concentrations (100, 250, 500, and 1000 µg/mL) compared to the positive control and negative control. Data are presented as mean  $\pm$  SD ( $n = 3$ ).

### Excitation and emission spectra of fluorescently labelled nanogels

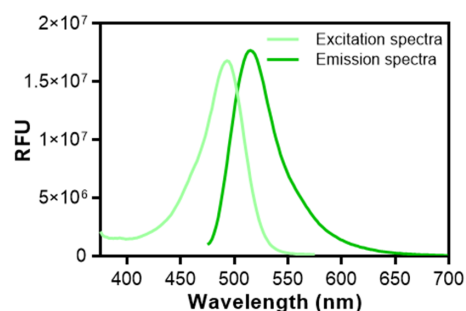


**Figure S8.** Excitation and emission spectra of fluorescently labelled nanogels. CLSM observation of nanogels uptake was recorded in FITC region (Ex max of 494 nm/Em max of 520 nm), which is similar to the above fluorescence spectra.

### Cellular uptake of TNG9-AM by HUVECs

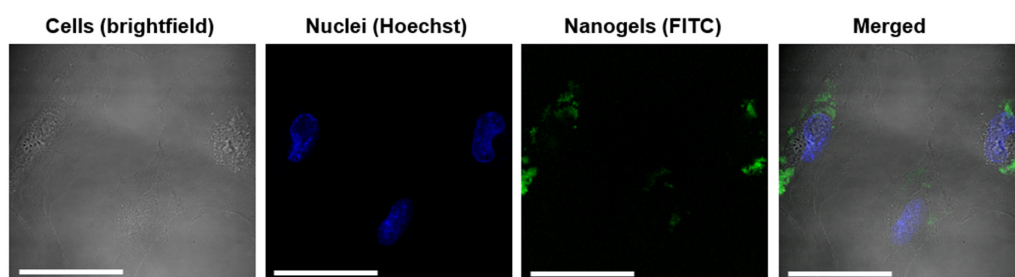


**Figure S9.** *In vitro* cell uptake of TNG9-AM by HUVECs observed under CLSM (500  $\mu\text{g}/\text{mL}$ , 3 h). Brightfield indicates HUVECs, blue color indicates cell nuclei, and green color indicates TNG9-AM (scale bars = 50  $\mu\text{m}$ ).

**STATEMENT 5**

I declare that my percentage contribution to the publication [P5] entitled “*Nanogels with covalently bound and releasable trehalose for autophagy stimulation in atherosclerosis*” (published in **J. Nanobiotechnol.** 2023, 21, 472. DOI: 10.1186/s12951-023-02248-9) was 30%.

Justification: As part of this work, I served as a co-author for various tasks, including the conceptualization of the study of using trehalose-releasing nanogels for treatment of atherosclerosis using mouse models. My experimental contributions involved synthesizing nanogels, conducting trehalose release study and enzymatic assay, measuring DLS and zeta potential, checking colloidal stability, preparing samples for cryoTEM, and synthesizing Cy5-labelled nanogels. Additionally, I was responsible for collecting and analyzing some part of the experimental data, participating in writing of manuscript, creating figures (including those with BioRender) and tables, managing citations, formatting the manuscript according to the journal’s style, assisting in revising the manuscript after peer review, and final proofreading.



Ali Maruf, M.Eng.

(PhD candidate)

As the corresponding author of the above-mentioned publication, which is part of the doctoral thesis of Mr. Ali Maruf, I declare that the percentage contribution of the remaining co-authors can be estimated as follows:

Group from Key Laboratory for Biorheological Science and Technology of Ministry of Education, State and Local Joint Engineering Laboratory for Vascular Implants, Bioengineering College, Faculty of Medicine, Chongqing University, China (Zhong Y, Qu K, Mou N, Cao Y, Wu W): 55%

Milewska M: 6%

Wandzik I: 9%



prof. dr hab. inż. Ilona Wandzik

(Supervisor / corresponding author)

## RESEARCH

## Open Access



# Nanogels with covalently bound and releasable trehalose for autophagy stimulation in atherosclerosis

Yuan Zhong<sup>1†</sup>, Ali Maruf<sup>2,3†</sup>, Kai Qu<sup>1</sup>, Małgorzata Milewska<sup>2,3</sup>, Ilona Wandzik<sup>2,3\*</sup>, Nianlian Mou<sup>1</sup>, Yu Cao<sup>1</sup> and Wei Wu<sup>1\*</sup>**Abstract**

Atherosclerosis, cholesterol-driven plaque formation in arteries, is a complex multicellular disease which is a leading cause of vascular diseases. During the progression of atherosclerosis, the autophagic function is impaired, resulting in lipid accumulation-mediated foam cell formation. The stimulation of autophagy is crucial for the recovery of cellular recycling process. One of the potential autophagy inducers is trehalose, a naturally occurring non-reducing disaccharide. However, trehalose has poor bioavailability due to its hydrophilic nature which results in poor penetration through cell membranes. To enhance its bioavailability, we developed trehalose-releasing nanogels (TNG) for the treatment of atherosclerosis. The nanogels were fabricated through copolymerization of 6-*O*-acryloyl-trehalose with the selected acrylamide-type monomers affording a high trehalose conjugation (~58%, w/w). TNG showed a relatively small hydrodynamic diameter ( $d_H$ , 67 nm) and a uniform spherical shape and were characterized by negative  $\zeta$  potential (-18 mV). Thanks to the trehalose-rich content, TNG demonstrated excellent colloidal stability in biological media containing serum and were non-hemolytic to red blood cells. In vitro study confirmed that TNG could stimulate autophagy in foam cells and enhance lipid efflux and in vivo study in ApoE<sup>-/-</sup> mice indicated a significant reduction in atherosclerotic plaques, while increasing autophagic markers. In conclusion, TNG hold great promise as a trehalose delivery system to restore impaired autophagy-mediated lipid efflux in atherosclerosis and subsequently reduce atherosclerotic plaques.

**Keywords** Atherosclerosis, Autophagy, Drug delivery, Nanogel, Trehalose**Introduction**

Atherosclerosis, commonly referred to as the “silent killer,” is a chronic disease involving lipid deposition-mediated inflammation in arterial walls that builds up plaques and causes narrowing blood vessels. The pathological inflammation of atherosclerosis is complex, where it involves different cells and cellular mechanisms [1]. During atherosclerosis progression, the cellular autophagy mechanism, i.e., cellular recycling process, is impaired due to the excessive reactive oxygen species (ROS) generation-mediated oxidative stress [2, 3]. Autophagy is essential in early and mid atherogenesis (fatty streak and intermediate lesion formation),

<sup>†</sup>Yuan Zhong and Ali Maruf contribute equally to this work.

\*Correspondence:

Ilona Wandzik

ilona.wandzik@polsl.pl

Wei Wu

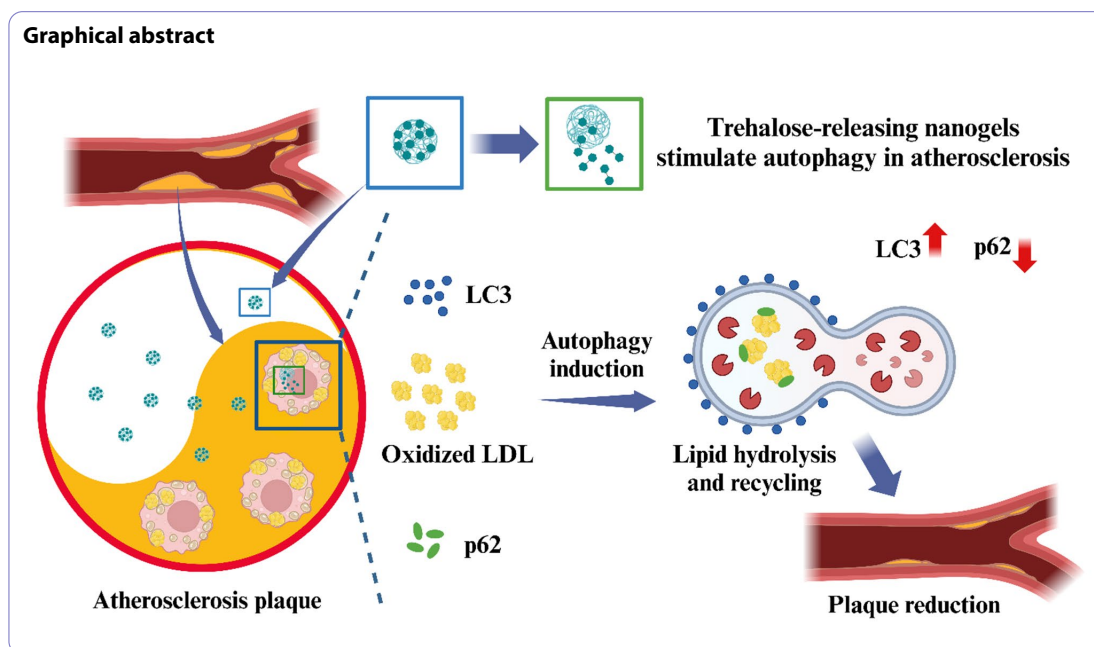
david2015@cqu.edu.cn

Full list of author information is available at the end of the article



© The Author(s) 2023, corrected publication 2023. **Open Access** This article is licensed under a Creative Commons Attribution 4.0 International License, which permits use, sharing, adaptation, distribution and reproduction in any medium or format, as long as you give appropriate credit to the original author(s) and the source, provide a link to the Creative Commons licence, and indicate if changes were made. The images or other third party material in this article are included in the article's Creative Commons licence, unless indicated otherwise in a credit line to the material. If material is not included in the article's Creative Commons licence and your intended use is not permitted by statutory regulation or exceeds the permitted use, you will need to obtain permission directly from the copyright holder. To view a copy of this licence, visit <http://creativecommons.org/licenses/by/4.0/>. The Creative Commons Public Domain Dedication waiver (<http://creativecommons.org/publicdomain/zero/1.0/>) applies to the data made available in this article, unless otherwise stated in a credit line to the data.





especially for lipid recycles [4–6]. Studies have shown that autophagy stimulation in macrophage-derived foam cells decelerated plaque development by enhancing cholesterol efflux [4–6]. Meanwhile, in advanced lesions, autophagy showed a protective role in maintaining plaque stabilization by promoting macrophage survival [7]. Autophagy is important in atherosclerosis not only in macrophages but also in smooth muscle cells and endothelial cells. The activation of autophagy in atherosclerotic smooth muscle cells maintains the cell phenotype and cell survival, which prevent smooth muscle cells transformation into synthetic, macrophage-like, and osteochondrogenic phenotypes [8]. Meanwhile, endothelial autophagy maintains cell alignment and protects blood vessels from shear stress-mediated atherosclerotic plaque formation by preventing endothelial apoptosis, senescence, and inflammation [9]. Taken together, the activation and recovery of autophagy as an intracellular degradation process is required in all stages of atherogenesis.

Among therapeutic drugs associated with cardiovascular disease and atherosclerosis treatments, lipid-lowering agents (e.g., statins and their derivatives) are the most commonly used due to their ability to support lowering low-density lipoprotein cholesterol (LDL-c), but they still showed adverse effects in some patients (<5%), which are particularly related to muscle symptoms [10]. Aspirin, on the other hand, is used as anti-platelet medication to reduce the risk of blood clot formation-mediated

thrombosis in atherosclerotic plaques, but not reducing the plaques [11]. Another commonly used drug is rapamycin and its derivatives as mTOR inhibitors, which are beneficial to suppress cell proliferation and promote autophagy, thereby reducing the plaques [12]. However, rapamycin has poor solubility and it might promote some adverse effects, such as hyperlipidemia and delayed re-endothelization in patients after stent angioplasty [13]. Recently,  $\alpha,\alpha$ -trehalose, an FDA-approved water-soluble autophagy inducer has been comprehensively studied for the treatment of impaired-autophagy related diseases (e.g., neurodegenerative disorders, diabetes and fatty liver diseases, and ischemic-related diseases) [14–19]. Trehalose has also been proved to be an effective autophagy inducer in atherosclerosis, which drives macrophage autophagy-lysosomal biogenesis [20–23], thus it is beneficial for a long-term treatment to diminish the accumulated lipids in the plaques. Trehalose, however, has low bioavailability that requires the use of relatively high concentrations to induce autophagy in cells [24, 25]. In animal studies, trehalose is usually administered intraperitoneally at the dose of 2–3 g/kg or by oral administration in drinking water (2–4% w/v) [24–27]. The hydrophilic nature of trehalose results in poor penetration through cell membranes. In addition, the presence of trehalase enzyme in the intestinal mucosa affects its pharmacokinetic behavior due to rapid hydrolysis. Therefore, there is a need for seeking effective trehalose delivery systems using nanocarriers, which could enhance the

bioavailability of trehalose, as well as deliver trehalose to atherosclerotic plaques for stimulating autophagy-mediated recovery of cellular recycling process.

Although a number of studies have explored the use of nanoparticles, particularly smart nanocarriers, for delivering ROS scavenging agents, matrix metalloproteinase (MMP) inhibitors, lipid-lowering agents, and photo thermal and photodynamic activating agents for atherosclerosis treatment, only few studies have focused on specifically restoring autophagy in atherosclerosis [28]. Very recently, three significant reports in this topic have been published. Firstly, Guo et al. (2022) reported the use of self-assembled LOX1-targeted siRNAs and conjugated rapamycin/DNA nanomicelles for stimulating autophagy in atherosclerosis. This approach was found to mediate lipid clearance and prevent the formation of foam cells by restoring the cellular recycling process [29]. Secondly, You et al. (2022) used atorvastatin-loaded graphene oxide quantum dots (GOQDs) modified with hybrid cell membrane coating for enhanced atherosclerosis targeting and autophagy stimulation [30]. Lastly, the first use of nanocarrier-based trehalose as an autophagy inducer was introduced by Wu et al. (2022) [31]. They developed self-assembled trehalose-bearing arginine and phosphatidylserine as nanomotors by accelerating penetration of nanomotors to target macrophages using nitric oxide (NO) as the driving force, which was generated from the reaction between arginine and ROS in the interstitial fluid of atherosclerotic lesions. Trehalose nanomotors-mediated autophagy activation in a mice model of atherosclerosis led to a significant reduction in macrophage foam cell formation, improvement in endothelial cell integrity, and most notably, a decrease in the lesion area [31]. Stimulation of autophagy to treat atherosclerosis is also targeted in the study from Li et al., who developed multi-loaded self-assembled nanovesicle systems composed of amphiphilic H9 peptide and hexadecyl phosphorylcholine loaded with physically entrapped trehalose and the (HP- $\beta$ -CD)/oridonin inclusion complex [32]. The synergistic effects of oridonin and trehalose could inhibit foam cell formation in RAW264.7 cells, reduce inflammatory cytokines IL-1 $\beta$ , IL-6, and TNF- $\alpha$ , and promote the formation of autophagosomes, as confirmed by the increased level of LC3 in foam cells.

Herein, we designed nanogels with covalently bound, and releasable trehalose for autophagy stimulation in atherosclerosis. Specifically, trehalose was incorporated within nanogels in free radical copolymerization through its 6-*O*-acryloyl derivative, affording nanogels with high trehalose conjugation (~58%, w/w). In order to achieve controlled release of trehalose under physiological conditions, we co-incorporated acrylamide (AM), which facilitates hydrolysis of the ester bond in 6-*O*-acryloyl-trehalose units, thus free trehalose can be sustainably

released from the nanogel network. Based on our preliminary study [33], a significant increase in trehalose release was noticed in the nanogels with high AM content in comparison to those without AM. We also found that high content of trehalose is beneficial for the colloidal stability in biological media, especially in serum-containing media [33]. More importantly, in vivo studies in transgenic *Drosophila* and zebrafish larvae showed a significant induction of autophagy after treatment with trehalose-releasing nanogels [33]. In the current study, we used a mice model of atherosclerosis to observe the efficacy of TNG for potential nanotherapy of atherosclerosis via autophagy modulation (Fig. 1).

## Results and Discussion

### Synthesis and characterization of trehalose-releasing nanogels

Nanogels, i.e., nanoparticles based on crosslinked hydrophilic polymeric networks, are among the most promising and widely studied nanocarriers as drug delivery systems due to their characteristics, such as high biocompatibility, high loading capacity, potential biodegradability and responsiveness to biological cues [34]. Nanogels were first introduced and applied as nanocarriers for the delivery of antisense oligonucleotides by Kabanov's group in 1999 [35], following massive studies.

In the current study, we designed nanogels with covalently bound and releasable trehalose, denoted as TNG, to treat atherosclerosis via autophagy recovery. Trehalose was incorporated within nanogels in free radical copolymerization through its 6-*O*-acryloyl derivative, yielding trehalose-rich nanogels with ~58% covalently bound trehalose. AM-type monomers were used to enhance the release of trehalose through ester bond hydrolysis at physiological conditions (Fig. 2A). As demonstrated previously, copolymerizing 6-*O*-acryloyl-trehalose with acrylamide-type monomers allows to fabricate materials that can sustainably release trehalose at pH 7.4 due to the interaction of the amide protons with the ester bond in adjacent acrylate units, which strongly accelerates ester hydrolysis [36, 37]. The presence of covalently bound trehalose and the purity of TNG was confirmed by <sup>1</sup>H NMR spectroscopy (Fig. 3A). The presence of broad signals typical for polymers in the range of 3.3–4.6 and 5.0–5.5 ppm, which are well correlated with proton signals of the trehalose monomer TreA, and the lack of signals from protons of the acrylate group in the range of 6.0–6.5 ppm, both prove successful incorporation of TreA into the TNG network. Signals originating from the protons of other key structural fragments, e.g., methylene groups from 4-AMBA (1.7–1.9, 2.3–2.5 and 3.1–3.3 ppm), and polymer backbone derived from acrylates and acrylamides (1.1–3.0 ppm) can also be easily identified.

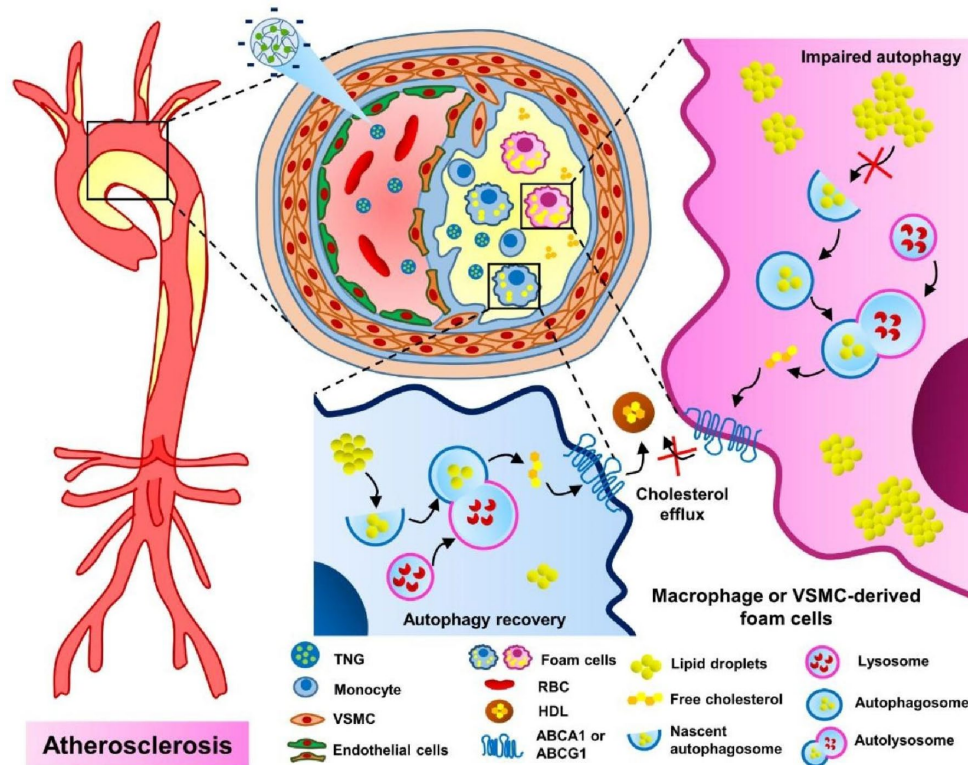


**Fig. 1** Scheme of the hypothesis of how trehalose-releasing nanogels (TNG) could promote atherosclerosis management via the autophagy recovery-mediated lipid recycling process and cholesterol efflux. TNG: trehalose-releasing nanogels, VSMC: vascular smooth muscle cell, RBC: red blood cell, HDL: high density lipoprotein, ABCA1: ATP Binding Cassette Subfamily A Member 1, ABCG1: ATP Binding Cassette Subfamily G Member 1

Based on our previous study [33], we noticed that an improved colloidal stability of nanogels in biological media was ensured by incorporating ionic monomer or high content of trehalose in the nanogel network. Trehalose seemed to have a significant role in improving the colloidal stability of nanogels especially in biological media, and particularly in serum-containing media. Thereby, to further prove the beneficial effect of trehalose on nanogel colloidal stability, in the current study we tested whether by replacing TreA monomer with 2-hydroxyethyl acrylate (HEA) monomer (hydrophilic monomer with one hydroxyl group) had a significant impact on the colloidal stability of AM-based nanogels. HEA-containing nanogels were synthesized by substituting TreA with HEA at both equimolar and equimass of TreA feed (Table S1) for obtaining HEA<sub>1</sub>NG and HEA<sub>2</sub>NG, respectively. Physicochemical characteristic of nanogels is shown in Table 1. The yield after polymerization of TNG, HEA<sub>1</sub>NG, and HEA<sub>2</sub>NG were 67, 75, and 69%, respectively.

From DLS measurement, the Z-average  $d_H$  and PDI of TNG, HEA<sub>1</sub>NG, and HEA<sub>2</sub>NG were 67, 78, and 80 nm and 0.277, 0.283, and 0.230, respectively. All nanogels were also characterized by a similar  $\zeta$  potential of about  $-18$  mV (Table 1). Cryo-TEM image showed that the diameter of TNG was  $\sim 50$  nm (Fig. 3B). The colloidal stability of nanogels was assessed by monitoring the transmittance in various biological media over time. The transmittance of TNG dispersions in water, PBS (pH 7.4), normal saline (NS), DMEM, and DMEM+10% FBS at high concentration of 1.0 mg/mL within 7 days of incubation at 37 °C, exceeded 95%, which indicated their excellent stability (Figure S1). In contrast, both HEA<sub>1</sub>NG, and HEA<sub>2</sub>NG were only stable in water but they aggregated immediately in PBS (pH 7.4), NS, DMEM, and the most aggregation was found in DMEM+10% FBS. It is possible that the hydrophilic nature of pendant trehalose may have a huge impact on their colloidal stability due to short-range repulsive hydration forces [38]. The aggregation of nanoparticles in biological media is not preferred both for in vitro and in vivo study, which might

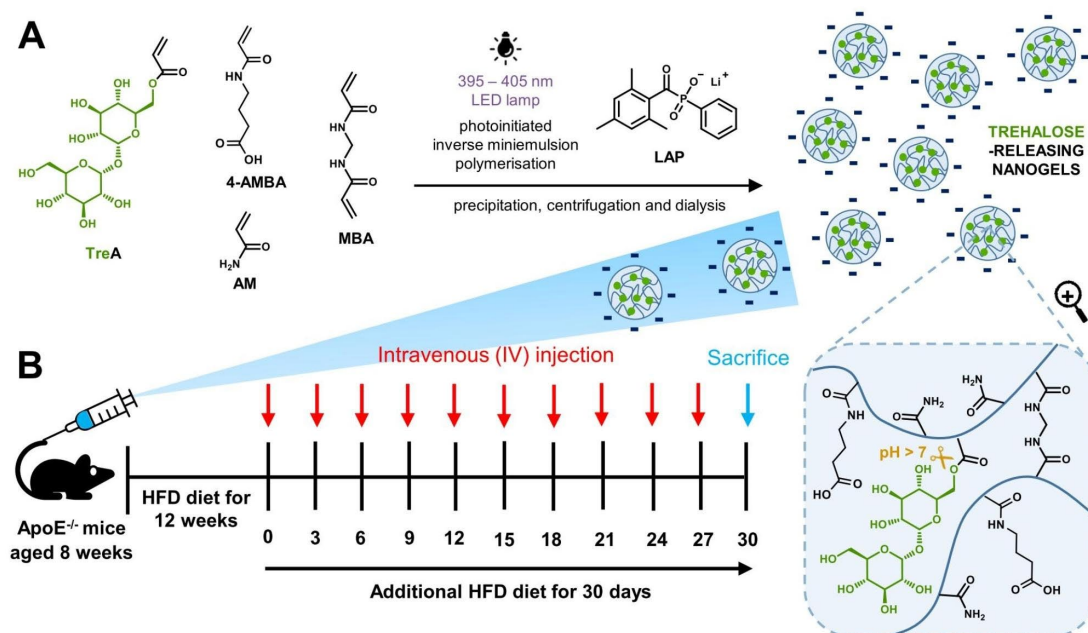


**Fig. 2** (A) The synthesis of trehalose-releasing nanogels (TNG), and (B) timeline for ApoE<sup>-/-</sup> mice pretreatment and systemic administration of TNG via the tail vein

result in cytotoxicity profile, low cellular uptake, misleading of specific targeting, and elimination by endothelial reticular system (RES) during nanoparticle circulation [39–41]. Further colloidal stability study was conducted by DLS to observe the stability of TNG in DMEM+10% serum. The result showed that the size distribution of TNG in DMEM+10% FBS remained stable within 24 h of incubation at 37 °C (Fig. 3C), which was plausible for preparation of intravenous (*i.v.*) injection. The amount of trehalose incorporated into TNG was determined enzymatically after pretreating nanogel with strong alkali. Under these conditions all trehalose was cleaved into solution. From the enzymatic assay, the content of trehalose in TNG was around 58% (w/w) (Table 1, Figure S3). The release study showed that trehalose could be sustainably released at pH 7.4, 37 °C, reaching nearly 55% release within 30 days, what corresponds to about 32 µg/mL of trehalose (at a total trehalose concentration of ~58 µg/mL) (Fig. 3D). The sustained release of trehalose from TNG would be desirable for *in vivo* study of atherosclerosis treatment within one month (Fig. 2B).

#### Biocompatibility of trehalose-releasing nanogels

Red blood cell compatibility is crucial to ensure that nanocarriers or nanoparticles do not cause hemolysis (rupture of red blood cells) or other adverse effects when interacting with red blood cells [42]. For the *in*

*vivo* drug delivery system, ensuring good blood compatibility is essential, along with low toxicity and appropriate nano-size. The evaluation of hemolytic activity of the administered nanogel is crucial to guarantee safety during administration. As seen in Figure S4, the results demonstrated that all tested samples showed no significant hemolysis, even at a very high concentration of 2 mg/mL, which was extremely higher than the practical concentration in the bloodstream. Although there was a slight increase in hemolysis compared to free trehalose, the hemolysis ratios of TNG remained below 5%. This percentage is generally considered safe for *in vivo* applications, according to the criterion outlined in the ASTM E2524-08 standard [42]. The standard states that materials with a hemolysis percent higher than 5% pose a risk of damaging red blood cells during *in vivo* applications. Therefore, the evaluated nanogel was demonstrated to be a favorable blood compatibility and met the safety requirements for subsequent *in vivo* application.

The cytotoxicity profile of TNG at different concentrations was also examined in the cultured HUVECs for 24 h. The results indicated that TNG at reasonable *in vitro* doses ( $\leq 200$  µg/mL) did not cause cytotoxic effects in HUVECs (more than 90% cell viability) (Figure S5), indicating the biocompatibility of TNG for further *in vitro* studies.

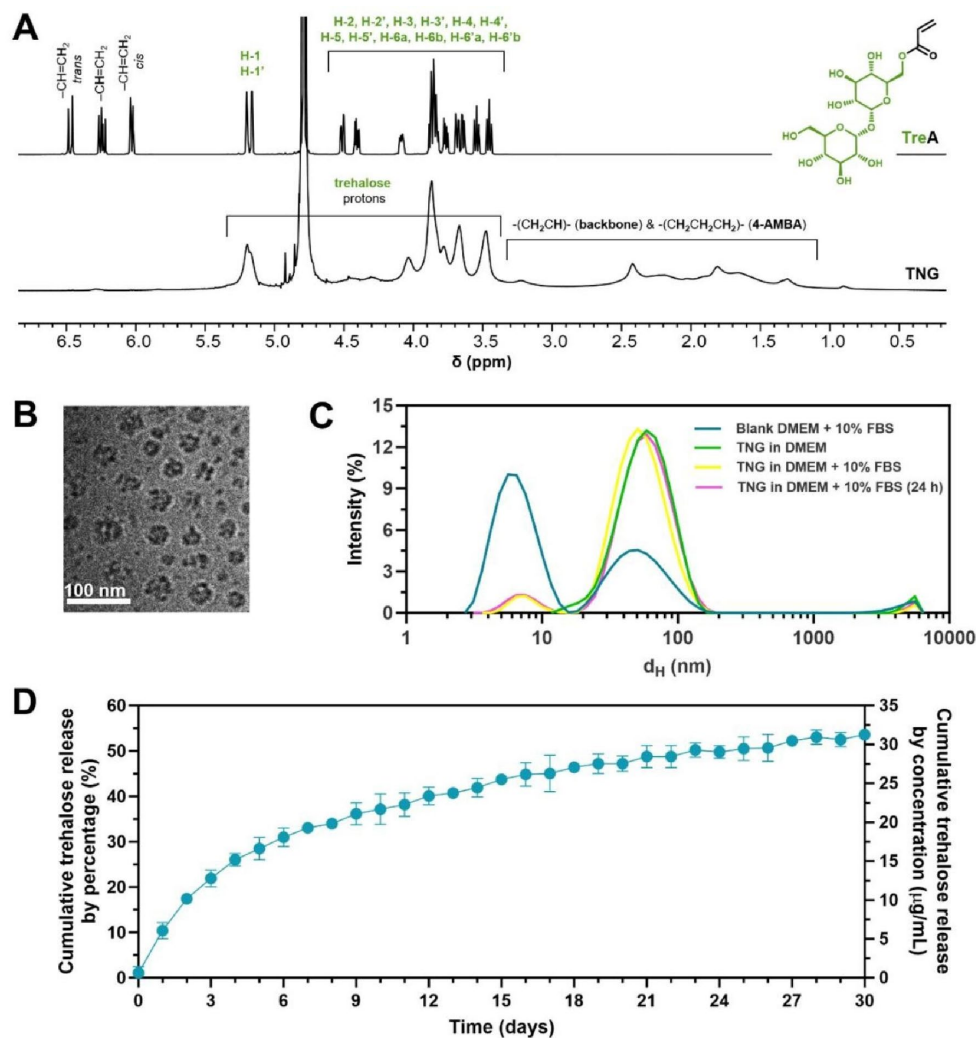


**Fig. 3** Characterization of trehalose-releasing nanogels (TNG). **(A)** Section of  $^1\text{H}$  NMR spectra of TreA (top) and TNG (bottom) proving covalent incorporation of trehalose into TNG ( $\text{D}_2\text{O}$ , 600 MHz). **(B)** Cryo-TEM micrograph of TNG in water. Scale bar: 100 nm. **(C)** Colloidal stability of TNG in DMEM + 10% FBS monitored by DLS measurement. **(D)** Trehalose release profile from TNG in PBS over one month (pH 7.4, 37 °C, TNG concentration: 100  $\mu\text{g}/\text{mL}$ ). Data are presented as mean  $\pm$  SD,  $n = 3$

**Table 1** Physicochemical characterization of nanogels

Sample	Trehalose conjugation (% w/w)	Yield (%)	Z-average $d_H$ (nm) (Pdl)	$\zeta$ potential (mV)
TNG	57.6	67	67 (0.277)	-17.6 $\pm$ 6.1
HEA <sub>1</sub> NG	-	75	78 (0.283)	-18.9 $\pm$ 5.3
HEA <sub>2</sub> NG	-	69	80 (0.230)	-19.4 $\pm$ 5.9

TNG - trehalose-releasing nanogels

HEA<sub>1</sub>NG and HEA<sub>2</sub>NG – 2-hydroxyethyl acrylate-based nanogels

Due to the hydrophilicity of trehalose, its ability to penetrate cell membranes is limited, hindering its bio-availability. To improve the membrane permeability and bioavailability of trehalose, the cellular uptake capacity of TNG was evaluated. The fluorescence intensity of TNG group was significantly higher than that of free trehalose group (Figure S6). Such results suggest that formulation manipulation may be a viable avenue to improve the pharmacokinetics of drugs.

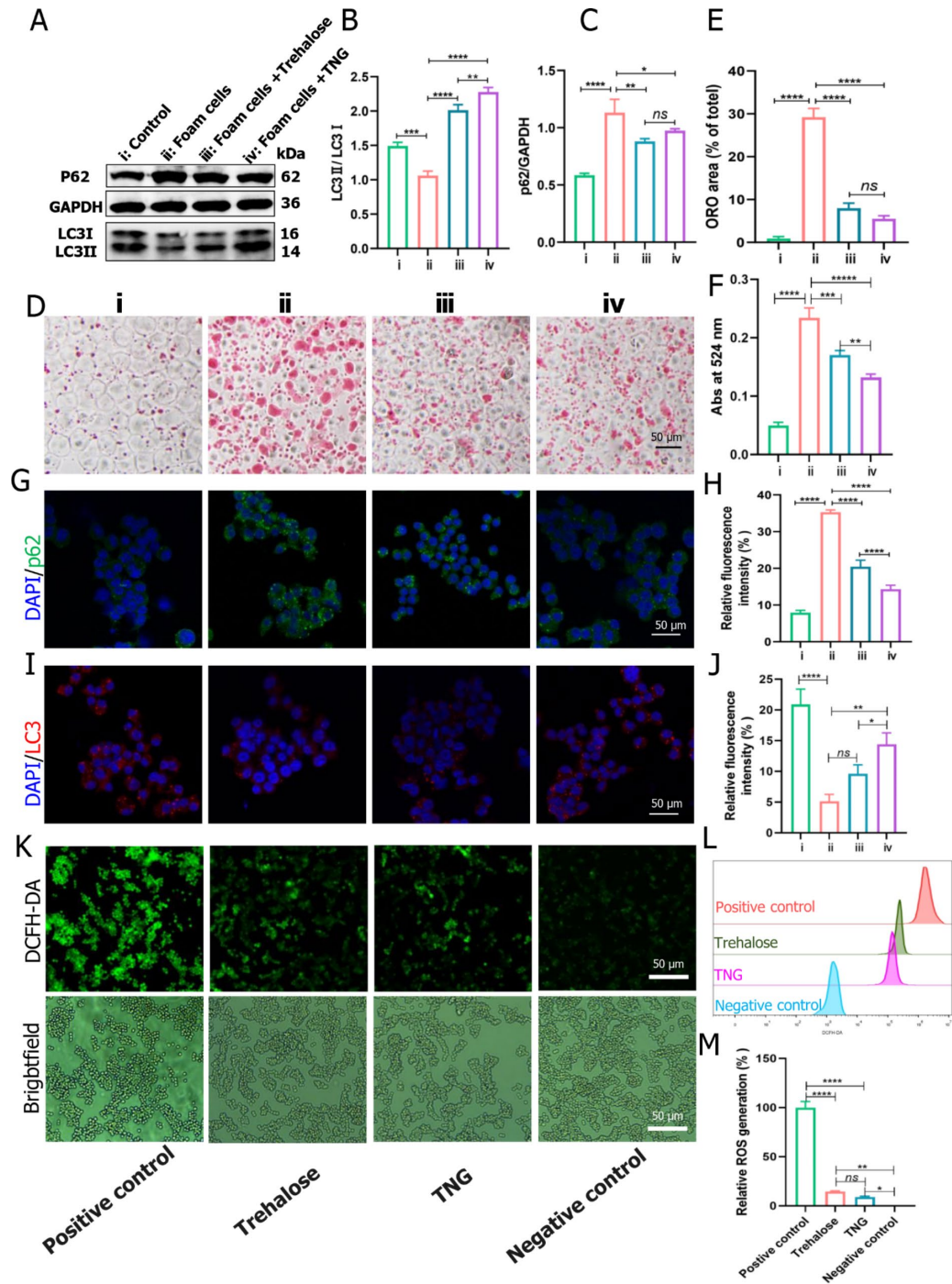


**Fig. 4** (See legend on next page.)

(See figure on previous page.)

**Fig. 4** In vitro autophagy stimulation and anti-atherosclerosis effects. **(A)** Western blot analysis of p62, LC3-I, LC3-II, and GAPDH protein expressions from foam cells treated with or without free trehalose and nanogel in comparison to the control; i=control, ii=foam cells, iii=foam cells+trehalose, and iv=foam cells+TNG. **(B, C)** Quantification of LC3-II/LC3-I and p62/GAPDH ratios from the Western Blot images. **(D)** Lipid profile in foam cells treated with or without free trehalose and nanogel in comparison to the control upon oil Red O (ORO) staining, following quantification of **(E)** lipid droplet area (% of total) and **(F)** Abs at 524 nm; i=control, ii=foam cells, iii=foam cells+trehalose, and iv=foam cells+TNG. **(G, I)** Fluorescence imaging and **(H, J)** quantification of p62 and LC3 expressions from foam cells treated with or without free trehalose and TNG in comparison to the control. **(K)** Fluorescence images and **(L, M)** quantification by flow cytometry showing intracellular ROS generation after treatment with different formulations and stimulation with H<sub>2</sub>O<sub>2</sub>. RAW264.7 cells were incubated with medium alone or trehalose or TNG for 4 h, followed by stimulation with H<sub>2</sub>O<sub>2</sub> for 0.5 h. Cells unstimulated with H<sub>2</sub>O<sub>2</sub> served as the negative control. Then fluorescence microscope and flow cytometric analyses were performed. Scale bar: 50 μm. Data are presented as mean ± SD, n=3, ns: no significance, \*p<0.05, \*\*p<0.01, \*\*\*p<0.001, and \*\*\*\*p<0.0001

#### In vitro assessment of autophagy stimulation and anti-atherosclerosis effects by trehalose-releasing nanogels

The in vitro autophagy stimulation and anti-atherosclerosis effects were assessed in macrophage-derived foam cells. The relationship between autophagy and LC3 is crucial in understanding the process of autophagy at the molecular level. LC3, specifically LC3-I (cytosolic form) and LC3-II (lipidated form), is an essential component of the autophagosomal membrane and plays a central role in autophagosome formation and maturation. In the in vitro study, macrophage-derived foam cells exhibited a decreased level of LC3 but an elevated level of p62 compared to the control group, as evidenced by Western blot analysis (Fig. 4A–C). However, upon treatment with trehalose and TNG, there was a significant increase in the LC3-II/LC3-I ratio, accompanied by a decrease in the p62/GAPDH ratio. These findings indicated that trehalose and TNG induced autophagy in the foam cells. Moreover, fluorescence analysis yielded similar results, showing a significant reduction in the p62 level in foam cells, which could be attributed to the degradation of p62 during the autophagy process (Fig. 4G, H). The activation of autophagy in atherosclerosis results in the interaction between p62 and autophagy substrates, forming a structure known as phagophore, which involves the participation of LC3 (conversion from LC3-I to LC3-II) [43, 44]. LC3-II acts as a key adaptor molecule in autophagy by binding to various autophagy-related proteins and interacting with cargo molecules, such as damaged proteins and organelles, to be sequestered into the autophagosome. This selective engulfment of cargo is essential for autophagy to degrade and recycle cellular components properly. The level of LC3-II is often used as a marker to monitor autophagic activity. Typically, there is a strong correlation between the upregulation of LC3-II expression relative to LC3-I and the downregulation of p62 expression, which indicate an enhancement in autophagic flux. Meanwhile, there was a significant increase in the LC3 fluorescence compared to the negative control, indicating that the autophagy was recovered (Fig. 4I, J). The absorbance of Oil Red O (ORO)-stained foam cells, subjected to free trehalose and TNG treatments, exhibited a reduction compared to untreated foam cells (Fig. 4D–F). Remarkably, TNG treatment manifested the

most pronounced efficacy, furnishing additional substantiation of its in vivo anti-atherosclerotic potential. To further investigate the ROS scavenging performance, TNG and trehalose were used to treat the RAW264.7 cells with the addition of H<sub>2</sub>O<sub>2</sub>. In the positive control group, RAW264.7 cells were simultaneously treated with 0.5 μM H<sub>2</sub>O<sub>2</sub>, while cells cultured with medium alone served as the negative control. After stimulation for 0.5 h and incubation with free medium for the additional 2 h, cells in the positive control displayed a considerably high level of ROS, as probed by a fluorescent dye 2',7'-dichlorofluorescein-diacetate (DCFH-DA) that emits green fluorescence under oxidative conditions (Fig. 4K). In contrast, fluorescent signals of DCFH-DA were dramatically decreased when activated macrophages were treated with free trehalose or TNG for 4 h. Further quantitative analysis by flow cytometry also demonstrated that the intracellular ROS production in stimulated macrophages could be effectively suppressed by treatment with TNG (Fig. 4L, M).

#### In vivo plaque targeting and biodistribution study of trehalose-releasing nanogels

To investigate the in vivo pharmacokinetic profile of TNG in C57BL/6 mice, after *i.v.* injection of Cy5-labeled TNG (Cy5-TNG) and free Cy5, the results indicated that Cy5 was gradually decreased and almost completely cleared out from blood until 24 h, while the fluorescence intensity of Cy5-TNG was nearly 30% of the initial one at the end of investigation (Figure S7). Then we investigated in vivo targeting capability of TNG in apolipoprotein E-deficient (ApoE<sup>-/-</sup>) mice. The Cy5-TNG and free Cy5 were administered through *i.v.* administration, and let them circulating in the bloodstream for a duration of 24 h. As illuminated by the results of fluorescent imaging, Cy5-TNG exhibited a conspicuous propensity for accumulation within aortic plaques, surpassing the observed accumulation of free Cy5, with an average Region of Interest (ROI) approximately 1.6 times that of free Cy5 (Fig. 5A, B). Additionally, in relation to other organs (heart, spleen, lung, and kidney), both Cy5-TNG and free Cy5 primarily accumulated in liver (Fig. 5C, D), given the liver's prominence as the body's largest metabolic organ. The results imply that Cy5-TNG possesses a preferential

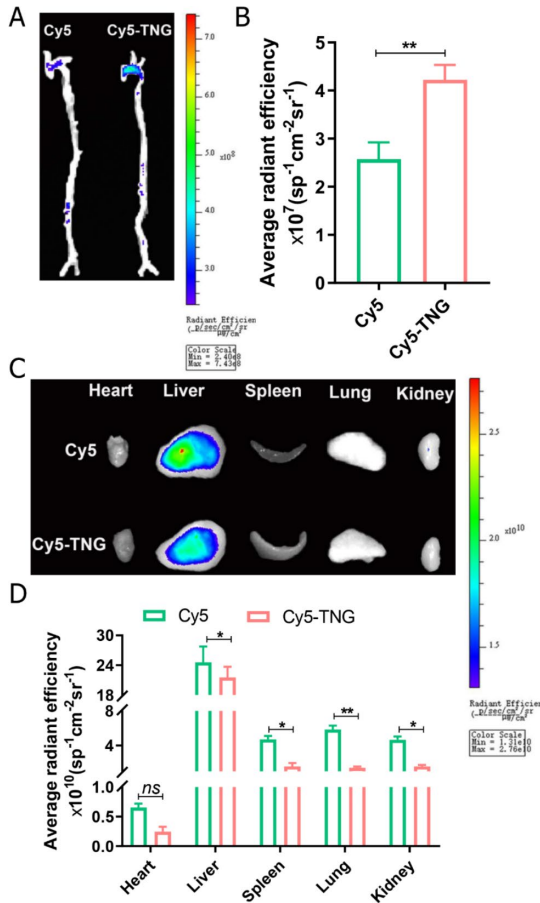


**Fig. 5** In vivo plaque targeting and biodistribution of trehalose-releasing nanogels in major organs. (A) The ex vivo fluorescence images of the aorta and (B) quantitative analysis of fluorescence signals accumulated in the aorta of ApoE<sup>-/-</sup> mice after 24 h of IV with Cy5-TNG and free Cy5. (C, D) The ex vivo biodistribution images of Cy5-TNG and free Cy5 in major organs (heart, liver, spleen, lung, and kidney). Data are presented as mean ± SD, n = 3, ns: no significance, \*p < 0.05 and \*\*p < 0.01

affinity for targeting plaques and manifest an extended blood half-life.

**In vivo assessment of autophagy stimulation and anti-atherosclerosis effects by trehalose-releasing nanogels**

After testing the ability of TNG in stimulating autophagy and lipid efflux in foam cells, we tested its effects in vivo. TNG and free trehalose were administered intravenously every three days, for one month, to ApoE<sup>-/-</sup> mice that had been treated with HFD for 12 weeks. The findings indicated that TNG exhibited a significant anti-atherosclerosis effect, leading to a reduction of approximately 60% in the overall plaque area after one month of treatments. Free trehalose was also confirmed to have the

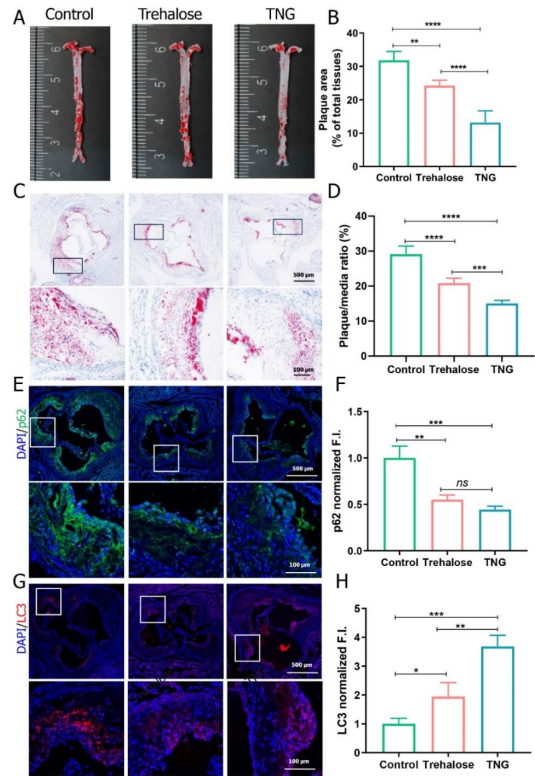


**Fig. 6** In vivo autophagy stimulation and anti-atherosclerosis effects of trehalose-releasing nanogels. (A) The en face oil red O (ORO)-stained images of aortas in ApoE<sup>-/-</sup> mice after one month of treatments with free trehalose and TNG compared to the control and (B) quantitative analysis of the lesion area. (C) ORO-stained images of aortic root sections in ApoE<sup>-/-</sup> mice after one month of treatments with free trehalose and TNG compared to the control and (D) quantitative analysis of the atherosclerotic plaque area. (E, G) CLSM images and (F, H) quantitative analysis of p62 (green fluorescence) and LC3 (red fluorescence) expressions in atherosclerotic plaques of the aortic root sections in ApoE<sup>-/-</sup> mice after one month of treatments with free trehalose and TNG compared to the control, scale bars: 500 and 100 μm, respectively. Data are presented as mean ± SD, (A–D) n = 5, (E–H) n = 3, ns: no significance, \*p < 0.05, \*\*p < 0.01, \*\*\*p < 0.001, and \*\*\*\*p < 0.0001

ability to decrease the total plaque area but to a lesser extent compared to TNG (Fig. 6A–D). This gap may be related to the poor bioavailability and disappointing pharmacokinetics of trehalose.

To assess the enhanced autophagy effect of TNG, we analyzed the p62 and LC3 expressions in the atherosclerotic plaque area using immunofluorescent staining. The findings revealed that mice treated with TNG exhibited a significant decrease in p62 levels, surpassing 50% reduction, and a nearly four-fold increase in LC3 levels. Similarly, the administration of free trehalose could promote autophagy in atherosclerosis, as evidenced by the



reduction in p62 levels and the elevation of LC3 levels (Fig. 6E–H). However, its effect on inducing autophagy was not as pronounced as that of TNG. These were consistent with the results of previous *in vitro* investigations. In the management of atherosclerosis, trehalose could activate TFEB, leading to the successful recovery of damaged autophagy in plaque. This repair process enhanced the elimination of p62-enriched aggregates and the expression of various components related to autophagy (such as LC3), which was conducive to the formation of autophagosomes [45]. Separate staining with anti-CD68 antibody indicated that TNG treatment effectively reduced the macrophage count in plaques (Figure S8A, B). As the degree of macrophage infiltration is positively correlated with plaque vulnerability, these findings indicate that TNG therapy has the potential to enhance the stability of atherosclerotic plaques and impede the progression of atherosclerosis more efficiently than free trehalose. It is surprising that, despite the important role of trehalose in restoring autophagy, there have been only a few studies focused on the development of nanocarriers to deliver trehalose to the atherosclerotic plaques. In addition, due to trehalose's high hydrophilicity and difficulty in crossing phospholipid bilayer of cell membranes [26, 27], the developments of nanocarriers that can deliver trehalose intracellularly are paramount important, particularly for atherosclerosis management. In the present work, we have demonstrated that our developed nanogels could significantly outperform free trehalose in promoting lipid removal, reducing plaque area, and efficiently enhancing autophagy in atherosclerosis.

#### **In vivo biosafety assessment of trehalose-releasing nanogels**

In the end of study, we examined the biosafety assessment of free trehalose and TNG compared to the control, which included H&E staining of the main organs, body weight, CBC profile, and blood lipid profile (Figure S9A–E, Tables S2–S4). The tissue morphology of the mice treated with free trehalose and TNG did not differ from the control group, and the liver and kidney function indexes fell within the normal reference range. TNG demonstrated the best lipid profile in comparison to the control group, with considerably lower levels of total cholesterol and LDL-C and higher levels of HDL-C. In addition, we observed fluctuations in serum of alanine aminotransferase (ALT), aspartate aminotransferase (AST), creatinine (CR) and uric acid (UA) but were within the normal reference range.

#### **Conclusion**

We have successfully developed trehalose-releasing nanogels (TNG) using a facile synthesis method through photo-initiated free radical polymerization

and mini-emulsion technique, yielding nanogels with exceptionally high content of covalently bound trehalose (~58%). TNG had a uniformly spherical shape with the average size of ~50 and 67 nm ( $d_{TEM}$  and  $d_H$ , respectively), and had a negative surface charge. Most importantly, TNG were capable of releasing trehalose in physiologically relevant conditions (pH 7.4, 37 °C) through the cleavage of trehalose-conjugating ester bonds facilitated by the co-presence of acrylamide-type units. Thanks to the trehalose-rich content, TNG were very stable in serum-enriched media and did not hemolyze red blood cells even at relatively high concentrations. Moreover, TNG were able to accumulate in atherosclerotic plaques with low accumulations in the main organs except liver. Finally, *in vitro* and *in vivo* studies in atherosclerosis confirmed that TNG could enhance the autophagy process, facilitate lipid removal, and reduce plaque area by approximately 60%. Taken together, TNG are promising trehalose delivery systems for atherosclerosis management.

#### **Materials and Methods**

##### **General methods**

Ultrasonication with Sonics VCX 130 (diameter of probe: 3 mm, Sonics & Materials, Inc., USA) was carried out during preparation of a miniemulsion (before photopolymerization) and redispersion of nanogel powder at amplitudes of 60% (5 min) and 40% (30 s), respectively. Each purification process was followed by dialysis and lyophilization in a freeze dryer (ALPHA 1–2 LDplus, CHRIST). NMR spectra were recorded in deuterated solvents (Deutero GmbH) with internal standards using an NMR spectrometer operating at 600 MHz (Varian). Fluorescence study was conducted in SpectraMax i3x Multi-Mode Microplate Reader (Molecular Devices, USA). Both the amount of conjugated trehalose and trehalose release profile were determined enzymatically using a Trehalose Assay Kit (Megazyme International, Ireland). Phosphate buffered saline (PBS, pH 7.0 and 7.4), potassium chloride (KCl), and normal saline (NS) solutions. Deionized water (DI water) was produced using a reverse osmosis system (conductivity < 2  $\mu$ S/cm).

##### **Materials and reagents for synthesis of nanogels**

Acrylamide (AM, Acros Organics), *N,N'*-methylenebisacrylamide (MBA, Acros Organics), 2-hydroxyethyl acrylate (HEA, Acros Organics), lithium phenyl-(2,4,6-trimethylbenzoyl) phosphinate (LAP, Carbosynth), sorbitane monooleate (Span 80, Sigma Aldrich), cyclohexane (Chempur), acetone (Chempur), sulfo-Cy5-amine (Lumiprobe), dialysis membrane (Spectrum™ Spectra/Por™ 2 RC Dialysis Membrane, MWCO: 12–14 kDa). 6-*O*-acryloyl- $\alpha,\alpha'$ -trehalose (TreA) was synthesized following our previously described method [36].

4-acrylamidobutanoic acid (4-AMBA) was synthesized according to Yaşayan et al. (2012) [46]. 4-acrylamidobutanoic acid 3-sulfo-*N*-hydroxysuccinimide ester sodium salt (4-AMBA-Sulfo-NHS) was synthesized based on the method reported by Tsuji et al. (2019) for the synthesis of homologous *N*-sulfosuccinyl-6-hexyloylacrylamide sodium salt [47] and the detailed synthesis procedure is provided in Supplementary Information.

#### **Synthesis of trehalose-releasing nanogels (TNG) and HEA-containing nanogels (HEA<sub>1</sub>NG and HEA<sub>2</sub>NG)**

TNG were synthesized via an inverse miniemulsion free-radical polymerization (FRP) according to our previously described method [33]. Briefly, a water-in-oil (w/o) miniemulsion (1:10, v/v) was created from monomers and photoinitiator-containing aqueous phase (PBS pH 6.0, 1.0 mL) and Span 80-containing organic phase (cyclohexane, 10.0 mL). MBA (20.0 mg), TreA (152.7 mg), AM (35.3 mg), and 4-AMBA (13.4 mg) were placed in a 4-mL dark vial and dissolved in PBS (pH 6.0). The solution of LAP initiator (2.3 mg, 51  $\mu$ L) was added, and the aqueous phase was then transferred into a 20-mL transparent vial containing the cold organic phase (4 °C). The miniemulsion was prepared by ultrasonication of the mixture in ice bath (60% amplitude, 5 min). After that, the vial was covered in aluminum foil and exposed for 0.5 h to high power light-emitting diodes (LEDs, 3 W, 395–405 nm) photoirradiation from the bottom of the vial. Following a precipitation step in 40 mL of acetone, the product was centrifuged at 14,610  $\times$ g for 10 min, twice rinsed with 40 mL of acetone and left to air dry overnight. In order to purify the product, the crude nanogels were suspended in DI water and dialyzed against H<sub>3</sub>PO<sub>4</sub> solution (pH 5.0, MWCO 12–14 kDa) for 24 h with multiple media changes and DI water as the last change. The nanogel dispersion was finally freeze-dried, producing a white fluffy powder that was kept at 4 °C until usage.

To investigate the role of trehalose in nanogel stability, HEA-based nanogels were synthesized using a similar procedure as described earlier. However, in this case, the TreA monomer was replaced with the HEA monomer in both equimolar and equimass of TreA feed (Table S1) for obtaining HEA<sub>1</sub>NG and HEA<sub>2</sub>NG, respectively.

#### **Synthesis of trehalose-releasing nanogels bearing active ester (NHS-TNG)**

To synthesize NHS-TNG, a similar procedure as described for the synthesis of TNG was applied with the difference that 4-AMBA-sulfo-NHS (4.0 mg, 0.011 mmol) was added and the aqueous phase was prepared in PBS neutralized with NaOH to pH 6.0. The crude NHS-TNG were kept at -20 °C without further purification for preparation of fluorescently labeled nanogels.

#### **Synthesis of Cy5-labeled trehalose-releasing nanogels (Cy5-TNG)**

NHS-TNG (10.0 mg) was redispersed in DMSO (250  $\mu$ L) containing sulfo-Cy5-amine (0.25 mg, 0.00033 mmol) and triethylamine (0.068 mg, 0.00067 mmol). Then the nanogel dispersion was shaken overnight in an orbital shaker (1000 rpm, 25 °C). On the next day, the volume was adjusted to 1.0 mL with DMSO, and then the product was precipitated with 3.6 mL of acetone. The suspension was then centrifuged at 14,610  $\times$ g (4 °C, 2 min) and washed six times with acetone. Nanogel precipitate was then redispersed in 800  $\mu$ L of DI water, ultrasonicated at 40% amplitude (30 s), and then dialyzed against H<sub>3</sub>PO<sub>4</sub> solution (pH 5.0, MWCO 12–14 kDa) for 24 h with multiple media changes and DI water as the last change. The pure Cy5-TNG dispersion was finally freeze-dried to obtain fine powder and kept at 4 °C prior to use.

#### **Dynamic light scattering (DLS) and electrophoretic light scattering (ELS)**

Z-average mean hydrodynamic diameter ( $d_{H}$ ) and polydispersity index (PDI) were measured by Dynamic Light Scattering (Malvern, Zetasizer Nano 90 S) (4 mV He-Ne ion laser,  $\lambda$ =633 nm, scattering angle: 90°). The sample was prepared from a TNG stock solution in water (10 mg/mL, prepared with sonication at 40% amplitude for 30 s) by dilution with 1 mM KCl (1.0 mg/mL). In addition, the  $\zeta$  potential of TNG was measured by Electrophoretic Light Scattering (Malvern, Zetasizer Nano ZC).

#### **Cryogenic transmission electron microscopy (cryo-TEM)**

Cryo-TEM analysis was carried out using a Tecnai F20 X TWIN microscope (FEI Company, Hillsboro, Oregon, USA). Images were recorded with a Gatan Rio 16 CMOS 4k camera (Gatan Inc., Pleasanton, California, USA) and processed with Gatan Microscopy Suite (GMS) software (Gatan Inc., Pleasanton, California, USA). Specimens were prepared from TNG dispersion in DI water (500  $\mu$ g/mL) via the vitrification of aqueous solutions on oxygen plasma-activated grids with holey carbon film (Quantifoil R 2/2; Quantifoil Micro Tools GmbH, Großlöbichau, Germany).

#### **Nuclear magnetic spectroscopy (NMR)**

<sup>1</sup>H NMR spectra were recorded in deuterated solvents by using Varian NMR instrument operating at 600 MHz. Chemical shifts are reported in ppm ( $\delta$ ) relative to tetramethylsilane (DMSO-*d*<sub>6</sub>) or 3-(trimethylsilyl)propionic-2,2,3,3-*d*<sub>4</sub> acid sodium salt (D<sub>2</sub>O) as an internal reference.

**Determination of conjugated trehalose (CTre)**

The content of trehalose in nanogels was determined after the alkaline hydrolysis of ester bonds in trehalose acrylate units. Briefly, 40  $\mu\text{L}$  of 1 M NaOH was added to 400  $\mu\text{L}$  of nanogel dispersion (100  $\mu\text{g}/\text{mL}$ ) in PBS (pH 7.4) and the mixture was incubated at 70  $^{\circ}\text{C}$  for 1 h. After neutralization with 40  $\mu\text{L}$  of 1 M HCl, the sample was subjected to enzymatic determination of trehalose by using Trehalose Assay Kit in a microplate assay procedure. CTre (% w/w) was calculated as the percentage of weight of trehalose in nanogel vs. weight of nanogel.

**Trehalose release study by enzymatic determination**

An initial stock dispersion of nanogels (10 mg/mL) was prepared by redispersing nanogel powder in DI water followed by ultrasonication (40% amplitude, 30 s). The stock was diluted to a final concentration of 100  $\mu\text{g}/\text{mL}$  (30 mL) in PBS (pH 7.4) containing 1% v/v antibiotic antimycotic solution in a 50-mL glass vial. Afterward, the nanogel dispersion was placed in an incubator at 37  $^{\circ}\text{C}$  with constant shaking (332  $\times g$ ). Aliquots (800  $\mu\text{L}$ ) were taken every 24 h over 30 days and frozen at -20  $^{\circ}\text{C}$ . After all samples were collected, they were thawed and the amount of trehalose was determined enzymatically.

**Colloidal stability of nanogels in various media**

Colloidal stability of nanogels (1.0 mg/mL, containing 1% v/v antibiotic antimycotic solution) was determined for 7 days at 37  $^{\circ}\text{C}$  in various biological media, including DI water, PBS (pH 7.4), NS, DMEM, and DMEM+10% FBS, by measuring the optical density (OD) at 650 nm on a microplate reader. The OD value was converted to % transmittance using the following equation:

$$\% \text{ Transmittance} = \text{antilog}(2 - \text{OD})$$

**Hemolytic rate of trehalose-releasing nanogels**

Fresh blood was collected from the auricular vein of healthy New Zealand white rabbits. The blood was then diluted with saline at a ratio of 4:5. In this experiment, three types of samples were prepared: a negative control (normal saline), a positive control (ultrapure water), and test samples (TNG at different concentrations). Each sample (1 mL) was immersed in a water bath at 37  $^{\circ}\text{C}$  for 30 min. After that, 20  $\mu\text{L}$  of the diluted rabbit blood was added to each tube.

The tubes were further incubated in a water bath at 37  $^{\circ}\text{C}$  for 1 h. Following the incubation, the samples were centrifuged at 500  $\times g$  for 5 min. The supernatant was carefully removed, and photographs were taken. The collected supernatant was then used to measure OD at a wavelength of 545 nm. The OD value was converted to % hemolytic rate using the following equation:

$$\% \text{ Hemolytic rate} = \frac{OD_t - OD_{nc}}{OD_{pc} - OD_{nc}} \times 100\%$$

Where  $OD_t$  is the OD test value obtained in the presence of trehalose or TNG,  $OD_{nc}$  is the negative control and the  $OD_{pc}$  is the positive control.

**In vitro cytotoxicity of trehalose-releasing nanogels**

The cell harmless nature of TNG is a prerequisite for biological research. The MTS Cell Proliferation and Cytotoxicity Detection Kit was used to measure cytotoxicity of TNG according to the manufacturer's instructions. Briefly, HUVECs were inoculated at a density of  $1 \times 10^4$  per well in 96-well plates. After 24 h, various concentrations of TNG (25, 100, 150, 200  $\mu\text{g}/\text{mL}$ ) were added, and the cells were co-cultured for 24 h. Then, 10  $\mu\text{L}$  of MTS was added to each well and incubated for additional 2–4 h, and finally OD value at 450 nm was measured. The OD value was converted to % cell viability using the following equation:

$$\% \text{ Cell viability} = \frac{OD_t - OD_b}{OD_c - OD_b} \times 100\%$$

Where  $OD_t$  is the OD test value obtained in the presence of TNG,  $OD_c$  is the OD test value obtained in the absence of TNG, and the  $OD_b$  is the OD test value of blank plate.

**In vitro cellular uptake of trehalose-releasing nanogels**

RAW264.7 cells were cultured on 20-mm round coverslip until cell adherence to ~50%. Then the medium was removed and replaced with fresh serum-free culture medium containing free trehalose and TNG labeled with Cy5 which have the equal trehalose concentration. After 1 or 3 h of co-incubation, the medium was removed, washed with PBS for 3 times, then fixed with 4% paraformaldehyde for 15 min, washed with PBS for 3 times again, the nuclei were finally labeled with DAPI and observed under confocal microscope.

**In vitro autophagy stimulation**

Raw 264.7 cells were cultured on 20-mm round coverslip at a density of  $1 \times 10^5$  and in 6-well plates until cell adherence to ~50%. Then the medium was removed and replaced with fresh serum-free culture medium containing 1  $\mu\text{g}/\text{mL}$  of lipopolysaccharide (LPS) and 40  $\mu\text{g}/\text{mL}$  of oxidized low-density lipoprotein (ox-LDL) for 12 h to induce the formation of foam cells.

Trehalose (100  $\mu\text{M}$ ) or TNG (at a concentration equivalent to 100  $\mu\text{M}$  of free trehalose) was added to the above foam cells, incubated for 12 h, then washed 3 times with PBS at 4  $^{\circ}\text{C}$ . Cells in 96-well plates were lysed with RIPA lysis buffer and protease inhibitor (phenylmethylsulfonyl fluoride, PMSF) were added and placed at 4  $^{\circ}\text{C}$ . After

manual scrapping, the lysates were collected and centrifuged at 15,000  $\times g$  for 20 min. Then, the loading buffer was added to the supernatants at a 1:4 ratio, mixed, and then boiled for 5 min before being stored at  $-80^{\circ}\text{C}$ . The sequestosome 1 (p62) and microtubule-associated protein 1 A/1B-light chain 3 (LC3) protein expressions were quantified by Western blot.

Additionally, cells on the round coverslip were also washed three times with PBS at  $4^{\circ}\text{C}$ , fixed with 4% paraformaldehyde for clarity, and then incubated overnight at  $4^{\circ}\text{C}$  with LC3 rabbit polyclonal antibody or p62/SQSTM1 rabbit polyclonal antibody. After rinsing the round coverslips five times with PBST (0.1% Tween-20 PBS), they were incubated for 1 h with fluorescently-labeled rabbit secondary antibodies under darkness. Subsequently, the coverslips were washed five times before the nuclei were finally labeled with DAPI. Fluorescence signals from DAPI, p62, and LC3 were detected by SP8 confocal microscopy.

#### **Intracellular ROS clearance in macrophages**

RAW264.7 cells were cultured in 12-well plates for 12 h. After cells were pretreated with trehalose (100  $\mu\text{M}$ ) or TNG (at a concentration equivalent to 100  $\mu\text{M}$  of free trehalose) for 4 h, they were stimulated with 0.5  $\mu\text{M}$   $\text{H}_2\text{O}_2$  for 0.5 h. The negative control group was treated with fresh medium, and the positive control group was only stimulated with 0.5  $\mu\text{M}$   $\text{H}_2\text{O}_2$  for 0.5 h. Subsequently, cells were rinsed and treated with DCFH-DA (10  $\mu\text{M}$ ) in serum-free DMEM for 30 min. After washing with PBS and the intracellular ROS clearance was observed in cell culture dishes by fluorescence microscope. Through similar procedures, the cells were harvested in PBS, intracellular fluorescent signals were measured via flow cytometry (CytoFLEX, Beckman Coulter) and analyzed using FlowJo software.

#### **In vitro lipid efflux**

Raw 264.7 cells were inoculated in 6-well plates at a cell density of  $2 \times 10^5$  per well. Cells were then stimulated with 1  $\mu\text{g}/\text{mL}$  of LPS and 40  $\mu\text{g}/\text{mL}$  of ox-LDL to form foam cells. The cells were treated with free trehalose (100  $\mu\text{M}$ ) or TNG (at a concentration equivalent to 100  $\mu\text{M}$  of free trehalose) for 24 h. Following this, the medium was removed, and the cells were washed twice with PBS before being fixed using a 4.0% paraformaldehyde (PFA) solution. Subsequently, the cells were incubated with Oil Red O (ORO) isopropanol working solution for 15 min. Then cells were observed by optical microscopy. In addition, the intracellular ORO was extracted by isopropanol and the ORO concentration was determined by measuring its absorbance at 524 nm via an UV-Vis spectroscopy.

#### **Animal models**

Male apolipoprotein E-deficient ( $\text{ApoE}^{-/-}$ ) mice, aged eight weeks, were obtained from the Hunan SJA Bioscience Co., Ltd. (Hunan, China). All animal care and experimental protocols comply with the relevant laws, regulations and standards concerning animal welfare ethics. This project has been supervised and approved by Laboratory Animal Welfare and Ethics Committee of Chongqing University (IACUC issue number: COU-IACUC-RE-202109-002).

#### **Atherosclerosis treatment with nanogels**

$\text{ApoE}^{-/-}$  mice were randomized into 3 groups (5 mice/group), and high fat diet (HFD) was given for 12 weeks. Then, the mice were subjected to different treatments for one month. The mice were injected with 0.9% saline as the untreated control group, while the other two groups were treated with either free trehalose at a dose of 2.5 g/kg of trehalose, or TNG at a concentration of 16 mg/kg every three days via tail vein injection. The body weight of mice was monitored during the treatment.

#### **In vivo pharmacokinetics evaluation of nanogels**

To evaluate the in vivo pharmacokinetics of TNG, the Cy5-labeled TNG (Cy5-TNG) was intravenously administered to C57BL/6 mice at dose of 16 mg/kg, while free Cy5 was intravenously injected at the equal concentration of Cy5 in Cy5-TNG. Then, 20  $\mu\text{L}$  of blood was collected at 0.5, 1, 2, 4, 8, 12, and 24 h after injection. The blood samples were diluted with 40  $\mu\text{L}$  PBS contained EDTA2K in 96-well black plates, and the fluorescence intensity was measured by fluorescence microplate reader (Hitachi, Japan).

#### **In vivo accumulation of nanogels in atherosclerotic lesion and biodistribution**

After atherosclerosis modeling, mice were injected with 150  $\mu\text{L}$  Cy5 (control group) or Cy5-TNG via tail vein. After 24 h, the mice were euthanized, and the aortas were isolated after perfusion with 0.9% saline containing heparin sodium. Additionally, heart, liver, spleen, lung, and kidney were harvested to analyze the biodistribution of nanogels in the main organs. Imaging and fluorescence quantification were performed using the Xenogen IVIS 200 system.

#### **Efficacy study and histological study of atherosclerotic plaques after treatment**

Quantitative analysis of atherosclerotic plaques after treatments: After the 10th round of trehalose and TNG treatments via intravenous injections (IV), the aortas from  $\text{ApoE}^{-/-}$  mice were harvested, spanning from the heart to the iliac bifurcation. Aortas were fixed by perfusion with 4% paraformaldehyde, dissected longitudinally,

and then stained with Oil Red O (ORO) to quantify the plaque area. The extent of atherosclerotic plaque at the aortic root was also determined by the same way. Quantitative analysis of atherosclerotic plaque areas was performed using Photoshop 2020 software.

The aortic roots were fixed with 4% paraformaldehyde in PBS for 1 h. Frozen sections were prepared from the fixed samples, and ORO staining was performed to quantify the plaque area. For immunofluorescence analysis, the sections were washed with PBS and then permeabilized/blocked using a solution containing 0.5% Triton-X100 in 5% BSA. Antibodies specific to p62, LC3 and CD68 were separately incubated with the sections overnight at 4 °C. After washing the sections five times with PBST (PBS with 0.1% Tween-20), they were incubated with secondary antibodies for 1 h. Nuclei were stained with DAPI in the dark. The fluorescence signals from DAPI, p62, LC3 and CD68 were detected using SP8 confocal microscopy (Leica, Germany). Sections of the main organs including heart, liver, spleen, lung, and kidney were analyzed by hematoxylin-eosin (HE) staining.

After one month of treatments, a complete blood routine analysis and serum biochemistry analysis were conducted. Blood samples were collected and analyzed using an automated hematology analyzer (Sysmex KX-21, Sysmex Co., Japan) to obtain the complete blood count (CBC) data. The concentrations of various biochemical markers, including alanine aminotransferase (ALT), aspartate aminotransferase (AST), creatinine (CR), uric acid (UA), high-density lipoprotein (HDL), low-density lipoprotein (LDL), triglyceride (TG), and total cholesterol (TC) in the serum, were quantified using an automated analyzer platform (Roche Cobas C501, Roche Co., Switzerland).

### Statistical analysis

The collected data were presented as mean  $\pm$  SD ( $n \geq 3$ ). The statistical analysis was performed using GraphPad Prism Version 8.4.3 software (GraphPad, USA). Tukey's test and one-way analysis of variance (ANOVA) were employed to identify group differences. To determine whether there is a significant difference between two specific groups, an unpaired *t*-test (two tails) was used. The significance thresholds for differences were set at \* $p < 0.05$ , \*\* $p < 0.01$ , \*\*\* $p < 0.001$ , \*\*\*\* $p < 0.0001$ , and *ns*, no significance.

### Supplementary Information

The online version contains supplementary material available at <https://doi.org/10.1186/s12951-023-02248-9>.

Supplementary Material 1

### Acknowledgements

We would like to thank the group members of Membrane based Biomimetic and Intelligent Nano-Carrier (MBINC) group, Bioengineering College, Chongqing University, for the help during experiments. The graphical abstract was created with BioRender.com.

### Author Contributions

YZ: Investigation, Formal analysis, Visualization, Data Curation, Writing - original draft preparation. AM: Investigation, Formal analysis, Visualization, Data Curation, Writing - original draft preparation. KQ: Animal study, Data Curation. MM: Conceptualization, Investigation, Writing - Review & Editing. IW: Conceptualization, Methodology, Writing - Review & Editing, Project administration, Funding acquisition. NLM: Animal study. YC: Biocompatibility study. WW: Conceptualization, Methodology, Writing - original draft preparation, Writing - Review & Editing, Supervision, Project administration, Funding acquisition.

### Funding

This work was supported by grants from the Fundamental Research Funds for the National Key R&D Project (2022YFF0710700), National Natural Science Foundation of China (31971301, 32171324), Natural Science Foundation of Chongqing (cstc2021jcyj-msxmX0149, CSTB2022NSCQ-BHX0724, CSTB2022NSCQ-BHX0718), and Fundamental Research Funds for Central Universities (2023CDJXY-051, 2022CDJXY-026, 2020CDJQY-A061). The authors are grateful to the help of Yu Zhang (Analytical & Testing Center, Chongqing University) of taking laser scanning confocal images. This study was co-financed by the PRELUDIUM BIS 1 (2019/35/O/ST5/02746) from the National Science Centre (NCN), Poland.

### Data Availability

All data contained in the study are in this article.

### Declarations

#### Ethics approval and consent to participate

All animal care and experimental protocols comply with the relevant laws, regulations and standards concerning animal welfare ethics. This project has been supervised and approved by Laboratory Animal Welfare and Ethics Committee of Chongqing University (IACUC issue number: COU-IACUC-RE-202109-002).

#### Competing interests

The authors declare no competing interests.

#### Author details

<sup>1</sup>Key Laboratory for Biorheological Science and Technology of Ministry of Education, State and Local Joint Engineering Laboratory for Vascular Implants, Bioengineering College, Faculty of Medicine, Chongqing University, Chongqing 400030, China

<sup>2</sup>Department of Organic Chemistry, Bioorganic Chemistry and Biotechnology, Faculty of Chemistry, Silesian University of Technology, Krzywoustego 4, Gliwice 44-100, Poland

<sup>3</sup>Biotechnology Center, Silesian University of Technology, Krzywoustego 8, Gliwice 44-100, Poland

Received: 25 August 2023 / Accepted: 3 December 2023

Published online: 08 December 2023

### References

- Libby P, Buring JE, Badimon L, Hansson GK, Deanfield J, Bittencourt MS, Tokgozoglu L, Lewis EF. Atherosclerosis. *Nat Rev Dis Primers*. 2019;5(1):56. <https://doi.org/10.1038/s41572-019-0106-z>.
- Klionsky DJ, Petroni G, Amaravadi RK, Baehrecke EH, Ballabio A, Boya P, Bravo-San PJ, Cadwell K, Cecconi F, Choi A. Autophagy in major human Diseases. *EMBO J*. 2021;40(19):e108863. <https://doi.org/10.15252/embj.2021108863>.
- Ouimet M, Franklin V, Mak E, Liao X, Tabas I, Marcel YL. Autophagy regulates cholesterol efflux from macrophage foam cells via lysosomal acid lipase. *Cell Metab*. 2011;13(6):655–67. <https://doi.org/10.1016/j.cmet.2011.03.023>.

- Hassanpour M, Rahbarghazi R, Nouri M, Aghamohammadzadeh N, Safaei N, Ahmadi M. Role of autophagy in Atherosclerosis: foe or friend? *J Inflamm (Lond)*. 2019;16:8. <https://doi.org/10.1186/s12950-019-0212-4>.
- Sergin I, Razani B. Self-eating in the plaque: what macrophage autophagy reveals about Atherosclerosis. *Trends Endocrinol Metab*. 2014;25(5):225–34. <https://doi.org/10.1016/j.tem.2014.03.010>.
- Emanuel R, Sergin I, Bhattacharya S, Turner J, Epelman S, Settembre C, Diwan A, Ballabio A, Razani B. Induction of lysosomal biogenesis in atherosclerotic macrophages can rescue lipid-induced lysosomal dysfunction and downstream sequelae. *Arterioscler Thromb Vasc Biol*. 2014;34(9):1942–52. <https://doi.org/10.1161/ATVBAHA.114.303342>.
- Liao X, Sluimer JC, Wang Y, Subramanian M, Brown K, Pattison JS, Robbins J, Martinez J, Tabas I. Macrophage autophagy plays a protective role in advanced Atherosclerosis. *Cell Metab*. 2012;15(4):545–53. <https://doi.org/10.1016/j.cmet.2012.01.022>.
- Salabei JK, Hill BG. Implications of autophagy for vascular smooth muscle cell function and plasticity. *Free Radic Biol Med*. 2013;65:693–703. <https://doi.org/10.1016/j.freeradbiomed.2013.08.003>.
- Vion AC, Kheloufi M, Hammoutene A, Poisson J, Lasselins J, Devue C, Pic I, Dupont N, Busse J, Stark K. Autophagy is required for endothelial cell alignment and atheroprotection under physiological blood flow. *Proc Natl Acad Sci U S A*. 2017;114(41):E8675–84. <https://doi.org/10.1073/pnas.1702231114>.
- Beltowski J, Wojcicka G, Jamroz-Wisniewska A. Adverse effects of statins - mechanisms and consequences. *Curr Drug Saf*. 2009;4(3):209–28. <https://doi.org/10.2174/157488609789006949>.
- Bavry AA, Elgendy IY, Elbez Y, Mahmoud AN, Sorbets E, Steg PG, Bhatt DL. Aspirin and the risk of cardiovascular events in Atherosclerosis patients with and without prior ischemic events. *Clin Cardiol*. 2017;40(9):732–9. <https://doi.org/10.1002/clc.22724>.
- Kurdi A, De Meyer GR, Martinet W. Potential therapeutic effects of mtor inhibition in Atherosclerosis. *Br J Clin Pharmacol*. 2016;82(5):1267–79. <https://doi.org/10.1111/bcp.12820>.
- Liu Y, Yang F, Zou S, Qu L. Rapamycin: a bacteria-derived immunosuppressant that has anti-atherosclerotic effects and its clinical application. *Front Pharmacol*. 2018;9:1520. <https://doi.org/10.3389/fphar.2018.01520>.
- Khalifeh M, Barreto GE, Sahebkar A. Trehalose as a promising therapeutic candidate for the treatment of parkinson's Disease. *Br J Pharmacol*. 2019;176(9):1173–89. <https://doi.org/10.1111/bph.14623>.
- Tanji K, Miki Y, Maruyama A, Mimura J, Matsumiya T, Mori F, Imaizumi T, Itoh K, Wakabayashi K. Trehalose intake induces chaperone molecules along with autophagy in a mouse model of Lewy Body Disease. *Biochem Biophys Res Commun*. 2015;465(4):746–52. <https://doi.org/10.1016/j.bbrc.2015.08.076>.
- Du J, Liang Y, Xu F, Sun B, Wang Z. Trehalose rescues alzheimer's Disease phenotypes in app/ps1 transgenic mice. *J Pharm Pharmacol*. 2013;65(12):1753–6. <https://doi.org/10.1111/jpph.12108>.
- Xu C, Chen X, Sheng WB, Yang P. Trehalose restores functional autophagy suppressed by high glucose. *Reprod Toxicol*. 2019;85:51–8. <https://doi.org/10.1016/j.reprotox.2019.02.005>.
- DeBosch BJ, Heitmeier MR, Mayer AL, Higgins CB, Crowley JR, Kraft TE, Chi M, Newberry EP, Chen Z, Finck BN. Trehalose inhibits solute carrier 2a (slc2a) proteins to induce autophagy and prevent hepatic steatosis. *Sci Signal*. 2016;9(416):a21. <https://doi.org/10.1126/scisignal.aac5472>.
- Liu S, Yang Y, Gao H, Zhou N, Wang P, Zhang Y, Zhang A, Jia Z, Huang S. Trehalose attenuates renal ischemia-reperfusion injury by enhancing autophagy and inhibiting oxidative stress and inflammation. *Am J Physiol Renal Physiol*. 2020;318(4):F994–F1005. <https://doi.org/10.1152/ajprenal.00568.2019>.
- Sergin I, Evans TD, Zhang X, Bhattacharya S, Stokes CJ, Song E, Ali S, Dehestani B, Holloway KB, Micevych PS. Exploiting macrophage autophagy-lysosomal biogenesis as a therapy for Atherosclerosis. *Nat Commun*. 2017;8:15750. <https://doi.org/10.1038/ncomms15750>.
- Evans TD, Jeong SJ, Zhang X, Sergin I, Razani B. Tfeb and trehalose drive the macrophage autophagy-lysosome system to protect against Atherosclerosis. *Autophagy*. 2018;14(4):724–26. <https://doi.org/10.1080/15548627.2018.1434373>.
- Sahebkar A, Hatamipour M, Tabatabaei SA. Trehalose administration attenuates Atherosclerosis in rabbits fed a high-fat diet. *J Cell Biochem*. 2019;120(6):9455–9. <https://doi.org/10.1002/jcb.28221>.
- Stachowicz A, Wisniewska A, Kuś K, Kiepusa A, Gebska A, Gajda M, Białas M, Totoró-Zuráfska J, Stachyra K, Suski M. The influence of trehalose on Atherosclerosis and hepatic steatosis in apolipoprotein e knockout mice. *Int J Mol Sci*. 2019;20(7):1552. <https://doi.org/10.3390/ijms20071552>.
- Hosseinpour-Moghaddam K, Caraglia M, Sahebkar A. Autophagy induction by trehalose: molecular mechanisms and therapeutic impacts. *J Cell Physiol*. 2018;233(9):6524–43. <https://doi.org/10.1002/jcp.26583>.
- Lee HJ, Yoon YS, Lee SJ. Mechanism of neuroprotection by trehalose: controversy surrounding autophagy induction. *Cell Death Dis*. 2018;9(7):712. <https://doi.org/10.1038/s41419-018-0749-9>.
- Montalto M, Gallo A, Ojetti V, Gasbarrini A. Fructose, trehalose and sorbitol malabsorption. *Eur Rev Med Pharmacol Sci*. 2013;17(Suppl 2):26–9.
- Richards AB, Krakowka S, Dexter LB, Schmid H, Wolterbeek AP, Waalkens-Berendsen DH, Shigoyuki A, Kurimoto M. Trehalose: a review of properties, history of use and human tolerance, and results of multiple safety studies. *Food Chem Toxicol*. 2002;40(7):871–98. [https://doi.org/10.1016/S0278-6915\(02\)00011-x](https://doi.org/10.1016/S0278-6915(02)00011-x).
- Maruf A, Wang Y, Yin T, Huang J, Wang N, Durkan C, Tan Y, Wu W, Wang G. Atherosclerosis treatment with stimuli-responsive nanoagents: recent advances and future perspectives. *Adv Healthc Mater*. 2019;8(11):e1900036. <https://doi.org/10.1002/adhm.201900036>.
- Guo Y, Qin J, Zhao Q, Yang J, Wei X, Huang Y, Xie M, Zhang C, Li Y. Plaque-targeted rapamycin spherical nucleic acids for synergistic Atherosclerosis treatment. *Adv Sci (Weinh)*. 2022;9(16):e2105875. <https://doi.org/10.1002/advs.202105875>.
- You P, Mayier A, Zhou H, Yang A, Fan J, Ma S, Liu B, Jiang Y. Targeting and promoting Atherosclerosis regression using hybrid membrane coated nano-materials via alleviated inflammation and enhanced autophagy. *Appl Mater Today*. 2022;26:101386. <https://doi.org/10.1016/j.apmt.2022.101386>.
- Wu Z, Zhou M, Tang X, Zeng J, Li Y, Sun Y, Huang J, Chen L, Wan M, Mao C. Carrier-free trehalose-based nanomotors targeting macrophages in inflammatory plaque for treatment of Atherosclerosis. *ACS Nano*. 2022;16(3):3808–20. <https://doi.org/10.1021/acsnano.1c08391>.
- Li Z, Zhang L, Xue C, Zhang Y, Yu Y, Guo X, Zhang Z. Hydroxypropyl- $\beta$ -cyclodextrin/oridonin and trehalose loaded nanovesicles attenuate foam cells formation and regulate the inflammation. *Eur Polym J*. 2022;180:111596. <https://doi.org/10.1016/j.eurpolymj.2022.111596>.
- Maruf A, Milewska M, Kovacs T, Varga M, Vellai T, Lalik A, Student S, Borges O, Wandzik I. Trehalose-releasing nanogels: a step toward a trehalose delivery vehicle for autophagy stimulation. *Biomater Adv*. 2022;138:212969. <https://doi.org/10.1016/j.bioadv.2022.212969>.
- Neamtu I, Rusu AG, Diaconu A, Nita LE, Chiriac AP. Basic concepts and recent advances in nanogels as carriers for medical applications. *Drug Deliv*. 2017;24(1):539–57. <https://doi.org/10.1080/10717544.2016.1276232>.
- Vinogradov S, Batrakova E, Kabanov A. Poly (ethylene glycol)-polyethyl-eneimine nanogel™ particles: novel drug delivery systems for antisense oligonucleotides. *Colloids Surf B*. 1999;16:191–304. [https://doi.org/10.1016/S0927-7765\(99\)00080-6](https://doi.org/10.1016/S0927-7765(99)00080-6).
- Burek M, Wandzik I. Trehalose-rich, degradable hydrogels designed for trehalose release under physiologically relevant conditions. *Polym (Basel)*. 2019;11(12). <https://doi.org/10.3390/polym11122027>.
- Burek M, Waskiewicz S, Lalik A, Wandzik I. Hydrogels with novel hydrolytically labile trehalose-based crosslinks: small changes – big differences in degradation behavior. *Polym Chem -UK*. 2018;27(9):3721–6. <https://doi.org/10.1039/C8PY00488A>.
- Moore TL, Rodriguez-Lorenzo L, Hirsch V, Balog S, Urban D, Jud C, Rothen-Rutishauser B, Lattuada M, Petri-Fink A. Nanoparticle colloidal stability in cell culture media and impact on cellular interactions. *Chem Soc Rev*. 2015;44(17):6287–305. <https://doi.org/10.1039/c4cs00487f>.
- Sukhanova A, Bozrova S, Sokolov P, Berestovoy M, Karaulov A, Nabiev I. Dependence of nanoparticle toxicity on their physical and chemical properties. *Nanoscale Res Lett*. 2018;13(1):44. <https://doi.org/10.1186/s11671-018-2457-x>.
- Corbo C, Molinaro R, Parodi A, Toledano FN, Salvatore F, Tasciotti E. The impact of nanoparticle protein corona on cytotoxicity, immunotoxicity and target drug delivery. *Nanomed (Lond)*. 2016;11(1):81–100. <https://doi.org/10.2217/nnm.15.188>.
- Albanese A, Chan WC. Effect of gold nanoparticle aggregation on cell uptake and toxicity. *ACS Nano*. 2011;5(7):5478–89. <https://doi.org/10.1021/nn2007496>.
- Mesdaghinia A, Pourpak Z, Naddafi K, Nodehi RN, Alizadeh Z, Rezaei S, Mohammadi A, Faraji M. An in vitro method to evaluate hemolysis of human red blood cells (rbcs) treated by airborne particulate matter (pm(10)). *MethodsX*. 2019;6:156–61. <https://doi.org/10.1016/j.mex.2019.01.001>.
- Tanida I, Ueno T, Kominami E. Lc3 and autophagy. *Methods Mol Biol*. 2008;445:77–88. [https://doi.org/10.1007/978-1-59745-157-4\\_4](https://doi.org/10.1007/978-1-59745-157-4_4).

44. Filali-Mouncef Y, Hunter C, Roccio F, Zagkou S, Dupont N, Primard C, Proikas-Cezanne T, Reggiori F. The menage a trois of autophagy, lipid droplets and Liver Disease. *Autophagy*. 2022;18(1):50–72. <https://doi.org/10.1080/15548627.2021.1895658>.
45. Rusmini P, Cortese K, Crippa V, Cristofani R, Cicardi ME, Ferrari V, Vezzoli G, Tedesco B, Meroni M, Messi E. Trehalose induces autophagy via lysosomal-mediated tfeb activation in models of motoneuron degeneration. *Autophagy*. 2019;15(4):631–51. <https://doi.org/10.1080/15548627.2018.1535292>.
46. Gökçen Y, Martin R, Johannes PM, Sebastian GS, Stephanie A, Martyn D, Cameron A, Francisco F. Well-defined polymeric vesicles with high stability and modulation of cell uptake by a simple coating protocol. *Polym Chem -UK*. 2012;3(9):2596–604.
47. Sotaro T, Yuji A, Hitomi O, Tomonari T. Polymeric water-soluble activated esters: synthesis of polymer backbones with pendant n-hydroxysulfosuccinimide esters for post-polymerization modification in water. *Polym J*. 2019;51(10):1015–22. [https://doi.org/10.1016/S0927-7765\(99\)00080-6](https://doi.org/10.1016/S0927-7765(99)00080-6).

**Publisher's Note**

Springer Nature remains neutral with regard to jurisdictional claims in published maps and institutional affiliations.

## *Supplementary Information*

*for*

### **Nanogels with covalently bound and releasable trehalose for autophagy stimulation in atherosclerosis**

Yuan Zhong<sup>1,†</sup>, Ali Maruf<sup>2,3,†</sup>, Kai Qu<sup>1</sup>, Małgorzata Milewska<sup>2,3</sup>, Ilona Wandzik<sup>2,3,\*</sup>, Nianlian Mou<sup>1</sup>, Yu Cao<sup>1</sup>, Wei Wu<sup>1,\*</sup>

<sup>1</sup> Key Laboratory for Biorheological Science and Technology of Ministry of Education, State and Local Joint Engineering Laboratory for Vascular Implants, Bioengineering College, Faculty of Medicine, Chongqing University, Chongqing 400030, China

<sup>2</sup> Department of Organic Chemistry, Bioorganic Chemistry and Biotechnology, Faculty of Chemistry, Silesian University of Technology, Krzywoustego 4, 44-100 Gliwice, Poland

<sup>3</sup> Biotechnology Center, Silesian University of Technology, Krzywoustego 8, 44-100 Gliwice, Poland

<sup>†</sup> The authors contribute equally to this work

\* Corresponding authors. E-mail addresses: david2015@cqu.edu.cn (WW), ilona.wandzik@polsl.pl (IW)



**Formulation of nanogels**

**Table S1.** Formulation of nanogels based on moles and mass feeding.

Samples	Formulation based on moles and mass (mmol (mg))					
	TreA	HEA	AM	4-AMBA	4-AMBA- sulfo-NHS	MBA
<b>TNG</b>	0.385 (152.7)	-	0.496 (35.3)	0.085 (13.4)	-	0.130 (20.0)
<b>HEA<sub>1</sub>NG</b>	-	0.385 (44.8)	0.496 (35.3)	0.085 (13.4)	-	0.130 (20.0)
<b>HEA<sub>2</sub>NG</b>	-	1.315 (152.7)	0.496 (35.3)	0.085 (13.4)	-	0.130 (20.0)
<b>NHS-TNG</b>	0.385 (152.7)	-	0.496 (35.3)	0.085 (13.4)	0.011 (4.0)	0.130 (20.0)

TNG: trehalose-releasing nanogels, HEA<sub>1</sub>NG and HEA<sub>2</sub>NG: 2-hydroxyethyl acrylate-containing nanogels, HEA: 2-hydroxyethyl acrylate, AM: acrylamide, 4-AMBA: 4-acrylamidobutanoic acid, TreA: 6-O-acryloyl- $\alpha$ , $\alpha'$ -trehalose, MBA: *N,N'*-methylenebisacrylamide.

Colloidal stability of TNG, HEA<sub>1</sub>NG and HEA<sub>2</sub>NG in different biological media for 7 days

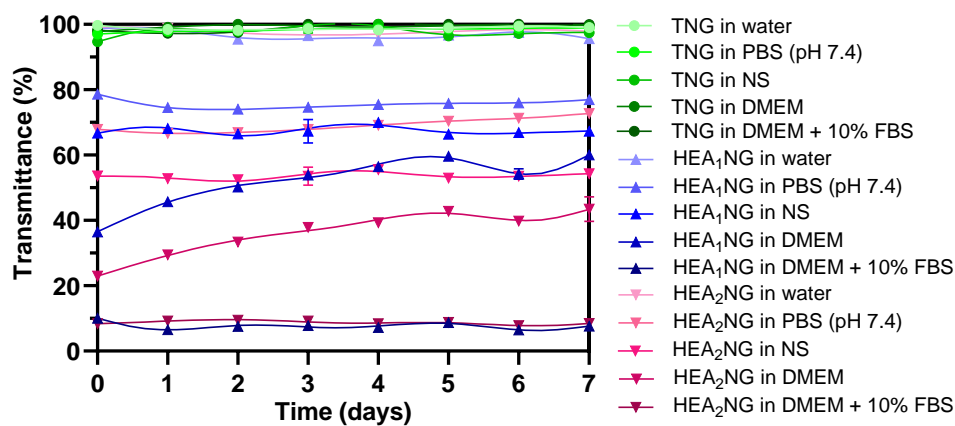
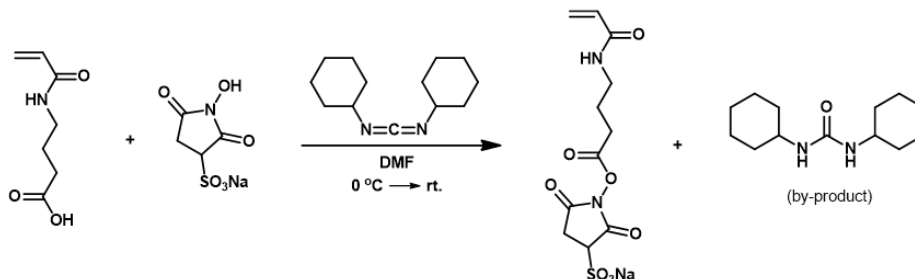


**Figure S1.** Colloidal stability of TNG, HEA<sub>1</sub>NG and HEA<sub>2</sub>NG in different biological media for 7 days. TNG: trehalose-releasing nanogels, HEA<sub>1</sub>NG and HEA<sub>2</sub>NG: 2-hydroxyethyl acrylate-containing nanogels.

**Synthesis of 4-acrylamidobutanoic acid 3-sulfo-*N*-hydroxysuccinimide ester sodium salt (4-AMBA-Sulfo-NHS)**



4-AMBA-Sulfo-NHS was synthesized based on the method reported by Tsuji et al. (2019) for the synthesis of homologous *N*-sulfosuccinyl-6-hexyloylacrylamide sodium salt. Briefly, sulfo-NHS (434.3 mg, 2.0 mmol) and 4-AMBA (314.3 mg, 2.0 mmol) were placed in a 25 mL round-bottom flask and dissolved in anhydrous DMF (6 mL) under argon atmosphere while stirring. The flask was then cooled in an ice bath for 15 min. A DCC solution (833.6 mg, 4.0 mmol) in 2.0 mL of anhydrous DMF was added dropwise into the mixture and kept 1 h in an ice bath, followed by another 20 h at room temperature. On the next day, the reaction mixture was transferred to the refrigerator (4 °C) for 30 min followed by filtration through Celite and washing with 3 mL of DMF. The product was then precipitated with 140 mL of diethyl ether, centrifuged at 14610 ×g (4 °C, 2 min) and washed four times with 20 mL of diethyl ether. The white precipitate was then dried under reduced pressure to give the final product (4-AMBA-Sulfo-NHS) with 49% yield.

**Reference:** S. Tsuji, Y. Aso, H. Ohara, and T. Tanaka, “Polymeric water-soluble activated esters: synthesis of polymer backbones with pendant *N*-hydroxysulfosuccinimide esters for post-polymerization modification in water,” *Polym J*, vol. 51, no. 10, pp. 1015–1022, Oct. 2019, doi:10.1038/s41428-019-0221-4.

**<sup>1</sup>H NMR** (DMSO-*d*<sub>6</sub>, 600 MHz) δ [ppm]: 8.18 (t, *J* = 5.6 Hz, 1H, –NHC(O)–); 6.20 (dd, *J* = 17.1, 10.2 Hz, 1H, –CH=CH<sub>2</sub>); 6.08 (dd, *J* = 17.1, 2.2 Hz, 1H, –CH=CH<sub>2</sub> *trans*); 5.58 (dd, *J* = 10.2, 2.2 Hz, 1H, –CH=CH<sub>2</sub> *cis*); 3.95 (bs, 1H, >CHSO<sub>3</sub>Na); 3.24–3.08 (m, 3H, –NHCH<sub>2</sub>–, –CH<sub>a</sub>H<sub>b</sub>CHSO<sub>3</sub>Na); 2.86 (dd, *J* = 18.4, 2.4 Hz, 1H, –CH<sub>a</sub>H<sub>b</sub>CHSO<sub>3</sub>Na); 2.75–2.65 (m, 2H, –CH<sub>2</sub>C(O)O–); 1.83–1.73 (m, 2H, –CH<sub>2</sub>CH<sub>2</sub>CH<sub>2</sub>–). **<sup>13</sup>C NMR** (DMSO-*d*<sub>6</sub>, 150 MHz) δ [ppm]: 168.77, 165.33 (2x –C(O)N<, –C(O)O–); 164.67 (–NHC(O)–); 131.68 (–CH=CH<sub>2</sub>); 125.03 (–CH=CH<sub>2</sub>); 56.27 (>CHSO<sub>3</sub>Na); 37.57 (–NHCH<sub>2</sub>–); 30.91 (–CH<sub>2</sub>CHSO<sub>3</sub>Na); 27.86 (–CH<sub>2</sub>C(O)O–); 24.26 (–CH<sub>2</sub>CH<sub>2</sub>CH<sub>2</sub>–).

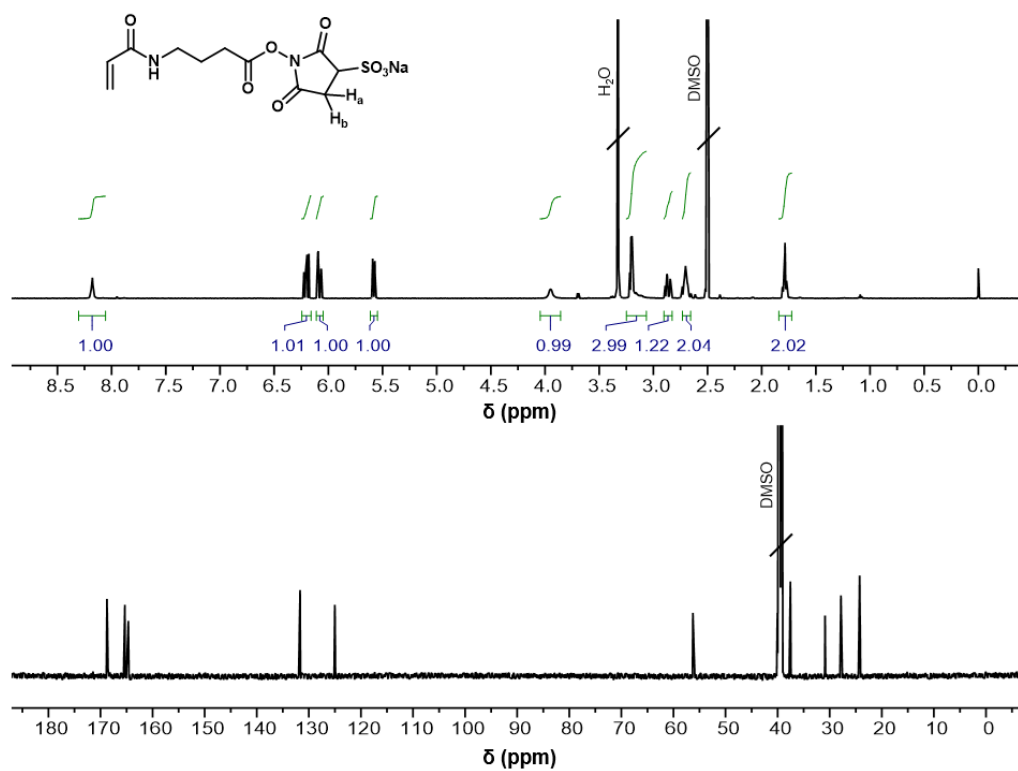


**Figure S2.**  $^1\text{H}$  (600 MHz) and  $^{13}\text{C}$  NMR (150 MHz) spectra of 4-acrylamidobutanoic acid 3-sulfo-*N*-hydroxysuccinimide ester sodium salt.

**Actual conjugated trehalose**

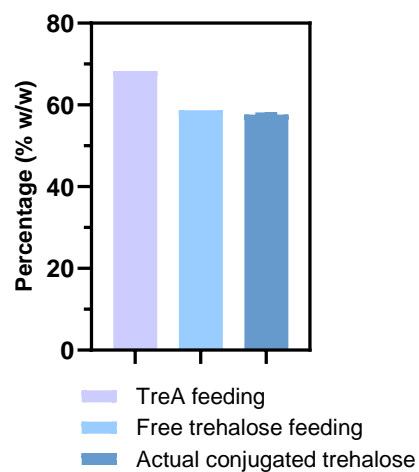


**Figure S3.** Actual conjugated trehalose compared to the recipe. TreA feeding and free trehalose feeding were determined based on the recipe. Actual conjugated trehalose was determined by enzymatic assay. Data are presented as mean  $\pm$  *SD* ( $n = 4$ ).

**Hemolysis profile of TNG**

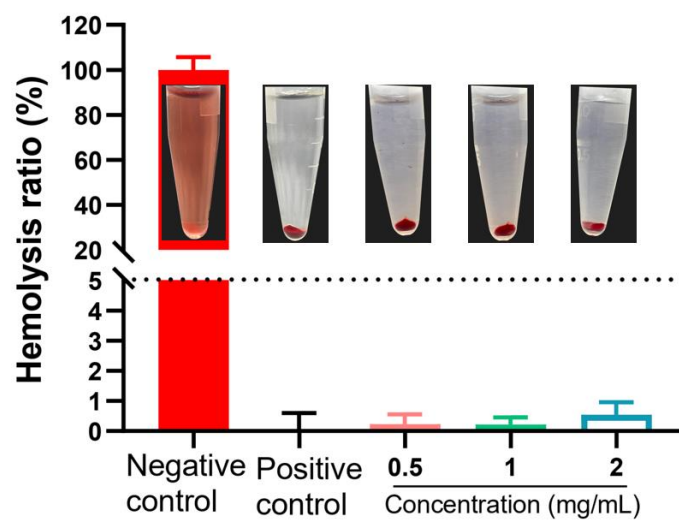


**Figure S4.** Hemolysis profile of trehalose-releasing nanogels (TNG) at different concentrations (0.5, 1.0, and 2.0 mg/mL) in red blood cells. Data are presented as mean  $\pm$  *SD* ( $n = 3$ ).

**Cytotoxicity profile of TNG**

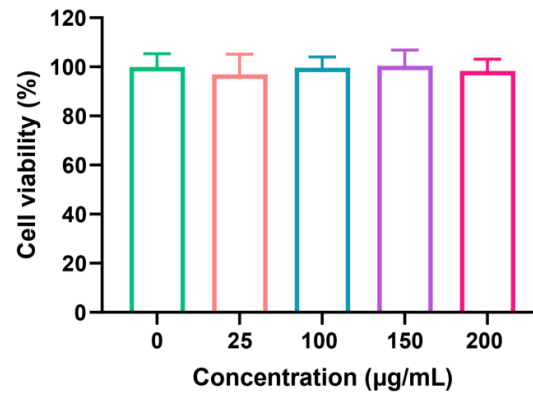


**Figure S5.** HUVECs viability after treatments with trehalose-releasing nanogels (TNG) at different concentrations (0, 25, 100, 150, and 200 µg/mL) for 24 h. Data are presented as mean  $\pm$  SD ( $n = 5$ ).

**Cellular uptake of TNG**

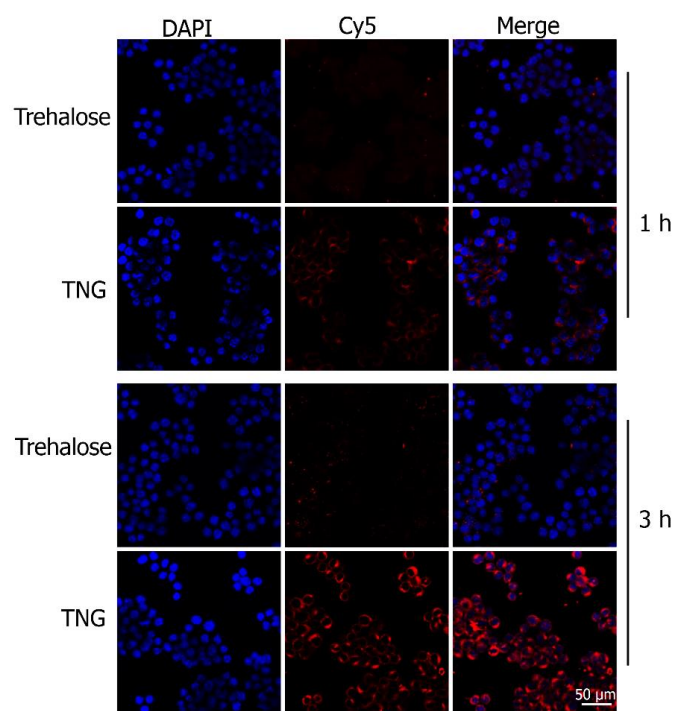


**Figure S6.** Confocal microscopy images of time-dependent cellular uptake of Cy5-TNG or trehalose. After RAW264.7 cells were incubated with Cy5-TNG or trehalose for various periods of time, nuclei were stained with DAPI (blue), Cy5 was red, scale bar: 50 μm.



*In vivo* pharmacokinetics evaluation of nanogels in mice

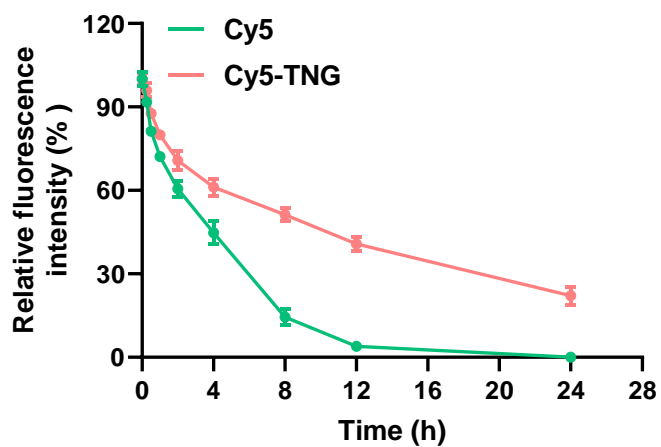


**Figure S7.** *In vivo* pharmacokinetics evaluation of nanogels in mice. TNG was fluorescently conjugated with Cy5. Cy5-TNG was intravenously injected at concentration of 16 mg/kg, while free Cy5 was injected at the equal concentration of Cy5 in Cy5-TNG.

**CD68 expression in atherosclerosis plaque after one-month treatment**

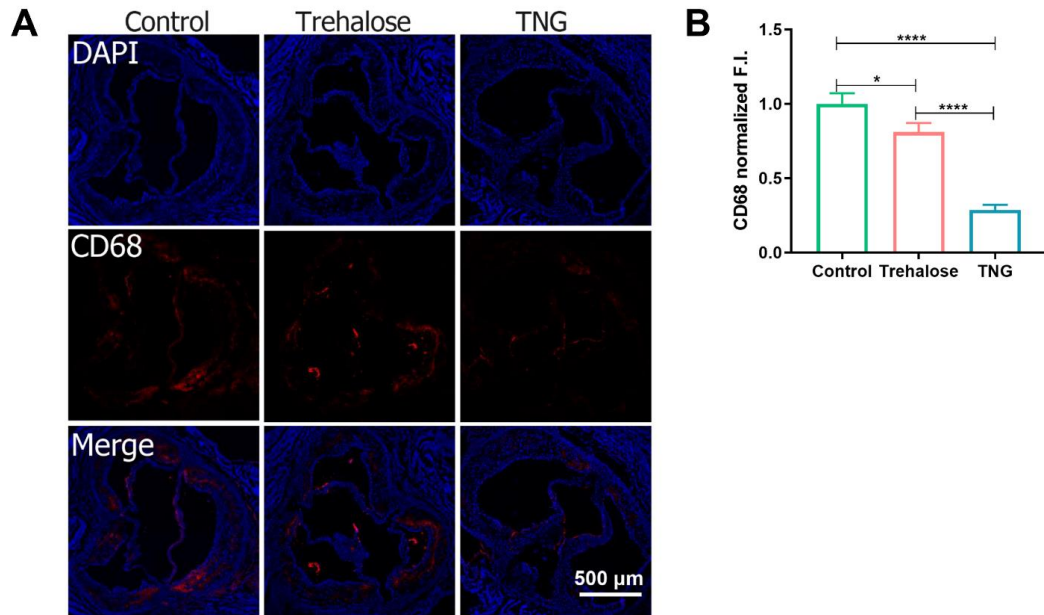


**Figure S8.** (A) CLSM images and (B) quantification of CD68 (red fluorescence) expressions in atherosclerotic plaques of the aortic root sections in ApoE<sup>-/-</sup> mice after one month of treatments with free trehalose and TNG compared to the control, scale bars: 500  $\mu$ m.

**In vivo biosafety assessment**

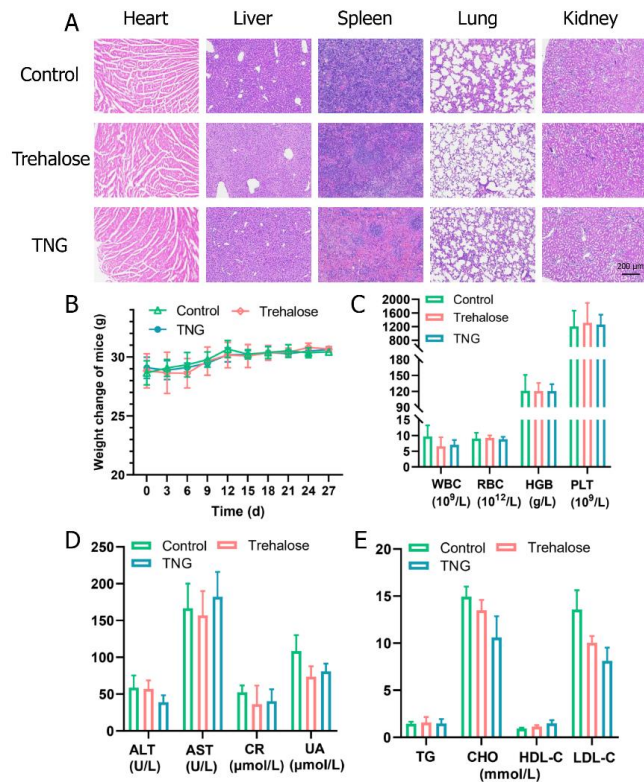


**Figure S9.** *In vivo* biosafety assessment of trehalose-releasing nanogels. **(A)** H&E-stained images of main organs from ApoE<sup>-/-</sup> mice after various treatments for one month. All the micrographs were acquired at 100× magnification, scale bar: 200 μm. **(B)** The body weight of ApoE<sup>-/-</sup> mice monitored over one month of treatments. **(C)** Complete blood count (CBC) profile of ApoE<sup>-/-</sup> mice after one month of treatments. WBC: white blood cells, RBC: red blood cells, HGB: hemoglobin, and PLT: platelets. **(D)** The biochemical assays of hepatic and kidney functions of ApoE<sup>-/-</sup> mice after one month of treatments. ALT: alanine aminotransferase, AST: aspartate aminotransferase, CR: creatinine, and UA: uric acid. **(E)** Blood lipid profile of ApoE<sup>-/-</sup> mice after one month of treatments. TG: triglycerides, CHO: total cholesterol, HDL-C: high-density lipoprotein (HDL) cholesterol, LDL-C: low-density lipoprotein (LDL) cholesterol. Data are presented as mean ± SD, n = 5.

## Publication [P5] Supplementary Information

Table S2. Comprehensive blood routine analysis and normal reference ranges in mice.

Samples	WBC ( $10^9/L$ )	RBC ( $10^{12}/L$ )	HGB (g/L)	PLT ( $10^9/L$ )
Reference range	0.8-10.6	6.5-11.5	110-165	400-1600
Control	$9.70 \pm 3.49$	$9.02 \pm 1.85$	$121.00 \pm 30.21$	$1207.60 \pm 461.50$
Trehalose	$6.54 \pm 2.88$	$9.22 \pm 0.84$	$120.60 \pm 15.42$	$1308.80 \pm 587.78$
TNG	$7.02 \pm 1.53$	$8.80 \pm 0.78$	$120.40 \pm 13.13$	$1260.80 \pm 290.49$

Table S3. Serum liver and kidney function indicators detection data and normal reference ranges in mice.

Samples	ALT (U/L)	AST (U/L)	CR ( $\mu\text{mol}/L$ )	UA ( $\mu\text{mol}/L$ )
Reference range	10.06-96.47	36.31-235.48	10.91-84.09	44.42-224.77
Control	$58.95 \pm 16.28$	$166.51 \pm 33.61$	$52.37 \pm 9.35$	$108.52 \pm 21.54$
Trehalose	$57.09 \pm 11.56$	$156.98 \pm 33.01$	$36.23 \pm 25.32$	$73.69 \pm 14.09$
TNG	$38.99 \pm 9.48$	$182.23 \pm 33.60$	$40.33 \pm 16.23$	$80.93 \pm 10.42$

Table S4. Serum lipid indicators detection data and normal reference ranges in mice.

Samples	TG (mmol/L)	CHO (mmol/L)	HDL-C (mmol/L)	LDL-C (mmol/L)
Reference range	0.84-2.72	2.05-4.16	1.28-2.65	0.12-0.26
Control	$1.43 \pm 0.22$	$14.94 \pm 1.06$	$0.94 \pm 0.09$	$13.58 \pm 2.05$
Trehalose	$1.57 \pm 0.59$	$13.49 \pm 1.10$	$1.14 \pm 0.15$	$10.04 \pm 0.72$
TNG	$1.47 \pm 0.47$	$10.62 \pm 2.24$	$1.49 \pm 0.33$	$8.13 \pm 1.39$

# Patent Application



URZĄD PATENTOWY  
RZECZYPOSPOLITEJ POLSKIEJ

al. Niepodległości 188/192  
00-950 Warszawa, skr. poczt. 203  
tel.: (+48) 22 579 05 55 | fax: (+48) 22 579 00 01  
e-mail: kontakt@uprp.gov.pl | www.uprp.gov.pl

Departament Zgłoszeń

Warszawa, 17.08.2021 r.

Nasz znak: DZ-NZ.P.438753.2.dbie

Wasz znak: RR6/PAT694/2021



t. 4651/64

rzecznik patentowy Katarzyna Borkowy  
POLITECHNIKA ŚLĄSKA  
ul. Akademicka 2 A  
44-100 Gliwice

## POTWIERDZENIE

Urząd Patentowy RP stwierdza, że dnia 2021-08-16 przyjęto w formie papierowej wnioski o udzielenie patentu na wynalazek pt.:

**Sposób otrzymywania nanożeli uwalniających kowalencyjnie związaną trehalozę**

Zgłoszenie oznaczono numerem: **P.438753**

[WIPO ST 10/C PL438753]

Zgłaszający: **POLITECHNIKA ŚLĄSKA, Gliwice, POLSKA**

Dominik Bielski

Specjalista

/podpisano kwalifikowanym podpisem elektronicznym/

Pismo wydane w formie dokumentu elektronicznego

### Pouczenie:

1. Strony oraz ich przedstawiciele i pełnomocnicy mają obowiązek zawiadomić Urząd o każdej zmianie swojego adresu. W razie zaniedbania tego obowiązku doręczenie pisma pod dotychczasowym adresem ma skutek prawny (art. 41 kpa).
2. O zgłoszeniu wynalazku Urząd Patentowy dokonuje ogłoszenia niezwłocznie po upływie 18 miesięcy od daty pierwszeństwa do uzyskania patentu. Zgłaszający może w okresie 12 miesięcy od daty pierwszeństwa złożyć wnioski o dokonanie ogłoszenia w terminie wcześniejszym (art. 43 ustawy z dnia 30 czerwca 2000r. Prawo własności przemysłowej (Dz. U. z 2021 r. poz. 324)).
3. W korespondencji należy powoływać się na nr P.438753.

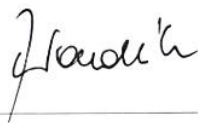

### Klauzula informacyjna

Zgodnie z art. 13 ust. 1 i 2 Rozporządzenia Parlamentu Europejskiego i Rady (UE) 2016/679 z dnia 27 kwietnia 2016 r. w sprawie ochrony osób fizycznych w związku z przetwarzaniem danych osobowych

# Patent Application

i w sprawie swobodnego przepływu takich danych oraz uchylenia dyrektywy 95/46/WE (dalej RODO) Urząd Patentowy Rzeczypospolitej Polskiej informuje, że:

1. Administratorem Pani/Pana danych osobowych jest Urząd Patentowy Rzeczypospolitej Polskiej z siedzibą w Warszawie, adres: al. Niepodległości 188/192, 00-950 Warszawa, skrytka pocztowa 203;
2. Inspektor Ochrony Danych, dane kontaktowe: adres: al. Niepodległości 188/192, 00-950 Warszawa, tel. bezpośredni (022) 579 00 25, fax (022) 579 00 01, e-mail: iod@uprp.pl;
3. Pani/Pana dane osobowe przetwarzane będą w celu realizowania zadań Urzędu Patentowego RP określonych przepisami ustawy z dnia 30 czerwca 2000 r. Prawo własności przemysłowej;
4. Podstawą prawną przetwarzania Pani/Pana danych osobowych jest ustawa z dnia 30 czerwca 2000 r. Prawo własności przemysłowej, rozporządzenia wykonawcze do ww. ustawy, umowy międzynarodowe oraz art. 6 ust. 1 lit. c RODO;
5. Pani/Pana dane osobowe mogą być przekazywane do podmiotów publicznych na zasadach obowiązujących w przepisach prawa oraz organizacjom międzynarodowym i organom unijnym, zgodnie z obowiązującymi przepisami prawa i umowami międzynarodowymi, po upływie terminów zastrzeżonych dla nieujawniania informacji o zgłoszeniu;
6. Pani/Pana dane osobowe będą przechowywane przez okres zgodny z zasadami archiwizacji dokumentów w Urzędzie Patentowym RP;
7. Posiada Pani/Pan prawo żądania dostępu do treści swoich danych osobowych, prawo ich sprostowania oraz prawo do ograniczenia ich przetwarzania;
8. Przysługuje Pani/Panu prawo wniesienia skargi do organu nadzorczego właściwego w zakresie ochrony danych osobowych gdy uzna Pani/Pan, że przetwarzanie Pani/Pana danych osobowych narusza przepisy RODO;
9. Podanie przez Panią/Pana danych osobowych jest wymogiem ustawowym niezbędnym do dalszego procedowania przez Urząd Patentowy RP.

Lp.	NAZWISKO i Imię	Udział współtwórców	Podpis
1.	WANDZIK Ilona	40%	
2.	MILEWSKA Małgorzata	40%	
3.	MARUF ALI	20%	